technische universität
dortmund

Dissertation zur Erlangung des
Doktorgrades der Naturwissenschaften

vorgelegt von

Daniel May[1]

Numerical Study of Magnetic Impurities in Graphene and Steady-State Transport in Quantum Impurity Systems

Technische Universität Dortmund
Fakultät Physik
Lehrstuhl für Theoretische Physik II

Januar 2020

[1]daniel.may@tu-dortmund.de

Erster Gutachter	Prof. Dr. Frithjof B. Anders
Zweiter Gutachter	Prof. Dr. Götz S. Uhrig

Contents

Publication List

- D. May, P.-W. Lo, K. Deltenre, A. Henke, J. Mao, Y. Jiang, G. Li, E. Y. Andrei, G.-Y. Guo, F. B. Anders, *Modeling of the gate-controlled Kondo effect at carbon point defects in graphene*, Phys. Rev. B **97**, 155419 (2018).
- Y. Jiang, P.-W. Lo, D. May, G. Li, G.-Y. Guo, F. B. Anders, T. Taniguchi, K. Watanabe, J. Mao, E. Y. Andrei, *Inducing Kondo screening of vacancy magnetic moments in graphene with gating and local curvature*, Nature Communications **9**, 2349 (2018).
- Y. Vinkler-Aviv, D. May, F. B. Anders, *Analytical and numerical study of the out-of-equilibrium current through a helical edge coupled to a magnetic impurity*, arXiv:1912.02838, submitted to Phys. Rev. B at the time of writing.

Acknowledgments

First and foremost I would like to thank my advisor Prof. Frithjof B. Anders for his support and advise during the last years. I would like to thank all members of the T2 department for the wonderful time. My special thanks goes to Fabian Eickhoff for our numerous discussions,to Natalie Jäschke for all the years since the beginning of our studies, and to my girlfriend Nina Fröhling for her support and understanding.

Chapter 1

Introduction

A fundamental problem in condensed matter physics is the low-temperature behavior of magnetic impurities in host materials. The study of these so-called 'quantum impurity problems' has become a mature field of work of condensed matter physics over the last couple of decades since the groundbreaking work of Anderson and Kondo in the early '60s [1, 2]. Their work has never been more relevant than today, especially due to the recent move towards nano-scale electronics, and the advent of research on spin based devices, dubbed 'spintronics'[3]. Knowledge of the underlying physics and accurate simulation of the electronic behavior in the proximity of such magnetic impurities is essential for the development of tunable devices that exploit the spin of the electrons in addition to their charge.

The existence and screening of local magnetic moments has been recently observed in carbon vacancies in graphene [4, 5, 6, 7, 8], a material that piqued the interest of the scientific community. One study in particular [9] found two different types of vacancies that differ only in the rippling inherent to the single-atom thick graphene sheet. They show magnetic or non-magnetic behavior depending on the local curvature and external voltage. In the first part of this thesis, we address the issue of these different types of vacancies. We develop a comprehensive model for the relevant electronic orbitals in proximity of such a carbon impurity, and explain successfully the underlying physics in detail. Our numerical method of choice is Wilson's Numerical Renormalization Group [10, 11], a staple technique for quantum impurity systems with unparalleled numerical precision.

We then turn away from graphene and thermal equilibrium and towards electron transport through strongly correlated nano-scale regions in the second part of this thesis. We first review electron transport in the context of a toy-model to establish the needed groundwork. We then turn to a realistic model for the helical current along the 1d edge of a Quantum Spin Hall Insulator when perturbed by a single magnetic impurity [12]. Our quantitative discussion relies on the time-dependent extension of the Numerical Renormalization Group [13, 14]. We finally attempt our own novel approach to steady-state problems by drawing

from Hershfield's theoretical work on the nature of the non-equilibrium distribution [15]. Our resulting adaption of the Numerical Renormalization Group is tailor-made for the steady-state. We discuss some preliminary results as well as the current limitations of our new approach.

Chapter 2

Quantum Impurity Systems and the Numerical Renormalization Group in Thermodynamic Equilibrium

Quantum impurity systems consist of a strongly correlated sub-system, for example a single magnetic moment or interacting orbital, coupled to a continuum of non-interacting electrons. Originally, this continuum is modeled after the conduction band of a metallic host while the localized magnetic moment stems from magnetic impurities. We introduce two of the most prominent and wide-spread models for these systems, the Kondo model [2] in Sec. 2.1 and the Single Impurity Anderson Model (SIAM) [1] in Sec. 2.2. Both exhibit non-trivial many-body physics despite their simplistic seeming nature.

Today these original models usually serve as well understood minimalist toy-problems, but modified versions are still used in recent publications in a multitude of circumstances. These modifications include among others multiple localized orbitals or magnetic moments and their interactions [11], pseudogap density of states for the host material [16, 17, 18, 19], bosonic baths [20, 21], single bosonic degrees of freedom [22, 23], or even superconductive bands [24]. Other studies discuss multi-channel Kondo problems, where impurities are coupled to multiple electronic bands [25], or multiple impurities [26, 27, 28, 29, 30]. A comprehensive introduction to multi-channel and multi-impurity systems can be found in the review by Bulla et al. [11].

We then introduce Wilson's Numerical Renormalization Group (NRG) technique for quantum impurity systems conceived originally in the 1970s [10]. Initially, the NRG was applied to solve the Kondo problem [2] which, despite prior efforts of Anderson and his Poor Man's Scaling [31], still lacked a completely satisfactory explanation. The NRG is designed to treat a range of widely different energy scales in a non-perturbative manner. These energy scales extend from several electronvolts on the scale of the bandwidth D down to exponentially small excitations. Its non-perturbative nature is key to the success of the NRG

which consequently allows studying of a whole class of problems that are plagued by infrared divergences in a perturbative approach.

2.1 The Kondo Problem and Anderson's Poor Man's Scaling

The origin of the physical problem, which has been later termed 'Kondo problem', dates back almost a century to experimental studies by de Haas, de Boer, and van den Berg [32, 33]. They measured the resistivity of gold that contained a small percentage of iron. The puzzling result was a bulk resistivity that showed a minimum as function of temperature at some finite value $T_{\min}$ and increased for $T < T_{\min}$. Kondo [2] was the first to realize the importance of magnetic scattering in these types of materials, and devised a formula for the resistivity based on a s-d Hamiltonian [34] almost 30 years after de Haas's, de Boer's, and van den Berg's discovery. The simplified version of Kondo's Hamiltonian reads

$$H_{\text{Kondo}} = \sum_{\vec{k}\sigma} \epsilon_{\vec{k}\sigma} c^{\dagger}_{\vec{k}\sigma} c_{\vec{k}\sigma} + J \vec{S}_{\text{imp}} \vec{s}_{\text{c}}, \tag{2.1.1}$$

where $c^{(\dagger)}_{\vec{k}\sigma}$ are fermionic annihilation (creation) operator with spin σ and momentum $\vec{k}$. The first term describes a non-interacting conduction band with dispersion $\epsilon_{\vec{k}\sigma}$. The second term comprises a coupling between a localized magnetic moment, $\vec{S}_{\text{imp}}$, to the spin density of the aforementioned conduction band at the impurity, $\vec{s}_{\text{c}}$, via an exchange coupling J. The spin operator of the band can be written in terms of the fermionic operators with help of the usual Pauli matrices $\vec{\sigma}$ (N equals the number of unit cells)

$$\vec{s}_{\text{c}} = \frac{1}{2N} \sum_{\vec{k}\vec{k}'} \sum_{\lambda\mu} c^{\dagger}_{\vec{k}\lambda} \vec{\sigma}_{\lambda\mu} c_{\vec{k}'\mu}. \tag{2.1.2}$$

The contribution to the resistivity, that stems from magnetic scattering at such an impurity up to third order in the anti-ferromagnetic couplings $J > 0$, takes the form [2, 35]

$$R^{\text{spin}}_{\text{imp}} = \frac{3\pi m J^2 S(S+1)}{2e^2 \hbar \epsilon_F} \Big[1 - J\rho_0(\epsilon_F) \ln\Big(\frac{k_{\text{B}} T}{D}\Big) \Big], \tag{2.1.3}$$

where $S = 1/2$, $\rho_0(\epsilon)$ is the density of states, ϵ_F the Fermi energy, and D the bandwidth. The key point is that for ferromagnetic coupling, $J < 0$, the spins of both the localized moment and the conduction band are aligned whereas they are antiparallel for $J > 0$. This antiparallel orientation enables two second-order spin-flip terms between energy degenerate spin states, which yield a logarithmically divergent low temperature contribution at ϵ_{F} [2, 35]. Such a divergence is called 'infrared divergence' in quantum field theory.

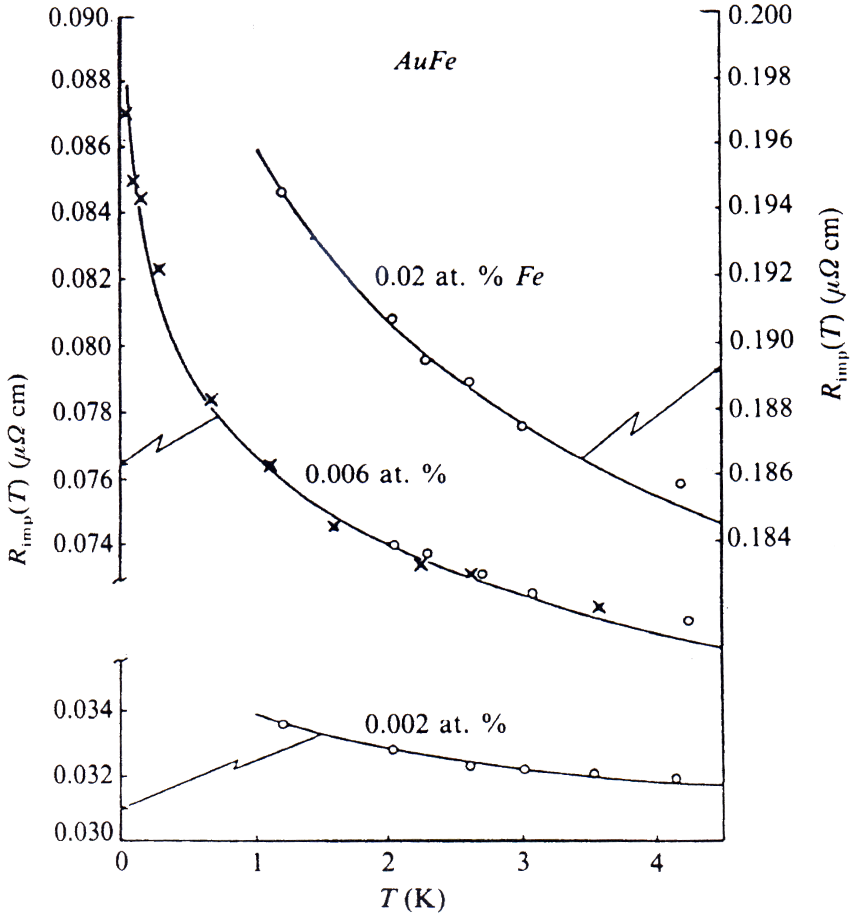

Figure 2.1: Kondo's logarithmic formula 2.1.4 applied to experimental results for the resistivity of AuFe for various concentrations of Fe. Taken from Ref. [35] which is again a reproduction from results published in Ref. [2].

The total resistivity including phonon scattering then reads

$$R(T) = aT^5 + c_{\text{imp}} R_0 - c_{\text{imp}} R_1 \ln\left(\frac{k_{\text{B}} T}{D}\right), \tag{2.1.4}$$

where a, R_0, R_1 are temperature independent constants and c_{imp} is the concentration of iron ions. The decoherence due to phonon scattering is strongly suppressed, $\sim T^5$, as the temperature vanishes, leaving a constant term due to potential scattering at the site of the impurities as well as a logarithmic contribution from the magnetic scattering. This formula is able to explain the experimental data extremely well (cf. Fig. 2.1). However, since the perturbation theory diverges at $T \to 0$, Kondo's approach is not feasible for all temperatures down to infinitesimal small values. One can define a characteristic temperature, called Kondo temperature, below which the scattering rate begins to diverge logarithmically

$$T_{\text{K}} = D\sqrt{\rho_0 J}\, \mathrm{e}^{-\frac{1}{\rho_0 J}}. \tag{2.1.5}$$

The search for a valid solution below T_K defines the 'Kondo problem'. Two approaches are of peculiar interest. Firstly, Anderson's Poor Man's Scaling [31] that draws on renormalization group (RG) techniques and grants us a tangible explanation for the breakdown of the perturbation series with flow equations for the renormalized couplings. Secondly, Wilson's Numerical Renormalization Group (NRG) [10] which provided the first complete and non-perturbative solution, and is used throughout this thesis.

Anderson used the more general form of the anisotropic Kondo model where the Heisenberg term is split into a transversal and a z-component

$$J\vec{S}_\mathrm{imp}\cdot\vec{s}_c = J_z S^z_\mathrm{imp}s^z_c + \frac{1}{2}J_\perp(S^+_\mathrm{imp}s^-_c + h.c.). \tag{2.1.6}$$

He employs a perturbative RG technique in which he eliminates high order excitations to generate an effective low-energy model. His approach is widely known in literature as 'Poor Man's Scaling'. Anderson derived a set of differential equations for the flow of the different coupling components,

$$\frac{\mathrm{d}\widetilde{J}_\perp}{\mathrm{d}\ln D} = -\widetilde{J}_\perp\widetilde{J}_z \qquad \text{and} \qquad \frac{\mathrm{d}\widetilde{J}_z}{\mathrm{d}\ln D} = -\widetilde{J}^2_\perp \tag{2.1.7}$$

with $\widetilde{J} = \rho_0 J$, to construct an effective model at energy scale D. Depending on the initial values for $J_\perp$ and J_z, the system evolves under the RG procedure until it arrives at a so-called fixed-point. These are points in parameter space where the flow of the couplings vanishes, i.e. where the flow equations assume a stationary value. Fig. 2.2 shows a schematic view for the flow of these equation. Anderson identified a local moment fixed-point (LM) which is reached for vanishing $J_\perp$ or for ferromagnetic $J_z < 0$ if $|J_\perp| \leq |J_z|$. In all other cases, the couplings flow to the so-called strong coupling fixed-point (SC) where $J_\perp, J_z \to \infty$, explaining the breakdown of any perturbative approach in J for $T \to 0$. In the isotropic case, $J = J_\perp = J_z$, the differential equations simplify and can be integrated analytically. The solution for $\widetilde{J}$ diverges at the Kondo temperature Eq. (2.1.5). The SC fixed-point is characterized by a singlet formation between localized moment and spin density of the conduction band. The screening cloud of this singlet extends inversely proportional to the Kondo temperature and can reach even macroscopic length scales due to the exponential dependency of T_K on the Kondo coupling [36, 37, 38]. The impurity spin is screened by the electron cloud of the conduction band and the singlet, called Kondo singlet, decouples from the band.

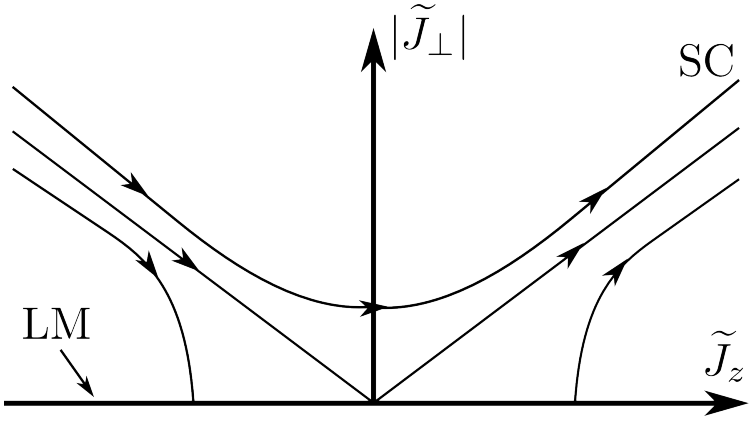

Figure 2.2: Schematic representation of the coupling's flow $\widetilde{J}_\perp$ and $\widetilde{J}_z$ for the anisotropic Kondo model (after [31]). The final stable fixed points depend on the initial values of $\widetilde{J}_\perp$ and $\widetilde{J}_z$: (i) For $-\widetilde{J}_z > |\widetilde{J}_\perp|$ and $\widetilde{J}_z < 0$ the system is driven towards a line of local moment (LM) fixed points (abscissa for $\widetilde{J}_z < 0$). In every other case, the system reaches a strong coupling fixed point (SC). Adopted after Ref. [31].

2.2 The Single Impurity Anderson Model

The Single Impurity Anderson Model (SIAM) [1] was proposed by Anderson in the early 1960s to describe the formation of local moments in transition metals or rare earth impurities in metals. When these ions are brought into the host material, they result in open d or f levels that are located in the conduction band of the host [35]. Anderson's Hamiltonian takes the form

$$H = \sum_\sigma \epsilon_d d_\sigma^\dagger d_\sigma + U n_\uparrow^d n_\downarrow^d + g\mu_B \vec{B}_{\text{ext}} \cdot \vec{S} + \sum_{\vec{k}\sigma} \epsilon_{\vec{k}} c_{\vec{k}\sigma}^\dagger c_{\vec{k}\sigma} + \sum_{\vec{k}\sigma} \left(V_{\vec{k}} d_\sigma^\dagger c_{\vec{k}\sigma} + h.c. \right), \tag{2.2.1}$$

where d_σ and $c_{\vec{k}\sigma}$ are the fermionic operators for the impurity level and the conduction band respectively with spin σ and reciprocal vector $\vec{k}$. The first three terms are the impurity part, H_{imp}, including an interaction with a local external magnetic field, $\vec{B}_{\text{ext}} \cdot \vec{S}$. Here, $\vec{S} = 1/2 \sum_{\lambda,\mu} d_\lambda^\dagger \vec{\sigma} d_\mu$ is the spin operator for the electrons on the impurity orbital written in terms of the fermionic creation and annihilation operators and the Pauli matrices $\vec{\sigma}$. Strictly speaking, the magnetic field applies to the electrons on the d orbital as well as to those in the conduction band. The latter contribution, however, simply results in a shift of the band edges, which is negligible.

Furthermore, the Hamiltonian comprises a Coulomb interaction U [35]

$$U = \mathrm{e}^2 \int \phi_d^*(\vec{r}) \phi_d^*(\vec{r}') \frac{1}{\vec{r} - \vec{r}'} \phi_d(\vec{r}) \phi_d(\vec{r}') \mathrm{d}r \mathrm{d}r', \tag{2.2.2}$$

where ϕ_d are the localized eigenfunctions of the atomic d orbital. Naive evaluation of Eq. (2.2.2) yields interactions up to 30 eV. Modern ab initio approaches correct

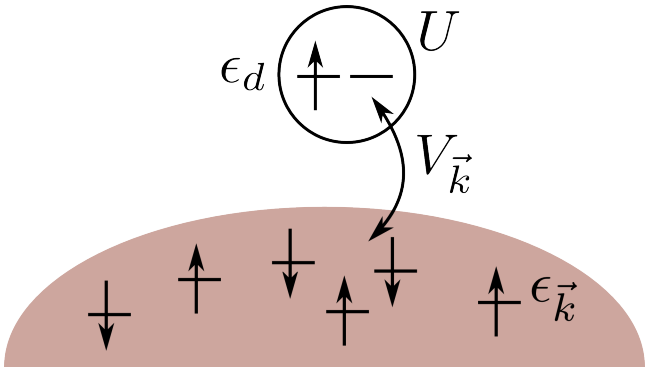

Figure 2.3: Schematic picture of a localized d orbital with spin-degenerate single particle energy ϵ_d coupled to a non-interacting electronic bath as described by the SIAM Hamiltonian Eq. (2.2.1). The model comprises a repulsive Coulomb interaction for electrons located on the d level and a hybridization between d sub-system and conduction band. The interaction with $\vec{B}_{\text{ext}}$ is not shown.

this value by incorporating, among others, screening effects [35, 39, 40] that results in a realistic repulsion strength of a few electronvolts. Accurate calculation of model parameters from Density Functional Theory is a broad topic beyond the scope of this work, and the interested reader is referred to Ref. [39, 40].

The last term in Eq. (2.2.1) contains a coupling between the d sub-system and the itinerant electrons via a hybridization $V_{\vec{k}}$ that stems from non-vanishing matrix elements

$$V_{\vec{k}} = \sum_n \mathrm{e}^{\mathrm{i}\vec{k}\cdot\vec{r}_n} \langle \phi_d | H | \psi_{\vec{r}_n} \rangle, \qquad \psi_{\vec{r}_n}(\vec{r}) = \frac{1}{\sqrt{N}} \sum_{\vec{k}} \mathrm{e}^{-\mathrm{i}\vec{k}\cdot\vec{r}_n} \phi_{\vec{k}}(\vec{r}). \tag{2.2.3}$$

The second equation defines the Wannier wavefunction of the conduction electrons, $\psi_{\vec{r}_n}$, at the location of the d shell [35, 1] in terms of the Bloch states $\phi_{\vec{k}}(\vec{r})$. The remaining two terms of the Hamiltonian (2.2.1) represent the level position ϵ_d and a free electron gas for the conduction electrons with dispersion $\epsilon_{\vec{k}}$. A schematic depiction of the model is shown in Fig. 2.3.

In the limit of vanishing intra-orbital Coulomb interaction, $U = 0$, the SIAM reduces to its non-interacting counterpart which can be solved analytically [35]. The Green's function for the impurity level d in frequency space can be readily obtained by an equation of motion ($z = \omega + \mathrm{i}\delta$)

$$G^{U=0}_{d_\sigma, d^\dagger_\sigma}(z) = \Big[z - \epsilon_d - \Delta_\sigma(z) \Big]^{-1}, \qquad \Delta_\sigma(z) = \sum_{\vec{k}} \frac{|V_{\vec{k}}|^2}{z - \epsilon_{\vec{k}}}, \tag{2.2.4}$$

where the only contribution to the self-energy, $\Delta_\sigma(z)$, stems from the hybridization with the conduction band. In the interacting case, $U \neq 0$, complex terms involving more fermionic operators enter the equation of motion. However, one can still write down a formal solution in terms of the self-energy $\Sigma^U(z)$

$$G_{d_\sigma, d^\dagger_\sigma}(z) = \Big[z - \epsilon_d - \Delta_\sigma(z) - \Sigma^U(z) \Big]^{-1}. \tag{2.2.5}$$

Let us consider the model in the 'atomic' limit for $V_{\vec{k}} = 0$. The Hilbert space consists of two distinct sub-spaces for the impurity and the band. The impurity part contains only four states: an entire unoccupied state with energy $E_0 = 0$, a doubly occupied state with energy $E_{\uparrow\downarrow} = 2\epsilon_d + U$, and two singly occupied states with degenerate energy $E_\sigma = \epsilon_d$. A ground state that belongs to the single occupation sector will yield a magnetic moment [35]. When the hybridization is turned on, electrons can transfer between both sub-systems. This hopping induces an effective anti-ferromagnetic coupling which results in a screening process of the local magnet moment analogous to the Kondo screening discussed in Sec. 2.1. As shown by Schrieffer and Wolff [41], the Anderson and Kondo model are closely related via a canonical transformation. The hybridization generates an effective anti-ferromagnetic exchange interaction between the localized spin and the conduction electrons. If the system is in the regime of a local magnetic moment and if the hybridization $V_{\vec{k}}^2/D \ll 1$ is small enough, then the Anderson Model is equivalent to the Kondo model [35].

The SIAM serves as foundation for a multitude of theoretical models. Since it also plays a major role within the scope of this work, we review the SIAM in more detail in the following sections.

2.3 Wilson's Numerical Renormalization Group in Thermodynamic Equilibrium

In this section we present the Numerical Renormalization Group (NRG) framework [10]. We discuss the core concepts such as the type of problems the NRG is suited for, the logarithmic discretization of the conduction band, the mapping of the Hamiltonian to a discrete chain of semi-infinite length, and the calculation of observables. A complete review of the method can be found in Ref. [11].

The core idea of the NRG algorithm is to map the Hamiltonian of an impurity problem onto a semi-infinite tight-binding chain with exponentially decreasing hopping parameters between consecutive chain sites. Instead of solving the whole Hamiltonian at once, one proceeds iteratively by adding one chain link after the other. Each successive iteration is associated with an exponentially smaller effective temperature due to the decreasing energy scale. This enables the formulation of a natural truncation process where in each iteration the set of eigenstates is partitioned according to their energy into either high or low energy excitations. The high energy states are discarded in order to tackle the otherwise exponentially growing Hilbert space.

In his original publication [10] Wilson focused on the solution of the Kondo problem. Krishna-Murthy et al. extended the NRG to the more general Anderson impurity including a throughout discussion of the nature of various fixed points [42, 43]. Each iteration of the NRG algorithm can be understood as per-

forming one renormalization group transformation R [11]

$$H_{N+1} = R(H_N) \tag{2.3.1}$$

that maps the old Hamiltonian H_N to the new Hamiltonian H_{N+1}. A fixed point H^* is reached when the mapping R does not alter the eigenspectrum of H^* any further. This can readily be verified by comparing the eigenenergies of successive Hamiltonians.

The NRG procedure can be applied for quantum impurity problems of the following form

$$H = H_{\text{imp}} + H_{\text{band}} + H_{\text{hyb}}, \tag{2.3.2}$$

where the total Hamiltonian comprises three parts. The first of which, H_{imp}, includes terms that involve only local degrees of freedom usually connected to a single ion or molecule. In the following, we explicitly use the SIAM (see Sec. 2.2) as a tangible example. In this case, H_{imp} comprises the first three terms of Eq. (2.2.1). The second part describes the conduction band of the host material where the electrons of the band are taken to be non-interacting (third term in Eq. (2.2.1) for the SIAM). The hybridization part, H_{hyb}, incorporates all terms that couple both the local and itinerant degrees of freedom. In case of the SIAM this includes the last term of Eq. (2.2.1). Every band degree of freedom couples via the hybridization $V_{\vec{k}}$ to the localized level. Oftentimes this hybridization is taken to be $\vec{k}$-independent.

The first step is to carry out a transformation from a discrete albeit large set of distinct $\vec{k}$-space values to a continuum description in terms of the energy. The new fermionic operators take the form

$$c_\sigma(\epsilon) = \mathcal{N}_\sigma(\epsilon) \sum_{\vec{k}\sigma} V_{\vec{k}} \delta(\epsilon - \epsilon_{\vec{k}}) c_{\vec{k}\sigma}, \tag{2.3.3}$$

where $\delta(\epsilon - \epsilon_{\vec{k}})$ is the Dirac δ-distribution, and $\mathcal{N}_\sigma(\epsilon) = \sqrt{\pi/\Gamma(\epsilon)}$ is the appropriate normalization factor to ensure the fermionic commutator relation $\{c_\sigma(\epsilon), c^\dagger_{\sigma'}(\epsilon')\} = \delta_{\sigma,\sigma'}\delta(\epsilon - \epsilon')$. Inserting this transformation into Eq.(2.2.1) yields

$$H = H_{\text{imp}} + \sum_\sigma \int_{-D}^{D} g(\epsilon) c^\dagger_\sigma(\epsilon) c_\sigma(\epsilon) \mathrm{d}\epsilon + \sum_\sigma \int_{-D}^{D} h(\epsilon) \Big(d^\dagger_\sigma c_\sigma(\epsilon) + h.c. \Big) \mathrm{d}\epsilon. \tag{2.3.4}$$

The integral extends over the full bandwidth $2D$ of the conduction band. The energy dependency can be freely shuffled between the dispersion $g(\epsilon)$ and coupling $h(\epsilon)$ as long as the hybridization function and thus the action remains the same [11, 16]. Here we also introduce the hybridization function

$$\Gamma(\epsilon) = \pi \sum_{\vec{k}} |V_{\vec{k}}|^2 \delta(\epsilon - \epsilon_{\vec{k}}) = \Im\Delta(\epsilon - \mathrm{i}\delta), \tag{2.3.5}$$

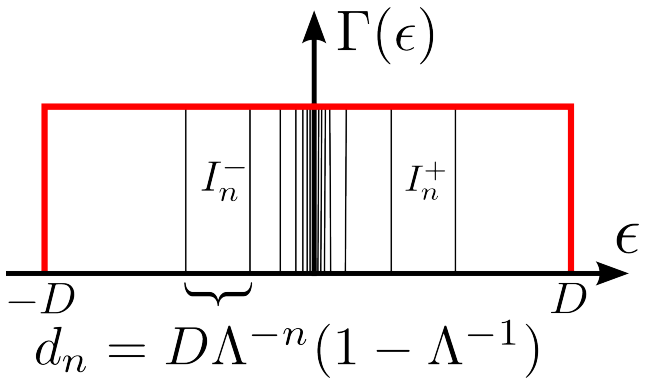

Figure 2.4: Schematic representation of a logarithmic discretization of a constant hybridization function with half-bandwidth D. The nth interval $I_n^\pm$ has the width d_n.

that describes the coupling of each energy shell to the impurity degrees of freedom. $\Delta(z)$ is defined in Eq. (2.2.4) as the self-energy contribution that stems solely from coupling to the band. For a $\vec{k}$-independent hybridization V and a constant density of states $\rho = (2D)^{-1}$ the hybridization function simplifies to

$$\Gamma(\epsilon) = \pi|V|^2\rho(\epsilon) = \frac{\pi|V|^2}{2D} \equiv \Gamma_0\Theta(D-|\epsilon|), \tag{2.3.6}$$

which us used throughout this work to define a relative energy scale for all parameters. The Heavyside function Θ cuts off the hybridization outside the band.

The second step is to logarithmically discretize the energy bands around the Fermi energy with a dimensionless discretization parameter $\Lambda > 1$ (cf. Fig. 2.4). The intervals are $I_n^s = \left[sD\Lambda^{-n}, sD\Lambda^{-(n+1)}\right]$ with a width $d_n = D\Lambda^{-n}(1-\Lambda^{-1})$. The superscript $s = \pm$ distinguishes between positive or negative energy. One defines new operators for each interval $I_n^\pm$ and expands the original operators in this new basis $a_{snp\sigma}$. Thus, the energy dependent band operators read

$$c_\sigma(\epsilon) = \sum_{n=0}^{\infty}\sum_{s=\pm}\sum_{p=-\infty}^{\infty} \psi_{np}^s(\epsilon)a_{snp\sigma}, \tag{2.3.7}$$

where $\psi_{np}^s(\epsilon)$ takes the form of a plane wave restricted to the nth interval

$$\psi_{np}^s(\epsilon) = \begin{cases} d_n^{-1/2}\mathrm{e}^{s\frac{2\pi \mathrm{i}p\epsilon}{d_n}}, & \epsilon \in I_n^s \\ 0, & \text{else.} \end{cases} \tag{2.3.8}$$

The inverse transformation reads

$$a_{snp\sigma} = \int_{-D}^{D} \left[\psi_{np}^s(\epsilon)\right]^* c_\sigma(\epsilon)\mathrm{d}\epsilon, \tag{2.3.9}$$

where the coefficient can be obtained from the fermionic commutator relation $\{a_{nsp\sigma}^\dagger, a_{n's'p'\sigma'}\} = \delta_{n,n'}\delta_{s,s'}\delta_{p,p'}\delta_{\sigma,\sigma'}$. We insert the transformation back into our Hamiltonian (2.3.4) and neglect all $p \neq 0$ modes. For a constant hybridization in

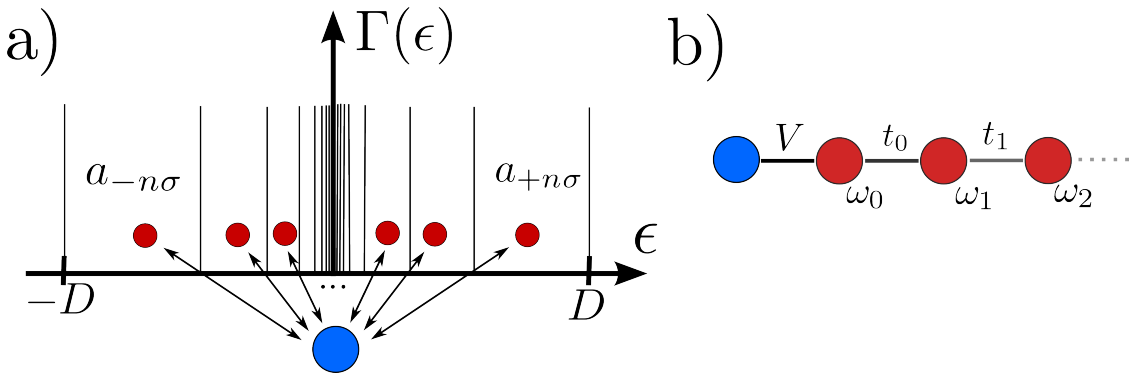

Figure 2.5: Schematic drawing of the NRG algorithm: (a) Each interval is represented by a single state only that couples to the local degrees of freedom (blue). (b) The system is mapped via a tridiagonalization algorithm onto a semi-infinite tight-binding chain with exponentially decreasing hopping parameters t_n. The hybridization is $\vec{k}$-independent.

each interval the hybridization term reduces to a coupling between the impurity and $p = 0$ states [11]. The $p \neq 0$ modes only indirectly couple with the local degrees of freedom. We follow the argument of Ref. [16] and shifting the energy dependence into the dispersion and introducing a hybridization that is constant in each interval. The new single particle energies of the transformed conduction band term can then be written as

$$\xi_{sn} = \frac{\int^{sn} \Gamma(\epsilon)\epsilon \mathrm{d}\epsilon}{\int^{sn} \Gamma(\epsilon)\mathrm{d}\epsilon}. \tag{2.3.10}$$

The integral $\int^{sn}$ is a shorthand notation for the integral over the nth interval for positive $s = +$ or negative $s = -$ energy. We drop the subscript $p = 0$ in the following for clarity. The discretized Hamiltonian then takes the form

$$H = H_{\mathrm{imp}} + \sum_{sn\sigma}^{\infty} \xi_{sn} a^{\dagger}_{sn\sigma} a_{sn\sigma} + \frac{1}{\sqrt{\pi}} \sum_{s\sigma n=0}^{\infty} \gamma_{sn} (d^{\dagger}_{\sigma} a_{sn\sigma} + h.c.), \tag{2.3.11}$$

where the factor γ_{sn} can be determined by comparison with Eq. (2.3.4) [11]

$$\gamma^2_{sn} = \int^{sn} \Gamma(\epsilon)\mathrm{d}\epsilon. \tag{2.3.12}$$

This Hamiltonian describes a local part still coupled to an infinite number of band degrees of freedom [Fig. 2.5 (a)]. The next step is the mapping of Eq. 2.3.11 onto a semi-infinite chain via a tridiagonalization algorithm. One can derive recursive relations that need a linear combination for the first chain site as initialization. The natural choice is to define the fermionic degree of freedom that couples to the impurity directly as starting point for the tridiagonalization

$$c_{0\sigma} = \frac{1}{\sqrt{\xi_0}} \sum_{sn} \gamma_{sn} a_{n\sigma}, \qquad \xi_0 = \int_{-D}^{D} \Gamma(\epsilon)\mathrm{d}\epsilon. \tag{2.3.13}$$

Note that for a $\vec{k}$-independent hybridization, $V_{\vec{k}} \equiv V$, the normalization factor simply reduces to $\xi_0 = \pi V^2$. For a more in-depth derivation and an explicit formula for the recursion refer to Ref. [21, 11]. Lastly, we want the final Hamiltonian to take the form of a tight-binding chain

$$H = H_{\text{imp}} + \sqrt{\frac{\xi_0}{\pi}} \sum_{\sigma} (d_\sigma^\dagger c_{0\sigma} + h.c.) + \sum_{\sigma n=0}^{\infty} (\omega_n c_{n\sigma}^\dagger c_{n\sigma} + t_n [c_{n\sigma}^\dagger c_{n+1\sigma} + h.c.]), \tag{2.3.14}$$

where $c_{n\sigma}$ are the fermionic operators of the nth chain site and ω_n and t_n are the chain-site energy and hopping stemming from the recursive relations [Fig. 2.5 (b)]. The energy for the sites vanish, $\omega_n = 0$, in case of a constant $\rho(\epsilon)$. A key point is that the hopping elements scale according to

$$t_n \propto \frac{1}{2}(1 + \Lambda^{-1})\Lambda^{-n/2} \tag{2.3.15}$$

in the limit of large n. They decrease exponentially with n as a result of the logarithmic discretization. This enables us to introduce a truncation scheme based on the separation of energy scales governed by Eq. (2.3.15) as the chain Hamiltonian (2.3.14) is yet to be solved efficiently. For this, we can rewrite it formally as a sequence of Hamiltonians

$$H = \lim_{N\to\infty} \Lambda^{-(N-1)/2} H_N, \tag{2.3.16}$$

where

$$\begin{aligned} H_N =& \Lambda^{(N-1)/2} \Big(H_{\text{imp}} + \sqrt{\frac{\xi_0}{\pi}} \sum_{\sigma} (d_\sigma^\dagger c_{0\sigma} + h.c.) \\ &+ \sum_{\sigma n=0}^{N} \omega_n c_{n\sigma}^\dagger c_{n\sigma} + \sum_{n\sigma=0}^{N-1} t_n [c_{n\sigma}^\dagger c_{n-1\sigma} + h.c.] \Big). \end{aligned} \tag{2.3.17}$$

Here, the factor $\Lambda^{(N-1)/2}$ is incorporated such that $t_{N-1}\Lambda^{(N-1)/2}$ is of order one for large N. Successive terms are connected to each other via an iterative relationship

$$\begin{aligned} H_{N+1} =& \sqrt{\Lambda} H_N + \Lambda^{N/2} \sum_{\sigma} \omega_{N+1} c_{N+1\sigma}^\dagger c_{N+1\sigma} \\ &+ \Lambda^{N/2} \sum_{\sigma} t_N (c_{N\sigma}^\dagger c_{N+1\sigma} + h.c). \end{aligned} \tag{2.3.18}$$

This iterative relation corresponds to the addition of the $N+1$st chain site in the language of our semi-infinite chain (cf. Fig. 2.6). Furthermore, we can link a chain of length N naturally with an energy or temperature scale [11]

$$D\beta_N \Lambda^{-(N-1)/2} = \overline{\beta}, \tag{2.3.19}$$

where $\beta_N = (k_B T_N)^{-1}$ is the inverse temperature for the Nth iteration and $\overline{\beta}$ is of order 1. Assume a chain of finite length and a finite $\Lambda > 1$. In order to evaluate

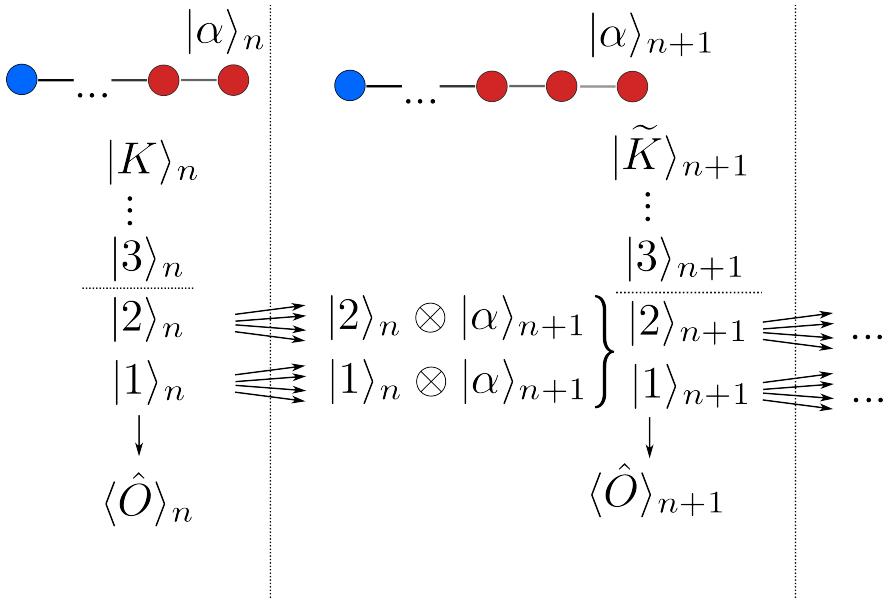

Figure 2.6: Schematic drawing of the addition of the $n+1$st chain site. The eigenstates $|k\rangle_n, k = 1, 2, 3, \ldots, K$ of the Hamiltonian in iteration n are partitioned according to their energy in high and low energy states. The low energy states are used to generate product states for the $n+1$st iteration by a Kronecker product with the degrees of freedom $|\alpha\rangle_{n+1}$ of the newly added site. The $n+1$st Hamiltonian is written in this basis and diagonalized; its eigenstates partitioned again for the addition of the next site. In each iteration, the eigenspectrum is used to calculate quantum mechanical expectation values.

expectation values for a temperature that lies in-between two iterations one can either change Λ and the iteration or adjust $\overline{\beta}$ slightly. From a technical point of view, $\overline{\beta}$ thus allows for a fine-tuning of the desired temperature.

If considered in isolation, an iterative formulation may not seem to provide any tangible benefit. However, in conjunction with an appropriate truncation scheme it enables us to generate and solve an effective low-energy Hamiltonian step-by-step circumventing an exponentially growing Hilbert space. Consider a chain of length N. By adding the next site we introduce a small energy splitting in the order of t_N since the hopping elements decrease exponentially. This is guaranteed if t_N is smaller than the largest kept eigenenergy. Therefore, states with a high (low) eigenenergy for a chain of length N will predominantly contribute to the high-energy (low-energy) spectrum of the next iteration. It is the low energy spectrum that is the most relevant to us since we are usually interested in low temperature properties. This leads to a truncation scheme where all eigenstates at a given chain length N are partitioned according to their eigenenergy. The high energy states are then discarded and only the low energy ones are coupled to the new fermionic degree of freedom. The NRG procedure thus restricts the full Hilbert space systematically to a smaller and more manageable set of relevant states.

The quality of the truncation is not apparent a priori. It depends foremost on

the discretization parameter Λ and the number of retained states N_{kept} and has to be checked in practice. For a simple problem a few hundreds states may be sufficient whereas a multi-band calculation will require several thousands states for any meaningful result.

With the truncation scheme at hand and the definition of the temperature for a given iteration N, Eq. (2.3.19), we turn to the actual calculation of static observables. We employ the conventional NRG assumption that the full Hamiltonian is adequately described by our truncated H_N with $H_N|r\rangle_N = E_r^N|r\rangle_N$. We then define the expectation value of an operator $\hat{O}$ as [11]

$$\langle\hat{O}\rangle(T_N) = \frac{1}{Z^{(N)}}\sum_r \mathrm{e}^{-\beta_N E_r^N}\ {}_N\langle r|\hat{O}|r\rangle_N \tag{2.3.20}$$

where

$$Z^{(N)} = \sum_r \mathrm{e}^{-\beta E_r^N}. \tag{2.3.21}$$

One can furthermore calculate the contribution to the entropy that stems from the impurity. It is defined as the difference between the entropy for the whole Wilson chain and a reference system that is missing the impurity degrees of freedom [10, 11]. The entropy for a temperature T_N reads

$$S_{\text{imp}}(T_N)/k_b \approx S^{(N)}/k_B - S_{\text{cb}}^{(N)}/k_B. \tag{2.3.22}$$

Here, $S^{(N)}$ is the entropy for the Wilson chain of length N including the impurity

$$S^{(N)}/k_B = \beta\langle H^{(N)}\rangle + \ln Z^{(N)}, \quad Z^{(N)} = \sum_r \mathrm{e}^{-\beta E_r^N}. \tag{2.3.23}$$

The second term, $S_{\text{cb}}^{(N)}$, stems from the bare conduction band without impurity. In practice, one carries out two separate NRG calculations, one including the impurity and one without, and determines the entropy for each iteration N via Eq. (2.3.23). An analogous approach is used for the impurity contribution to the specific heat or the magnetic susceptibility [11].

2.3.1 Complete Basis Set and Sum-rule Conserving Calculation of Equilibrium Green's Functions

One of the most important quantities is the local Green's function and its spectral density. The NRG has been extended to provide an accurate description of both. However, calculation of the Green's function in the NRG framework requires a full basis set. We present the argumentation of Anders and Schiller [44, 14], who first identified such a set. We furthermore review the derivation of a sum-rule conserving calculation scheme for the Green's function [45, 46]. The basis set is

closely related to the non-equilibrium framework for the NRG which is discussed in detail in Sec. 4.4.

Anders and Schiller [44, 14] found a complete basis set by reinterpreting the iterative NRG algorithm. Normally, a Wilson chain of finite length is extended by adding an additional chain site each iteration. This expansion leads to an exponential number of states given by the tensor product

$$|r\rangle_{m+1} = |l\rangle_m \otimes |\alpha\rangle_{m+1}, \tag{2.3.24}$$

where $|r\rangle_{m+1},\ r = 1, \ldots, K_{m+1}$ are the new states belonging to the enlarged cluster, $|l\rangle_m,\ l = 1, \ldots, K_m$ are all eigenstates of H_m, and $|\alpha\rangle_{m+1},\ \alpha = 1, \ldots, d$ are the degrees of freedom of the new chain site. The alternative picture introduced in Ref. [44, 14] starts with the whole chain of length N but with each hopping elements between neighboring sites set to zero $t_m = 0$. At the beginning of each iterative step, the next hopping element is switched on. This means conceptually that the series of Hamiltonians along the chain now always acts on the Fock space of the N site chain. The degrees of freedom that belong to the dormant chain sites are reinterpreted as environmental degrees of freedom that are steadily incorporated into the Wilson chain.
Let us consider a chain with maximum length N and let H_m be the Hamiltonian for $m \leq N$ active chain sites. Each eigenenergy of H_m has an additional d^{N-m} degeneracy where d is the number of possible states introduced by each new site, e..g. $d = 4$ for a SIAM. If $m = N$, then all environmental degrees of freedom are incorporated into the chain. If $m = N - 1$, then each energy has a d-fold degeneracy because H_m still acts on the full Fock space F_N. We can naturally partition the whole chain into an active chain H_m and dormant rest $R_{m,N}$.

Let us adjust our notation (2.3.24) to this new picture. First, let $|r; m\rangle$ and E_r^m denote the r-th eigenstate and eigenenergy of H_m when acting on a m-site chain. Each dormant site $n > m$ contributes to the environment with $|\alpha_n\rangle$. The total effect of the rest chain $R_{m,N}$ can then be written as a tensor product $|e; m\rangle = |\alpha_{m+1}, \ldots, \alpha_N\rangle$. The full eigenstate is then given by yet another tensor product

$$|r, e; m\rangle = |r; m\rangle \otimes |\alpha_{m+1}, \ldots, \alpha_N\rangle. \tag{2.3.25}$$

In other words, $|r, e; m\rangle$ represents the situation where the full chain is partitioned into active and dormant part after the mth chain site. The variable r enumerates the eigenstates of the active chain while e encodes the configuration of all dormant chain sites. Furthermore, the eigenenergy E_m^r of H_m does not depend on the environmental degrees of freedom e as H_m includes only terms of the first m chain sites. As a result, E_m^r is highly degenerate. Proceeding with the NRG algorithm lifts this artificial degeneracy for further eigenenergies.

We now turn to the truncation scheme. Let m_{min} be the first iteration at which states are discarded. We partition all states into discarded high-energy $|l, e; m_{\text{min}}\rangle_{\text{dis}}$ and kept low-energy states $|k, e; m_{\text{min}}\rangle_{\text{kpt}}$ which participate in the

tensor product Eq. (2.3.25) during the next iteration $m_{\min+1}$. The key accomplishment is the realization that the set of all discarded states including all states of the last iteration make up a complete basis set for the whole Fock space F_N [44, 14]. If we formally label all states of the last iteration N as discarded, we can write the following completeness relation [14]

$$\mathbb{1} = \sum_{m=m_{\min}}^{N} \sum_{l,e} |l, e; m\rangle_{\text{dis dis}}\langle l, e; m|, \tag{2.3.26}$$

where the indices l and e depend implicitly on the iteration m. This completeness relation can be partitioned into the sum of two operators [14]

$$\begin{aligned} \mathbb{1} &= \mathbb{1}_m^- + \mathbb{1}_m^+ \\ \mathbb{1}_m^+ &= \sum_{k,e} |k, e; m\rangle_{\text{kpt kpt}}\langle k, e; m| \\ \mathbb{1}_m^- &= \sum_{m'=m_{\min}}^{m} \sum_{l',e'} |l', e'; m'\rangle_{\text{dis dis}}\langle l', e'; m'|. \end{aligned} \tag{2.3.27}$$

The first term projects onto the subspace of all discarded states for iterations $n \leq m$ whereas the second operator includes only the kept states of iteration m.

This complete basis set enables the calculation of sum-rule conserving Green's functions in and out of thermal equilibrium [45, 46, 47]. We sketch the cornerstones for the equilibrium algorithm and discuss Bulla's improvement by using an equation of motion [48]. We are interested in the Lehmann representation of the Green's function $G_{A,B}(z)$ in Fourier space

$$G_{A,B}(t) = -\mathrm{i}\Theta(t)\,\mathrm{Tr}\left\{\rho[A(t), B]_{-s}\right\}, \qquad [A, B]_{-s} = AB - sBA \tag{2.3.28}$$

$$G_{A,B}(z) = \int_0^\infty \mathrm{e}^{\mathrm{i}zt} G_{A,B}(t)\mathrm{d}t \tag{2.3.29}$$

for two fermionic ($s = -1$) or bosonic ($s = +1$) operators A, B. These operators are considered 'local' operators in the framework of the NRG in the sense that they only act on the first few Wilson sites that can still be diagonalized without truncation of the Fockspace.
We insert the completeness relation into the commutator under the trace in Eq. (2.3.28). The time evolution operators that occur in $A(t) = \exp(\mathrm{i}Ht)A\exp(\mathrm{i}Ht)$ are evaluated with help of the conventional NRG approximation $H|s, e; m\rangle \approx E_s^m|s, e; m\rangle$ where $|s, e; m\rangle$ is an eigenstate of H_m and E_s^m the corresponding eigenvalue. After reorganizing the sum indices one ends up with three contributions to the Green's function. The first part includes only contributions from the last iteration N and reads [45]

$$G_{A,B}^i(z) = \frac{1}{Z}\sum_{l,l'} \langle l; N|A|l'; N\rangle\langle l'; N|B|l; N\rangle \frac{\mathrm{e}^{-\beta E_L^N} - s\mathrm{e}^{-\beta E_{l'}^N}}{z + E_l^N + E_{l'}^N}. \tag{2.3.30}$$

The other two terms deal with every other iteration up to $m_{\min}$ before which no states were discarded during truncation. They comprise one part each of the commutator in Eq. (2.3.28). The contribution that includes the fermionic or bosonic label is [45]

$$G^{ii}_{A,B}(z) = \sum_{m=m_{\min}}^{N-1} \sum_{l} \sum_{k,k'} A_{l,k'}(m) \rho^{\mathrm{red}}_{k',k}(m) B_{k,l}(m) \frac{-s}{z + E^m_l - E^m_k}, \tag{2.3.31}$$

while the last term can be written as [45]

$$G^{iii}_{A,B}(z) = \sum_{m=m_{\min}}^{N-1} \sum_{l} \sum_{k,k'} B_{l,k'}(m) \rho^{\mathrm{red}}_{k',k}(m) A_{k,l}(m) \frac{1}{z + E^m_k - E^m_l}. \tag{2.3.32}$$

Here $\rho^{\mathrm{red}}_{k',k}(m)$ is the reduced density matrix

$$\rho^{\mathrm{red}}_{k,k'}(m) = \sum_{e} \langle k, e; m | \hat{\rho} | k', e; m \rangle. \tag{2.3.33}$$

The full Green's function is thus the sum of all three contributions

$$G_{A,B}(z) = G^{i}_{A,B}(z) + G^{ii}_{A,B}(z) + G^{iii}_{A,B}(z). \tag{2.3.34}$$

The Green's function defined in this way overcomes the shortcomings of previous approaches [49, 50, 51] which in a nutshell suffered from not having a systematic way to sum over states from different iterations resulting in overcounting of contributions [45] and the need for phenomenological patching algorithms [49, 45].

Calculation of the Green's function in context of the NRG requires summation over the eigenenergies E^m_k. Albeit the total number of states involved will be large for reasonable chain lengths, it is still finite. Therefore, the resulting discrete set of delta peaks has to be transformed into a continuous function via broadening of the δ-distribution by a suitable function. This function is oftentimes a Gaussian distribution on a logarithmic mesh [52, 53, 45]

$$\delta(\omega - \omega_n) \to \frac{\mathrm{e}^{-b^2/4}}{b\omega_n\sqrt{\pi}} \exp\left\{ -\left(\frac{\ln(\omega/\omega_n)}{b} \right)^2 \right\}, \tag{2.3.35}$$

where b is the broadening parameter. Bulla et al. [49] have proposed an alternative broadening by replacing the logarithmic Gaussian by a conventional Lorentz peak for small excitation energy.
Arguably the most important improvement is the calculation of the self-energy and expressing $G_\sigma(z)$ via $[G^{-1}_{\sigma,0}(z) - \Sigma_\sigma(z)]^{-1}$ [48]. In their paper the authors study the SIAM but their method can readily applied to a multitude of different models. They use the equation of motion for the Green's function and derived

an expression for the correlation part of the self-energy $\Sigma_\sigma^U(z)$ that is induced by the interaction U [48]:

$$\Sigma_\sigma^U(z) = U\frac{F_\sigma(z)}{G_\sigma(z)}. \tag{2.3.36}$$

The index σ represents the spin and the variable U stands for the Coulomb interaction. The Green's function $G_\sigma(z)$ is the quantity of interest and $F_\sigma(z) = G_{d_\sigma d_{\overline{\sigma}}^\dagger d_{\overline{\sigma}}, d_\sigma^\dagger}(z)$ arises due to the many body interaction U. The label $\overline{\sigma}$ is a shorthand notation for the opposite spin of σ. Both Green's functions are evaluated simultaneously with the same broadening and logarithmic mesh, and the resulting total self-energy $\Sigma_\sigma(z) = \Delta(z) + \Sigma_\sigma^U(z)$ is used to calculate $G_\sigma(z)$ a second time

$$G_\sigma(z) = \frac{1}{z - \epsilon_d - \Sigma_\sigma(z)}. \tag{2.3.37}$$

Here, $\Delta(z)$ is the contribution to the self-energy that arises solely from hybridization with the band. It turns out that the arbitrariness introduced by the broadening is suppressed when taking the ratio, and re-calculating $G_\sigma(z)$ yields highly accurate results [48]. The non-interacting Green's function even becomes exact.

2.3.2 The Numerical Renormalization Group Applied to a SIAM

Let us go back to the SIAM and apply the NRG procedure described above. For this we choose a discretization parameter $\Lambda = 2.5$, a bandwidth $D/\Gamma_0 = 50$, and a chain length of $N = 40$. Furthermore, we keep $N_{\text{kept}} = 2000$ states each iteration and adjust the local parameters to be particle-hole symmetrical $\epsilon_d = -U/2$.

Let us first look at the entropy in Fig. 2.7. For high T it is equally likely for the impurity orbital to be empty, singly or doubly occupied, and the entropy S_{imp} thus tends to $k_B \ln(4)$ [Fig. 2.7 (a)]. The Coulomb interaction starts to suppress charge fluctuations as the temperature decreases which results in the formation of a localized moment. The system is close to a so-called local moment fixed-point where the Coulomb interaction stabilizes a single occupied impurity orbital. The entropy approaches $k_B \ln(2)$ since the system respects spin-symmetry and both states $|\uparrow\rangle$ and $|\downarrow\rangle$ are equivalent. The onset of the crossover from the high-temperature limit to the local moment fixed-point depends on the ratio $U/\Gamma_0 \sim U/V^2$: a higher hybridization promotes electron delocalization and hinders the formation of a local moment.

The local moment fixed-point, however, is unstable which can be seen when the temperature is reduced further. The Kondo temperature $T_K/D = \sqrt{\frac{8\Gamma_0}{\pi U}} \mathrm{e}^{-\frac{\pi U}{8\Gamma_0}}$ defines a second crossover from the local moment to the strong coupling fixed-point. A higher U/Γ_0 yields an exponentially smaller Kondo scale and a prolonged unstable local moment fixed-point [Fig. 2.7 (a)].

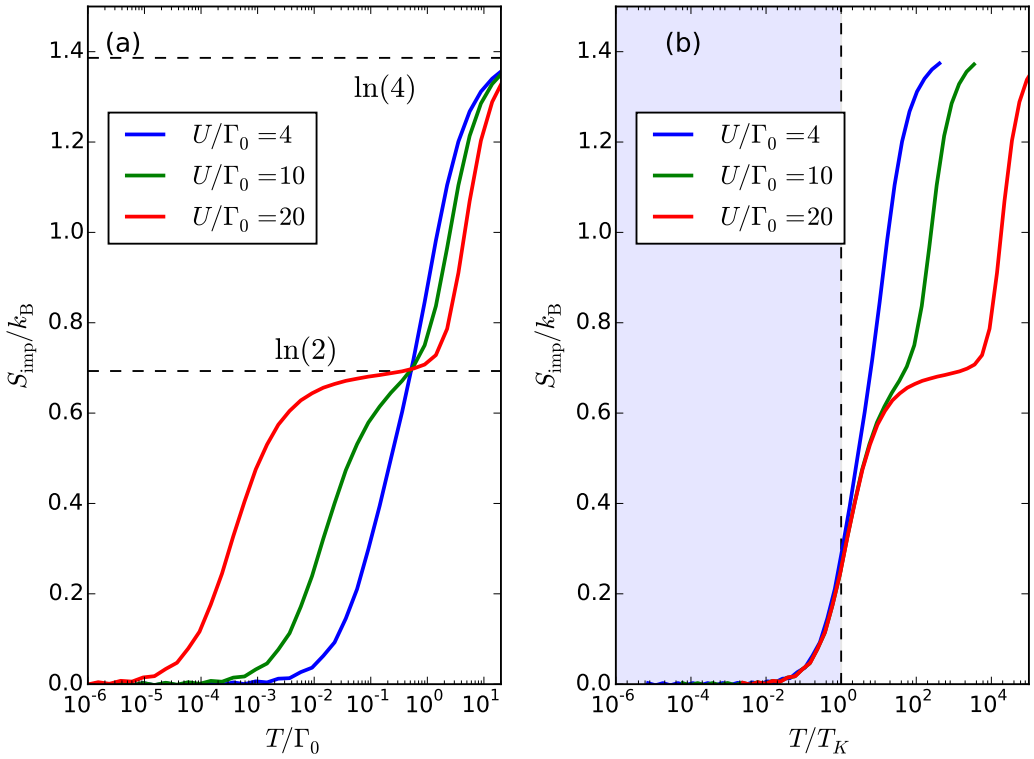

Figure 2.7: (a) Impurity entropy S_{imp} as a function of T/Γ_0 for different particle-hole symmetrical local parameters. The dashed lines indicate the entropy of the different unstable fixed points. (b) The same results as a function of temperature in natural units T/T_k. The Kondo temperature (dashed line) defines a crossover scale below which all curves fall onto each other (shaded blue area). The parameters are $\epsilon_d/\Gamma_0 = -5$ and $U/\Gamma_0 = 10$.

We calculate T_K by applying a small local magnetic field to the impurity orbital and measuring the magnetization $\langle M_{\mathrm{loc}}\rangle(T)$. The Kondo temperature is then obtained from the magnetic susceptibility $\chi(T) = \langle M_{\mathrm{loc}}\rangle/B$ by employing Wilson's definition [10, 11].

$$4T_K\chi(T_K) = 0.413. \tag{2.3.38}$$

The local moment is screened by the band electrons below T_K which results in the formation of a singlet state, the so-called Kondo singlet, and therefore a vanishing entropy S_{imp}. The Kondo temperature defines a natural energy scale below which all curves show the same universal behavior [Fig. 2.7 (b)].

The Kondo effect is also visible in the spectral density $\rho^r_\sigma(\omega)$ as a pronounced peak at the Fermi energy $\omega = 0$ [Fig. 2.8 (a)]. The height of this Kondo peak is $1/(\pi\Gamma_0)$ in a particle-hole (PH) symmetric setup reflecting the Fermi liquid nature of the fixed point, and its full width at half the maximum height (FWHM) can be traced back to the Kondo temperature [35, 54]. Since the FWHM not only depends on T_K but also on e.g. the occupation and PH asymmetry, it is more

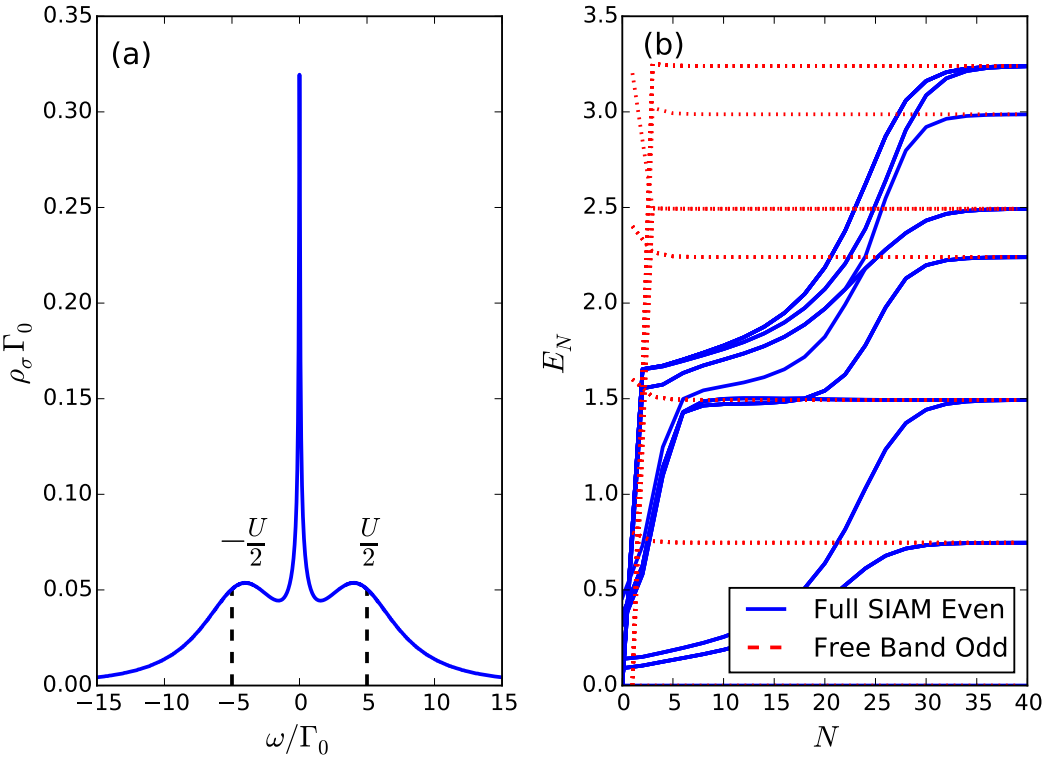

Figure 2.8: (a) Spectral density $\rho_\sigma(\omega)$ for $T/T_k = 6 \cdot 10^{-5}$, $\epsilon/\Gamma_0 = -5$, $U/\Gamma_0 = 10$, and broadening $b = 0.8$. At $\omega = 0$ the spectral density shows the characteristic Kondo peak. At $\omega \approx \pm U/2$ there are two Hubbard peaks. (b) Lowest energy levels for the full SIAM of each even (blue solid lines) and for the free band (red dotted lines) of each odd NRG iteration. The parameters are $\epsilon/\Gamma_0 = -10$ and $U/\Gamma_0 = 20$. The system is close to an unstable local moment fixed point between iteration $N \approx 5$ and $N \approx 15$ before crossing over to the final stable strong coupling fixed point.

beneficial to rely on different calculation schemes for T_K. One example is the aforementioned definition by Wilson that uses the magnetic susceptibility or the empirical Goldhaber-Gordon fit of the zero-bias conductance [55].

Most importantly, the NRG scheme generates the lowest eigenenergies in each iteration. They reflect the renormalization group flow and yield valuable insight in the nature of the various fixed points. One has to distinguish between even and odd iterations as the energy degeneracy of the states will differ. A simplified example would be a chain of half-filled electronic orbitals of length N coupled by a hopping term. A chain of length two has a singlet ground state, but if one includes another link, the ground state will change to a doublet. It will continue alternating even in the limit of $N \to \infty$ while the physical properties will converge if N is just large enough. This even-odd oscillations is also inherent to the NRG which renders a comparison of eigenenergies for two consecutive iterations meaningless.

If the system is close to a stable fixed point, the energies for even and odd

iterations remain constant [cf. $N > 30$ in Fig. 2.8 (b)]. However, if the system is close to an unstable fixed point, there will be some drift left until another crossover occurs at some later iteration [cf. $5 < N < 15$ in Fig. 2.8 (b)]. The Kondo (or strong coupling) fixed point exhibits one additional peculiarity: the even level energies converge to the same values as the odd energies for the bare electronic band without any impurity [Fig. 2.8 (b)]. This provides a practical tool to identify a strong coupling fixed point and can be easily understood in terms of the Wilson chain: below T_K the spin of the impurity is screened by the electron bath forming a singlet state. The simplified picture is that the electron of the impurity and the first chain link form a singlet state effectively decoupling from the rest of the chain. This leaves a chain of $N - 1$ chain sites that form a free electron bath, i.e. without an impurity. Since the length is reduced compared to the regular free chain, we see a shift from even to odd.

There is a multitude of other thermodynamic quantities widely discussed already in the literature, ranging from magnetic susceptibility to impurity occupation numbers or correlation functions [11]. We saw how the NRG is capable of providing us with an excellent numerical solution for a quantum impurity system using the example of the SIAM. We reviewed some of the most common and practical quantities like the entropy and the spectral density and discussed how they aid us with identifying and explaining the underlying physics and fixed points. In the following, we will build upon the foundation laid out in this chapter and move on to a more realistic model for magnetic carbon vacancies in graphene.

Before we turn to the case of graphene, let us briefly mention some important developments for the NRG method over the years. A major keystone was the aforementioned identification of a complete basis set [44, 14] that put the calculation of Green's functions that were hitherto plagued by a multitude of problems on a firm theoretical basis [45, 13]. A second consequence of this new basis was the extension of the NRG to time-dependent quenching problems (TDNRG) [44, 14] which we discuss in detail in Sec. 4.4. The TDNRG has been successfully combined [56, 57] with the Density Matrix Renormalization Group (DMRG) [58] technique. The NRG is used to generate a accurate low-energy Hamiltonian that can then be treated by the time dependent DMRG to access exponentially long time scales.
Another approach deals with the exponentially increased numerical complexity when including multiple bands. In order to tackle multi-band problems in an efficient manner the so-called Interleaved NRG [59] has been developed in recent years.
On a different note, the NRG has been successfully extended to systems with bosonic baths as well. First applications cover the static and dynamic properties of the (sub/super-) Ohmic Spin Boson Model [20, 21].

Chapter 3

Tunable Kondo Effect in Defective Graphene

We focused on simplified model Hamiltonians, like the SIAM or Kondo model, in the previous chapter to establish the NRG method. These models are already able to capture the essential physics of systems on a qualitative level despite their simplicity. However, depending on the impurity problem at hand, one needs to include more correlated localized orbitals and their interactions, realistic hybridization functions, or phononic degrees of freedom in order to quantitatively describe more nuanced behavior.

In this chapter, we focus on a realistic model for irradiated graphene sheets and their rich physics. We start by introducing pristine samples of graphene in Sec. 3.1 and Sec. 3.1.1 where we review the unique electronic properties included in the (next) nearest neighbor tight-binding approximation. We discuss the remarkable pseudo-gap band structure of graphene with its linear low energy density of states around the Dirac Points.

We continue with the different ways of disturbing the perfect honeycomb lattice of graphene in Sec. 3.2. Our focus here lies on graphene with missing carbon atoms, called carbon vacancies. Of particular interest is the case where impure graphene is subject to external gate voltages that act as a chemical potential. We summarize the experimental and theoretical evidence for the formation of stable magnetic moments in these defective graphene sheets in Sec. 3.3. We review the findings of one particular experimental study [9] where the authors identified three types of carbon vacancies in the same setup. We develop an effective two-orbital impurity model in Sec. 3.4 in order to describe these different types of vacancies in one go. One of these orbitals is a remnant of the broken in-plane σ bonds while the other is a vacancy-induced bound state located in the pseudogap called 'zero-mode'.

In Sec. 3.4.1, we introduce the local hybridization strength as the crucial parameter that differentiates between the experimentally observed regimes. We

develop a simplified yet sound picture of the low temperature behavior of carbon vacancies that depends on two free parameters, chemical potential μ and hybridization strength Γ_0, alone.

We employ the NRG to this model in Sec. 3.5. We begin by mapping the parameter space and identifying the different regimes in Sec. 3.5.2 before we look at each regime in detail in Sec. 3.5.3. We continue with various discussions about the Kondo temperature, numerical stability, and possible enhancements. We summarize our results in Sec. 3.5.10. The majority of our findings presented in this chapter are published in Ref. [19] and, to a lesser extend, in Ref. [9].

3.1 Pristine Graphene

Graphene is a carbon-based allotrope with a thickness of just a single layer of atoms arranged in a honeycomb lattice. Its unique two-dimensional character in combination with a distinctive electronic structure and the bonding flexibility of carbon grants graphene numerous remarkable physical properties such as extremely high tensile strength [60, 61, 62], high thermal conductivity [63, 64], and an optical conductivity that is a universal constant [65, 66, 67]. This results in an opacity of roughly 2.3% and the fact that one can even see a single layer of graphene with the naked eye [67].

The earliest theoretical model of the electronic properties of graphene trace back to Wallace [68] in 1947. He introduced the popular tight-binding formulation, which is still the foundation for modern studies of graphene, to calculate the band structure of graphite. Graphite can be seen as stacks of multiple layers of graphene that form a three-dimensional crystal hold together by weak van der Waals forces. Drawing from his work, McClure, Slonczewski and Weiss brought forth a comprehensive study of the electronic properties of graphite [69, 70].
In the subsequent decades, Wallace's model also found some application in different fields [71, 72], notably the most important being Haldane's description of the quantum Hall effect (QHE) [73] where Haldane used a suitable magnetic field breaking time reversal but keeping the spatial symmetry intact.
The integer quantum Hall effect in graphene has been observed experimentally almost 20 years later by Novoselov et al. and Zhang et al. [74, 75]. Furthermore, Kane and Mele used graphene as a model system to postulate a completely new type of quantum spin Hall effect (QSHE) in a series of papers in 2005 [76, 77]. They based their work on the existence of a presumable strong spin-orbit coupling which, in the end, turned out to be a false assumption. Nevertheless, with their work they kick-started the modern field of topology and topological insulators.

One of the most remarkable features of graphene is its low-energy linear energy dispersion that yields massless and chiral quasi-particle excitations that show a striking resemblance to solutions of the Dirac equation for relativistic and massless electrons. This similarity is rooted in the honeycomb structure of graphene and the fact that the low-energy physics is determined by two distinct points in

reciprocal space, called Dirac points (DPs), and their proximity. As a result, a number of effects of quantum electrodynamics (QED) also appear in graphene albeit at much smaller velocity compared to the speed of light [78, 79, 80].

The quasi-two dimensional shape of graphene builds the bridge to the field of soft membranes [81] as suspended graphene sheets show spatial disorder in form of out-of-plane ripples [82]. This leads to the existence of vibrational phonons, which are not present in regular three-dimensional crystals, as well as crumpling [81].

Graphene samples of mesoscopic length scale [83, 84, 85, 78, 86, 87], i.e. up to several μm, are of particular interest as well. Here, one distinguishes usually between zigzag and armchair edges. Cutting along the edge of multiple carbon hexagons with an angle of 120° between two successive cuts yields a zigzag edge while cutting through the middle of each second hexagon results in an armchair arrangement. Both samples show distinctive differences, e.g. zigzag edges supporting localized edge states [84, 83]

Despite the recurring theoretical work done over the decades, experimental studies were notably absent until recently. One reason being the decisiveness of the Mermin-Wagner theorem [88] that essentially forbids thermodynamical stable 2D crystals to form spontaneously. As a result, graphene is not completely two-dimensional. Instead, the single carbon layers exhibit the formation of out-of-plane ripples [82].

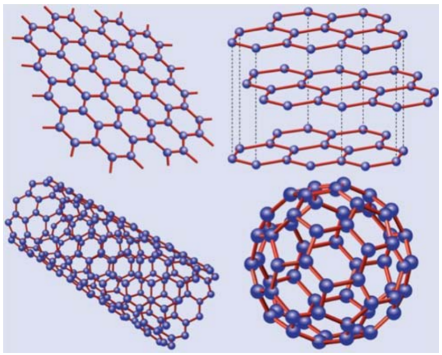

Figure 3.1: Visualization of: graphene (top left) which is a single layer of carbon arranged in a honeycomb lattice, graphite (top right) which are stacked graphene layers hold together by van der Waals forces, carbon nanotubes (bottom left) that are rolled up graphene sheets and fullerene (bottom right) which are zero-dimensional molecules. The figure was taken from Ref.[78].

Although graphene might not occur naturally, it can still be obtained as a long-lived pseudo-2D crystal [67] from graphite by the means of exfoliation [89, 74, 90]. The discovery of this simple yet ground-breaking process by a group led by Andre Geim at Manchester University marks the beginning of a flood of publications. Their method is, on one hand, both inexpensive and can yield high-quality samples [67, 89, 90], yet, on the other, labor intensive and due to the small sample size unfortunately unsuited for large-scale production. The process starts with macroscopic big graphite crystal flakes like natural graphite, kish or highly oriented pyrolitic graphite that are pressed onto Scotch tape to remove a thin layer of graphite which is then applied onto a Si/SiO_2 substrate. The thickness of the sample can subsequently be determined with an atomic force microscope measurement or Raman spectroscopy.
In addition to simple exfoliation there are a couple of other processes like chemi-

cal vapor deposition on metallic surfaces [91], surface graphitization and epitaxial growth on SiC crystals [92, 93, 94], open flame synthesis [95], solution-based exfoliation [96], or by using colloidal suspensions [97].

Apart from graphite, the natural three-dimensional extension of the 2d graphene, there are a couple of other arrangements that sparked scientific interest over the years. If the honeycomb lattice is disturbed by changing some of the hexagons into pentagons, one effectively introduces positive curvature defects that result in a curl up [98, 78, 81]. The resulting molecule, fullerene C_{60}, consists of carbon atoms that are ordered spherically. It can essentially be considered a zero-dimensional object due to its round shape. A second popular application are carbon nanotubes [99, 100] that are made up of rolled-up graphene. Here, a finite sheet of graphene is rolled along an axis to form a cylinder. The carbon atoms located at either edge form their conventional sp^2 bonds holding the whole structure together. This rolling thus retains the perfect honeycomb lattice on the surface of the cylinder.
The four different arrangements, graphene, graphite, fullerene, and carbon nanotubes, are visualized in Fig. 3.1. In this work we focus exclusively on single graphene sheets strapped onto a SiO_2 substrate.

3.1.1 Electronic Properties of Single Layers of Graphene: Tight-Binding Approximation

On an atomic level, graphene consists purely of carbon atoms that form hexagons with a nearest-neighbor distance $a \approx 1.42\,\text{Å}$. Alternatively, it can be visualized as two triangular sub-lattices that are shifted to each other by a, or as a single hexagonal Bravais lattice with two atoms per unit cell [Fig. 3.2 (a)]. In this case, the lattice vectors can be written as

$$\vec{a}_1 = \frac{a}{2}\begin{pmatrix}3\\ \sqrt{3}\end{pmatrix}, \quad \vec{a}_2 = \frac{a}{2}\begin{pmatrix}3\\ -\sqrt{3}\end{pmatrix}. \tag{3.1.1}$$

The nearest-neighbor (n.n.) vectors take the form

$$\vec{\delta}_1 = \frac{a}{2}\begin{pmatrix}1\\ \sqrt{3}\end{pmatrix}, \quad \vec{\delta}_2 = \frac{a}{2}\begin{pmatrix}1\\ -\sqrt{3}\end{pmatrix}, \quad \vec{\delta}_3 = -a\begin{pmatrix}1\\ 0\end{pmatrix}, \tag{3.1.2}$$

while the six next nearest-neighbors (n.n.n.) vectors are

$$\vec{\delta}'_{1,\pm} = \pm\vec{a}_1, \quad \vec{\delta}'_{2,\pm} = \pm\vec{a}_2, \quad \vec{\delta}'_{1,\pm} = \pm(\vec{a}_2 - \vec{a}_1). \tag{3.1.3}$$

The reciprocal vectors can be calculated from the lattice vectors

$$\vec{b}_1 = \frac{2\pi}{3a}\begin{pmatrix}1\\ \sqrt{3}\end{pmatrix}, \quad \vec{b}_2 = \frac{2\pi}{3a}\begin{pmatrix}1\\ -\sqrt{3}\end{pmatrix}, \tag{3.1.4}$$

such that $\vec{a}_i \cdot \vec{b}_j = 2\pi\delta_{ij}$. The Brillouin zone (BZ), which can then be constructed in the usual manner, has a hexagonal form as well. The BZ is shown in

Fig. 3.2 (b). Only two of the six corner points of the BZ, labeled K and K', are linear independent while the others arise from translation of the lattice. These two points are called Dirac points and they play a crucial role in the low energy behavior of graphene. Their positions in momentum space are

$$\vec{K} = \begin{pmatrix} \frac{2\pi}{3a} \\ \frac{2\pi}{3\sqrt{3}a} \end{pmatrix}, \quad \vec{K'} = \begin{pmatrix} \frac{2\pi}{3a} \\ -\frac{2\pi}{3\sqrt{3}a} \end{pmatrix}. \tag{3.1.5}$$

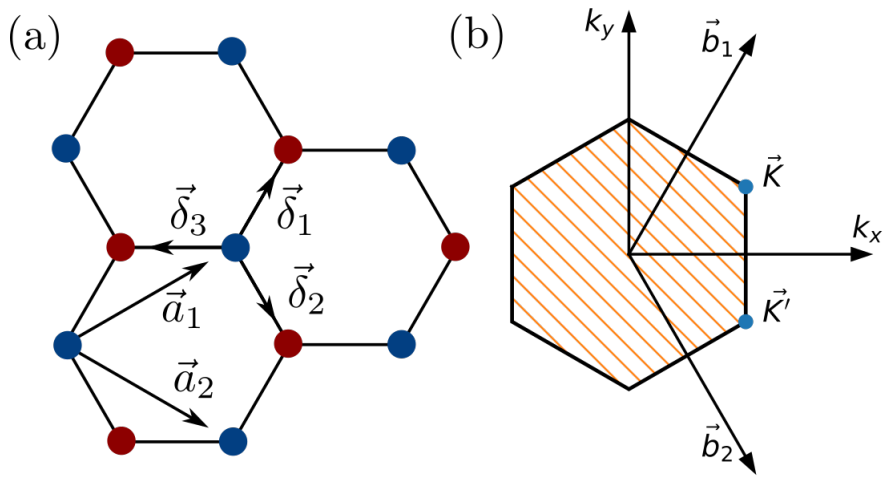

Figure 3.2: (a) Hexagonal lattice structure of graphene. The blue and red dots represent the carbon atoms of different triangular sublattices. $\vec{a}_i$ are the lattice vectors and $\vec{\delta}_i$ the n.n. vectors. (b) Reciprocal space, reciprocal vectors $\vec{b}_i$, and Brillouin zone (shaded are). Both Dirac points are located at a corner of the BZ.

We can now write down the tight-binding Hamiltonian where electrons are able to hop between nearest neighbor atoms (hopping between sub-lattices) as well as between next nearest neighbors (same sub-lattice) [81]

$$H = -t \sum_{\langle i,j\rangle,\sigma} (a^\dagger_{\sigma,i} b_{\sigma,j} + h.c.) \tag{3.1.6}$$

$$- t' \sum_{\langle\langle i,j\rangle\rangle,\sigma} (a^\dagger_{\sigma,i} a_{\sigma,j} + b^\dagger_{\sigma,i} b_{\sigma,j} + h.c.). \tag{3.1.7}$$

Here, t, t' are the inter- and intra-sub-lattice hooping amplitudes respectively. The creation and annihilation operators with spin σ for the different sub-lattices are labeled $a^{(\dagger)}_{\sigma,i}$ and $b^{(\dagger)}_{\sigma,i}$. The sums are restricted to either nearest ($\langle \ldots \rangle$) or next nearest ($\langle\langle \ldots \rangle\rangle$) neighbors. The Hamiltonian is bilinear and can readily be

diagonalized by Fourier transformation. It yields two energy bands [68, 81]

$$E_{\pm}(\vec{k}) = \pm t\sqrt{3 + f(\vec{k})} - t' f(\vec{k}), \tag{3.1.8}$$

$$f(\vec{k}) = 2\cos(\sqrt{3}k_y a) + 4\cos\left(\frac{\sqrt{3}k_y a}{2}\right)\cos\left(\frac{3k_x a}{2}\right). \tag{3.1.9}$$

Figure 3.3 shows both bands over the whole BZ for n.n. hopping only $t' = 0$. Both bands become simultaneously zero at six distinct points, two of which are independent. These are the aforementioned Dirac points, K and K', that are responsible for the low energy physics of graphene. Expanding the dispersion near either DP yields [68, 81]

$$E_{\pm}(\vec{q}) = \pm v_F|\vec{q}| + O((q/K)^2), \tag{3.1.10}$$

where $\vec{q}$ is a small vector relative to the respective DP and $v_F = 3ta/2 \approx 10^6\,\mathrm{m/s}$ is the Fermi velocity. The dispersion near the DPs resembles that of relativistic massless particles. One can expand the tight-binding Hamiltonian for $t' = 0$ close to these points. The resulting effective Hamiltonian has a matrix structure and consists essentially of two copies of the massless Dirac Hamiltonian for momenta close to K or K' [81]. The electronic wave function in real space is a vector with two components and obeys the 2d Dirac equation. Furthermore, the wave function close to either DP, $\psi_{\vec{K}}(\vec{r})$ or $\psi_{\vec{K}'}(\vec{r})$, is an eigenfunction of the helicity operator [81]

$$h = \frac{1}{2}\vec{\sigma}\cdot\frac{\vec{p}}{|\vec{p}|}, \tag{3.1.11}$$

where $\vec{\sigma} = (\sigma_x, \sigma_y)^T$ are the Pauli matrices. The electronic states close to either DP have a well defined chirality or helicity that links momentum and pseudospin. This pseudospin is not the real physical spin but rather a manifestation of the two bands crossing at the Dirac points [81]. This helical property holds true only close to either DP.

It is possible to write down an analytical solution for the density of states (DOS) per unit cell in the case of vanishing n.n.n. hopping [101, 81]. For the general case, where $t' \neq 0$, it is sufficient to sample over the BZ and evaluate

$$\rho(\epsilon) = \frac{1}{N_a N_k}\sum_{\pm,\vec{k}} \delta(\epsilon - E_{\pm,\vec{k}}) \tag{3.1.12}$$

numerically, where $E_{\pm,\vec{k}}$ is defined in Eq. (3.1.8), N_k is the number of sampled $\vec{k}$-points and $N_a = 2$ is the number of atoms in the unit cell.

We recall that the DOS enters in the definition of the hybridization function, Eq. (2.3.5), and we can likewise determine the hybridization V by

$$V^2 = \sum_{\vec{k}\sigma} |V_{\vec{k}}|^2 = \frac{1}{\pi}\int_{-\infty}^{\infty} \Gamma(\omega)\mathrm{d}\omega. \tag{3.1.13}$$

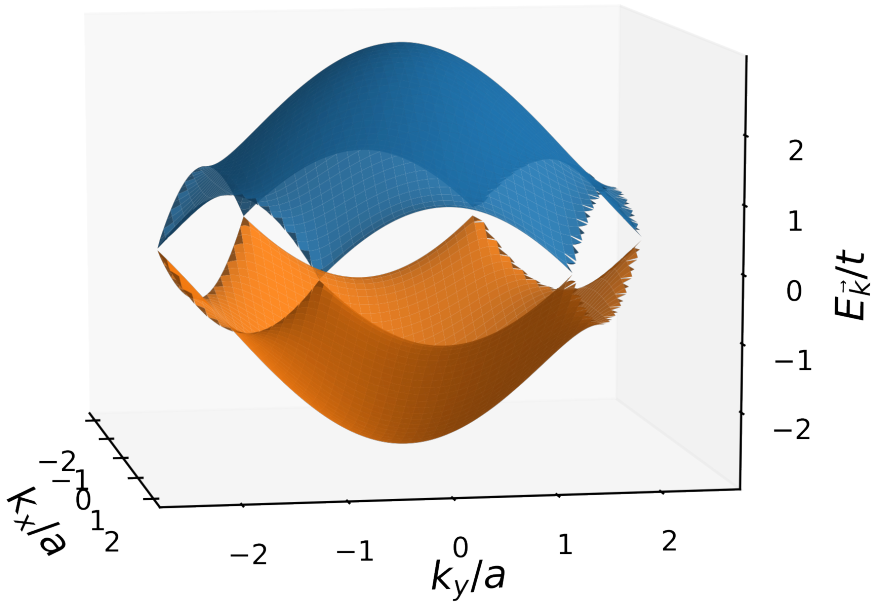

Figure 3.3: Tight-binding dispersion Eq. (3.1.8) for $t' = 0$ evaluated at a discrete set of $N_k = 10^6$ points in the Brillouin zone. The calculated values are used for an interpolation to arrive at a smooth surface plot. Rough edges are an artifact of the numerical interpolation.

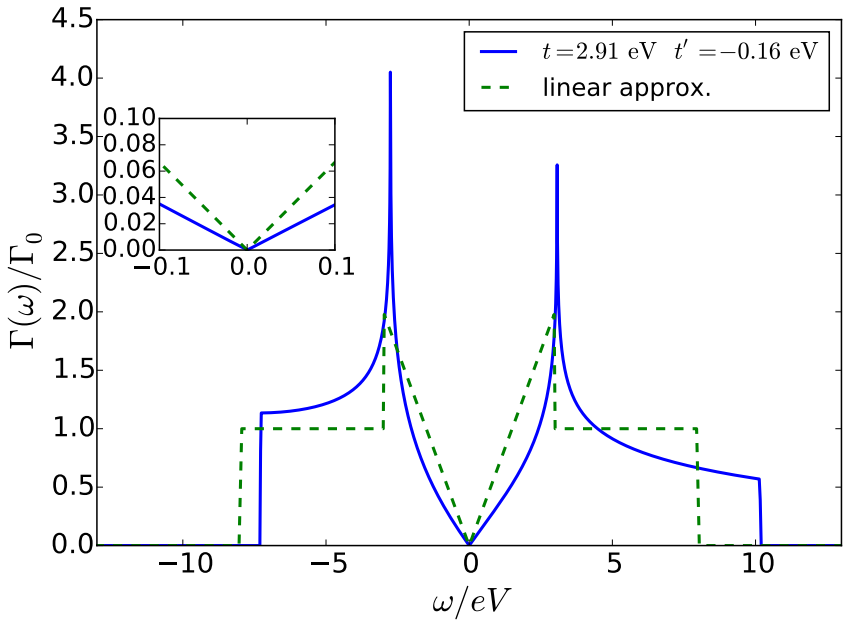

Figure 3.4: Two different approximations for $\Gamma(\omega)$ for pristine graphene. Solid curve: t, t' tight-binding approximation with $t = 2.91\,eV$ and $t' = -0.16\,eV$ [102, 103]. The frequency is shifted such that the DP coincides with $\omega = 0$. Dashed curve: Linear approximation Eq. (3.1.14). Taken from Ref. [19].

The characteristic feature of the DOS and thus of the hybridization function is the linear behavior near the DP for $\omega \to 0$. A simpler approximation than our tight-binding approach may be used where

$$\Gamma(\omega) = \Gamma_0 \begin{cases} \frac{2|\omega|}{D_{\text{eff}}}, & \text{if } |\omega| < D_{\text{eff}} \\ 1, & \text{if } D_{\text{eff}} \leq |\omega| \leq D \\ 0, & \text{otherwise.} \end{cases} \tag{3.1.14}$$

Here, $D = 8\,eV$ determines the band edges and $D_{\text{eff}} = 3\,eV$ pins the van Hove singularities. This analytic approximation captures the essential behavior for small energies. Fig. 3.4 shows a comparison between analytic and sampled tight-binding hybridization functions.
Note, that the next nearest neighbor tight-binding solution is inherently particle-hole asymmetric. As a result the pseudo-gap is shifted to finite ω. We define the pseudo-gap as a reference point for $\omega = 0$ even for finite t' since it is used as zero bias gauge in the experimental study [9], allowing a direct comparison of our results to the experimental data below.

3.2 Defects in Graphene: Existence of Stable Magnetic Moments and Kondo Physics

Albeit pristine graphene provides us with an abundance of different physical effects already, it lacks the open d or f shells of transition-metal elements and the concomitant formation of local magnetic moments and Kondo physics. On its own, graphene is strongly diamagnetic [104, 5]. This picture changes, however, when the perfect honeycomb structure of graphene is disturbed by impurities. It has been shown that graphite exhibits magnetic ordering [105, 106, 8] that has been linked with lattice defects [107] or edges [83, 108].

In principle, there are several sources of disorder and ways to introduce defects or impurities into graphene. The two most prominent are adsorption of foreign atoms and the removal of single carbon atoms. One example of the adsorption effect are isolated Co atoms that are placed on the surface of graphene [109, 110, 111].
The removal of carbon atoms from the honeycomb lattice is realized by ion irradiation, creating carbon vacancies [112, 113, 114]. These vacancies not only show the formation of local magnetic moments [7, 8, 5, 4] but also the rise of a (tunable) Kondo effect [6, 115, 116, 9]. These lattice impurities and their influence on the local electronic structure has been extensively studied over the last decade [112, 115, 7, 5, 4, 110, 117]. The microscopic behavior that leads to a tunable Kondo effect has been understood just recently in a series of two papers [19, 9].

Graphene in its pristine form is held together by the formation of three strong σ bonds at every lattice site that are each made up out of two sp^2 orbitals from neighboring sites [Fig. 3.5 (a)]. These sp^2 orbitals are in turn constituted of

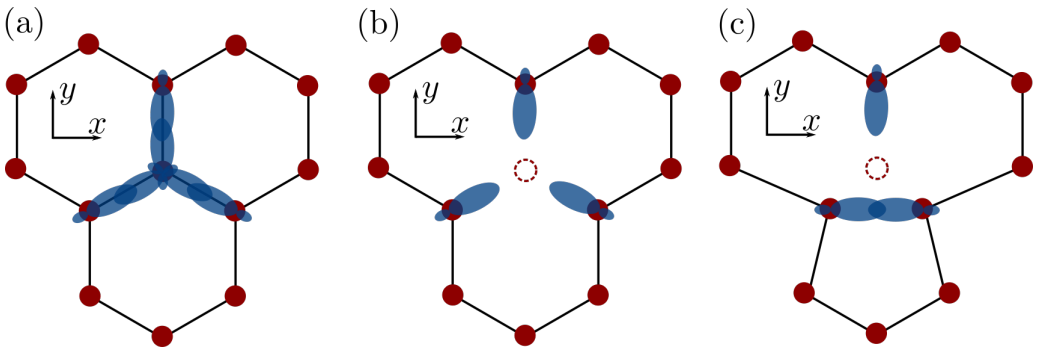

Figure 3.5: Schematic view of the orbitals in xy plane for the honeycomb lattice of graphene with a single carbon vacancy. Orbitals perpendicular to the xy plane are not shown. (a) Formation of σ bonds out of neighboring sp^2 orbitals (blue). (b) Single carbon vacancy (dashed circle) disrupts three σ bonds. (c) Lattice reconstruction and Jahn-Teller deformation. Two broken σ bonds recombine leaving one dangling sp^2 orbital at the opposite carbon atom. The vacancy has a triangle form.

atomic s, p_x and p_y orbitals. These covalent σ bonds are significantly stronger than the weak out of plane π bonds that result from a lateral overlap of p_z orbitals (Fig. 3.6). The π bonds are responsible for the dispersion of graphene.
Irradiation by ions removes a single atom and thus breaks three σ bonds [Fig. 3.5 (b)]. This induces four states in the proximity of the vacancy: three are remnants of the broken σ bonds and one is a semi-localized state, the 'zero mode' or π state, whose energy is exactly zero in the next neighbor tight-binding approximation [117]. Two of the now unpaired sp^2 orbitals will recombine resulting in the formation of a carbon pentagon [Jahn-Teller deformation of the lattice, Fig. 3.5 (c)]. This reconstruction of the lattice leaves a single dangling σ bond unpaired [117, 118, 116]. The stable configuration is reached by lowering the spatial symmetry.
In neutral graphene, there are four orphan electrons in total, one from each of the broken sp^2 bonds as well as one from the π system, that occupy the new vacancy states [117].

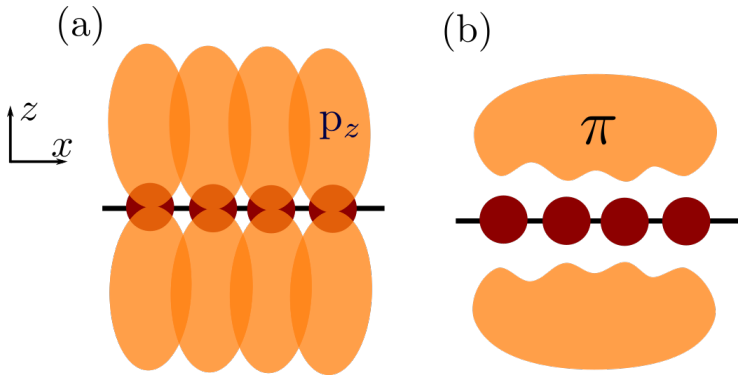

Figure 3.6: Schematic view of π bonding in graphene. σ bonds lying in the xy plane are not shown. (a) Hybridization of neighboring p_z orbitals results in (b) formation of π bonds.

Due to symmetry, the σ and π bands that stem from the bulk material do not hybridize. This, however, applies only to the case where the σ bonds are strictly perpendicular to the p_z orbitals. In case of graphene, rippling of the surface occurs via sp^2-sp^3 hybridization which mixes the σ and the p_z orbital at a carbon site [116]. Furthermore, if a dangling σ bond located at a carbon vacancy participates in the sp^2-sp^3 hybridization, the resulting orbital is not perpendicular to the π band anymore and will couple to the DOS of the π sub-system. The effective hybridization is estimated to be substantial even for small deviations [116]. This leads to an effective hopping between π electrons to the σ orbital and an anti-ferromagnetic exchange interaction.

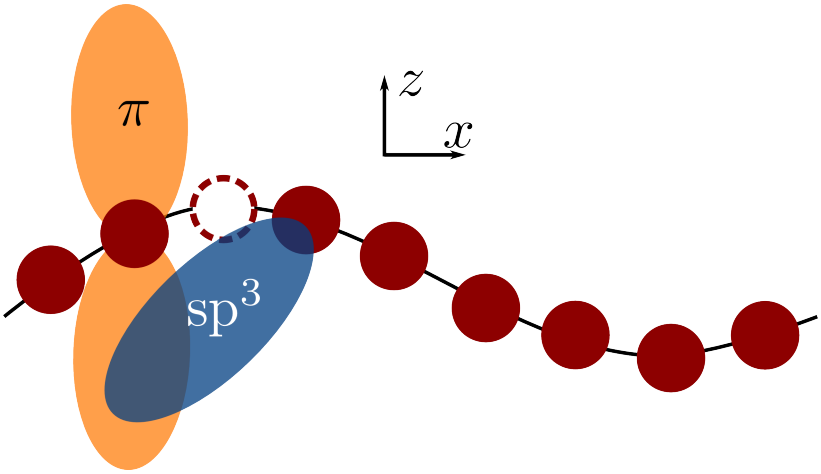

Figure 3.7: Schematic view of coupling between σ and π subsystem induced by rippling and sp^3 hybridization. Only one lobe of the sp^3 orbital is shown for simplicity.

3.2.1 Vacancy induced σ states

Let us first focus on the three states belonging to the σ sub-system that are induced by carbon defects and ignore the p_z states for the time being. As discussed above, we are left with three sp^2 orbitals that are remnants of the broken σ bonds after removal of a single carbon atom. Let us label the three orbitals by $i = 1, 2, 3$ where the orbital with index $i = 1$ resides at the top and the orbitals with $i = 2, 3$ at the base of the triangle in Fig. 3.5 (b). We can write down a simple tight-binding Hamiltonian [118, 117]

$$H = -h(s_1^\dagger s_2 + s_1^\dagger s_3 + h.c.) - h'(s_2^\dagger s_3 + h.c.), \tag{3.2.1}$$

where $s_i^{(\dagger)}$ are the annihilation (creation) operator at site i and $h, h' > 0$ the transfer integrals. The on-site energy can be neglected since the sp^2 orbitals rest near the Fermi energy without their bonding partner [117]. Both transfer integrals are the same in the case where the imperfect lattice shows the same symmetry as the undisturbed crystal and differ ($h' > h$) when the symmetry is reduced due

to the Jahn-Teller effect. DFT calculations suggest that $h'/h \simeq 5$ [119, 118, 117] favoring a reduced two-fold symmetrical configuration. The eigenvalues

$$E_{1,2} = \frac{-h' \pm \sqrt{8h^2 + h'^2}}{2}, \quad E_3 = h' \tag{3.2.2}$$

and corresponding eigenstates are readily obtained by diagonalization

$$|\psi_{1,2}\rangle = C_{\pm}|s_1\rangle \mp \frac{1}{\sqrt{2}} C_{\mp}(|s_2\rangle + |s_3\rangle), \tag{3.2.3}$$

$$|\psi_3\rangle = \frac{1}{\sqrt{2}}(|s_2\rangle - |s_3\rangle), \tag{3.2.4}$$

with

$$C_{\pm} = \Big[\frac{1}{2}\Big(1 \pm \frac{h'}{\sqrt{8h^2 + h'^2}}\Big)\Big]^{1/2} \tag{3.2.5}$$

$$\Rightarrow C_+ \to 1 \qquad C_- \to 0, \tag{3.2.6}$$

where the limit holds for the DFT ratio $h'/h \simeq 5$. The list of states in ascending order is thus

$$|\psi_1\rangle \to (|s_2\rangle + |s_3\rangle)/\sqrt{2} \tag{3.2.7}$$

$$|\psi_2\rangle \to |s_1\rangle \tag{3.2.8}$$

$$|\psi_3\rangle \to \frac{1}{\sqrt{2}}(|s_2\rangle - |s_3\rangle) \tag{3.2.9}$$

In neutral graphene the bonding combination $|\psi_1\rangle$ is doubly occupied while the sp^2 orbital located opposite of the shortened base of the triangle is singly occupied [117, 118].

3.2.2 Vacancy Induced Zero-Mode

In addition to the reconstruction of the σ bonds and the concomitant lattice deformation, a carbon vacancy also induces a localized state at the center of the π local density of states (LDOS) called 'zero-mode' [120]. This state is localized around the vacancy site and its wavefunction falls off with r^{-1} [120, 121, 117]. Interestingly, the zero-mode state is completely confined to the opposite sub-lattice with respect to the vacancy site, i.e. if the missing carbon atom is located on sub-lattice A then the zero-mode must be located entirely on sub-lattice B [117]. The state is not part of the itinerant π bands and therefore does not hybridize with the conduction electrons.

A simple yet powerful approach to examine the zero-mode is based on the Green's function of the impurity [117] which we review in the following. One starts with a n.n. tight-binding Hamiltonian

$$H_0 = -t \sum_{i\alpha, j\beta} c^{\dagger}_{i\alpha} c_{j\beta} + h.c., \tag{3.2.10}$$

where i numerates the unit cell and $\alpha = A, B$ iterates over the sub-lattice. At the site of the vacancy $\vec{r}_{0A}$ we introduce a potential term

$$V = U c_{0A}^{\dagger} c_{0A}, \quad U > 0, \tag{3.2.11}$$

that hinders electrons on neighboring sites to hop onto the vacancy site. The limit $U \to \infty$ corresponds to a missing carbon atom since the site is effectively removed from any hopping processes. The full Hamiltonian then takes the form

$$H = H_0 + V(U), U \to \infty. \tag{3.2.12}$$

Analogous to Sec. 3.1 one first transforms the unperturbed Hamiltonian into momentum space by using Bloch wavefunctions $|\vec{k}\alpha\rangle = N_k^{-1/2} \sum_i \mathrm{e}^{\mathrm{i}\vec{k}\cdot\vec{r}_{i\alpha}} |i\alpha\rangle$ where $\vec{r}_{i\alpha} = \vec{R}_i + \vec{\tau}_\alpha$ is the position of the αth atom in the ith unit cell. The transformed Hamiltonian takes on a 2x2 matrix shape

$$H_{\vec{k}} = \begin{pmatrix} 0 & f(\vec{k}) \\ f^*(\vec{k}) & 0 \end{pmatrix}, \tag{3.2.13}$$

with $f(\vec{k}) = -t(\mathrm{e}^{\mathrm{i}\vec{k}\cdot\vec{\delta}_1} + \mathrm{e}^{\mathrm{i}\vec{k}\cdot\vec{\delta}_2} + \mathrm{e}^{\mathrm{i}\vec{k}\cdot\vec{\delta}_3})$ and $\vec{\delta}_i$ being the n.n. vectors defined in Sec. 3.1 in Eq. (3.1.2). The second step is to calculate the Green's function for the unperturbed system in momentum space

$$g_{\alpha,\beta}(\vec{k},\omega) = \langle \vec{k}\alpha | g(\omega) | \vec{k}\beta \rangle = \frac{\omega + \mathrm{i}\eta + H_{\vec{k}}}{(\omega + \mathrm{i}\eta)^2 - |f(\vec{k})|^2}, \tag{3.2.14}$$

from which the real-space GF by Fourier transform

$$g_{i\alpha,j\beta}(\omega) = \frac{1}{N_k} \sum_{\vec{k}} \mathrm{e}^{\mathrm{i}\vec{k}(\vec{r}_{i\alpha} - \vec{r}_{j\beta})} g_{\alpha,\beta}(\vec{k},\omega) \tag{3.2.15}$$

is obtained. We are interested in the Green's functions for the perturbed lattice which is related to the unperturbed one via a Dyson's equation $G = g + gVG$. Inserting Eq.(3.2.11) yields

$$G_{i\alpha,j\beta}(\omega) = g_{i\alpha,j\beta}(\omega) + U g_{i\alpha,0A}(\omega) G_{0A,j\beta}(\omega). \tag{3.2.16}$$

We need the diagonal elements since we are interested LDOS

$$G_{i\alpha,i\alpha}(\omega) = g_{i\alpha,i\alpha}(\omega) + U g_{i\alpha,0A}(\omega) G_{0A,i\alpha}(\omega). \tag{3.2.17}$$

Here, $G_{0A,i\alpha}(\omega)$ can be expressed by Eq. (3.2.16) again which finally yields

$$G_{i\alpha,i\alpha}(\omega) = g_{i\alpha,i\alpha}(\omega) + \frac{U g_{i\alpha,0A}(\omega) g_{0A,i\alpha}(\omega)}{1 - U g_{0A,0A}(\omega)}. \tag{3.2.18}$$

We arrive at the LDOS of site $i\alpha$ by taking $\rho_{i\alpha}(\omega) = -1/\pi \Im G_{i\alpha,i\alpha}(\omega)$. Taking the trace over a single sub-lattice only yields after some lengthy algebra the total DOS of the respective sub-lattice

$$\rho_A(\omega) = \rho_0 + \frac{1}{N_k} \frac{-U[(1 - UF_0(\omega))\Im\xi(\omega) - \pi U \rho_o(\omega)\Re\xi(\omega)]}{\pi[(1 - UF_0(\omega))^2 + (\pi U \rho_0(\omega))^2]} \tag{3.2.19}$$

and

$$\rho_B(\omega) = \rho_0 + \frac{1}{N_k} \frac{-U[(1 - UF_0(\omega))(\pi\rho_0'(\omega) - \Im\xi(\omega)) + \pi U\rho_0(\omega)(F_0'(\omega) + \Re\xi(\omega))]}{\pi[(1 - UF_0(\omega))^2 + (\pi U\rho_0(\omega))^2]}, \tag{3.2.20}$$

where $\xi(\omega) = 1/N_k \sum_{\vec{k}} \left[g_{AA}(\vec{k}, \omega)\right]^2$ and $F_0(\omega) = \Re g_{0A,0A}(\omega)$.

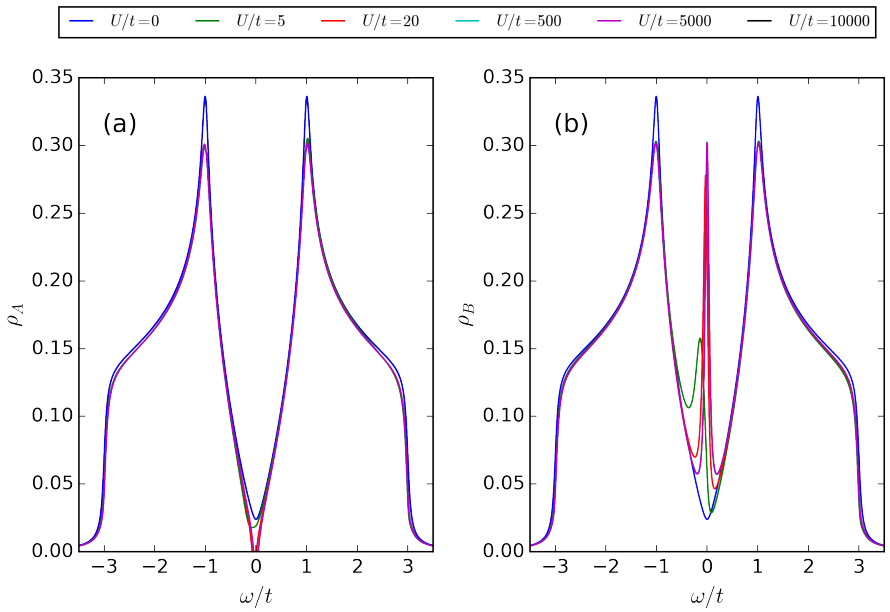

Figure 3.8: DOS for (a) same sub-lattice as single carbon vacancy site and (b) other sub-lattice as function of the potential U. Eq. (3.2.19) and Eq. (3.2.20) are evaluated on a (k_x, k_y) mesh with $N_k = 3000 \times 3000$ points. The zero-mode peak is confined to the sub-lattice B opposite to the sub-lattice A of the vacancy. The number of points N_k in Eq. (3.2.19) and Eq. (3.2.20) is taken as $N_k = 20$ for visual clarity. The legend applies to both sub-plots.

Fig. 3.8 shows the total density of states Eq. (3.2.19) and Eq. (3.2.20) evaluated directly on (k_x, k_y) mesh for each sub-lattice respectively. The total lattice includes a single carbon vacancy located on sub-lattice A. Since the zero-mode is localized around the vacancy site, it is not visible in the limit $N_k \to \infty$ in the total DOS. We use a mesh of $N_k = 3000 \times 3000$ points but use $N_k = 20$ in Eq. (3.2.19) and Eq. (3.2.20) for plotting. The zero-mode peak becomes more pronounced as U increases and is converged for $U/t \sim 10000$. Following the approach of Ref. [117], we can extend this scheme from calculating the total DOS for a given sub-lattice to the LDOS at any lattice point in real space. Furthermore, one can calculate the fraction of the zero-mode peak that is spread over the nearest neighbor site of our vacancy, the so-called Z factor. In case of a carbon vacancy, this factor is rather small $Z \approx 0.07$ [117, 19] due to the extended nature of the zero-mode.

3.2.3 Scanning Tunneling Microscopy (STM) and Spectroscopy (STS)

In the last sections, we reviewed the formation of the different orbitals at carbon vacancies. Before we discuss experimental evidence of local moments and Kondo physics, let us briefly outline the cornerstones of scanning tunneling microscopy (STM) and spectroscopy (STS). STM and STS are often the experimental method of choice for quantum impurity systems due to their excellent energy and spatial resolution down to the atomic scale [122, 123].
The general idea is that electrons tunnel between a sample and the tip of a sharp metallic probe generating a small but measurable current. In this setup, the probe hovers above the surface of the sample. Measurement of the tunneling current allows, among others, for three-dimensional imagining of the surface or reconstruction of the LDOS.

Over the years, STM/STS has become a staple technique in numerous fields such as (high temperature) superconductors [124, 123], quantum impurity systems in general, and graphene in particular [67, 125, 126, 127, 115, 9].

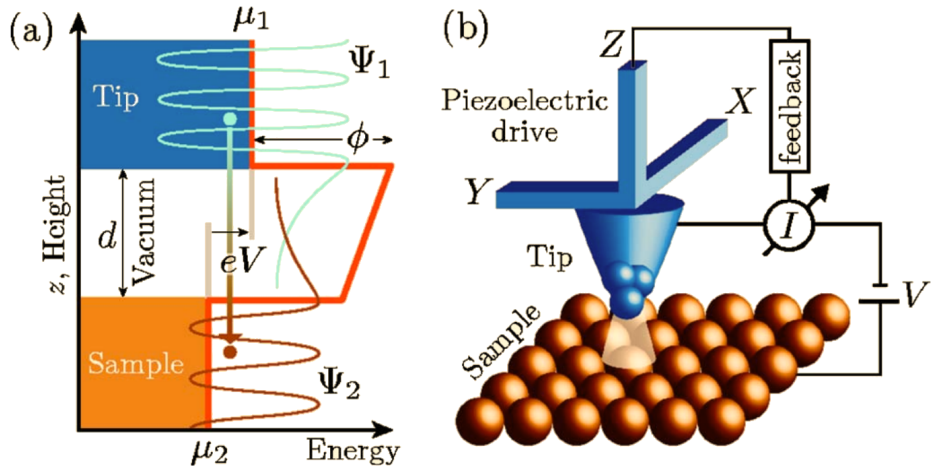

Figure 3.9: (a) Schematic electron tunneling between tip of probe and sample. The tip and the sample are in thermodynamic equilibrium at chemical potential $\mu_{1/2}$ respectively. ϕ is the so-called work function. (b) Schematic sketch of scanning tunneling microscope. The z actuator is linked to a piezoelectric drive that uses the tunneling current as input. The figure is taken from Ref. [123].

The underlying physical phenomenon, namely quantum tunneling between two electrodes via a potential barrier, has been well-known since the beginnings of quantum mechanics. A schematic depiction of the apparatus and process is shown in Fig. 3.9 (a). The tip hovers over the sample's surface in a distance z where the spacer in-between is usually vacuum. Electrons are confined to either material by a potential barrier ϕ (also called work-function). A finite bias voltage V introduces a shift in the chemical potential of tip and sample skewing the potential barrier. We know from basic quantum mechanics that an electron may

tunnel from one material to the other even if it cannot classically muster enough energy to overcome the potential barrier. As the wavefunction of the electron is suppressed exponentially beyond the barrier, the tunneling probability depends strongly on the thickness of the spacer z. If tip and sample are close enough, the individual tunneling processes may accumulate to a macroscopic and measurable current and the whole system will assume a steady-state driven by the applied bias voltage.

Giaever's measurement of the superconducting gap [124] together with Bardeen's theoretical work [128] laid down the foundation of tunneling spectroscopy as a new experimental method in the 1960s. A decisive improvement to these early applications was the invention of the modern scanning tunneling microscope [129] with its sharp metallic tip that can be moved freely over the surface via x, y actuators. The tip is brought in near proximity (a few angstroms) to the surface and a bias voltage is applied between sample and probe. Depending on the sign of the voltage the electrons either tunnel from tip to into empty states in the sample (positive voltage) or from occupied sample states into the tip (negative voltage) [67]. The resulting current is measured and used, via a feedback loop, to control the z actuator and thus the height of the tip [Fig. 3.9(b)].

The tunneling current takes the form [128, 67]

$$\begin{aligned} I(z,V) = \frac{4\pi e}{\hbar}\int_{-\infty}^{\infty}[f(E_F - eV + \epsilon) - f(E_F + \epsilon)] \\ \times \rho_T(E_F - eV + \epsilon)\rho_S(E_F + \epsilon)|M(z)|^2 \mathrm{d}\epsilon, \end{aligned} \tag{3.2.21}$$

where f is the Fermi function, E_F the Fermi energy, V the bias voltage and, $M(z)$ the tunneling matrix that shows a strong dependence on the distance z between sample and tip. In addition, the electronic densities of states of tip ρ_T and sample ρ_S both enter into the convolution integral. Usually, one would like the tip material to have a featureless density of states and a well-defined Fermi surface. For this reason, some of the most commonly used materials are Au, W, Ir, and PtIr [123]. Under the assumption of a constant ρ_T and for small temperatures the expression for the current reduces to [123, 67]

$$I(z,V) \propto \mathrm{e}^{-2z\kappa}\int_{-\infty}^{eV}\rho_S(\epsilon)\mathrm{d}\epsilon, \quad \kappa = \sqrt{\frac{2m\phi}{\hbar^2}} \approx 0.5\sqrt{\phi}\,\text{Å}^{-1} \tag{3.2.22}$$

where the work function $\phi \sim 5\,eV$ for a typical metal [123]. This exponential dependence on the distance means that for every additional angstrom of spacer the current will drop off roughly one order of magnitude. This, in combination with the piezoelectric drive, enables the microscope to reach its unparalleled high resolution.

In general, there are two distinctive operating modes for the microscope: either the tip is swept over the sample while maintaining a constant tunneling current or the feedback loop is turned off and the probe remains at a constant absolute height. In the first mode, if the DOS is approximately homogeneous

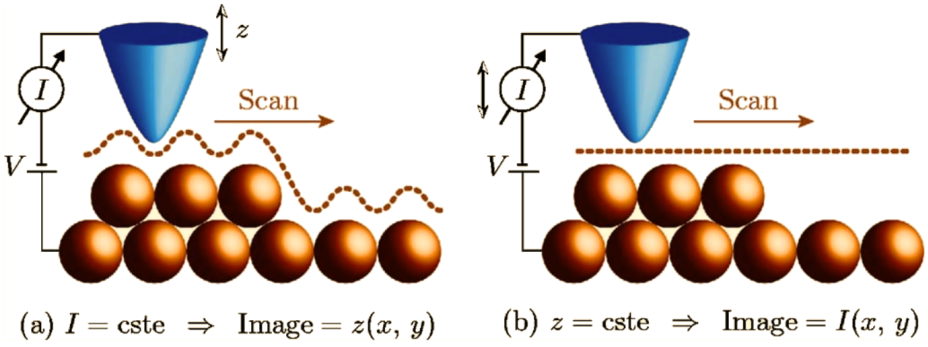

Figure 3.10: Different STM imaging modes. (a) Constant current and (b) constant height. The figure is taken from Ref. [123].

over the scanned area, the image corresponds to the three-dimensional surface of the sample [123]. The speed of this mode is inherently limited by the bandwidth of the feedback loop ($\sim$ kHz) as the tip has to be adjusted constantly. In the second mode, the tunneling current varies due to changes in the distance between sample surface and tip and thus also grants access to the surface topography. Since the speed is limited by bandwidth of the measurement of the current and not by the feedback loop, this mode is generally faster. However, for surfaces that show a significant modulation in height it might result in crashes of tip and sample. Both modes are visualized schematically in Fig. 3.10.

One of the most remarkable features is tunneling spectroscopy. Here, the connection between tunneling current and density of states is exploited in order to reconstruct the local electronic structure of the sample from the measured current derivation [130, 123]

$$\frac{\mathrm{d}I}{\mathrm{d}V}(V) \propto \rho_S(\epsilon = eV), \tag{3.2.23}$$

setting $E_F = 0$. One measures the tunneling current as a function of applied bias voltage: a positive voltage results in a tunneling from the tip into the unoccupied sample states whereas the electrons will tunnel out of the occupied states for negative bias [123]. The $\mathrm{d}I/\mathrm{d}V$ spectrum can then be calculated numerically or via a lock-in amplifier. In either case, the scanning tunneling spectroscopy technique provides a valid measurement of the local electronic structure of the sample at the position of the tip which, among others, allows for direct access of the Kondo peak.

3.3 Gate Controlled Kondo Effect in Graphene Sheets

In the last sections, we discussed the established theory regarding carbon vacancies in graphene. The existence of stable magnetic moments in these irradiated

graphene sheets [7, 8, 5, 4] and the occurrence of Kondo physics [6, 115, 116, 9] are well-known in literature.

Here, we focus on the existence and evolution of the Kondo peak as a function of the applied gate voltage or, equivalently, the chemical potential. We summarize the most important experimental studies that were carried out in the last couple of years.

Experimentally, a tunable Kondo effect in graphene has been observed by Chen et al. [6] in 2011. They measured the resistivity as a function of temperature and gate voltage of graphene sheets that were treated with ion irradiation in ultra-high vacuum. The temperature range extends from 300 mK to room temperature (290 K). Their findings were compared with untreated graphene membranes to identify the effect of the carbon vacancies on the resistivity. They found that the resistivity can be described by a temperature-independent contribution and a temperature-dependent part that follows the behavior expected for a spin 1/2 Kondo impurity [6]. They calculated the Kondo temperature by directly fitting the shape of the resistivity curve [6] which resulted in quite high Kondo temperatures between $30 - 90$ K as shown in Fig. 3.11.

The Kondo temperature calculated in such a way shows a pronounced dip at around $V_{\text{gate}} = 10$ V which is to be expected as the π DOS that is responsible for screening the impurity spin vanishes linearly for $\omega \to 0$. However, the Kondo temperature should vanish entirely at the Dirac point by the same logic, which is not observed in experiment. This poses the questions whether the measurement of the resistivity, which is inherently a simultaneous measurement of an ensemble of different carbon vacancies, is too limited and if the underlying model of a spin 1/2 Kondo effect regardless of gate voltage is too simplistic.

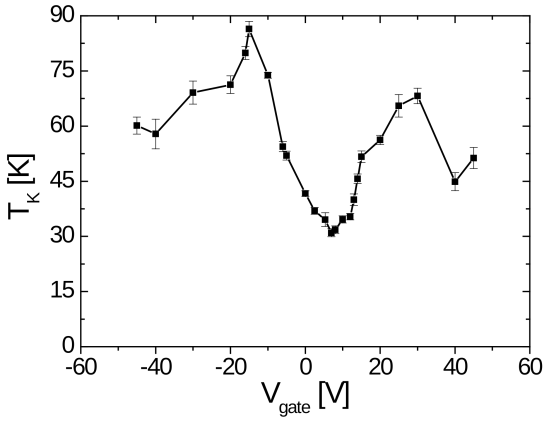

Figure 3.11: Kondo temperature T_K in Kelvin as a function of the applied gate voltage V_G. The figure was taken from arXiv:1004.3373v2 and later published in Ref. [6].

Both questions are addressed in a series of two papers [19, 9] where the authors relied experiment-wise on STS measurements that probe the LDOS in proximity of individual carbon vacancies. The formulation and treatment of a suitable model is discussed in Sec. 3.4 and Sec. 3.5 in detail. Here we summarize the experimental results that are mainly published in Ref. [9].

In order to create single carbon vacancies, graphene membranes are at first treated by low-energy ion sputtering and exposed to in situ annealing. The samples are fixed on a SiO_2 substrate and the $\mathrm{d}I/\mathrm{d}V$ spectra measured at a vacancy site are compared to spectra from regular sites to establish the presence

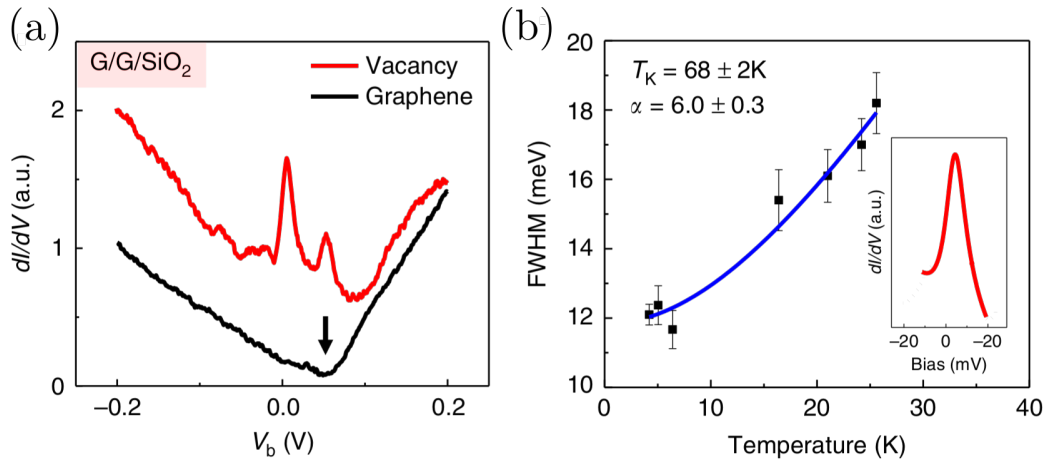

Figure 3.12: (a) $\mathrm{d}I/\mathrm{d}V$ curve of a carbon vacancy of a double layer of graphene on a SiO_2 substrate (red curve) compared to regular graphene (black curve) for $\mu = -54\,\mathrm{meV}$. The vacancy shows a Kondo peak at zero bias and the ZM peak at the Dirac point. The black arrow indicates the position of the DP. (b) Temperature evolution of the FWHM. A Fano fit (inset) is used to determine T_K. All error and error bars are obtained from the fitting procedure. Both figures are taken from Ref. [9].

of Kondo physics. Fig. 3.12 (a) shows the spectra for a chemical potential $\mu = -54\,\mathrm{meV}$ for a vacancy site (red curve) and far away from any vacancy (black curve). The chemical potential is calculated from the applied external gate voltage

$$\mu = \hbar v_F \sqrt{\pi c_{\mathrm{eff}} |V_G - V_D|}, \tag{3.3.1}$$

where V_G is the applied gate voltage, V_D is the offset of the charge neutrality point, and c_{eff} is the effective capacitance. A gate voltage in the order of $V_G \sim 50\,\mathrm{V}$ is needed in order to reach the desired high values for the chemical potential $|\mu| \sim 80\,\mathrm{meV}$ [9]. We define p ($\mu < 0$) and n ($\mu > 0$) doping via the external gate voltage and Eq. (3.3.1). The small black arrow in Fig. 3.12 (a) indicates the position of the Dirac point. At the site of the vacancy, one finds two peaks: the Kondo peak at zero bias and the ZM at the position of the DP. The spectra for pristine graphene exhibits the pseudogap behavior around the DP.

The Kondo temperature is estimated from fitting the line shape of the peak with a Fano curve [9]. The peak exhibits a temperature related broadening which can be taken into account by measuring the line shape at different temperatures and extrapolating via [131]

$$\Gamma_{LW} = \sqrt{(\alpha k_{\mathrm{B}} T)^2 + (2 k_{\mathrm{B}} T_K)^2}. \tag{3.3.2}$$

An example fit is shown in Fig. 3.12 (b) which yields equivalently high Kondo temperatures as observed in Ref. [6].

The authors categorized the single carbon vacancies into two different types according to their gate dependent $\mathrm{d}I/\mathrm{d}V$ curves. The first type of vacancy shows

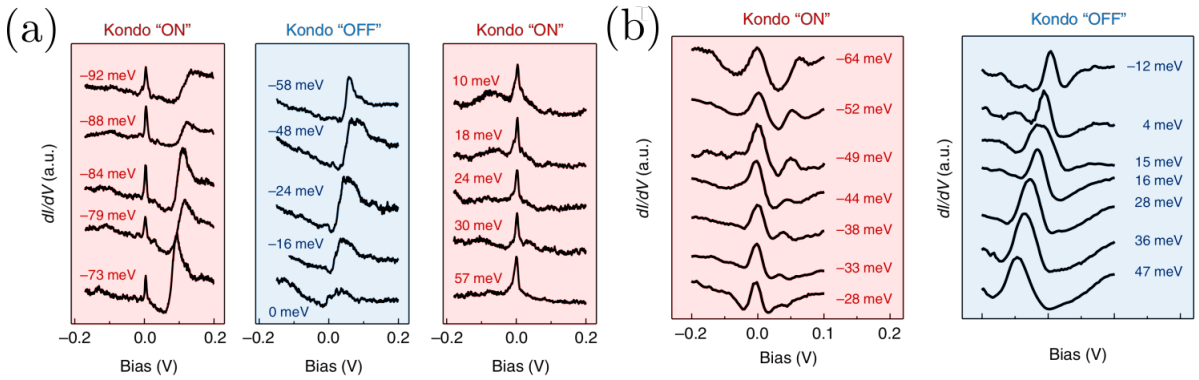

Figure 3.13: $\mathrm{d}I/\mathrm{d}V$ signature curves for different μ (written next to each curve) for both observed types. (a) Vacancy of type I: zero-bias anomaly is present for strong p ($\mu < 0$) and n doping ($\mu > 0$); see left and right subplot. The Kondo peak vanishes for intermediate chemical potential; see middle plot. (b) Vacancy of type II: Kondo peak for p doping (left) but not for n doping (right). For $\mu > 0$ a single peak is shifted linear with the chemical potential. Both figures are taken from Ref. [9]. Note that the x-axis labels in sub-plot (b) are wrong in the original publication as well. In both cases, the axis should extend from $V_{\mathrm{bias}} = -100\,\mathrm{meV}$ to $200\,\mathrm{meV}$.

a Kondo peak for either n or strong p doping but not for vanishing to moderate p doping [Fig. 3.13 (a)]. The second type of vacancy exhibits a Kondo peak only for p doping. A single peak is formed for $\mu \approx 0$ around $V_{\mathrm{bias}} = 0$ which is then shifted linearly to smaller energies with increasing chemical potential such that it resides roughly at $V_{\mathrm{bias}} = -\mu$. No Kondo peak is present for n doping [Fig. 3.13 (b)].

The different types of vacancies are linked to the out-of-plane displacement and therefore the rippling strength at the vacancy site [9]. As discussed in Sec. 3.2, a carbon vacancy site results in an effective hybridization between σ and π subsystem which may lead to Kondo physics. The hybridization strength (and to a degree the Kondo temperature) is therefore directly proportional to the intensity of the curvature at the defect.

3.3.1 Single Orbital Model and Dynamically Screened Coulomb Interaction

The measurements are accompanied by a simplified single orbital model with a gate voltage dependent $U_{\mathrm{eff}}(\mu)$ to account for dynamical screening effects and reproduce the experimental STS data [9]. The full model Hamiltonian reads [9]

$$\begin{aligned} H = &\sum_{\sigma} (\epsilon_d - \mu) f_\sigma^\dagger f_\sigma + U_{\mathrm{eff}}(\mu) f_\uparrow^\dagger f_\uparrow f_\downarrow^\dagger f_\downarrow + \sum_{\sigma} \int_{-D}^{D} \frac{\omega + \mu}{D} c_\sigma^\dagger(\omega) c_\sigma(\omega) \mathrm{d}\omega \\ &+ \sum_{\sigma} \int_{-D}^{D} \sqrt{\frac{\Gamma(\omega)}{\pi D}} \left[c_\sigma^\dagger(\omega) f_\sigma + h.c. \right] . \end{aligned} \tag{3.3.3}$$

Here, $f_\sigma^{(\dagger)}$ are the fermionic operators for a single local orbital at the vacancy site and $c_\sigma^{(\dagger)}(\omega)$ describe the conduction band. Two key points are of particular importance: firstly, the hybridization function $\Gamma(\omega)$ is approximated by [9]

$$\Gamma(\omega) = \begin{cases} \Gamma_0 \frac{|\omega+\mu|}{D_{\text{eff}}}, & \frac{|\omega+\mu|}{D_{\text{eff}}} \leq 1 \\ \Gamma_0, & \frac{|\omega+\mu|}{D_{\text{eff}}} > 1, \frac{|\omega|}{D_{\text{eff}}} \leq \frac{D}{D_{\text{eff}}} \\ 0, & \text{else.} \end{cases} \tag{3.3.4}$$

The linear slope of the pseudo-gap extends to $D = 2\,\text{eV}$ beyond which the hybridization is constant to the edge of the band. Secondly, the Coulomb interaction comprises a dynamic term that results from the filling of the ZM [9]

$$U_{\text{eff}} = \begin{cases} U, & \mu \leq 0 \\ U + \min(U_{\pi f}, \alpha\mu), & \mu > 0, \end{cases} \tag{3.3.5}$$

where α is a positive constant. The rationale behind this parameterization is that the ZM is empty if $\mu < 0$. Therefore, the ZM influences the local orbital only in the p doped regime. There, it is postulated that the effect of an additional electron in the ZM can reasonably be approximated by a renormalized Coulomb interaction. The larger μ the larger the filling and thus the additional Coulomb term.

This model, on one hand, fits the experimental observed Kondo peaks, but, on the other hand, cannot explain the interplay between zero-mode and broken σ bond sufficiently on a microscopic level. The ZM is completely dismissed except for a change of U. The justification for this parameterization is not satisfactory since one easily encompasses the effect of the ZM directly into the model. The adaptive U term becomes a fitting parameter without any real physical meaning. In the following, we present the more elaborate two-orbital model of Cazalilla et al. [116] on which we base our NRG calculations.

3.4 Formulation of an Effective Two-Orbital Model for Carbon Vacancies in the Isolated Limit

The experimental evidence indicates the formation of local moments and existence of Kondo physics in non-pristine graphene sheets as we discussed in Sec. 3.2. Furthermore, we saw in Sec. 3.3 that it is possible to apply a gate voltage, that acts as a chemical potential, in order to control formation and width of the emerging Kondo peak [9]. Naturally, one may ask whether there is a microscopic model that provides a compelling explanation for this behavior. The goal is to describe both types of carbon vacancies discussed in Sec. 3.3 in a single model. The model parameter for both cases should be similar since both vacancies are found on the same graphene membranes and their only apparent difference is the local curvature.

We recall that single carbon vacancies result in the formation of a dangling σ orbital and the π zero-mode that are orthogonal to each other and to the π bands in case of pristine graphene as we discussed preliminarily in Sec. 3.2.1 and Sec. 3.2.2. This orthogonality is lifted by the local curvature in the proximity of the defect. The sp^2 orbital undergoes sp^3-hybridization with the p_z orbital which leads to an out-of-plane oriented lobe and an effective coupling of broken σ bond and π conduction bands. The orthogonality between zero-mode and π bands is likewise broken via hybridization with the slanted sp^3 lobe. This indirect hybridization is thus smaller then the coupling between sp^3 orbital and π band and will be neglected in the following.

The zero-mode lies energetically at $\omega = 0$ in n.n. tight-binding approximation while the sp^3 orbital is energetically located below Fermi energy [117]. Ab-initio calculations suggest that a single electron occupies both orbitals close to charge neutrality [117]. Both orbitals are exposed to various inter- and intra-orbital Coulomb interactions. DFT calculations state that the electrons' spins align ferromagnetically according to a strong inter-orbital Hund's rule coupling $J_H \approx 0.35\,\mathrm{eV}$ [117]. In addition, electrons on the lower lying hybrid orbital are strongly correlated by a Coulomb repulsion U. The exact value of U is debated over the literature [132, 133, 134, 4, 135] and estimates range from $U = 0.5\,\mathrm{eV}$ [4] over $U = 2\,\mathrm{eV}$ [132, 135] to $U = 10\,\mathrm{eV}$ [134, 133]. The Coulomb repulsion for electrons in the zero-mode state is estimated to be roughly two to three orders of magnitude smaller ($\sim 0.001\,\mathrm{eV}$) than that of the hybrid orbital [116] due to its extended nature and inter-orbital repulsion is likewise roughly an order of magnitude smaller $\sim 0.1\,\mathrm{eV}$ [116].

In the following, we use the index d for the sp^3 hybrid orbital that stems from the broken σ bond whereas the index σ will stand for the spin degree of freedom to avoid confusion. The index π will be used to label the zero-mode state.

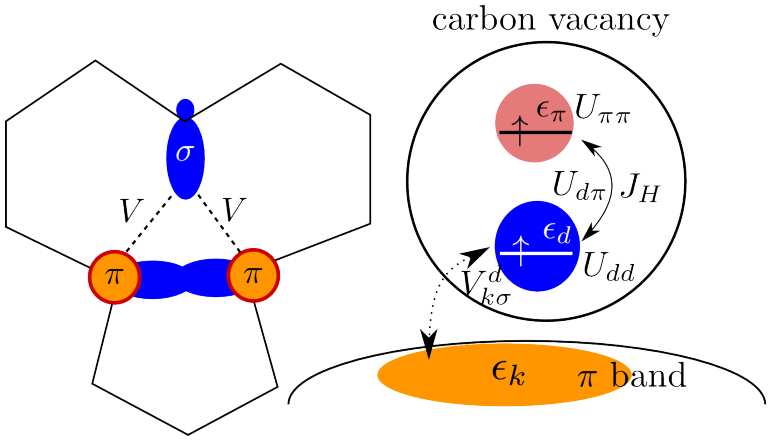

Figure 3.14: Schematic view of the two-orbital model and the different interaction terms. Left: Triangle shape of the carbon vacancy. Hybridization between broken σ bond and π orbitals. Right: d orbital and π state. Only the d orbital is directly couples to the π bands. Taken from Ref. [19].

The full Hamiltonian consists of three parts: a fully localized H_{loc} that comprises d orbital and π state, H_{band} that describes the pseudogap π DOS, and H_{hyb} which contains the hybridization between d orbital and π band

$$H = H_{\mathrm{loc}} + H_{\pi-\mathrm{band}} + H_{\mathrm{hyb}}. \tag{3.4.1}$$

The local Hamiltonian then takes the form [116, 19]

$$\begin{aligned} H_{\mathrm{loc}} = &\sum_{\sigma}(\epsilon_d n_{d\sigma} + \epsilon_\pi n_{\pi\sigma}) + U_{dd} n_{d\uparrow} n_{d\downarrow} \\ &+ U_{\pi\pi} n_{\pi\uparrow} n_{\pi\downarrow} + U_{d\pi} \sum_{\sigma\sigma'} n_{d\sigma} n_{\pi\sigma'} - J_H \vec{S}_\pi \vec{S}_d \\ &- J_H (d^\dagger_{d\uparrow} d^\dagger_{d\downarrow} d_{\pi\downarrow} d_{\pi\uparrow} + h.c.). \end{aligned} \tag{3.4.2}$$

The first two terms describe the single particle energies $\epsilon_{d,\pi}$ for both effective orbitals while the many-body interaction is split into its various contributions: U_{dd} and $U_{\pi\pi}$ represent the intra-orbital Coulomb interaction only, i.e. between electrons on the same orbital but with different spin degree of freedom. Inter-orbital interactions are further split into a density-density $U_{d\pi}$ and a spin-spin term which is in addition augmented by pair-hopping processes to ensure rotation symmetry in spin space [136]. The second part of the Hamiltonian comprises the tight-binding approximation for the π sub-system [Eq. (3.1.6)] that we already discussed in Sec. 3.1.1. Alternatively, we can employ the linear approximation for the hybridization [Eq. (3.1.14)] where the band has a simplified non-constant DOS. The last part captures the coupling between local and itinerant degrees of freedom. It takes the form

$$H_{\mathrm{hyb}} = \sum_{\vec{k}\sigma\tau} V^d_{\vec{k}} (c^\dagger_{\vec{k}\sigma\tau} d_\sigma + d^\dagger_\sigma c_{\vec{k}\sigma\tau}), \tag{3.4.3}$$

where $\tau = \pm$ denotes the band index. We only include a direct hybridization between d orbital and π band. The whole model is depicted schematically in Fig. 3.14.

Let us focus on the local part of the Hamiltonian and neglect hybridization and bands for now. At charge neutrality there should be one electron localized on the vacancy. It will occupy the low-lying d orbital in accordance with ab-initio calculations [117]. For p doping, the d orbital will normally remain singly occupied due to the strong Coulomb repulsion while the occupation of the π orbital depends sensitively on its level position ϵ_π since $U_{\pi\pi}$ is weak. If ϵ_π is close to the Fermi energy and the d orbital is only partially filled, the Hund's rule coupling will result in triplet alignment. However, the π orbital will become completely filled if ϵ_π is lowered enough such that the energy gain of a second π electron will outweigh the Hund's rule energy reduction. On the other side of the spectrum, the π orbital will become unoccupied if ϵ_π rests too high. In all cases, the d orbital will be singly occupied as long as the level position is not unreasonable low. There will be a local magnetic moment due to the d orbital

or, in case of the triplet alignment, due to both orbitals. If we now include the hybridization, this moment will be screened below T_K by the conduction electrons resulting in Kondo physics albeit with vastly different Kondo temperatures.

For n doping, three different ground states (GS) are realistic depending on the single particle energies and chemical potential. In the first arrangement, one electron occupies each orbital with their spins aligned due to the ferromagnetic Hund's rule coupling J_H. The situation resembles the triplet configuration for p doping and will equally result in Kondo screening. The magnetic moment, however, will be underscreened since the total spin is $s = 1$. The ground state energy of the isolated vacancy model is then [19]

$$E_T = \epsilon_d + \epsilon_\pi + U_{d\pi} - J_H - 2\mu. \tag{3.4.4}$$

When we lower the π level slightly, it becomes doubly occupied rapidly. Both electrons form a singlet while the sole d electron remains dangling. The ground state is thus a doublet state with total energy [19]

$$E_D = \epsilon_d + 2\epsilon_\pi + U_{\pi\pi} - 3\mu \tag{3.4.5}$$

and Kondo screening is possible when the hybridization is switched on.

The third configuration is reached when the π level is raised instead and is unoccupied while simultaneously lowering the ϵ_d until two electrons occupy the d level. The ground state is a singlet state with energy [19]

$$E_S = 2\epsilon_d + U_{dd} - 2\mu. \tag{3.4.6}$$

Here, Kondo screening cannot take place as the d orbital effectively decouples from the conduction band.

3.4.1 Hybridization Dependent Level Repulsion

We now combine the two local orbitals and the pseudo-gap DOS into a single model. The three different ground states of the vacancy in the atomic limit, outlined above, serve as precursors for the different vacancy types observed in experiment [19, 9]. The local triplet and singlet configuration for n doping in particular are directly related to vacancies of type I and II respectively. The situation for n doping is summarized in Fig. 3.15. We recall that the singlet and triplet GS differ by one electron in the π orbital. If we keep all Coulomb interactions constant, we can trigger a change of GS by adjusting the level positions $\epsilon_{d/\pi}$. A larger ϵ_π and smaller ϵ_d quickly empties the orbital and breaks the ferromagnetic triplet state in favor of the singlet configuration. The physical origin of this level shift is a curvature induced hybridization between d orbital and π orbitals on neighboring carbon sites [116, 118] which generates a hopping term between zero-mode and d orbital. In perfectly flat graphene, the local orbitals

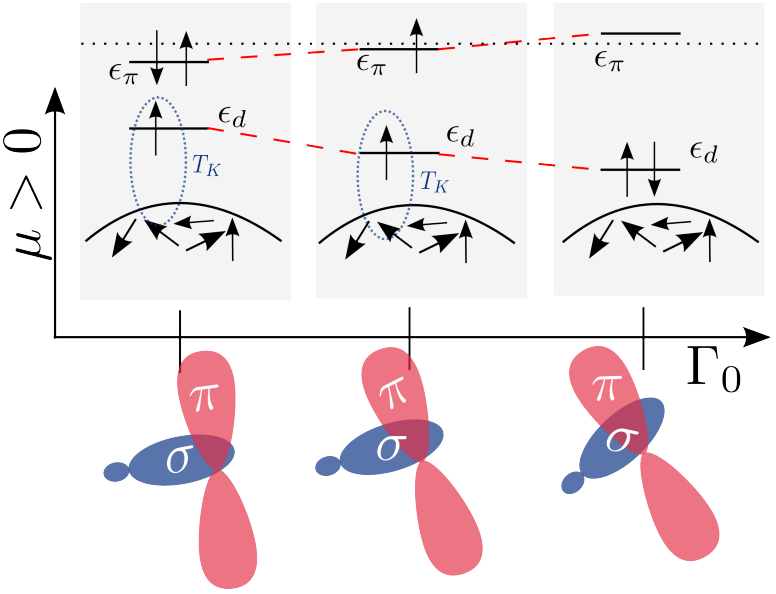

Figure 3.15: Schematic representation of microscopic behavior for n doping. Left: Hybridization is small and both states lie below E_F. The d orbital is singly occupied due to strong Coulomb repulsion and can form a Kondo singlet. Center: Hybridization is increased and both levels move apart due to level repulsion. Total occupation is lowered and the electron's spins form a triplet that is partially screened. Right: Even higher hybridization leads to doubly occupied d orbital. Kondo effect breaks down. Taken from Ref. [19].

are orthogonal and $\epsilon_{d/\pi}$ assume some value. Ripples break this orthogonality mixing the d and π orbital. The stronger the rippling the larger the admixture. This results in an effect called 'level-repulsion' where the lower lying orbital gets shifted to even smaller and the upper orbital to even higher energy. We can write down a simple single-particle Hamiltonian

$$H^{sp}_{\text{loc}} = U^\dagger \begin{pmatrix} \epsilon'_d & 0 \\ 0 & \epsilon'_\pi \end{pmatrix} U = \begin{pmatrix} \epsilon_d & \sqrt{Z}V \\ \sqrt{Z}V & \epsilon_\pi \end{pmatrix}, \tag{3.4.7}$$

where V is the curvature induced hybridization [Eq. (3.1.13)], $Z \approx 0.07$ [117, 19] is the Z factor of the zero-mode at the neighboring site (Sec. 3.2.2), and U is a unitary transformation matrix. The new orbitals d' and π' are linear combinations of the original d and π orbital with hybridization dependent eigenenergies $\epsilon'_{d,\pi}(V)$. The stronger the hybridization, i.e. the more curved the graphene membrane at the vacancy, the larger the admixture of π and d orbital. The new level positions will drift apart as the hybridization is increased. This repulsion then causes the transition from the triplet to the singlet ground state and therefore links both types of vacancy together: larger hybridization and thus stronger rippling corresponds to the singlet configuration and smaller hybridization to the triplet.

We can simplify the level repulsion by a more empirical approach. Instead of deriving the level positions from one set of parameters via Eq. (3.4.7), we can try

to identify the characteristic regimes directly by treating $\epsilon_{d/\pi}$ as free variables. Once we have established the regimes, we can simply interpolate between both level energies over the desired range. The interpolation takes the form

$$\epsilon'_{d/\pi}(\Gamma_0) = \epsilon'_{d/\pi}(\Gamma_0^{\mathrm{i}}) + \frac{\epsilon'_{d/\pi}(\Gamma_0^{\mathrm{s}}) - \epsilon'_{d/\pi}(\Gamma_0^{\mathrm{i}})}{\Gamma_0^{\mathrm{s}} - \Gamma_0^{\mathrm{i}}}(\Gamma_0 - \Gamma_0^{\mathrm{i}}), \tag{3.4.8}$$

where $\Gamma_0^{\mathrm{i/s}}$ is the empirically determined hybridization strength for the intermediate or strong hybridization regime respectively and $\epsilon_{d/\pi}(\Gamma_o^{\mathrm{i/s}})$ are the corresponding level positions.

3.5 The Numerical Renormalization Group applied to Graphene

In the past sections we laid out the realistic two-orbital impurity model including peculiar pseudo-gap density of states of graphene. The Hamiltonian is solved using the NRG presented in Sec. 2.3. The main focus of this section are our results that are published in two papers [19, 9]. We find that our simplified picture, discussed in Sec. 3.4, holds up well when tested numerically. Two of the three groundstates of the isolated model lead naturally to both different regimes observed in experiment distinguished by a change in hybridization strength. The third regime has been observed as well but not explicitly labeled. We name the three regimes according to their hybridization strength as 'weak', 'intermediate', and 'strong'.

The carbon vacancies in the experimental study are located on the same samples but nonetheless show qualitatively completely different $\mathrm{d}I/\mathrm{d}V$ spectra. The goal of our study is to explain all spectra in a single model with only small parameter adjustments and as few parameters as possible. The parameters are not expected to change drastically between different vacancies as the vacancies are all located on the same graphene sheets.

Since we tied the level positions to the hybridization strength in Sec. 3.4.1, we are left with two undetermined parameters: chemical potential μ and hybridization strength Γ_0. We begin by sketching the different scenarios qualitatively in Sec. 3.5.1. This sketch summarizes the key findings and serves as guideline and orientation in the following sections. We then map the resulting parameter space as a whole in Sec. 3.5.2 for (i) $T = 4.2\,\mathrm{K}$ as used in experiment [9] and for (ii) $T \to 0$. We proceed to examine each regime independently in Sec. 3.5.3. We analyze the spectral density for the π orbital in Sec. 3.5.4 before we compare the Kondo temperature calculated from the line shape of the spectra density versus zero-bias conductance in Sec. 3.5.5. We continue by checking our results for stability against deviation from our parameter set in Sec. 3.5.6. The underlying physics does not depend on the exact set of parameters, and a small deviation is generally acceptable. However, the Kondo temperature plummets drastically if

U_{dd} becomes too small. We investigated the dependence of T_K on the chemical potential and found that close to $\mu = 0$ the Kondo temperature is exponentially suppressed (Sec. 3.5.7). We continue with an attempt to adjust the Coulomb matrix dynamically in Sec. 3.5.8 before finishing with a summary in Sec. 3.5.10.

3.5.1 Unified Picture of the Different Regimes

Before we review our numerical results, let us compile everything into a single schematic diagram as a guideline for the following sections. Fig. 3.16 shows the local orbitals and their filling for the weak [Subplots 3.16 (a)-(c)], the intermediate [Subplots 3.16 (d)-(f)], and the strong hybridization regime [Subplots 3.16 (g)-(i)]. We depict the arrangement for p and n doping as well as for charge neutrality ($\mu \approx 0$). Around $\mu \approx 0$, the pseudo-gap DOS suppresses Kondo screening. It is indicated by the schematic V-shape of the band. The different regimes and various fixed points are discussed later in detail.

In the weak hybridization regime, the vacancy shows a unscreened local moment for most μ except for large n doping. The Kondo temperature surpasses T only for large $\mu > 0$. The d orbital is always half-filled due to the high Coulomb repulsion whereas the π orbital is prone to double filling. The strong Hund's rule coupling aligns the spins, and level repulsion is weak due to the small hybridization.
The intermediate hybridization regime is characterized by Kondo screening for large p and n doping. The d orbital is still half-filled, but the π orbital is either empty or singly occupied as a result of the stronger level repulsion. The spins of the electrons again form a triplet due to the Hund's rule coupling.
In the strong hybridization regime, the π orbital remains empty for any chemical potential because it is shifted above the Fermi level. This time there is a Kondo screening for p doping. On the other hand, the d orbital fills up for n doping creating a singlet and preventing the Kondo effect to occur.

3.5.2 Mapping of the Parameter Space

Let us first look at the whole parameter space at the experimental $T = 4.2\,\mathrm{K}$ [9]. All calculations in this section are done for a DOS sampled in reciprocal space (solid line in Fig. 3.4) and level repulsion based on the Z factor Eq. (3.4.7). We use a discretization parameter $\Lambda = 1.81$ and keep $N = 2000$ states after every NRG truncation. We reach the desired temperature for a Wilson chain of length $N_{\mathrm{it}} = 34$ and $\overline{\beta} = 1.225$. The results of this chapter are for the most part published in Ref. [19].

The physics at $T = 4.2\,\mathrm{K}$ can roughly be partitioned into the three different regimes discussed above based on the hybridization strength Γ_0. The boundaries between these regimes do not represent sharp phase boundaries but broad

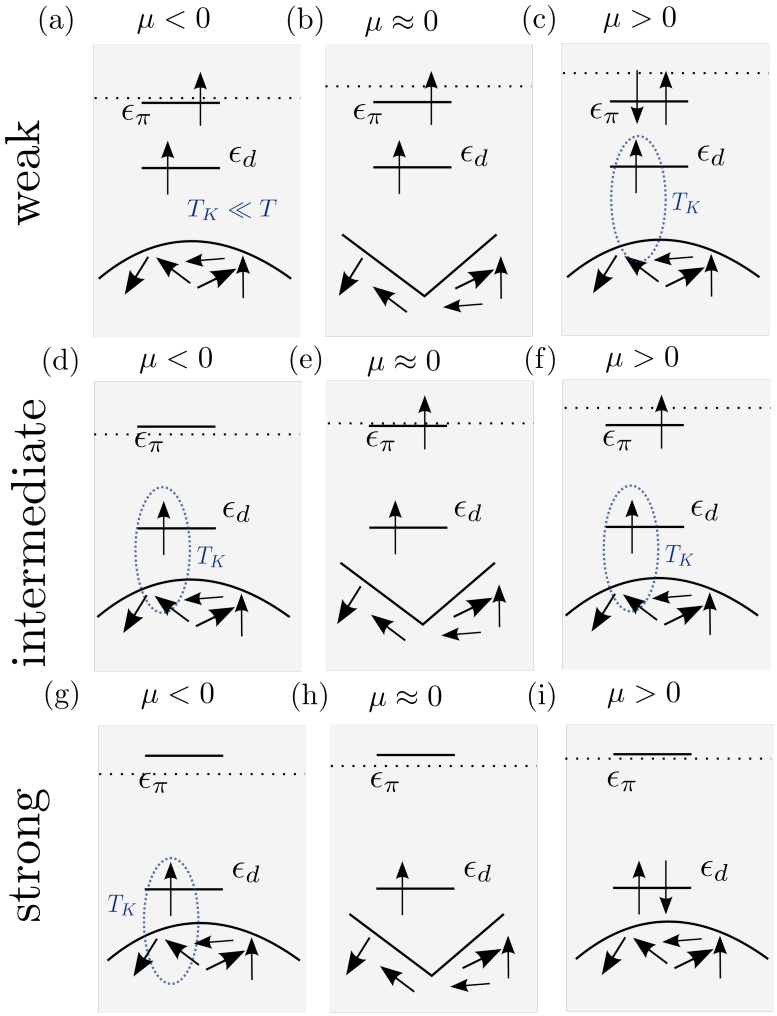

Figure 3.16: Schematic representation of the vacancy levels and filling for the weak (top row), intermediate (middle row), and strong hybridization regime (bottom row)for p doping ($\mu < 0$), around charge neutrality ($\mu \approx 0$), and for n doping ($\mu > 0$). The dotted line represents the Fermi energy. The pseudo-gap DOS is portrayed by the linear slope for $\mu \approx 0$.

Table 3.1: Level positions and Coulomb interactions for the sampled DOS and Z factor based level repulsion for each of the three different regimes. Data published in Ref. [19].

Regime	DOS	level repulsion	ϵ_d/eV	ϵ_π/eV	U_{dd}/eV	$U_{d\pi}$/eV	$U_{\pi\pi}$/eV	J_H/eV	Γ_0/eV
weak	t, t'	Z factor	−1.21	0.01	2.00	0.10	0.01	0.35	1.00
intermediate	t, t'	Z factor	−1.38	0.18	2.00	0.10	0.01	0.35	1.70
strong	t, t'	Z factor	−1.47	0.27	2.00	0.10	0.01	0.35	2.10

crossover regions instead. The Coulomb interactions and level positions for a single representative Γ_0 for each regime are listed in Tab. 3.1.

As we vary the chemical potential and the hybridization strength, the system approaches one of seven different fixed points (cf. differently colored areas in

Fig. 3.17): three local moment configurations (LM-a, LM-b, LM-c), three strong coupling (SC-a, SC-b, SC-c), and one frozen impurity (FI) fixed point. Not all FPs are stable, as we are going to see. Fig. 3.17 shows the color coded product of the total local occupation times impurity entropy. The entropy is calculated as discussed in Sec. 2.3.
The local occupation of the vacancy changes twice as we sweep from weak to strong hybridization regardless of the applied chemical potential. The only exception is a narrow region for high p doping $\mu < -70\,\mathrm{meV}$ where both local orbitals are half-filled even for the smallest hybridization strength considered here.

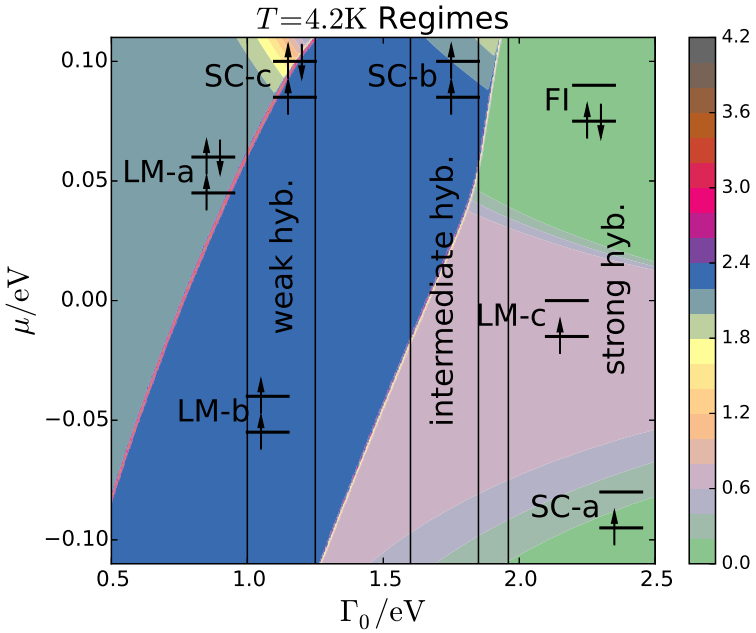

Figure 3.17: Different regimes for finite temperature $T = 4.2\,\mathrm{K}$ as function of chemical potential μ and hybridization strength Γ_0. The plot is colored according to the product of local occupation and local entropy $n_{\mathrm{loc}} S_{\mathrm{loc}}$. The used parameters are listed in Tab. 3.1. Solid black lines indicate the three different regimes (weak, intermediate, and strong hybridization). Each colored area is labeled by the fixed point of the system for finite $T = 4.2\,\mathrm{K}$ as well as the impurity occupation of the ground state. Taken from [19].

Let us transverse through the parameter space by picking a number of selected hybridization strengths and varying the chemical potential. For the weakest hybridization taken into consideration, $\Gamma_0 \approx 0.5\,\mathrm{eV}$, the system approaches one of two local moment fixed points depending on μ (LM-a and LM-b in Fig. 3.17). Interestingly, the lower lying d orbital is only half filled in both cases while the π orbital is either doubly occupied (LM-a) or singly occupied (LM-b). This inverted occupation where the orbital with the higher single particle energy gets filled first is a direct result of the vastly different intra-orbital Coulomb repulsion $U_{dd} \gg U_{\pi\pi}$. If we decrease the chemical potential while keeping Γ_0 constant, an electron gets delocalized and there is a charge crossover line from three to two

electrons (LM-a to LM-b) defining a charge crossover chemical potential $\mu_{\mathrm{cc}}^{3\to2}(\Gamma_0)$. These crossover values are not critical values due to the finite temperature as we discuss later in Sec. 3.5.2.1 and Sec. 3.5.3.

A third fixed point emerges for slightly higher, but still relatively weak hybridization $\Gamma_0 = 1\,\mathrm{eV}$ which represents the 'weak hybridization regime'. The LM-a fixed point is unstable and we see a crossover to a strong coupling fixed point (SC-c) for large positive μ. The electrons in the π orbital form a singlet and the dangling spin of the d electron gets screened below a Kondo scale T_K. For μ smaller than the charge crossover value $\mu_{\mathrm{cc}}^{3\to2}(1\,\mathrm{eV}) \approx 60\,\mathrm{meV}$, the spins align ferromagnetically in a local triplet state. This spin $s = 1$ LM fixed point extends to p doping and is unstable as the triplet will eventually be screened partly by the conduction band (underscreened or undercompensated Kondo effect [137]). However, the Kondo temperature T_K for the underscreened triplet is small compared to T. If we decrease T further, we find another crossover to a SC fixed point (see Fig. 3.18 for slightly larger $\Gamma_0 \sim 1.25\,\mathrm{eV}$). This picture changes when we increase $\mu > \mu_{\mathrm{cc}}^{3\to2}$ above the charge crossover value. Because both π electrons form a singlet state, the single d electron is left alone providing a dangling spin that is then screened by the conduction electrons. The smaller μ the smaller the Kondo scale T_K regardless of the nature of the SC fixed point (conventional or underscreened) as the effective coupling is diminished by the linearly decreasing DOS. The difference in Kondo temperatures between underscreened triplet (p doped) and conventional screening (n doped) has already been observed in recent NRG calculations [138]. In addition, it has been shown that flipping the sign of the chemical potential but keeping the absolute value does not result in a symmetric T_K even for a conventional $s = 1/2$ Kondo problem [17, 110]. Thirdly, the hybridization function is asymmetric on its own (cf. Fig. 3.4) naturally leading to different effective hybridization strengths for n and p doping.

The 'intermediate hybridization regime' can be found for $\Gamma_0 \simeq 1.7\,\mathrm{eV}$ where both local orbitals drift apart even further which in turn leads to a second charge crossover line $\mu_{\mathrm{cc}}^{2\to1}$. At this fixed Γ_0, the crossover occurs for $\mu_{\mathrm{cc}}^{2\to1} \approx 10\,\mathrm{meV}$ (Fig. 3.17). Below this crossover value the vacancy is only occupied by one single electron that rests in the lower d orbital. The system is therefore close to an $s = 1/2$ local moment fixed point (LM-c) for $\mu < \mu_{\mathrm{cc}}^{2\to1}$. The moment is screened by the conduction band if the system resides deep in the p doped regime ($\mu \approx -90\,\mathrm{meV}$, SC-a). For intermediate but negative μ the Kondo temperature $T_K < T$ and the moment remains unscreened at finite $T > T_K(\mu)$.
For $\mu > \mu_{\mathrm{cc}}^{2\to1}$, the system stays close to the LM-b fixed point. This fixed point, however, is unstable and the triplet eventually gets partly screened. Since the Kondo scale depends exponentially on the chemical potential due to the pseudogap DOS, the strong coupling fixed point is only reached for high n doping $\mu \approx 100\,\mathrm{meV}$.

We now turn to the 'strong hybridization regime' for $\Gamma_0 = 2.1\,\mathrm{eV}$. The p doped region remains the same compared to $\Gamma_0 = 1.7\,\mathrm{eV}$. It is partitioned into LM-c for small and SC-a fixed point for large absolute chemical potential. The n

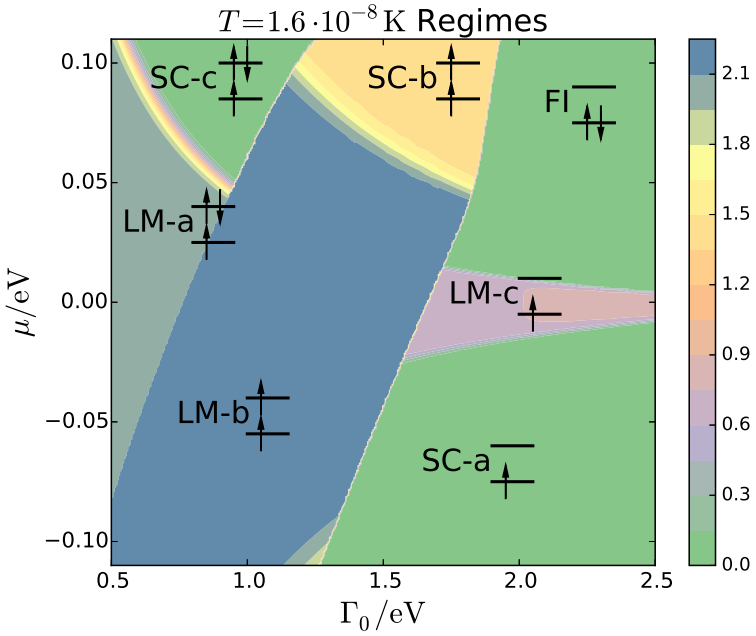

Figure 3.18: Different regimes for $T = 1.6 \cdot 10^{-8}\,\mathrm{K}$ as function of chemical potential μ and hybridization strength Γ_0. The plot is colored according to the product of local occupation and local entropy $n_{\mathrm{loc}} S_{\mathrm{loc}}$. The used parameters are listed in Tab. 3.1. Taken from [19].

doped regime, on the other hand, changes drastically due to level repulsion and increased coupling. It is dominated by a single stable frozen impurity fixed point (FI) where the π orbital is completely empty while the d orbital is partly filled. Interestingly, it is neither singly or doubly occupied but exhibits a fractional filling close to the valence fluctuation point value $n_d \approx 4/3$. The exact value depends on Γ_0 and μ and varies slightly. However, the ground state calculated during the NRG is a doubly occupied state. A fractional part of the second electron is therefore delocalized and spread over the first sites of the Wilson chain. Only a third of the electron is actually localized at the vacancy while two third rest in the band.

Let us now lower the temperature $T = 1.6 \cdot 10^{-8}\,\mathrm{K}$ and examine the stability of each fixed point (Fig. 3.18). Overall, the LM regimes shrink at the expense of the SC regimes while the FI regime is stable. The LM-c regime for strong hybridization strength vanishes almost completely and is reduced to a small corridor around the only stable line of LM fixed points $\mu = 0$. Apart from this line, we expect the LM to be eventually screened by the band if T is only sufficiently small. We investigate the $T_K(\mu)$ behavior in Sec.3.5.7. In addition, all charge crossover lines cease to be broad crossovers and turn into sharp transitions.

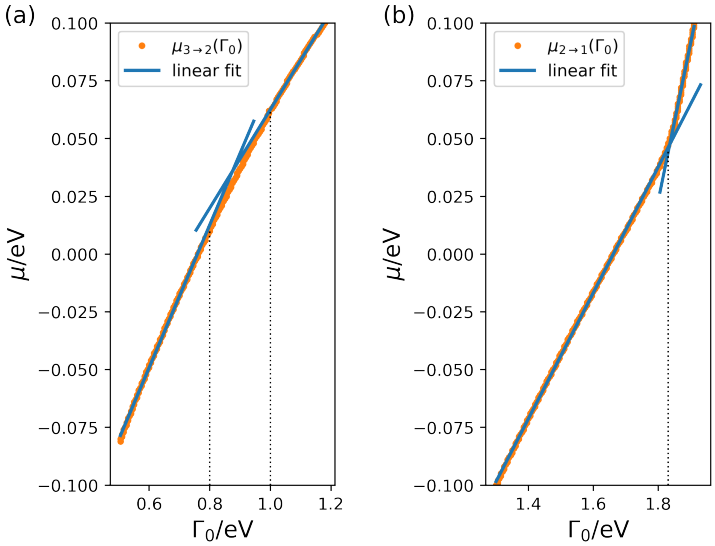

Figure 3.19: Charge crossover potential μ_{cc} as function of Γ_0. The points are the local maxima of $\mathrm{d}N_{\mathrm{loc}}/\mathrm{d}\Gamma_0$. The crossover curve is approximated by two linear fits. (a) Crossover $N_{\mathrm{loc}} = 3 \to 2$. (b) Crossover $N_{\mathrm{loc}} = 2 \to 1$. The fitting parameter and ranges are listed in Tab. 3.2.

3.5.2.1 Local Charge Crossover

Our vacancy mode exhibits two charge crossovers as shown in Fig. 3.17. Both crossover curves show an almost linear $\mu_{\mathrm{cc}}(\Gamma_0)$ dependency for the most part and can be reasonable approximated by two 1st order polynomials each (Fig. 3.19, fitting parameters in Tab. 3.2).

Table 3.2: Fitting parameter for 1st order polynomial $\mu(\Gamma_0) = a\Gamma_0 + b$. Column Γ_0^{r} indicates the range that is used for the fitting procedure.

Occupation change	Γ_0^{r}/eV	a	b/eV
$N_{\mathrm{loc}} = 3 \to 2$	$[0.50, 0.80]$	0.3091	-0.2346
	$[1.00, 1.18]$	0.2133	-0.1506
$N_{\mathrm{loc}} = 2 \to 1$	$[1.30, 1.83]$	0.2725	-0.4527
	$[1.00, 1.18]$	0.6830	-1.206

Fig. 3.20 shows the spectral density and local occupation at the charge crossover between $N_{\mathrm{loc}} = 2$ and $N_{\mathrm{loc}} = 1$ electrons for $\Gamma_0 = 1.7\,\mathrm{eV}$. For finite $T = 4.2\,\mathrm{K}$ the crossover takes place between $\mu = 8 - 12\,\mathrm{meV}$. All ρ_d tend to zero for $\omega \approx 20\,\mathrm{meV}$ regardless of μ [Fig. 3.20 (a)]. The behavior for positive frequency differs depending on the local occupation. For μ smaller than the crossover scale $\mu_{\mathrm{cc}}^{2\to1}$ the spectral density shows a peak at $\omega \approx 50\,\mathrm{meV}$. This peak gradually shifts towards higher energy $\omega \approx 150\,\mathrm{meV}$ as the chemical potential increases. Note that all curves cross each other in a small region around $\mu \approx 110\,\mathrm{meV}$. The shift is accompanied by a filling of the π orbital [Fig. 3.20 (b)]. The d orbital, on the other hand, remains approximately half-filled. The π orbital is empty for small

μ and half-filled for chemical potential above the crossover scale. This crossover turns into a quantum phase transition for $T \to 0$, and the occupancy jumps at $\mu = 9.6\,\mathrm{meV}$ for $\Gamma_0 = 1.21\,\mathrm{eV}$.

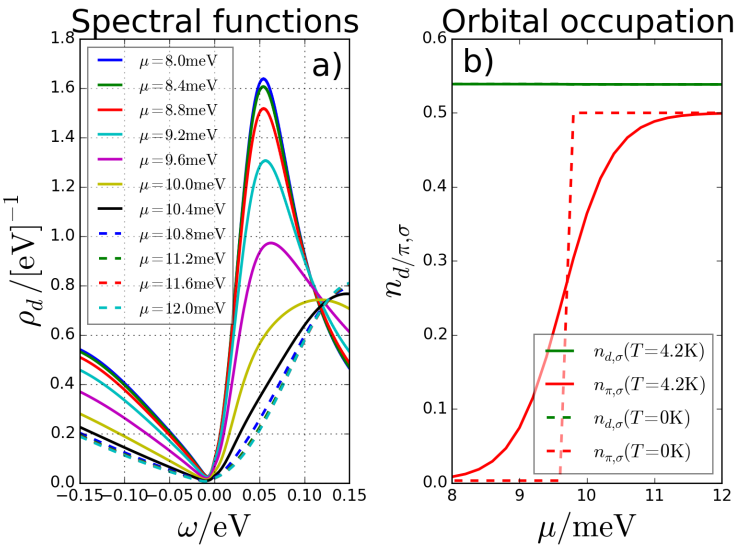

Figure 3.20: (a) Spectral functions for fixed hybridization strength $\Gamma_0 = 1.7\,\mathrm{eV}$ and small span of μ. The smallest values correspond to double occupation while the largest one belong to The used parameters are listed in Tab. 3.1. Taken from [19].

3.5.2.2 Influence of the DOS and Interpolation Scheme

Before we touch upon each regime individually, we show that they are a generic feature of our model. For this we map the different regimes in the parameter space in Fig. 3.21 for the approximate linear hybridization function as defined in Eq. (3.1.14). Instead of using the Z factor for level repulsion, we determine both level positions for the intermediate and strong hybridization regime empirically and linearly interpolate between these values. Tab. 3.3 lists the relevant level positions.

The main features presented in the previous mapping Fig. 3.17 are also visible for the simplified level repulsion and DOS. The main difference is that we only find one occupation change $N_{\mathrm{loc}} = 2 \to 1$ instead of two charge crossovers. The second charge transition is expected to occur for smaller Γ_0 than we considered here. A second difference is that the charge crossover line has a different shape compared to the almost piecewise linear curve in Fig. 3.19 (b). Apart from these minor differences, the regimes and fixed-points stay the same. However, the Kondo temperature is generally slightly higher due to the steeper slope of the DOS close to the Dirac point and SC regimes are more pronounced for the same temperature.

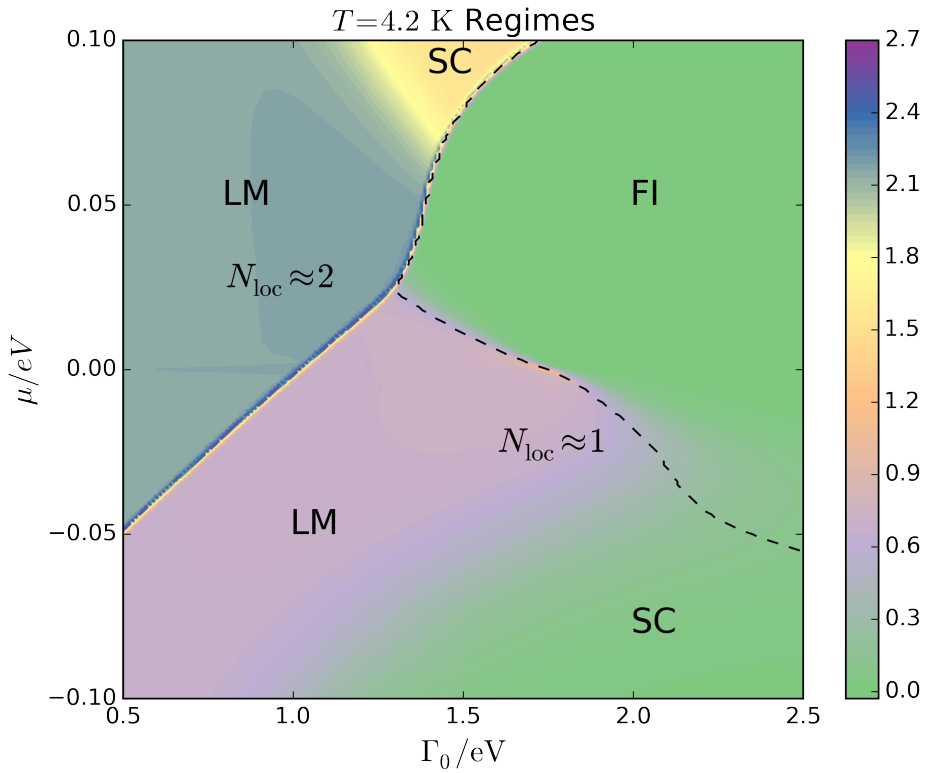

Figure 3.21: Regimes for $T = 4.2\,\mathrm{K}$ for the approximate linear hybridization function Eq. (3.1.14) and empirical level repulsion Eq. (3.4.8). All parameters are listed in Tab. 3.3. Only the intermediate and strong hybridization regime are visible for this parameter set. The dashed line indicates the change of the ground state to better differentiate between FI and SC regime.

The suppression of the Kondo effect close to $\mu = 0$ is driven by the pseudo-gap and present for both choices for the DOS. The exact slope or asymmetry of the DOS manifests itself only in minor corrections. The same is true for the type of level repulsion. Diagonalization based on the Z factor is arguably the more realistic method but a simple linear interpolation is sufficient and captures the essential physics.

3.5.3 Individual Regimes for Finite and Vanishing Temperature

In the following we present each regime individually by choosing a single representative Γ_0 and varying the chemical potential. We characterize the weak, intermediate, and strong hybridization regime by means of the local entropy, local occupation, electron arrangement, and spectral function. We compare three different setups: (i) t, t' DOS and Z factor level repulsion, (ii) t, t' DOS and linear interpolation, and (iii) approximate DOS and linear interpolation. The

Table 3.3: Level positions and Coulomb interactions for the approximated and sampled DOS and linear interpolation level repulsion for each of the three different regimes.

Regime	DOS	level repulsion	ϵ_d/eV	ϵ_π/eV	U_{dd}/eV	$U_{d\pi}$/eV	$U_{\pi\pi}$/eV	J_H/eV	Γ_0/eV
weak	t, t'	linear interp.	-0.93	-0.02	2.00	0.10	0.01	0.35	1.10
intermediate	approx.	linear interp.	-1.20	0.15	2.00	0.10	0.01	0.30	1.21
	t, t'	linear interp.	-1.40	0.17	2.00	0.10	0.01	0.35	1.80
strong	approx.	linear interp.	-1.37	0.18	2.00	0.10	0.01	0.30	1.96
	t, t'	linear interp.	-1.60	0.25	2.00	0.10	0.01	0.35	2.10

general behavior stays the same regardless of DOS and level repulsion scheme emphasizing the generic character of the different regimes.

We begin with the weak hybridization regime ($\Gamma_0 \approx 1\,\text{eV}$). It is characterized by an almost featureless spectral density around $\omega = 0$ for $\mu < 0$ [Fig. 3.22 (a)] that changes only cautiously as the chemical potential is increased. Kondo physics emerge gradually for strong n doping $\mu \geq 60\,\text{meV}$, which can be seen by the onset of a Kondo peak at $\omega = 0$. However, this peak is not yet fully developed and the system is still moving towards the stable low energy strong coupling fixed point, i.e. lowering the temperature further keeps modifying the form of the spectral density.

The change in spectral density at high n doping is accompanied by an increase in local orbital occupation. The occupation of the π orbital switches from one to two electrons while the occupation of the lower d orbital is basically unaffected [cf. Fig. 3.23 (a)]. The ferromagnetic Hund's rule coupling can only stabilize a triplet state successfully if the chemical potential is small enough. As the potential increases, J_H and $U_{\pi\pi}$ are too weak to prevent localization of another electron in the π orbital leaving one effective spin $s = 1/2$ [Fig. 3.23 (a)]. Thus, the overall picture is that of an underscreened or undercompensated [137] Kondo problem for $\mu < 50\,\text{meV}$. Both local electrons align due to the ferromagnetic coupling while the hybridization strength is yet too small, diminished by the vanishing pseudo-gap DOS, to drive the system away from a local moment fixed point. This picture changes as soon as one crosses over to high n doping. The third electron pairs off with the already present π electron, creating a singlet. This renders the underscreened to a conventional Kondo problem with a higher Kondo temperature as before [138].

When we increase the hybridization ($\Gamma_0 \approx 1.7\,\text{eV}$) we arrive in the intermediate hybridization regime. Here, the spectral density reflects the influence of the pseudo-gap DOS: Kondo physics is exponentially suppressed close to the Dirac Point $|\mu| \to 0$ and present for stronger doping (Fig. 3.24). The finite temperature spectral density shows a Kondo peak that is only visible for either high p or n doping while T_K vanishes for small absolute values of μ. In the p doped region, an onset of the Kondo peak appears around $\mu = -40\,\text{meV}$ albeit not yet fully developed for $T = 4.2\,\text{K}$. The peak continues to grow if the chemical potential is further lowered. The n doped regime shows similar behavior. Here, a Kondo peak starts to develop around $\mu = 60\,\text{meV}$ and continues to grow as μ increases.

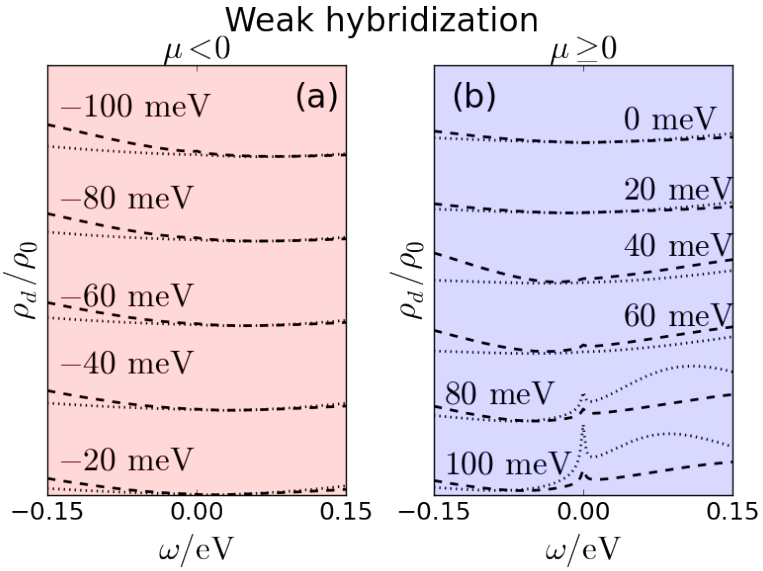

Figure 3.22: Spectral density of the d orbital $\rho_d(\omega)$ for the weak hybridization regime normalized by the maximum ρ_0 of all $\rho_d(\omega)$. The curves are partitioned according to (a) p doping and (b) n doping. The numbers inside the panels represent μ. The dashed line stands for the realistic t, t' hybridization and the dotted line depicts the realistic t, t' hybridization with the addition of level repulsion based on the Z factor. The used parameters are listed in Tab. 3.1 and Tab. 3.3. Taken from [19].

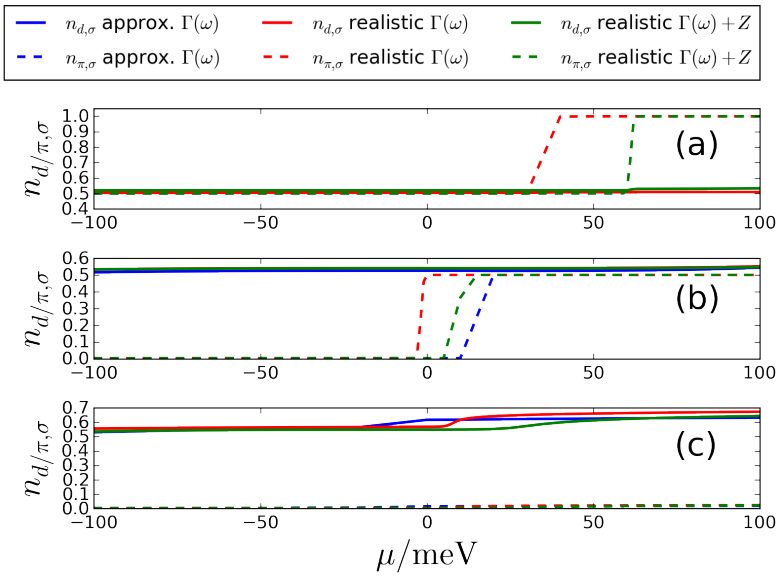

Figure 3.23: Spin dependent occupation of both the d orbital, $n_{d,\sigma}$ (solid), and ZM, $n_{\pi,\sigma}$ (dashed). The hybridization is obtained by (i) approximated $\Gamma(\omega)$ (blue), (ii) t, t' TB calculations (red), (iii) t, t' TB calculations with the addition of level repulsion based on the Z factor (Eq. (3.4.7), green). The occupation is shown for each regime: (a) weak hybridization, (b) intermediate hybridization, (c) strong hybridization. The used parameters are listed in Tab. 3.1 and Tab. 3.3. Taken from [19].

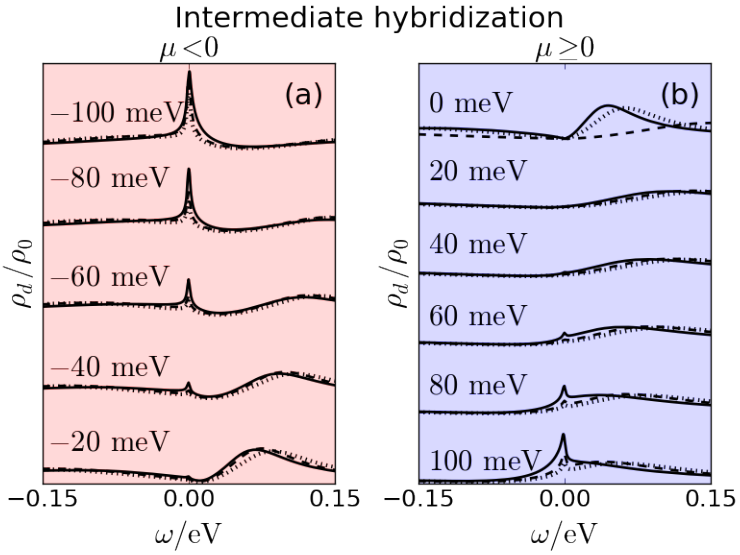

Figure 3.24: Spectral density of the d orbital $\rho_d(\omega)$ for the intermediate hybridization regime normalized by the maximum ρ_0 of all $\rho_d(\omega)$. The curves are partitioned according to (a) p doping and (b) n doping. The numbers inside the panels represent μ. The solid line stands for the approximated $\Gamma(\omega)$, the dashed line for the realistic t, t' hybridization, and the dotted line depicts the realistic t, t' hybridization with the addition of level repulsion based on the Z factor. The used parameters are listed in Tab. 3.1 and Tab. 3.3. Taken from [19].

The overall tendency is the same for n and p doping, i.e. higher absolute values of μ yield more pronounced peaks.

The microscopic picture is distinctly different from the weak hybridization regime in case of p and n doping. Starting from small chemical potential the d orbital is half-filled while the ZM is essentially empty [Fig. 3.23 (b)]. The electron creates a local moment that is in turn screened by the band resulting in the pronounced Kondo peak for small chemical potential [Fig. 3.24 (a)]. The peak vanishes gradually as the chemical potential is increased due to the DOS while the occupation remains unchanged. The system is located in-between a strong coupling fixed point for large negative chemical potential and an unstable local moment fixed point closer to $\mu = 0$. The Kondo temperature shows a strong μ dependence so that sweeping through μ corresponds to traversing the crossover between local moment and strong coupling.

A second electron will be localized on the impurity around $\mu = 0$. Due to the strong U_{dd} Coulomb repulsion on the lower lying d orbital and the significant ferromagnetic Hund's rule coupling between d and π orbital, the second electron is localized in the π orbital [Fig. 3.23 (b)]. This change is visible in the spectral density by a shift of spectral weight from around $\omega = 50\,\text{meV}$ to higher energies (Fig. 3.24 (b) curves for $\mu = 0$ and $\mu = 20\,\text{meV}$). Both electrons form a triplet state due to J_H which is then screened by the band resulting in an underscreened Kondo effect. The crossover from the $s = 1$ unstable local moment fixed point

to the stable underscreened Kondo fixed point is analogous to the crossover for p doping. A Kondo peak, yet not fully developed, is visible as μ is increased.

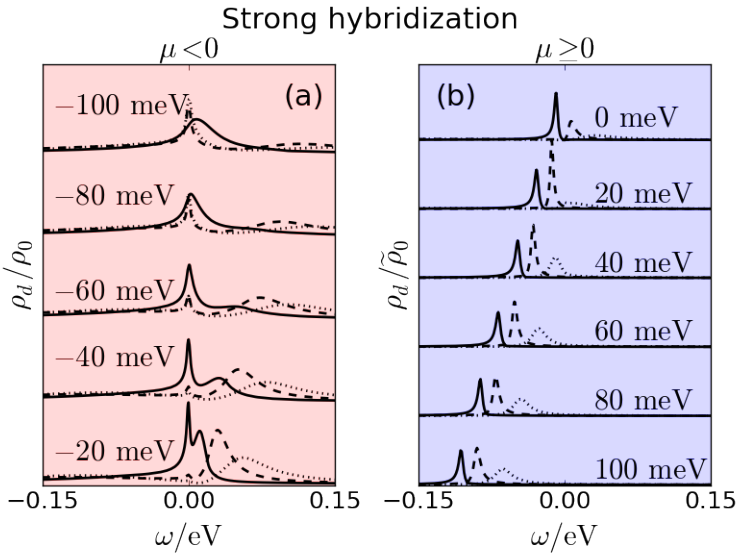

Figure 3.25: Spectral density of the d orbital $\rho_d(\omega)$ for the strong hybridization regime normalized by the maximum ρ_0 of all $\rho_d(\omega)$. The curves are partitioned according to (a) p doping and (b) n doping. The numbers inside the panels represent μ. The solid line stands for the approximated $\Gamma(\omega)$, the dashed line for the realistic t, t' hybridization, and the dotted line depicts the realistic t, t' hybridization with the addition of level repulsion based on the Z factor. The used parameters are listed in Tab. 3.1 and Tab. 3.3. Taken from [19].

The strong hybridization regime for $\Gamma_0 = 2.1\,\mathrm{eV}$ differs from the previous regimes in two key aspects: the π orbital remains essentially empty for all relevant chemical potentials and the stable low temperature fixed point for n doping is a frozen impurity and not a strong coupling one. High p doping yields a singly occupied d orbital as it was the case for weak and intermediate hybridization as well [Fig. 3.23 (c)]. There is only a small evolution in the d occupation from $n_{d,\sigma} \approx 0.55$ to $n_{d,\sigma} \approx 0.65$ as μ is changed. This shift occurs for small n doping, the exact value depending on hybridization function and level repulsion. For the parameters used here, the approximate hybridization results in the earliest shift (solid blue curve) at around $\mu = 0$ while the realistic t, t' DOS and Z factor based level repulsion causes a crossover at $\mu = 30\,\mathrm{meV}$.

We turn to the impurity entropy. Before, we showed the entropy times local occupation for singular temperature points when we mapped the parameter space. Fig. 3.26 depicts the impurity entropy for $\Gamma_0 = 1\,\mathrm{eV}$ as a function of the temperature T and the chemical potential μ. Subplot (a) shows the evolution down to the experimental accessible regime $T = 4.2\,\mathrm{K}$ and subplot (b) extends the temperature range to $T \approx 10^{-8}\,\mathrm{K}$. For finite temperature $T = 4.2\,\mathrm{K}$ the system has yet to reach its stable fixed points. The system is clearly divided at the charge crossover $\mu_{\mathrm{cc}}^{2\to3}$ by a sharp quantum phase transition. For $\mu > \mu_{\mathrm{cc}}^{2\to3}$ and

low T, the impurity entropy assumes $S_{\mathrm{loc}} = 0$. This reflects the formation of the Kondo singlet and screening of the magnetic moment of the d electron. For higher temperature $T \approx T_K$ there is a crossover to $S_{\mathrm{loc}} \propto \ln(2)$ which corresponds to the unstable LM fixed point. Even higher T results in multiple additional crossovers where the energy difference between ground state and the next lowest states become small compared to T. For the low temperature region where $\mu < \mu_{\mathrm{cc}}^{2\to3}$, $S_{\mathrm{loc}} \propto \ln(3)$ as the local configuration is that of a triplet.

Fig. 3.27 shows the entropy for intermediate hybridization strength. We again find a sharp phase transition for $T \to 0$ at $\mu_{\mathrm{cc}}^{1\to2}$. For $\mu > \mu_{\mathrm{cc}}^{1\to2}$, the entropy assumes $S_{\mathrm{loc}} \propto \ln(2)$ for small T since the configuration is that of a underscreened triplet with a dangling $s = 1/2$ spin. For $T > T_K$, the entropy tends to $\ln(3)$ and eventually $S_{\mathrm{loc}} > \ln(3)$ as T increases further. On the other side of the phase transition the stable fixed point is a conventional SC. Only a single electron occupies the d orbital and the entropy is thus $S_{\mathrm{loc}} = 0$ for small T and $S_{\mathrm{loc}} \propto \ln(2)$ for larger temperature. For μ close to zero, T_K is suppressed and we find either $S_{\mathrm{loc}} \propto \ln(3)$ or $\propto \ln(2)$ depending on μ with respect to $\mu_{\mathrm{cc}}^{1\to2}$.

The behavior for strong hybridization is different in the sense that there is no sharp transition present even for small T (Fig. 3.28). For small temperature the entropy assumes either zero or $\propto \ln(2)$. Finite entropy corresponds to a conventional LM fixed point with a single electron occupying the d orbital which, however, is only stable for $\mu = 0$. There is a small range around $\mu = 0$ where $S_{\mathrm{loc}} \neq 0$ still but where a lower T will eventually result in vanishing entropy. The FI and SC regime both correspond to $S_{\mathrm{imp}} = 0$. The crossover is accompanied by a slight increase of d orbital occupation which can occur for small p or n doping (discussion in Sec. 3.5.3, Fig. 3.23).

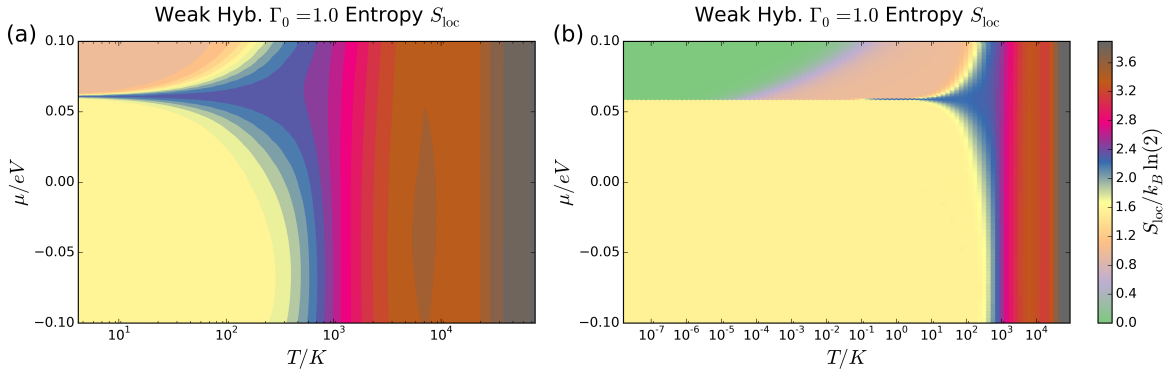

Figure 3.26: Local entropy $S_{\mathrm{loc}}(T,\mu)$ for the weak hybridization regime $\Gamma_0/\mathrm{eV} = 1$, t, t' hybridization function and z factor interpolation. (a) Temperature down to $T = 4.2\,\mathrm{K}$ (experimental accessible regime). (b) $S_{\mathrm{loc}}(T,\mu)$ down to $T = 1.6 \cdot 10^{-8}\,\mathrm{K}$. The colorbar applies to both plots.

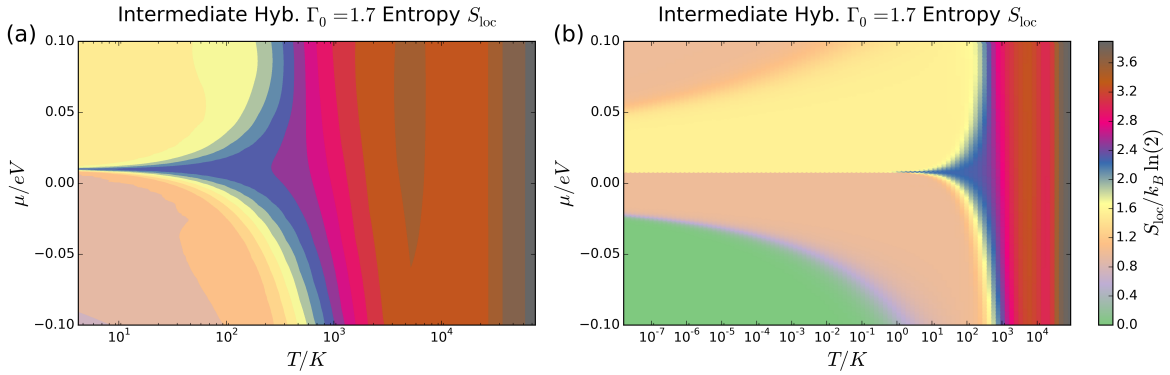

Figure 3.27: Local entropy $S_{\mathrm{loc}}(T,\mu)$ for the intermediate hybridization regime $\Gamma_0/\mathrm{eV} = 1.7$, t, t' hybridization function and z factor interpolation. (a) Temperature down to $T = 4.2\,\mathrm{K}$ (experimental accessible regime). (b) $S_{\mathrm{loc}}(T,\mu)$ down to $T = 1.6 \cdot 10^{-8}\,\mathrm{K}$. The colorbar applies to both plots.

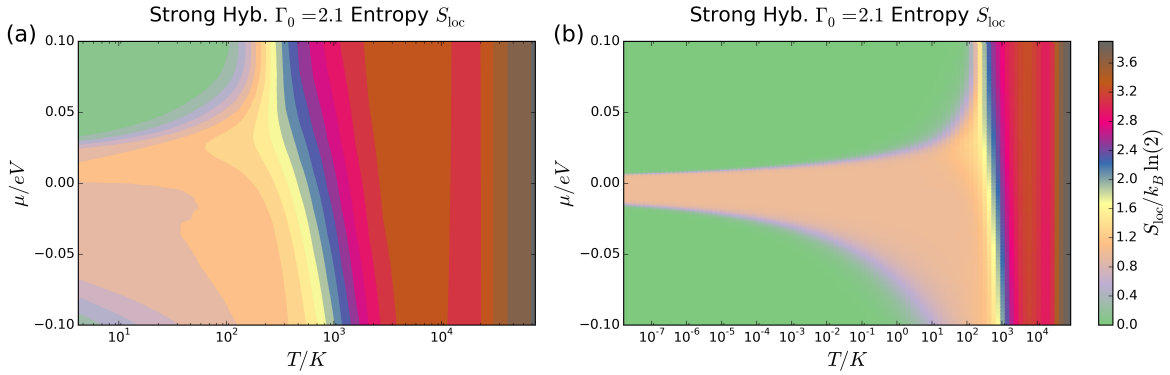

Figure 3.28: Local entropy $S_{\mathrm{loc}}(T,\mu)$ for the strong hybridization regime $\Gamma_0/\mathrm{eV} = 2.1$, t, t' hybridization function and z factor interpolation. (a) Temperature down to $T = 4.2\,\mathrm{K}$ (experimental accessible regime). (b) $S_{\mathrm{loc}}(T,\mu)$ down to $T = 1.6 \cdot 10^{-8}\,\mathrm{K}$. The colorbar applies to both plots.

3.5.4 Green's Functions of the π Orbital and Zero-Mode Peak

Until now we focused on the spectral densities for the d orbital since the d orbital governs the Kondo physics. The tunneling current measured in experiment, however, is a superposition of contributions from d orbital, π orbital, and the substrate. The experimental $\mathrm{d}I/\mathrm{d}V$ curves therefore show also features that are related to the π orbital, for example the position of the zero-mode peak.

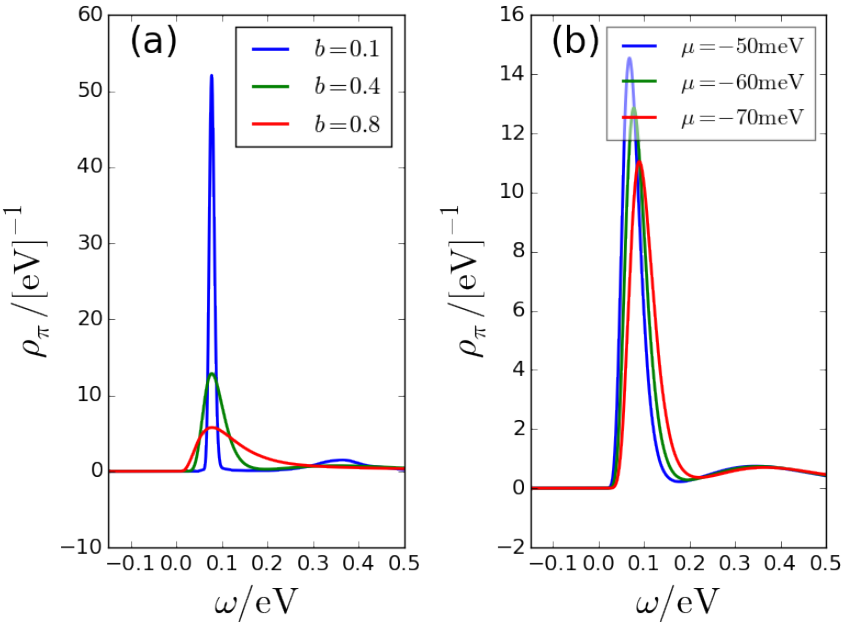

Figure 3.29: $\rho_\pi(\omega)$ by Lehmann representation for $T = 4.2\,\mathrm{K}$ in the intermediate hybridization regime $\Gamma_0 = 1.21\,\mathrm{eV}$. (a) For $\mu = -60\,\mathrm{meV}$ and different broadening parameter b. (b) For varying μ and constant $b = 0.4$. The approximate DOS and linear interpolation for level repulsion were used. The parameters are listed in Tab. 3.3. The figure is taken from Ref. [19].

Fig. 3.29 shows the spectral density for the π orbital $\rho_\pi(\omega)$ for $T = 4.2\,\mathrm{K}$ in the intermediate hybridization regime for the approximate DOS and linear interpolation based level repulsion. The vacancy parameters are listed in Tab. 3.3. We calculate ρ_π by a Lehmann representation of the NRG data (cf. Sec. 2.3.1 and Ref. [45, 46]).
Subplot 3.29 (a) depicts the spectral density as a function of the broadening parameter b. It is used in a logarithmic Gaussian broadening function [11] to transform the discrete set of excitations into a continuous function. ρ_π exhibits two main features: a single sharp peak (ZM) located slightly above Fermi energy around $\omega \approx 75\,\mathrm{meV}$, as well as a much smaller peak at higher energy $\omega \approx 350\,\mathrm{meV}$ that we link to Hund's rule excitations. If $b = 0.8$, this smaller peak becomes washed out to such a degree that it is not visible any more. Since the calculations are done in thermodynamic equilibrium, the fluctuation-dissipation theorem (see

for example Ref. [139]) holds that connects the spectral density to the lesser Green's function $G^<(\omega)$ via the Fermi function $G^<(\omega) \propto \rho(\omega) f(\omega - \mu)$. We can thus visualize the filling of the π orbital because the integral over the lesser Green's function equals the electronic occupation. Almost all spectral weight rests above the Fermi energy and, therefore, the π occupation is zero. This is in accordance with the occupation in Fig. 3.23 (b).
The ZM in Fig. 3.29 (b) shows the same simple dependence on μ as in experiment (Fig. 2 (a) in Ref. [9]) where higher μ shifts the peak closer to $\omega = 0$. The vanishing occupation eventually changes as the ZM is shifted to smaller energies when $\mu > \mu_{\mathrm{CC}}^{1\to 2}$ increases beyond the charge crossover.

While the d orbital governs the Kondo physics in our model, the π spectral function provides us with additional insight about the ZM. We do not have a theory for the admixture of d, π, and substrate to model the experimental $\mathrm{d}I/\mathrm{d}V$ curves. The mixing should show at least a Γ_0 dependence as the hybridization strength parameterizes the local curvature, but might include non-trivial effects due to the high applied voltages. Consequently, we did not attempt to superpose d and π spectral densities to precisely match the experimental results.

3.5.5 Calculation of Kondo Temperature

Hitherto, we looked at spectral functions that, depending on the finite temperature regime, showed a more or less developed Kondo peak pinned to zero bias. The width of the peak is tightly linked to T_K, as discussed in Sec. 2.1. The Kondo resonance develops at $\omega = 0$ as the temperature is lowered below T_K. Although it is fully fleshed out only well below T_K, a small onset of a peak will be visible for temperatures above T_K. This formation as well as the concomitant screening process is continuous, hence T_K being a crossover scale. Knowledge of this characteristic energy is thus crucial for any secondary experimental study or even technical application.

In this section, we compare T_K calculated from experimental STM $\mathrm{d}I/\mathrm{d}V$ curves [9] to our NRG results [19]. We employ two different methods for this comparison. First, we apply a Fano fit (FF) directly to the spectral density for finite temperature in close analogy to the experiments. Then we calculate the zero-bias conductance and use the empirical Goldhaber-Gordon (GG) formula [55] to determine T_K in the limes $T \to 0$.

Fig. 3.30 shows the experimental values for T_K ordered by hybridization strength from top to bottom [9]. The first two curves represent the strong hybridization regime where there is only a Kondo peak for p doping. The width of the peak is substantial with a corresponding maximum $T_K \approx 200\,\mathrm{K}$. Furthermore, the resonance remains almost constant in width up to $\mu \approx -40\,\mathrm{meV}$ where T_K vanishes rapidly and remains zero afterwards.

The next three curves belong to the intermediate hybridization regime where a finite T_K is found for p and n doping. The p doped regime is similar to before:

below $\mu = -75\,\mathrm{meV}$, $T_K \approx 50\,\mathrm{K}$ stays almost constant until it drops sharply to zero. Above the DP, $T_K \approx 50\,\mathrm{K}$ again after an equal steep rise. This rise sets in in close proximity to the DP ($\mu \approx 10\,\mathrm{mev}$) in case of the third data set (purple curve).

The last curve (black) has been assigned to the same regime as the purple, green, and blue curves in Ref. [9]. We will, however, follow our argument in Ref. [19] and classify this data set as weak hybridization. There is no Kondo peak visible until $\mu = 50\,\mathrm{meV}$ above which $T_K \approx 50 - 100\,\mathrm{K}$.

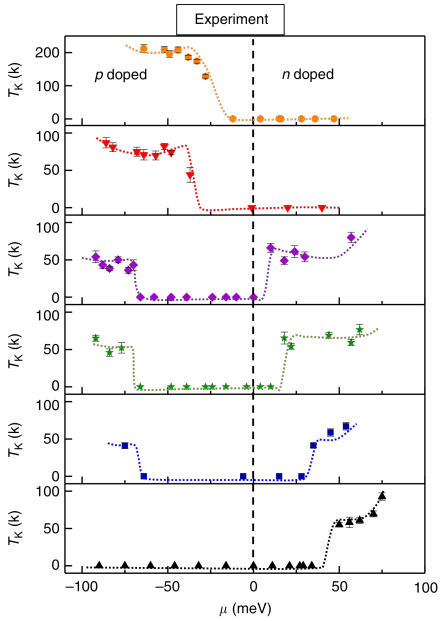

Figure 3.30: T_K calculated via Fano fit of the experimental $\mathrm{d}I/\mathrm{d}V$ zero-bias anomaly line shape. The first two curves (orange, red) belong to the strong, the next three (purple, green, blue) to the intermediate, and the last (black) to the weak hybridization regime. If there is no measurable peak at zero bias, $T_K = 0$. The dashed lines are a guide to the eye. Taken from Ref. [9].

Fig. 3.31 compares the different T_K calculated from the NRG data. The solid lines represent Kondo temperatures via FFs for $T = 4.2\,\mathrm{K}$ while the dashed lines stand for calculations by the empirical GG formula. The GG approach requires that the zero-bias conductivity as a function of T is already converged and that it assumes a plateau value for small T. We therefore reduce the temperature to $T = 1.6 \cdot 10^{-8}\,\mathrm{K}$. A FF could be performed at finite T, however, it will show a strong temperature dependence. Here, we forgo a small temperature extrapolation and show the values for $T = 4.2\,\mathrm{K}$ only.

The first two curves (orange, red) belong to the strong hybridization regime. At around $\mu = -100\,\mathrm{meV}$ both calculations yield similar results $T_K \approx 100\,\mathrm{K}$ and $T_K \approx 40\,\mathrm{K}$ for $\Gamma_0 = 2.4\,\mathrm{eV}$ and $\Gamma_0 = 2.1\,\mathrm{eV}$ respectively. Below $\mu = -100\,\mathrm{meV}$ the Kondo temperature for the GG approach is larger $T_K^{\mathrm{GG}} > T_K^{\mathrm{FF}}$. For $-100\,\mathrm{meV} < \mu < 0$ the FF gives almost constant T_K^{FF} while the GG values drop off rapidly. This discrepancy can be understood when taking finite temperature corrections to the FF into account. The Kondo resonance for the given temperature is still developing, i.e. the temperature is still above the true Kondo scale, and the system has yet to reach its stable low temperature fixed point. The peak is much smaller and the value T_K^{FF} is thus strongly modified since the width at half maximum height of the peak differs from the $T \to 0$ result. Close to the DP, T_K^{FF} abruptly vanishes as there is no resolvable peak in $\rho_d(\omega)$. The GG calculation still yields a finite result albeit exponentially small due to the pseudo-gap DOS (further discussion about the

behavior close to the DP can be found in Sec. 3.5.7). There is no Kondo effect for n doping and thus $T_K = 0$.

The next two lines (purple and green) represent the intermediate hybridization regime with a Kondo effect for p and n doping. The Kondo temperature T_K^{FF} exceeds T_K^{GG} significantly almost everywhere by one order of magnitude. The main difference comes about due to the finite temperature and shrunken Kondo peak. We find that $T_K^{\mathrm{FF}} \approx 20-40\,\mathrm{K}$ except close to the DP while T_K^{GG} is negligible except for high p or n doping.

The last curve (blue) belongs to the weak hybridization regime. The p doped region does not show a Kondo effect at all while it sets in for n doping at around $\mu \approx 60\,\mathrm{meV}$. FF calculation yields Kondo temperatures of $\sim 20\,\mathrm{K}$ whereas T_K^{GG} is significantly smaller and just barely reaches $\mathcal{O}(1\,\mathrm{K})$ for $\mu \geq 100\,\mathrm{meV}$.

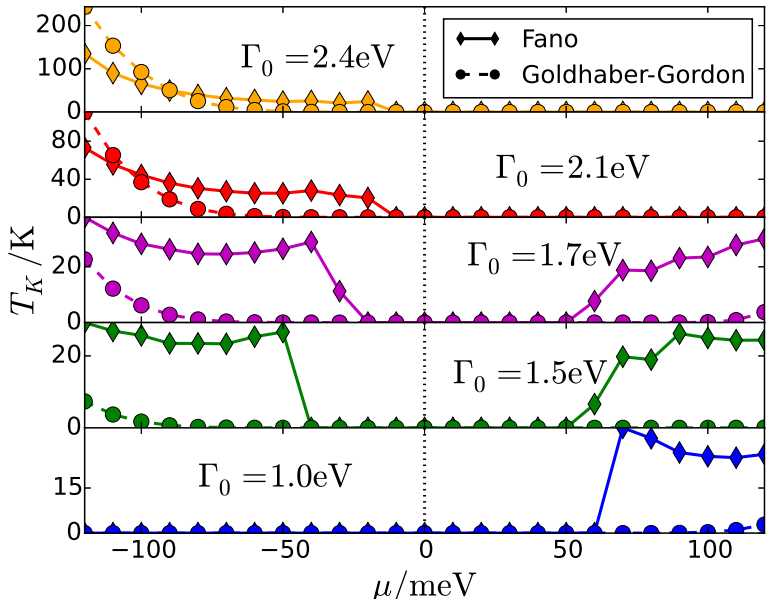

Figure 3.31: T_K calculated by Fano fit from the zero-bias anomaly of $\rho_d(\omega)$ for finite $T = 4.2\,\mathrm{K}$ (solid lines, rhombus) and via Goldhaber-Gordon fit of the zero-bias conductivity (dashed lines, circle) for $T = 1.6 \cdot 10^{-8}\,\mathrm{K}$. The t, t' DOS and Z factor level repulsion is used. The first two curves belong to the strong, the next two to the intermediate, and the last to the weak hybridization regime. The lines are understood to be guides to the eye. Taken from Ref. [19].

Overall, our model reproduces the experimental results [9] qualitatively very well. We find a good agreement when comparing finite temperature FFs to the experimental values. They match in order of magnitude and show the same μ dependence to a first approximation, i.e. a plateau like behavior for doping away from the DP. However, we find that the results from our NRG calculations are generally off by a factor of two in comparison to the experimental data across all regimes. For example, in the intermediate regime the authors of Ref. [9] observe

$T_K \approx 50\,\mathrm{meV}$ for p and n doping while our findings are $T_K \approx 25 - 30\,\mathrm{meV}$. This difference raises the question if our model misses a key physical process that would boost T_K. Yet, introducing more interactions is not expedient at the current state: our model is already complex to such a degree that T_K is a highly non-trivial function that depends sensitively on all local parameters. The different regimes are intrinsic to our model, as we discuss in Sec. 3.5.6, but the shape of the spectral density $\rho_d(\omega)$, and hence T_K, does change significantly. Also, the fitting procedure itself is rather unreliable in such a way that different starting parameters or a varied number of data points result in different T_K. It is therefore hard to justify another interaction based on present qualitative discrepancies.

Still, one main quantitative difference between the experimental and our calculated T_K is the existence of a Kondo peak close to the DP in the intermediate hybridization regime. In the experiments, a Kondo peak as close as $\mu \approx 20\,\mathrm{meV}$ is observed (Fig. 3.30, purple curve) which we could not reproduce in our calculations for any parameter set taken into consideration even when using a finite temperature FF. This inability might be due a number of reasons such as a different location of the DP in the experiment or missing modifications to the DOS that strengthen PH asymmetry further. The DP does not rest at zero bias for realistic graphene as can already be seen from next-nearest neighbor tight-binding considerations [Eq. (3.1.8)]. It is rather chosen to be located at zero bias in the framework of STM by applying a voltage and by shifting the DP to $\omega = 0$ in the context of the NRG. An offset in the location of the DP could explain different results. Another possibility is a missing asymmetry term that further increases the linear slope of the DOS pushing T_K accordingly. We only considered next-nearest neighbor tight-binding interactions but we might require a more elaborate modeling due to (i) the high applied voltages $\sim 20\,V$ that influence the electronic structure or (ii) modification to the local DOS by adjacent carbon vacancies. However, we did not delve into any specific adjustment to our model any further.

3.5.6 Stability Against Parameter Deviations: Variation of U_{dd} and ϵ_d

We investigate the stability of the different regimes by varying the level position ϵ_d and the Coulomb repulsion U_{dd}. Fig. 3.32 compares the d orbital spectral density for ϵ_d listed in Tab 3.1 (reference curves, black) to calculations where ϵ_d is shifted by 15% percent to either $\epsilon_d^+ = -0.85|\epsilon_d|$ (red curves) or $\epsilon_d^- = -1.15|\epsilon_d|$ (blue curves). We refer to the reference energy as ϵ_d^0 and to the shifted variables as $\epsilon_d^\pm$ in the following. Since $\epsilon_d^0 < 0$, this means $\epsilon_d^- < \epsilon_d^0 < \epsilon_d^+$. We define 'higher' and 'lower' with regard to this inequation, i.e. ϵ_d^+ is higher than ϵ_d^0. All other parameters remain the same.

Fig. 3.32 (a) shows the weak hybridization regime. Here, the formation of a Kondo peak in the n doped regime is significantly enhanced by a energetically lower lying d orbital (blue curve). The Kondo effect sets in around $\mu = 60\,\mathrm{eV}$

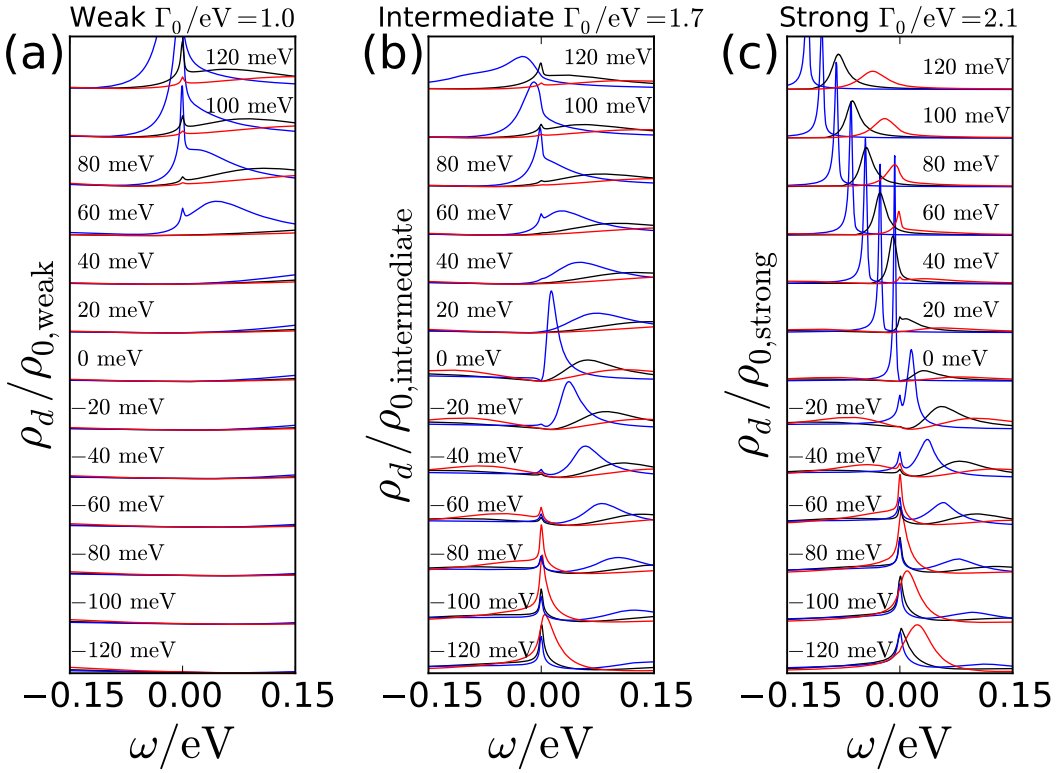

Figure 3.32: $\rho_d(\omega)$ for (a) weak, (b) intermediate, and (c) strong hybridization strength and varying ϵ_d while all other parameters are kept the same, see Tab. 3.1. The t, t' DOS and Z factor interpolation is used in all cases. The black curves stand for the original parameter set, ϵ_d^0, and the blue and red curves represent calculations with $\epsilon_d^{\pm} = -|\epsilon_d^0(-1 \pm 0.15)|$ respectively. The curves in each subplot are divided by the maximum $\rho_{0,\mathrm{regime}}$ of the original parameter set, i.e. maximum of the black curves, where the subscript stands for weak, intermediate, and strong regime. The chemical potential is listed next to each curve. The curves are shifted by an constant offset for better visibility.

while a visible peak only appears at $\mu = 80\,\mathrm{eV}$ for the reference parameter set and an even higher ϵ_d^+ (red curves) hampers Kondo physics further. The p doped regime is mainly unaffected by any small change in ϵ_d as both electrons that occupy the vacancy form a triplet state and adding another electron or hole must overcome the triplet binding energy.

The spectral functions for high p doping in the intermediate hybridization regime in Fig. 3.32 (b) show the opposite behavior: the higher ϵ_d the stronger the Kondo peak. The Kondo peak is noticeable deformed and largely broadened as it begins to shift away from zero bias for $\mu = -120\,\mathrm{meV}$ and ϵ_d^+. When the chemical potential increases, the peak vanish at around $\mu = -40\,\mathrm{meV}$ as hybridization is suppressed by the vanishing DOS regardless of ϵ_d. The curve for ϵ_d^- shows a pronounced peak that is shifted gradually towards $\omega = 0$. It vanishes rapidly around $\mu = 20\,\mathrm{meV}$ as the total vacancy occupation changes from one to

two electrons and a triplet state is formed. The lower ϵ_d^- initially favors Kondo screening in the n doped regime yielding a strongly pronounced Kondo peak at $\mu = 80\,\mathrm{meV}$. However, higher μ results in a breakdown of Kondo physics and gradual deformation of the Kondo peak as it separates from zero bias. This behavior is not unexpected since an ever increasing μ must result in yet another charge crossover from two to three and eventually four electrons. The smaller ϵ_d the earlier this crossover sets in, and the triplet state is destabilized.

We find the same tendency for p doping in the strong hybridization regime in Fig. 3.32 (c) as for intermediate hybridization. The higher ϵ_d^+ (red curve) tends to boost T_K as long as μ is not around $\mu = 100\,\mathrm{meV}$ or smaller. Here, the small chemical potential hinders even a half-filled d orbital and local moment and Kondo singlet formation is suppressed. The Kondo peak vanishes as one approaches $\mu = 0$ with the curve for ϵ_d^- (blue curve) being the exception. For this parameter set, a Kondo peak is still visible at $\mu = -20\,\mathrm{meV}$. In the n doped regime, all curves show the same behavior: a single peak that is shifted from zero bias as μ increases. However, the smaller ϵ_d the earlier this peak begins to separate from $\omega = 0$.

The underlying regimes are stable as ϵ_d is varied. The two charge crossovers lines and competition between local triplet, singlet, and doublet state are generic features of our two-orbital model that are not affected by a small change in ϵ_d. Note, that not every parameter configuration produces reasonable results when compared to experiment. A key problem is the filling of the d and π orbital deep in the p or n doped regime where the orbitals are prone to either becoming quickly unoccupied or doubly occupied. Both level positions must be adjusted carefully in order to yield a significant Kondo effect at both edges of the spectrum. Generally speaking, a high ϵ_d might boost T_K for e.g. p doping in the intermediate regime while simultaneously hampering Kondo screening for $\mu > 0$ and vice-versa.

Next, let us address the widely different estimates for the Coulomb interaction that are used in literature [4, 132, 134, 133]. Due to the controversy regarding the absolute value of U_{dd}, we adopt a pragmatic approach and considered U_{dd} to be more of a fitting parameter. In this paragraph, we assume a rather small $U_{dd} = 0.5\,\mathrm{eV}$ [4] in comparison to the Hund's rule coupling $J_H \approx 0.35\,\mathrm{eV}$ from density functional calculations [117]. Smaller U_{dd} increases local charge fluctuations which in turn boosts T_K if one uses a Schrieffer-Wolff transformation as a guideline [41]. Another advantage is that, at least in a SIAM, the ratio U_{dd}/Γ_0 determines T_K. This means that one must increase the hybridization for a larger U_{dd} to still get a comparable T_K. The quite large Γ_0 remains a key problem in our approach, as we discuss later in Sec. 3.5.10, and smaller hybridization would thus be desirable. However, a change in any Coulomb matrix element influences the local occupation. If U_{dd} is to small, the lower level will quickly become doubly occupied and Kondo physics will be cut off. As a countermeasure, one can lower the hybridization as well since the d orbital position is dynamically lowered because of the hybridization with the bands. This shift is then weakened and the local moment stabilized. Unfortunately, this will reduce T_K as well. The effect of

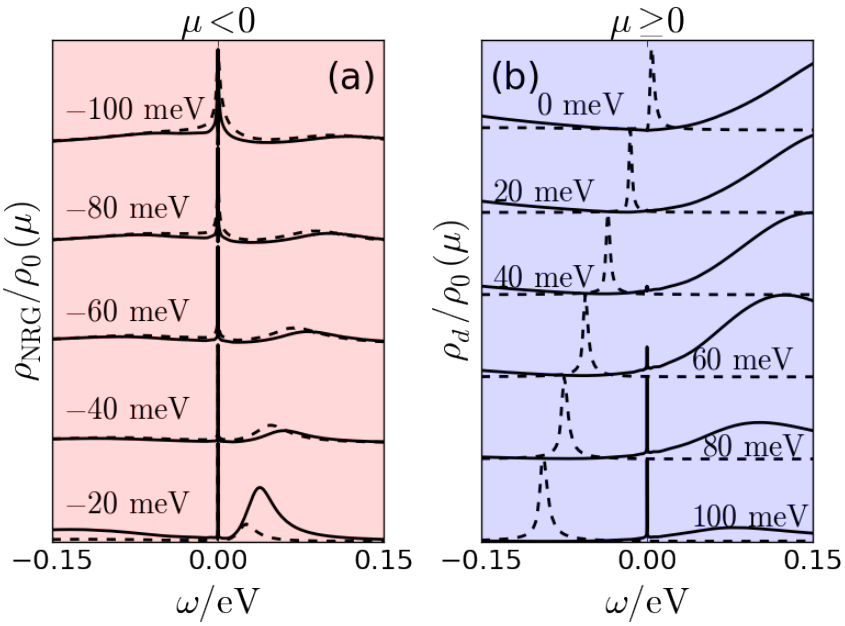

Figure 3.33: $\rho_d(\omega)$ for intermediate (strong) hybridization regime represented by solid (dashed) curves. The Coulomb repulsion is $U_{dd} = 0.65\,\text{eV}$ and $J_H = 0.35\,\text{eV}$. The level positions and hybridization strengths for both regimes are $\Gamma_0 = 0.4(0.5)\,\text{eV}$, $\epsilon_d = -0.37(-0.40)\,\text{eV}$, $\epsilon_\pi = 0.20(0.23)\,\text{eV}$. The temperature is $T = 1.6 \cdot 10^{-5}\,\text{K}$. The approximate hybridization function Eq. (3.1.14) is used. The Kondo peak is present but very narrow. All curves are divided by the spectral maximum $\rho_0(\mu)$ of each respective chemical potential. Taken from Ref. [19].

a smaller U_{dd} is therefore non trivial and hard to predict a priori.

The main problem with a small U_{dd} is the tendency to quickly occupy the d orbital twice leaving only small room for further parameter adjustment. We have to increase $U_{dd} = 0.65\,\text{eV}$ in order to stabilize local moment formation and Kondo screening. We use the analytical hybridization Eq. (3.1.14) as the most basic approximation to keep the calculations simple. The spectral density ρ_d is shown in Fig. 3.33 for intermediate (solid lines) and strong (dashed lines) hybridization simultaneously. The general behavior of intermediate and strong hybridization regime can be verified, however, the Kondo temperature is extremely small and order of magnitude smaller than anything observed in experiment [19, 9].

3.5.7 Exponentially Suppressed Kondo Temperature Close To Dirac Point

We now focus on the influence of the pseudo-gap DOS close to the Dirac Point at $\mu = 0$. For this we rely on the particle-hole symmetrical analytical DOS. Fig. 3.34 shows the Kondo temperature calculated by a Goldhaber-Gordon fit of the zero-bias conductance for the intermediate hybridization regime in close

proximity to the Dirac Point. The Kondo scale decreases exponentially as $|\mu| \to 0$ albeit asymmetrically for p and n doping. Since the DOS is symmetrical, this asymmetry results from the inherently particle-hole asymmetrical parameters for both vacancy orbitals. In general, T_K for n doping is higher than for $\mu < 0$. Because of the exponentially declining Kondo temperature, we cannot resolve T_K closer to the Dirac Point. But since there is a small remaining DOS for finite chemical potential, we still expect to see the formation of Kondo physics below T_K. The vacancy decouples from the conduction bands for $\mu = 0$ and the Kondo effect breaks down.

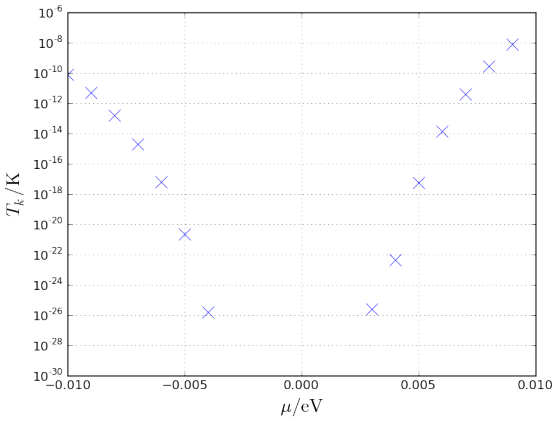

Figure 3.34: $T_K(\mu)$ close to the DP for the analytical PH-symmetrical DOS in the intermediate hybridization regime $\Gamma_0 = 1.21\,\text{eV}$. The parameters are in Tab. 3.3. T_K is suppressed exponentially as $|\mu| \to 0$. The asymmetric slope is due to the PH-asymmetric vacancy.

3.5.8 Rotation of Coulomb Matrix

The d and π orbital are indirectly coupled to each other through the hybridization. This leads to a re-diagonalization of the effective singe particle Hamiltonian, Eq. (3.4.7), where the actual orbitals d' and π' are linear combinations of the isolated orbitals as we discussed in Sec. 3.4.1. We adopt the prime notation explicitly in this section to emphasize the difference between the hybridization-free and the rotated orbitals. The new orbitals can be written as

$$|d'\rangle = \alpha_{d'}|d\rangle + \beta_{d'}|\pi\rangle \tag{3.5.1}$$
$$|\pi'\rangle = \alpha_{\pi'}|\pi\rangle + \beta_{\pi'}|\pi\rangle, \tag{3.5.2}$$

where α_i and $\beta_i, i = d, \pi$ fulfill standard normalization restriction $|\alpha_i|^2 + |\beta_i|^2 = 1$. The coefficients depend on the hybridization V meaning that mixing does not occur if $V = 0$ where thus $|d'\rangle = |d\rangle$ and $|\pi'\rangle = |\pi\rangle$.

This mixing implies that the whole Coulomb matrix, including inter- and intra-orbital interactions, ought to be rotated into the new base. Ideally, the

off-diagonal matrix element in Eq. (3.4.7), $\sqrt{Z}V$, would be small compared to the isolated level energies, and the prime orbitals would thus retain their original non-primed character with minor corrections. The intra-orbital repulsion $U_{\pi'\pi'}$ would grow slightly at the expense of $U_{d'd'}$ which helps to stabilize the occupation of the π' orbital and the Kondo effect in the intermediate regime.

However, the off-diagonal element is (presumably unrealistically) large in our case $\sqrt{Z}V \sim \mathcal{O}(\mathrm{eV})$. This leads to a strong admixture of both orbitals and a likewise strong rotation of the Coulomb matrix elements. All parameters, except μ, are now directly dependent on the hybridization strength Γ_0. This increases the complexity while simultaneously destabilizing the regimes tremendously. Even if one arrives at a configuration for e.g. the intermediate hybridization regime, the strong mixing and concomitant change of the Coulomb matrix elements will destroy the other regimes. Since our model already incorporated a multitude of parameters, we omitted this level of additional complexity before.

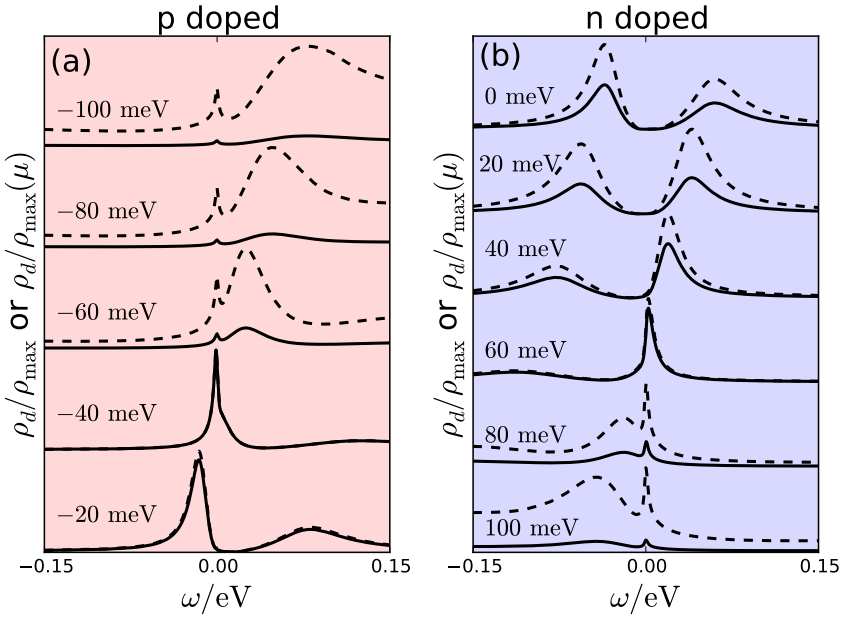

Figure 3.35: Spectral density $\rho_d(\omega)$ for the d orbital and for a rotated Coulomb matrix for (a) p doping and (b) n doping. The curves are either divided by the maximum of all spectral densities $\rho_{\max}$ (solid lines) or by the maximum of the spectral density for the respective chemical potential $\rho_{\max}(\mu)$ (dashed lines). The parameters are ($V = 0$) $\epsilon_d = -0.8904\,\mathrm{eV}$, $\epsilon_\pi = 0.0804\,\mathrm{eV}$, $\Gamma_0 = 0.7\,\mathrm{eV}$, $U_{dd} = 2\,\mathrm{eV}$, $U_{\pi\pi} = 0.01\,\mathrm{eV}$, $U_{d\pi} = 0.1\,\mathrm{eV}$, $J_H = 0.35\,\mathrm{eV}$. The admixture to the primed orbitals is $|\alpha_{d'}|^2 \approx 0.85, |\beta_{d'}|^2 \approx 0.15$ [see Eq. (3.5.1)]. Lines for consecutive μ are shifted by a constant offset. μ is written next to each line. This choice of parameters correspond to the intermediate hybridization regime.

In the experiment, the STM current is generated by tunneling into all local orbitals as well as the underlying π bands of graphene. This results in a complicated tunnel matrix [140] that adds another layer of complexity to our model. We

focused on the spectral function for the d' orbital before because we were mainly interested in the Kondo physics, and dropped the complicated linear combination.

In the following, we adjust ϵ_d and ϵ_π as well as Γ_0 by hand in order to find a configuration that resembles the intermediate hybridization regime. The Coulomb matrix is then rotated as described above, and we make use of the inverse of the Γ_0-dependent rotation matrix to calculate the Green's function for the d orbital. Fig. 3.35 shows ρ_d for $\Gamma_0 = 0.7\,\mathrm{eV}$ for (a) p doping and (b) n doping. The spectral density is depicted twice for each μ: on an absolute scale (solid lines), i.e. the heights of the functions are directly comparable to each other, and divided by the maximum of $\rho_d(\mu)$ (dashed lines).
One finds a Kondo effect again for high p or n doping. The effect breaks down close to the DP, as expected for the pseudo-gap, and the spectral density is dominated by two side-peaks. Compare this to Fig. 3.24 where we found only a single broad shoulder.

3.5.9 Anisotropic Hybridization

Let us analyze the hybridization between d orbital and neighboring π orbitals in more detail. The vacancy is surrounded by three carbon atoms forming a slightly distorted triangle shape as shown in Fig. 3.36. At the top of the triangle resides the unpaired d orbital while there is a π orbital at each atom at the base of the triangle. In a realistic description, electrons can move between d orbital and both π orbitals. The absolute value as well as the phase of this hopping element determine the shape of the hybridization function [118].

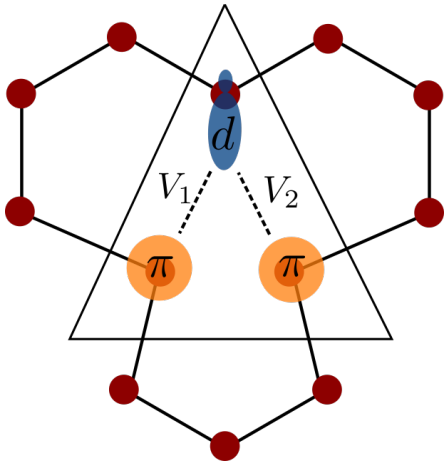

Figure 3.36: Schematic representation of carbon vacancy with the single unpaired d orbital at the top of the triangle (blue) and two neighboring π orbitals at the base of the triangle (orange). V_1 and V_2 are the hopping elements.

The hybridization Hamiltonian can then be written as [118, 19]

$$H_{\mathrm{Hyb}} = \sum_{\sigma} (V_1 a_{1\sigma}^{\dagger} d_{\sigma} + V_2 a_{2\sigma}^{\dagger} d_{\sigma} + h.c.), \tag{3.5.3}$$

where $a_{i\sigma}^{\dagger}$ creates an electron in the π orbital located at $\vec{\delta}_{1,2} = a/2(1, \pm\sqrt{3})^T$ from the missing carbon atom and $V_j = |V_j| \mathrm{e}^{\mathrm{i}\phi}$ are the corresponding hopping elements. We expect $V_1 = V_2$ in a perfectly symmetrical setup. Here, we explicitly allow both hopping elements to have different phases ϕ_i as a result of the deformation of the lattice induced by the vacancy. The superposition $V c_{0\sigma} = V_1 a_{a\sigma} + V_2 a_{2\sigma}$ results in an effective hybridization function

$$\widetilde{\Gamma}(\omega) = \frac{1}{N} \sum_{\tau \vec{k} \sigma} (|V_1|^2 + |V_2|^2 + 2\Re[V_1 V_2^* \mathrm{e}^{\mathrm{i}\vec{k}(\vec{\delta}_1 - \vec{\delta}_2)}]) \delta(\omega - \epsilon_{\vec{k}}^{\tau}), \tag{3.5.4}$$

where τ labels the two π bands. If the absolute values of the hybridization are the same, $|V_1| = |V_2|$, one can define a new set of orthogonal operators for even (+) and odd (-) parity [118, 26, 141]. The respective hybridization function can then be determined via correctly normalizing the new fermionic commutator relations. They then take the form

$$\Gamma_{\pm}(\omega) = \frac{4|V_1|^2}{N} \sum_{\tau \vec{k} \sigma} \delta(\omega - \epsilon_{\vec{k}}^{\tau}) \begin{cases} \cos^2\left(\frac{\vec{k}(\vec{\delta}_1 - \vec{\delta}_2) + \phi_2 - \phi_1)}{2}\right), & \text{even parity} \\ \sin^2\left(\frac{\vec{k}(\vec{\delta}_1 - \vec{\delta}_2) + \phi_2 - \phi_1)}{2}\right), & \text{odd parity.} \end{cases} \tag{3.5.5}$$

Only the even combination contributes whereas the odd linear combination decouples if both π orbitals hybridize equally with the d orbital (the situation in Ref. [118]).

We calculate $\Gamma_+(\omega)$ and $\Gamma_-(\omega)$ for the full t, t' tight-binding dispersion and for vanishing phases $\phi_i = 0$. The results are shown in Fig. 3.37. We still find the pseudo-gap behavior for both hybridization functions, $\Gamma_{\pm}(\omega) \sim |\omega|$. However, the even superposition yields a significant flatter slope than the odd combination or the conventional t, t' hybridization. This flatter slope is directly correlated to a much smaller Kondo scale and thus detrimental to explaining the higher T_K in experiment. Fig. 3.38 compares $\rho_d(\omega)$ for the even, odd, and conventional t, t' hybridization for the same set of parameters to get a rough estimation of the influence on the Kondo scale.

One can turn on a finite phase difference $\Delta\phi = \phi_1 - \phi_2 \neq 0$. If $\Delta\phi = \pi$, even and odd hybridization function are switched since $\cos^2(x + \pi/2) = \sin^2(x)$ and vice versa. We suspect that V_1 and V_2 might differ in phase and maybe even in absolute value due to the lattice deformation. This changes the slope of the hybridization function, which then affects the Kondo temperature. However, a microscopic theory that describes the local rippling and hybridization elements V_i is beyond the scope of this work. Our preliminary results in Fig. 3.38 suggest that the qualitative behavior due to the pseudo-gap is retained, and we did not delve into the subject any further.

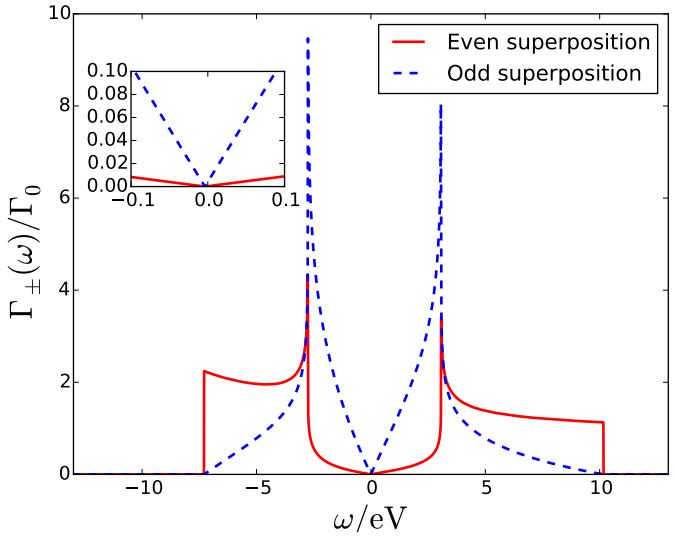

Figure 3.37: $\Gamma_\pm(\omega)$ from Eq. (3.5.5) for $\phi_1 = \phi_2 = 0$. The sum over $\vec{k}$ was directly evaluated on a fine mesh. Both hybridization functions show the linear decline near the DP. Taken from Ref. [19].

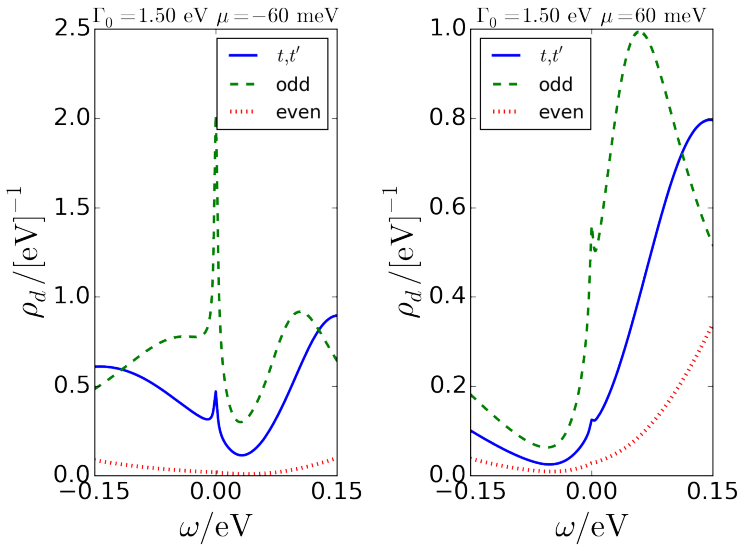

Figure 3.38: $\rho_d(\omega)$ for our conventional hybridization function (blue, solid line), the even (red, dotted line), and the odd superposition (green, dashed line). $\Gamma_0 = 1.5\,\text{eV}$ and $\mu = \pm 60\,\text{meV}$. In all three cases we used the impurity parameter for the original t, t' calculation. The ρ_d shown belong to the intermediate regime. Taken from Ref. [19].

3.5.10 Conclusion of the Graphene Chapter

In the last chapter, we focused on theoretical modeling of single carbon vacancies in mono-layer graphene sheets and the interplay between embedded localized magnetic moments and surrounding electronic band structure. We first reviewed pristine graphene, the nature of the Dirac Point, and a simple tight-binding approach for the π electrons that yielded the characteristic pseudo-gap density of states. The well-known linear electronic dispersion close to the DP is a key ingredient for graphene's various properties. We continued with a discussion about breaking the perfect honeycomb lattice by means of single carbon vacancies that is experimentally realized by low energy ion sputtering. We saw how a single state, the so-called 'zero-mode', emerged at the location of a carbon vacancy by relying on a simple Green's function approach know from literature. We then exemplified how the broken electronic σ bonds in the vicinity of the missing carbon atom lead to a Jahn-Teller distortion and a new σ bond.

Next, we moved away from established literature and presented the findings of our joint collaboration published in a series of two papers [9, 19]. Firstly, we presented the different characteristic STM spectra observed in experiments carried out by our colleagues at Rutgers University, New Jersey, USA in the group of Eva Andrei. We continued with a brief discussion about a simplified single orbital model, its achievements, limitations, and downfalls. Then, we reviewed a two-orbital model by Cazalilla et al. [116] that served as foundation for our numerical study and examined three different parameter regimes in the atomic limit. We finally applied the equilibrium NRG technique and saw how the three different local configurations serve as precursors to the different experimental regimes. We discussed the regimes and various aspects in detail and mapped the whole parameter space for finite and vanishing temperature. We found an excellent qualitative agreement between our calculations and experiment and could capture the different regimes and their characteristic $\mathrm{d}I/\mathrm{d}V$ curves.

However, the model at hand is complex and various aspects are still unsatisfying. First of all, the Kondo temperature tends to be roughly a factor of two too small compared to the experimental results [9]. This discrepancy is negligible if viewed in context: there are numerous sources of possible deviations in the theoretical and numerical approach alone that lead to corrections to T_K. A short and not extensive list includes different parameter sets (Sec. 3.5.6), modifications to the DOS (Sec. 3.5.9), or even different starting parameters for the fitting procedure. We know that Fano line shape calculations require modifications for particle-hole asymmetric problems [142] that were omitted in experiment as well as interpolation for zero temperature. Furthermore, the coupling strength at the STM tip to the various local orbitals is unknown, and, therefore, we did not add the Fano-effect explicitly. We conclude that a factor of two is insignificant and well in the bounds of any systematic error. Even so, it is unlikely that a better numerical agreement in terms of the raw value of the Kondo temperature provides further insight into the underlying physics.

In addition to the quantitative deviation, $T_K \sim \mathcal{O}(\mathrm{K})$ close to the DP in the intermediate regime which is not observed in our numerical study. Since strong parameter variations will alter the Kondo effect in every regime, one can try to cautiously adjust the local parameters to push T_K for n doping by lowering the level positions $\epsilon_{d/\pi}$ for example (Sec. 3.5.6). This results generally in a higher impurity occupation and thus in a formation of a triplet LM and underscreened Kondo effect for smaller μ. However, the lowered levels might easily lead to double occupied local orbitals if not compensated by larger Coulomb repulsion which, in turn, effects T_K as well in a hard to predict manner. It is unlikely that mere fiddling with the parameters will increase T_K close to the DP due to the vanishing DOS. For $\mu \to 0$, the DOS plays a crucial role and suppresses any Kondo effect tremendously (Sec. 3.5.7). It is rather likely that our model misses the physical process responsible for a finite T_K for $0 < \mu < 40\,\mathrm{meV}$. There might be modifications to the LDOS beyond our simple tight-binding approximation close to a carbon vacancy. Also, the presumed Kondo resonance measured in the experiment might instead be a regular excitation peak since one cannot easily distinguish between both types of resonances in the experiment. For small n doping, this peak would rest close to zero bias and yield a fake high T_K while the real Kondo effect takes over seamlessly for stronger doping. This two-peak assumption would circumvent the need for an otherwise unrealistic large hybridization function close to $\mu = 0$.

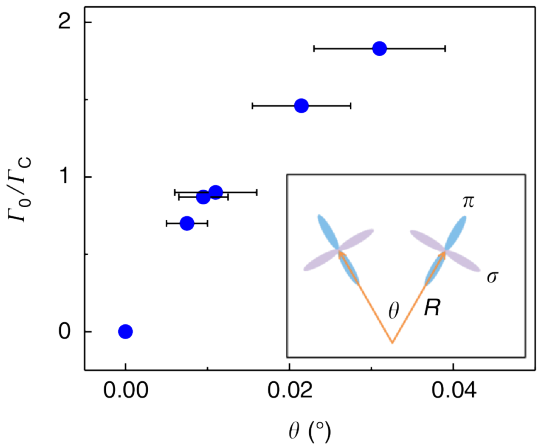

Figure 3.39: Hybridization strength Γ_0 as a function of curvature angle θ at the vacancy by local topography measurements. The error bars represent the uncertainty in the measurement. Γ_0 is measured in units of Γ_c which defines the transition from LM to FI ground state for $\mu = 0$ in Ref. [9]. $\Gamma_0 > \Gamma_c$: strong hybridization regime. $\Gamma_0 < \Gamma_c$: intermediate or weak hybridization regime. Inset: schematic view of the angle and the neighboring orbitals. Taken from Ref. [9].

This brings us to the hybridization strength Γ_0 which is another point of concern. Currently, it is quite high as is the hybridization $V = \sqrt{\frac{2D\Gamma_0}{\pi}} \sim \mathcal{O}(\mathrm{eV})$ for usual values of Γ_0. Even in the small hybridization regime where $\Gamma_0 \approx 1\,\mathrm{eV}$ and $D = 8\,\mathrm{eV}$ for graphene we obtain $V \approx 2.3\,\mathrm{eV}$ which is comparable to the nearest-neighbor hopping element t employed in our tight-binding approximation. We recall that the physical origin of the hybridization is the local rippling and breaking of the orthogonality of the π and σ subsystems. Fig. 3.39 [9] shows the measures angle θ at the local vacancy. Stronger hybridization is indeed linked to larger angles. However, the absolute values for θ are rather small and it is unknown how such a small curvature can induce such a large. An extensive theory likely requires ab-initio calculations and is beyond the scope of this work.

Furthermore, the value of the hybridization has direct influence on the Coulomb matrix as discussed in Sec. 3.5.8. If $\sqrt{Z}V$ is comparable to the single particle level energies, admixture of π and d orbital to the new degrees of freedom is high which in turn leads to a large rotation of the local Coulomb matrix. As a result, the three different regimes are hard to pinpoint as any change in Γ_0 has a quite large effect on the orbital occupation and Coulomb matrix elements.

This illustrates the major trade-off and also shortcoming of the theory presented here. On one hand, one needs a high hybridization strength to ensure just as high Kondo temperatures, especially close to $|\mu| \to 0$. On the other hand, the high hybridization is questionable, its origin not yet fully understood, and even counterproductive if one tries to extend the theory and reduce the number of free parameters.

Despite this criticism, the explanatory power of our model and numerical calculations is excellent. The major features and different types of vacancies observed in experiment can be explained by and traced back to a curvature dependent hybridization, the peculiar DOS of graphene, as well as a two-orbital local model that includes the vacancy induced 'zero-mode'.

Chapter 4

Strongly Correlated Non-equilibrium Steady-State Tunneling Problems

In this chapter we turn away from quantum impurity system in thermal equilibrium and focus on non-equilibrium problems. Non-equilibrium dynamics and electron transport through nanoscale devices have become a major field of research over the last decades.A multitude of different approaches have been developed, but no single technique could be established as the predominant approach to non-equilibrium problems despite major effort. Among these techniques are the Kadanoff-Baym-Keldysh non-equilibrium perturbation expansion [143, 144], Hamiltonian flow-equations [145], the real-time renormalization-group [146], real-time quantum Monte Carlo (QMC) [147, 148, 149], time-dependent Density Matrix Renormalization Group [150, 151], Quantum Master Equation in combination with NEQ-DMFT (QME-DMFT) [152], or the time-dependent Numerical Renormalization Group (TDNRG) [44, 14]. Some methods like the analytical flow-equations are restricted to weak-coupling between central quantum system and conduction bands, some are perturbative (Kadanoff-Baym-Keldysh) or mean-field in nature (QME-DMFT), and some can only access short time scales (QMC) or have difficulties reproducing the steady-state limit faithfully (TDNRG).

Before we discuss our numerical method of choice, the time-dependent Numerical Renormalization Group (TDNRG) and its steady-state adaption, we review the fundamentals of non-equilibrium steady-state transport. The prime toy-model consists of two non-interacting leads with a small (interacting) region in-between. This model will guide us throughout this chapter. We start in Sec. 4.1 with the Landauer-Büttiker formalism [153, 154] for the current through a non-interacting central region. This formalism significantly shaped the view of coherent, i.e. non-phase breaking, transport and serves as a foundation for the fully interacting case.

We continue with a very short introduction to non-equilibrium Green's function in Sec. 4.2 which we later need for the steady-state current. In this context,

we briefly mention the Kadanoff-Baym-Keldysh approach [143, 144] without going into more detail. This framework systematically translates the perturbative expansion of the Green's function in powers of the interaction to the non-equilibrium domain.

We discuss the Meir-Wingreen formula for electron transport through a fully interacting central region [155] in Sec. 4.3. It generalizes the Landauer-Büttiker formula albeit expressed in terms of the non-equilibrium Green's function.

We review the TDNRG [44, 14] in Sec. 4.4 before we discuss the Scattering-States NRG (SNRG) [13] in Sec. 4.5. The SNRG combines from the TDNRG with Hershfield's reformulation of the steady-state in terms of an Y operator [15].

We employ the SNRG to a realistic problem with two spin filtered bands of counter-propagating electrons in Sec. 4.6. Our model describes the edges of a Quantum Spin Hall Insulator (QSHI) coupled to a magnetic impurity. We analyze how the local spin-spin interaction may scatter electrons via spin-flips and induce a backscattering current depending on the symmetry of the system. The results presented in this section are published in Ref. [12].

We then attempt a completely new approach to steady-state transport in Sec. 4.7. Instead of relying on the TDNRG algorithm to generate the correct steady-state density matrix, we calculate the Y operator directly. We discuss the implementation in the NRG framework as well as some preliminary considerations and results in Sec. 4.8.

We close with a summary of our findings in Sec. 4.9.

4.1 Non-interacting Tunneling: Landauer-Büttiker Formalism

The Landauer-Büttiker (LB) formalism [153, 154] describes the coherent transport through a non-interacting nanoscale junction via a scattering or transfer matrix where electrons tunnel without loosing phase information. Its applicability ranges from electron transport through nanostructures, single molecules or even weakly interacting systems like many semiconductor quantum dots [156]. The LB method lies at the heart of a single particle coherent transport theory and provides useful insight to electron transport in general. We briefly discuss the cornerstones of the LB formalism before we move on to the more interesting case of interacting systems. The details can be found in any modern compendium such as Ref. [156].

In the LB formalism one considers a nanoscale quantum junction that consists of two large electrodes (usually labeled as left and right), each resting at their respective thermal equilibrium, and a central region that connects both electrodes. Electronic scattering inside the central region is completely elastic in nature and

transport is entirely coherent through the junction. The electrodes, on the other hand, quickly thermalize any incoming electron through inelastic scattering. A suitable ansatz for transport in such a system is by a wave function that is split into incoming, transmitted, and reflected wave and a junction. One can define the so-called transfer matrix or alternatively the scattering matrix that connects incoming and outgoing wave amplitudes as well as the transmission T and reflection coefficients R where $T + R = 1$. This approach can easily be extended to more complicated geometries with different scattering barriers by matrix multiplication of the individual transfer matrices [156]. Landauer proposed that the zero-temperature conductance G for a single channel junction can be traced back to the transmission T and reflection coefficients R resulting in the so-called 'first Landauer formula' [153, 157, 154, 156]

$$G = \frac{e^2}{h}\frac{T}{1-T} = \frac{e^2}{h}\frac{T}{R}. \tag{4.1.1}$$

For spin degenerate transport G is multiplied by 2. If transmission is small $T \to 0$, the conductance vanishes linearly with T in accordance to perturbation theory [156]. For perfect transmission $T \to 1$, or alternatively $R \to 0$, the conductance diverges.

A second derivation can be found in literature using linear response theory arriving at a seemingly different result [158, 159]

$$G = \frac{e^2}{h}T. \tag{4.1.2}$$

The difference is due to different points of measurements [156]. In the case of Eq. (4.1.1) the conductance is taken inside the junction whereas the authors of Ref. [158, 159] defined the conductance with respect to the electrodes [156].

A generalization of the Landauer formula for finite temperature T and voltage V reads [156]

$$I(V) = \frac{e}{h}\int_{-\infty}^{\infty} T(\omega, V)\left[f_L(\omega) - f_R(\omega)\right]\mathrm{d}\omega \tag{4.1.3}$$

where I is the current instead of the conductance, $T(\omega, V)$ is the voltage dependent transmission function, and $f_\alpha(\omega)$ are the Fermi-Dirac distributions of the left and right electrodes including the respective chemical potential μ_α

$$f_\alpha(\omega) = \frac{1}{\mathrm{e}^{\beta(\omega-\mu_\alpha)}+1} \qquad \beta = (k_B T)^{-1}. \tag{4.1.4}$$

For small T, both Fermi functions effectively reduce to sharp step functions defining a window of width $V = \mu_L - \mu_R$ (without loss of generality $\mu_L > \mu_R$). In this case, only the behavior for $\mu_R < \omega < \mu_L$ plays a role for the low T dependency of G as both leads are either completely occupied or empty outside of this window.

4.2 Short Overview of Non-equilibrium Green's Functions and Keldysh Contour

The Landauer formalism discussed above is only concerned with the limit of non-interacting central regions. A generalization to fully interacting systems has been accomplished by Meir and Wingreen [155] who relied on the non-equilibrium Keldysh formalism [143]. We briefly outline the key points of this approach to non-equilibrium Green's functions following the introductions presented in Ref. [139, 160].

In the equilibrium formalism, the Hamiltonian is split into an easy to solve part H_0 and a difficult contribution V containing the many-body interactions. All operators are transformed to the interaction picture where H_0 governs the time evolution. The Green's function is expressed with the help of the so-called S matrix [139, 160, 161]

$$S(t,t') = T\exp\left\{-\mathrm{i}\int_{t'}^{t} V(t_1)\mathrm{d}t_1\right\} \tag{4.2.1}$$

where T is the time-ordering operator. This matrix is a convenient way to propagate the field operators from time t' to time t

$$\psi(t) = S(t,t')\psi(t'), \qquad S(t,t') = U(t)U^{\dagger}(t'). \tag{4.2.2}$$

Furthermore, one can even connect the non-interacting ground state $|\Phi_0\rangle$ and the fully exact ground state $|\Psi_0\rangle$ via the Gell-Mann and Low theorem [139]

$$|\Psi_0\rangle = S(0,-\infty)|\Phi_0\rangle, \qquad \langle\Psi_0| = \langle\Phi_0|S(\infty,0) \tag{4.2.3}$$

The Green's function is written with the help of the S matrix [139, 160]

$$G(x,t;x',t') = -\mathrm{i}\frac{\langle\Phi_0|T\{S(\infty,-\infty)\psi(x,t)\psi^{\dagger}(x',t')\}|\Phi_0\rangle}{\langle\Phi_0|S(\infty,-\infty)|\Phi_0\rangle}, \tag{4.2.4}$$

before it is expanded in orders of the interaction term V. The occurring expectation values are evaluated by Wick's theorem resulting in Feynman's famous diagrammatic perturbative expansion. The key point is that, even if one acquires a complex phase when applying Eq. (4.2.3) to the denominator of the Green's function, this phase is canceled by an equivalent term accumulated by the nominator [139, 162]. This, however, is not true in the non-equilibrium case in general. It is not guaranteed and rather the exception that the system returns to its initial state after asymptotically large times in non-equilibrium [139, 160, 162].

Despite this it is still possible to formulate a perturbative expansion that is even structurally equivalent to the conventional diagrammatic approach in equilibrium. One starts with a fully time-dependent Hamiltonian which can be partitioned into [139]

$$H = h + H'(t), \quad h = H_0 + H_i. \tag{4.2.5}$$

Here, h comprises the time-independent terms and is split into a bilinear H_0, needed for Wick's theorem, and H_i which contains many-body interactions. The deviation $H'(t)$, that drives the system out of equilibrium, is assumed to vanish for $t < t_0$. It is often reasonable to shift $t_0 \to -\infty$, especially for steady-state problems. The problem is then simplified at the cost of potential initial correlations [160] which should be negligible anyway once steady-state is reached.

The plan of attack is similar to the equilibrium case as one transforms all operators to the interaction picture governed by H_0. The process is complicated by the occurrence of H_i and $H'(t)$ which must both be dealt with in a two-step transformation [139]. We start by defining the contour ordered Green's function [139]

$$G(1,1') = -\mathrm{i}\Big\langle T_C\left[\psi_H(1)\psi_H^\dagger(1')\right]\Big\rangle \tag{4.2.6}$$

where T_C is the time-ordering operator along the contour C, $1 = (x_1, t_1)$ is a compound notation and ψ_H are the fermionic field operators in the Heisenberg picture. The contour C follows along the real axis from t_0 over t_1 to t_1' and C_2 then back to t_0. We can split C into two sub-contours: C_1 that comprises the first part from $t_0 \to t_1'$ and C_2 going back to t_0. Since our Green's function is defined for two distinct time labels, we end up with four different possible combinations [139]

$$G(1,1') = \begin{cases} G_c(1,1'), & t_1, t_1' \in C_1 \\ G^>(1,1'), & t_1 \in C_2, t_1' \in C_1 \\ G^<(1,1'), & t_1 \in C_1 t_1' \in C_2 \\ G_{\tilde{c}}(1,1'), & t_1, t_1' \in C_2. \end{cases} \tag{4.2.7}$$

Here, G_c is the causal or time-ordered Green's function

$$G_c(1,1') = -\mathrm{i}\theta(t_1 - t_{1'})\langle\psi_H(1)\psi_H^\dagger(1')\rangle + \mathrm{i}\theta(t_{1'} - t_1)\langle\psi_H^\dagger(1')\psi_H(1)\rangle, \tag{4.2.8}$$

$G_{\tilde{c}}$ the antitime-ordered Green's function

$$G_{\tilde{c}}(1,1') = -\mathrm{i}\theta(t_{1'} - t_1)\langle\psi_H(1)\psi_H^\dagger(1')\rangle + \mathrm{i}\theta(t_1 - t_{1'})\langle\psi_H^\dagger(1')\psi_H(1)\rangle, \tag{4.2.9}$$

$G^<$ the lesser Green's function

$$G^<(1,1') = \mathrm{i}\langle\psi_H^\dagger(1')\psi_H(1)\rangle, \tag{4.2.10}$$

and $G^>$ the greater Green's function

$$G^>(1,1') = -\mathrm{i}\langle\psi_H(1)\psi_H^\dagger(1')\rangle. \tag{4.2.11}$$

It turns out that only three of the four Green's functions are independent which can be exploited to define a more convenient set of functions. Instead of (anti)time-ordered Green's functions, one commonly introduces the advanced [139]

$$G^a(t,t') = \mathrm{i}\theta(t_{1'} - t_1)\Big\langle\left\{\psi_H(1), \psi_H^\dagger(1')\right\}\Big\rangle \tag{4.2.12}$$

and retarded Green's function.

$$G^r(t,t') = -\mathrm{i}\theta(t_1 - t_{1'})\Big\langle \Big\{\psi_H(1), \psi_H^\dagger(1')\Big\} \Big\rangle, \tag{4.2.13}$$

where the curly brackets represent the anticommutator since we consider fermionic field operators. The four functions are coupled via the relation $G^r - G^a = G^> - G^<$ that encodes their linear dependency.

Next, the time dependence for the fields in Eq. (4.2.6) is changed from H to H_0 in two steps analogous to the equilibrium case. With the time ordering according to the Keldysh contour the final result is formally equivalent to the equilibrium case [139, 160] enabling the use of Wicks's theorem and Feynman's diagrammatic approach. Equilibrium and non-equilibrium formalism differ in one crucial detail: instead of real axis integrals one now has to evaluate contour integrals and time ordering is defined on said contour. These contour integrals are evaluated by analytical continuation, i.e. by shifting the integrals back to the real axis. This process can be formalized by a set of handy rules, known as Langreth rules or the Langreth theorem [163] which can be found in any compendium on the topic [139, 160]. The first rule describes how to calculate the lesser/greater or retarded/advanced component of a product of correlation functions $D = \int_C ABC$ under the contour C (analogous for greater and advanced GF)

$$D^< = \int_t [A^r B^r C^< + A^r B^< C^a + A^< B^a C^a] \tag{4.2.14}$$

$$D^r = \int_t A^r B^r C^r. \tag{4.2.15}$$

We recall that the correlation functions A, B, C, D are still two-time functions. The integral $\int_t$ is a shorthand notation for integration over all intermediate indices, e.g.

$$\begin{aligned} D^<(t,t') = \int\int \big[&A^r(t,t_1)B^r(t_1,t_2)C^<(t_2,t') + A^r(t,t_1)B^<(t_1,t_2)C^a(t_2,t') \\ &+ A^<(t,t_1)B^a(t_1,t_2)C^a(t_2,t')\big]\mathrm{d}t_1\mathrm{d}t_2. \end{aligned} \tag{4.2.16}$$

As a final note, the fluctuation-dissipation theorem connects lesser Green's function and spectral density $\rho(\omega)$ in an equilibrium context (see for example Ref. [139]). In this case, only the time difference $\tau = t - t'$ is important and the Green's function depends on the relative time $G(\tau)$. One can then calculate the Green's function in frequency space, $G(\omega)$, by using a Fourier transformation. In the end, the lesser Green's functions is proportional to $\Im G^r(\omega)$ times the Fermi function [139]

$$G^<(\omega) = -2\Im G^r(\omega) f(\omega). \tag{4.2.17}$$

Here

$$f(\omega) = \frac{1}{\mathrm{e}^{\beta(\omega-\mu)} + 1}, \quad \beta = (k_B T)^{-1} \tag{4.2.18}$$

and μ is the chemical potential.

4.3 Meir-Wingreen Formula for the Electronic Current Through an Interacting Region

With the introduction of the non-equilibrium Green's function and the Keldysh contour we return to the problem of electron transport through an interacting nanoscale region. We sketch the derivation of the Meir-Wingreen formula [155] which bears a resemblance to the Landauer equation (4.1.3) for electron transport through a non-interacting region. However, one has to keep in mind that the Green's function appearing in the Meir-Wingreen formalism represents the full Green's function for the completely interacting Hamiltonian containing inelastic processes, spin flips, and multi-scattering events [155].

For the derivation, we again use the two-lead model including a small and possibly interacting nanoscale region in-between both leads. The intermediate region is described by a discrete-level model, e.g. a single orbital or multiple orbitals describing a molecule. The electrodes are assumed to be ideal, i.e. non-interacting and large enough such that incoming electrons are thermalized without influence on the chemical potential. The intermediate nanoscale quantum system may be subject to Coulomb interaction and can be described through a Hubbard Hamiltonian.

The full Hamiltonian takes the form [156, 155]

$$H = H_C^{(0)} + H_{ee} + H_L + H_R + H_T, \tag{4.3.1}$$

where $H_C^{(0)}$ describes the non-interacting contribution of the central region, H_{ee} is the electron-electron interaction term, $H_{L/R}$ are the Hamiltonians for the left and right electrodes, and H_T comprises tunneling between electrodes and central region. The Hamiltonian can be modified to incorporate electron-vibron interactions in the middle region as well [156]. The quasi-continuous electronic degrees of freedom in lead α with spin σ are described by the creation/annihilation operators $c_{\alpha k\sigma}^{(\dagger)}$. The central region may be more complicated and comprise several orbitals and interactions for which we use the fermionic operators $d_i^{(\dagger)}$. We emphasize that i is a compound label that may include different orbitals in addition to the spin σ.

The current from lead α to the central region is given by the expectation value of the time derivative of the number operator $N_\alpha = \sum_{\alpha k\sigma} c_{\alpha k\sigma}^\dagger c_{\alpha k\sigma}$. The time evolution is evaluated by Heisenberg's equation of motion [155, 156]

$$I_\alpha(t) = -e\Big\langle \Big(\frac{\mathrm{d}N_\alpha}{\mathrm{d}t}\Big)\Big\rangle = -\frac{\mathrm{i}e}{\hbar}\Big\langle\, [H_T, N_\alpha]\,\Big\rangle, \tag{4.3.2}$$

where H_T is the hopping Hamiltonian that reads

$$H_T = \sum_{\alpha k\sigma, i} \left(V_{\alpha k\sigma, i} c_{\alpha k\sigma}^\dagger d_i + V_{\alpha k\sigma, i}^* d_i^\dagger c_{\alpha k\sigma} \right). \tag{4.3.3}$$

After some commutator algebra, the current reduces to

$$I_\alpha(t) = \frac{\mathrm{i}e}{\hbar}\sum_{k\sigma,i}\left[V_{\alpha k\sigma,i}\langle c^\dagger_{\alpha k\sigma} d_i\rangle - V^*_{\alpha k\sigma,i}\langle d_i^\dagger c_{\alpha k\sigma}\rangle\right] \tag{4.3.4}$$

$$= \frac{2e}{\hbar}\Re\left(\sum_{\alpha k\sigma} V_{\alpha k\sigma,i} G^<_{i,\alpha k\sigma}(t,t)\right) \tag{4.3.5}$$

with

$$G^<_{i,\alpha k\sigma}(t_1,t_2) = \mathrm{i}\langle c^\dagger_{\alpha k\sigma}(t_2) d_i(t_1)\rangle \tag{4.3.6}$$

being the lesser Keldysh Green's introduced in Sec. 4.2. We are interested in the time-independent steady-state where the two-time functions can be expressed by a single time difference, and $I_L = -I_R$ holds. We can therefore combine left- and right-flowing current into a symmetrized expression for the total current [155]. After a Fourier transformation, exploiting the Dyson equations for $G^<_{\alpha,ik\sigma}(\omega)$, and some algebra we arrive at [155]

$$I = \frac{\mathrm{i}e}{2h}\int \mathrm{Tr}\left\{\left[f_L(\omega)\boldsymbol{\Gamma}^L - f_R(\omega)\boldsymbol{\Gamma}^R\right](\boldsymbol{G}^r - \boldsymbol{G}^a) + (\boldsymbol{\Gamma}^L - \boldsymbol{\Gamma}^R)\boldsymbol{G}^<\right\}\mathrm{d}\omega, \tag{4.3.7}$$

where we switched to a matrix notation for the different orbitals indicated by a bold notation. The matrix $\boldsymbol{G}$ refers to the fully dressed Green's functions of the central region and $\boldsymbol{\Gamma}^\alpha$ describes the hybridization between each central orbital and lead α. For the common case of a single orbital with spin label only and equal density of states for both leads, $\rho_\alpha(\omega) = \rho(\omega)$, the hybridization and Green's function therefore read

$$\boldsymbol{\Gamma}^\alpha = \begin{pmatrix}\pi|V_\uparrow|^2\rho(\omega) & 0\\ 0 & \pi|V_\downarrow|^2\rho(\omega)\end{pmatrix} \qquad \boldsymbol{G}^< = \begin{pmatrix} G^<_{d^\dagger_\uparrow,d_\uparrow}(\omega) & 0\\ 0 & G^<_{d^\dagger_\downarrow,d_\downarrow}(\omega)\end{pmatrix}, \tag{4.3.8}$$

and the trace collapses to a summation over the spin σ. The calculation is analogous for the retarded and advanced Green's function.
If the coupling to the leads differs only by a factor, $\Gamma^L(\omega) = \lambda\Gamma^R(\omega)$, then the current takes the form [155, 156]

$$I = \frac{e}{2\pi\hbar}\int [f_L(\omega) - f_R(\omega)]\,\mathrm{Tr}\left\{\frac{\boldsymbol{\Gamma}^L(\omega)\boldsymbol{\Gamma}^R(\omega)}{\boldsymbol{\Gamma}^L(\omega)+\boldsymbol{\Gamma}^R(\omega)}\boldsymbol{A}(\omega)\right\}\mathrm{d}\omega, \tag{4.3.9}$$

where $\boldsymbol{A} = \mathrm{i}(\boldsymbol{G}^r - \boldsymbol{G}^a)$ is the spectral function in matrix notation. Note that the spectral function involves the fully dressed Green's function including many-body excitation. In the non-interacting case, the Meir-Wingreen formula reduces to the usual Landauer-Büttiker formula [155, 156].

4.4 Time-dependent Numerical Renormalization Group

The equilibrium NRG algorithm has been successfully adopted over the years to the realm of non-equilibrium problems by Anders and Schiller [44, 14]. At the

heart of this time-dependent NRG (TDNRG) lies the identification of a full many-body basis set from the ensemble of all states generated by the NRG algorithm. This basis is essential to overcome the shortcomings of prior attempts [51], where the authors attempted to calculate non-equilibrium Green's functions where each Wilson shell is linked to a single frequency interval.

In the following, we give an overview over the TDNRG algorithm as described in Ref. [44, 14]. We already introduced the complete basis set in Sec. 2.3.1. We continue with the basic terminology, combine the complete basis with the reduced density matrix approach, and finally arrive at the core time evolution formula.

In the TDNRG, the system is prepared in an initial state H^i (usually for $t < 0$) that still complies with the standard three part structure of impurity, band, and hybridization for a quantum impurity system. At $t = 0$, an additional term ΔH is switched on ('quench') such that the final Hamiltonian takes the form

$$H^f = H^i + \Delta H \theta(t), \tag{4.4.1}$$

where $\theta(t)$ is the Heavyside function. The final Hamiltonian governs the time evolution for $t > 0$. The expectation value of any operator O for time t reads

$$\langle O \rangle(t) = \mathrm{Tr}\left(\rho(t) O(t)\right), \tag{4.4.2}$$

where $\rho(t)$ evolves according to

$$\rho(t) = \mathrm{e}^{-\mathrm{i}H_f t} \rho_0 \mathrm{e}^{\mathrm{i}H_f t}. \tag{4.4.3}$$

At the heart of any NRG lies the logarithmic discretization of the band, iterative solution of the chain Hamiltonian, and truncation of states (cf. Sec. 2.3). We just recall that a Wilson chain of length N with a corresponding Hamiltonian H_N is an approximate solution of the full Hamiltonian for an energy scale $\omega_N \sim \Lambda^{-N/2}$ or analogous for a temperature $T_N \sim \omega_N$ [10]. However, since all energy scales greater than T_N contribute to the non-equilibrium dynamics, we need a complete basis set of the Fock space F_N [14]. Anders and Schiller found such a basis by re-interpreting the NRG algorithm as already discussed in context of the Green's function in Sec. 2.3.1.

Let us rewrite the time evolution with the help of the completeness relation Eq. (2.3.27)

$$\langle O \rangle(t) = \sum_{m=m_{\min}}^{N} \sum_{l,e} {}_{\mathrm{dis}}\langle l, e; m | \rho(t) \mathbb{1} O | l, e; m \rangle_{\mathrm{dis}}. \tag{4.4.4}$$

After inserting $\mathbb{1}$ and some rearranging of the resulting sums, the time evolution takes the form

$$\langle O \rangle(t) = \sum_{m=m_{\min}}^{N} \sum_{r,s}^{\mathrm{trunc}} \sum_{e,e'} \langle s, e; m | \rho(t) | r, e'; m \rangle \langle r, e'; m | O | s, e; m \rangle, \tag{4.4.5}$$

where the truncated sum $\sum_{r,s}^{\text{trunc}}$ enforces the restriction that at least one the states r or s must be discarded at iteration m. If both states belong to the low-energy sector, they carry on to the next iteration and contribute further down the chain. At a first glance, Eq. (4.4.5) seems not very helpful as we are now left with evaluating $\langle r, e'; m|O|s, e; m\rangle$ that involves all environmental degrees of freedom e. In order to simplify the calculations, we therefore restrict O to a local operator, i.e. O acts only on the first few chain sites for which no states have been discarded. Most commonly used operators fulfill this requirement as they usually deal with the degrees of freedom of the impurity alone, e.g. local occupation or spin-spin correlation functions. The operator O thus does not act on the environmental degrees of freedom for the dormant rest chain and

$$\langle r, e'; m|O|s, e; m\rangle = \delta_{e,e'} O^m_{r,s}. \tag{4.4.6}$$

The Kronecker delta simplifies the calculation for the density matrix elements $\langle s, e; m|\rho(t)|r, e'; m\rangle$, which comes down to evaluation of $H|k, e; m\rangle$ in the end. We recall that the final Hamiltonian Eq. (4.4.1) governs the time evolution of the density matrix. We resort to the conventional NRG approximation, $H^f_N|k, e; m\rangle \approx E^m_k|k, e; m\rangle$ [10], and evaluate the matrix elements

$$\langle s, e; m|\rho(t)|r, e; m\rangle \approx \mathrm{e}^{\mathrm{i}(E^m_r - E^m_s)t}\langle s, e; m|\rho_0|r, e; m\rangle. \tag{4.4.7}$$

In the end, the time evolution takes the form [44, 14]

$$\langle O\rangle(t) = \sum_{m=m_{\min}}^{N} \sum_{r,s}^{\text{trunc}} \mathrm{e}^{\mathrm{i}(E^m_r - E^m_s)t} O^m_{r,s} \rho^{\text{red}}_{s,r}(m), \tag{4.4.8}$$

where

$$\rho^{\text{red}}_{s,r}(m) = \sum_e \langle s, e; m|\rho_0|r, e; m\rangle \tag{4.4.9}$$

is the reduced density matrix [44, 14] at iteration m.

Next, we need to actually calculate the reduced density matrix in the TDNRG framework. In Eq. (4.4.8) ρ^{red} is expressed in the eigenstates of the final Hamiltonian H^f since the time evolution is governed by H^f. However, the (reduced) density matrix is typically much easier to obtain in thermal equilibrium where $\rho_0 = \exp(-\beta H^i)/Z_i$ with Z_i as partition function. Anders and Schiller have shown that one can connect both these matrix representations of the reduced density matrix if time evolution starts from thermal equilibrium [14]. For clarity states and indices that belong to the set of eigenstates of the initial Hamiltonian (or denote its quantum numbers) are labeled with an additional i as index. Also, $e_i = e$ since the environmental label e describes the decoupled rest chain that is unchanged. Then we can write the reduced density matrix in the eigenbasis of H^i

$$\rho^{\text{red},0}_{s_i,r_i}(m) = \sum_{e_i} \langle s_i, e_i; m|\rho_0|r_i, e_i; m\rangle. \tag{4.4.10}$$

The superscript 0 is used to distinguish the reduced density matrix from the representation in the eigenbasis of H^f. One inserts the completeness relation for H^i into the formula for the reduced density in the final basis Eq. (4.4.9) and, after some calculations, ends up with [14]

$$\rho^{\mathrm{red}}_{s,r}(m) = \rho^{++}_{s,r}(m) + \rho^{+-}_{s,r}(m) + \rho^{-+}_{s,r}(m) + \rho^{--}_{s,r}(m), \tag{4.4.11}$$

where

$$\rho^{p,p'}_{s,r}(m) = \sum_e \langle s, e; m | \mathbb{1}^p_{i,m} \rho_0 \mathbb{1}^{p'}_{i,m} | r, e; m \rangle, \tag{4.4.12}$$

and $\mathbb{1}^p_{i,m}$ is either the plus or minus projection operator that together constitute the completeness relation for the set of states of H^i in Eq. (2.3.27). Only the $p = p' = +$ component can be traced back to the initial reduced density matrix $\rho^{\mathrm{red},0}_{s_i,r_i}(m)$. One introduces the overlap matrices $S(m)$, that translate between initial and final eigenbasis, and writes [14]

$$\rho^{++}_{s,r}(m) = \sum_{q,q'_i} S^*_{q'_i}(m) \rho^{\mathrm{red},0}_{q'_i,q_i}(m) S_{q_i,r}(m), \tag{4.4.13}$$

for which the overlap matrix elements read

$$\langle q_i, e_i; m | r, e; m \rangle = \delta_{e,\epsilon_i} S_{q_i,r}(m). \tag{4.4.14}$$

All other terms do not follow from knowledge of the initial reduced density matrix $\rho^{\mathrm{red},0}(m)$ alone and require generally overlap elements between states that belong to different NRG iterations. In the end, these matrix elements depend on the environmental degrees of freedom in a complex way preventing simple tracing as in Eq. (4.4.10) [14]. However, these contributions are zero if the initial density operator describes thermal equilibrium because they incorporate coupling of high- and low-energy states within ρ_0 [14]. For time evolution starting not from thermal equilibrium, all contributions have to be taken into account [164].

In case the system is initially in thermal equilibrium the density operator in the NRG approximation reads [14, 10]

$$\rho_0 = \frac{1}{Z_i} \sum_{l_i} \mathrm{e}^{-\beta E^N_{l_i}} |l_i; N\rangle\langle l_i; N|, \qquad Z_i = \sum_{l_i} \mathrm{e}^{-\beta E^N_{l_i}}. \tag{4.4.15}$$

We neglect all discarded states for iterations $m < N$ as they carry only exponentially small weight for $T \sim T_N$. The initial reduced density matrix then has the elements

$$\rho^{\mathrm{red},0}_{s_i,r_i}(N) = \delta_{s_i,r_i} \frac{1}{Z_i} \mathrm{e}^{-\beta E^N_{s_i}} \tag{4.4.16}$$

from which one can calculate all $\rho^{\mathrm{red},0}(m)$ that belong to the initial Hamiltonian H^i recursively. The recursive relation reads [14]

$$\rho^{\mathrm{red},0}_{s_i,r_i}(m) = \sum_{\alpha_{m+1}} \sum_{k_i,k'_i}^{\mathrm{retain}} P_{k'_i,s_i}[\alpha_{m+1}] P^*_{k_i,s_i}[\alpha_{m+1}] \rho^{\mathrm{red},0}_{k'_i,k_i}(m+1), \tag{4.4.17}$$

where the matrix elements

$$P_{k_i',s_i}[\alpha_{m+1}] = \langle s_i, e_i; m | k_i', e_i'; m+1 \rangle \tag{4.4.18}$$

are automatically generated during the diagonalization of the Hamiltonian H_{N+1}. Now that we have the reduced density matrix in the eigenbasis of H^i for any iteration m we need to calculate $\rho^{\mathrm{red}}(m)$ that is needed for the time evolution. It follows from Eq. (4.4.13) and the approximation $\rho^{\mathrm{red}}_{s,r}(m) \approx \rho^{++}_{s,r}(m)$. The latter being valid for quenches that drive the system out of equilibrium.

The TDNRG algorithm reduces to the following steps. Two distinct equilibrium NRG calculations are carried out simultaneously: one for the initial and one for the final Hamiltonian. During this calculation one automatically accumulates the necessary overlap matrices between consecutive iterations Eq. (4.4.18). The starting point for the recursion is the last iteration and the reduced density matrix as defined in Eq. (4.4.16). From there one constructs the series $\rho^{\mathrm{red},0}(m)$ via Eq. (4.4.17). The $\rho^{\mathrm{red},0}(m)$ are expressed in terms of the eigenbasis of the initial Hamiltonian and need to be rotated into the basis of H^f by use of Eq. (4.4.13) and the overlap matrix defined in Eq. (4.4.14). Now we can evaluate the expectation value for all desired time points t via Eq. (4.4.8).

4.4.1 Non-equilibrium Green's Functions in the Numerical Renormalization Group

Anders [47] extended the Green's function algorithm to the non-equilibrium domain by introducing yet another reduced density matrix $\widetilde{\rho}^{\mathrm{red}}$. The calculation itself is similar to the equilibrium case albeit more tedious and complex due to the second reduced density matrix. For a complete and in detail derivation we refer the reader to Ref. [47]. Here, we simply state the final results.

The fully time dependent retarded Green's function is defined as

$$G_{A,B}(t,t') = -\mathrm{i}\Theta(t)\,\mathrm{Tr}\left\{\rho(t')[A(t),B]_s\right\}, \tag{4.4.19}$$

where $s = \pm$ for fermionic or bosonic operators A, B as before. For visibility the commutator is split into individual terms. We focus on one part of the trace

$$I(t',t) = \mathrm{Tr}\left\{\rho(t')A(t)B\right\}. \tag{4.4.20}$$

The derivation relies again heavily on the completeness relation Eq. (2.3.27). Anders showed that $I(t',t)$ takes the form [47]

$$\begin{aligned} I(t',t) = &\sum_{m=m_{\min}}^{N} \sum_{r,s}^{\mathrm{trunc}} \sum_{k} \mathrm{e}^{\mathrm{i}(E_r^m - E_s^m)t'} A^m_{r,k} \mathrm{e}^{\mathrm{i}(E_r^m - E_k^m)t} B^m_{k,s} \rho^{\mathrm{red}}_{s,r}(m) \\ &+ \sum_{m=m_{\min}}^{N-1} \sum_{l'}^{\mathrm{trunc}} \sum_{k_2,k_2} A^m_{k_1,l'} \mathrm{e}^{\mathrm{i}(E^m_{k_1} - E^m_{l'})t} B^m_{l',k_2} \widetilde{\rho}^{\mathrm{red}}_{k_2,k_1}(m,t'), \end{aligned} \tag{4.4.21}$$

where the truncated sums $\sum^{\text{trunc}}$ require at least one state to be discarded at iteration m, $\rho^{\text{red}}_{s,r}(m)$ are the matrix elements of the reduced density matrix as defined before in Eq. (4.4.9), and $\widetilde{\rho}^{\text{red}}_{k_2,k_1}(m,t')$ are a set of new reduced density matrices. These new matrices follow a recursive relation resembling Eq. (4.4.17) for $\rho^{\text{red},0}_{s,r}(m)$. We omit their definition here and refer the interested reader to Ref. [47]. The second term of the commutator can be calculated analogous to Eq. (4.4.21).

4.5 Scattering-States NRG and Lippmann-Schwinger Transformation

In the previous Section 4.4, we reviewed the time-dependent extension to the NRG for non-equilibrium problems. There is a specific type of problem for large times where the system, on one hand, does not follow an equilibrium Boltzmann distribution, but, on the other hand, also does not show explicit time dependency. These system assume a non-equilibrium steady-state.

The prime example for such a steady-state system is again our toy-model that consists of a single discrete orbital coupled to two macroscopic large and quasi-continuous leads with a difference in chemical potential for left- and right-moving electrons. The single orbital may be subject to many-body interactions. Let us assume that the system is in equilibrium for $t < 0$ where $\mu = 0$ for each lead. The problem then corresponds to the two-channel Kondo problem [27, 11]. Electrons may move through the local orbital from one to the other lead although no macroscopic current develops since the mean electron transfer vanishes. We then apply a voltage difference at $t = 0$ between left and right lead. The arising current is described in terms of the non-equilibrium Green's functions and the Meir-Wingreen formalism (4.3.7).

The observables will in general be time-dependent near $t = 0$. However, in the limes of large times, $t \to \infty$, they cease to be time-dependent, and the system approaches a time independent steady-state. Although the eigenstates of the system are not occupied according to the Boltzmann distribution, that governs systems in thermal equilibrium, one can still cast the density operator in the conventional Boltzmann form with the help of the so-called 'Y-operator' introduced by Hershfield [15] which we discuss in detail in Sec. 4.5.2.

Anders [13] proposed another extension to the NRG drawing from the ideas of Hershfield's Y-operator [15], Oguri's application of Lippmann-Schwinger (LS) states [165], and the prior development of the TDNRG [44, 14]. In this approach, the Lippmann-Schwinger states (or scattering states) intermingle the fermionic operator of the local orbital and those of both leads. The resulting new fermionic operators diagonalize the Hamiltonian for a non-interacting resonant level model. The idea is to discretize the continuum of Lippmann-Schwinger states. The LS

transformation ensures the correct boundary condition needed for transport phenomena as propagation direction is encoded in the scattering states directly via a phase factor. This adaption of the NRG, termed Scattering States NRG (SNRG), is explicitly designed for quantum transport in steady-state problems.

Let us review this approach [13, 166] for the single orbital model coupled to two leads mentioned above. The Hamiltonian in its discrete notation takes the form

$$H = \sum_{\sigma} \epsilon_d d_\sigma^\dagger d_\sigma + \sum_{\alpha\vec{k}\sigma} \epsilon_{\alpha\vec{k}} c_{\alpha\vec{k}\sigma}^\dagger c_{\alpha\vec{k}\sigma} + \sum_{\alpha\vec{k}\sigma} (V_{\alpha\vec{k}} d_\sigma^\dagger c_{\alpha\vec{k}\sigma} + V_{\alpha\vec{k}}^* c_{\alpha\vec{k}\sigma}^\dagger d_\sigma). \tag{4.5.1}$$

Instead of using the discrete formulation we change to the continuous energy representation. The new fermionic operators for the bath are

$$c_{\alpha\sigma}(\epsilon) = N_\alpha(\epsilon) \sum_{\vec{k}} V_{\alpha\vec{k}} \delta(\epsilon - \epsilon_{\alpha\vec{k}}) c_{\alpha\vec{k}\sigma}, \quad N_\alpha(\epsilon) = \sqrt{\frac{\pi}{\Gamma_\alpha(\epsilon)}}, \tag{4.5.2}$$

where $N_\alpha(\epsilon)$ is the appropriate normalization given by the fermionic commutator relation $\{c_{\alpha\sigma}(\epsilon), c_{\alpha'\sigma'}^\dagger(\epsilon')\} = \delta_{\alpha,\alpha'}\delta_{\sigma,\sigma'}\delta(\epsilon - \epsilon')$ and $\Gamma_\alpha(\epsilon)$ is the hybridization function for the lead $\alpha = L, R$. The total hybridization function is given by

$$\Gamma(\epsilon) = \Gamma_L(\epsilon) + \Gamma_R(\epsilon) = \pi(V_L^2 + V_R^2)\rho(\epsilon) = \pi\overline{V}^2\rho(\epsilon), \tag{4.5.3}$$

where we assumed a $\vec{k}$ independent hybridization $V_{\alpha\vec{k}} = V_\alpha$. We can define a dimensionless fraction that describes the hybridization asymmetry

$$r_\alpha^2 = \frac{V_\alpha^2}{V_L^2 + V_R^2} \qquad \Rightarrow \qquad \Gamma_\alpha(\epsilon) = r_\alpha^2 \Gamma(\epsilon). \tag{4.5.4}$$

In the following we generally focus on the case of symmetrical coupling where $r_\alpha^2 = 1/2$. The Hamiltonian in this new representation is

$$H = \sum_{\alpha\sigma} \int \epsilon c_{\alpha\sigma}^\dagger(\epsilon) c_{\alpha\sigma}(\epsilon) \mathrm{d}\epsilon + \sum_{\alpha\sigma} r_\alpha \int \sqrt{\frac{\Gamma(\epsilon)}{\pi}} (d_\sigma^\dagger c_{\alpha\sigma}(\epsilon) + c_{\alpha\sigma}^\dagger(\epsilon) d_\sigma) \mathrm{d}\epsilon + \sum_\sigma \epsilon_d d_\sigma^\dagger d_\sigma. \tag{4.5.5}$$

We can cast the scattering state into its continuous form

$$\gamma_{\alpha\sigma}(\epsilon) = a_{\alpha\sigma}(\epsilon) c_{\alpha\sigma}(\epsilon) + b_{\alpha\sigma}(\epsilon) d_\sigma + \sum_{\alpha'} \int e_{\alpha\sigma,\alpha'\sigma}(\epsilon, \epsilon') c_{\alpha'\sigma}(\epsilon') \mathrm{d}\epsilon', \tag{4.5.6}$$

where $a_{\alpha\sigma}(\epsilon)$, $b_{\alpha\sigma}(\epsilon)$, and $e_{\alpha\sigma,\alpha'\sigma}(\epsilon, \epsilon')$ are yet to be determined complex numbers. The most straightforward way to determine these factors is by calculating the commutator $[\gamma_{\alpha\sigma}(\epsilon), H]$ and comparing the coefficients. It reads

$$\begin{aligned}
[\gamma_{\alpha\sigma}(\epsilon), H] = {} & a_{\alpha\sigma}(\epsilon)\epsilon c_{\alpha\sigma}(\epsilon) \\
& + \left(\epsilon_d b_{\alpha\sigma}(\epsilon) + r_\alpha \sqrt{\frac{\Gamma(\epsilon)}{\pi}} a_{\alpha\sigma}(\epsilon) + \int \sum_{\alpha'} r_{\alpha'} \sqrt{\frac{\Gamma(\epsilon')}{\pi}} e_{\alpha\sigma,\alpha'\sigma}(\epsilon, \epsilon') \mathrm{d}\epsilon' \right) d_\sigma \\
& + \sum_{\alpha'} \int \left(\epsilon' e_{\alpha\sigma,\alpha'\sigma}(\epsilon, \epsilon') + r_{\alpha'} \sqrt{\frac{\Gamma(\epsilon')}{\pi}} b_{\alpha\sigma}(\epsilon) \right) c_{\alpha'\sigma}(\epsilon') \mathrm{d}\epsilon'.
\end{aligned} \tag{4.5.7}$$

Because the scattering states diagonalize H, we can alternatively write

$$H = \sum_{\alpha} \int \widetilde{\epsilon} \gamma^{\dagger}_{\alpha\sigma}(\epsilon)\gamma_{\alpha\sigma}(\epsilon)\mathrm{d}\epsilon. \tag{4.5.8}$$

We calculate the commutator again for the diagonal Hamiltonian and find

$$\begin{aligned}[\gamma_{\alpha\sigma}(\epsilon), H] = \widetilde{\epsilon} a_{\alpha\sigma}(\epsilon) c_{\alpha\sigma}(\epsilon) + b_{\alpha\sigma}(\epsilon)\widetilde{\epsilon} d_{\sigma} \\ + \widetilde{\epsilon} \sum_{\alpha'} \int e_{\alpha\sigma,\alpha'\sigma}(\epsilon,\epsilon') c_{\alpha'\sigma}(\epsilon')\mathrm{d}\epsilon'.\end{aligned} \tag{4.5.9}$$

Comparing the coefficients yields three equations

$$\begin{aligned}
&\text{I} \quad \widetilde{\epsilon} a_{\alpha\sigma}(\epsilon) &&= \epsilon a_{\alpha\sigma}(\epsilon) \\
&\text{II} \quad \widetilde{\epsilon} b_{\alpha\sigma}(\epsilon) &&= \epsilon_d b_{\alpha\sigma}(\epsilon) + r_{\alpha}\sqrt{\frac{\Gamma(\epsilon)}{\pi}} a_{\alpha\sigma}(\epsilon) + \sum_{\alpha'} r_{\alpha'} \int \sqrt{\frac{\Gamma(\epsilon')}{\pi}} e_{\alpha\sigma,\alpha'\sigma}(\epsilon,\epsilon')\mathrm{d}\epsilon' \\
&\text{III} \quad \widetilde{\epsilon} e_{\alpha\sigma,\alpha'\sigma}(\epsilon,\epsilon') &&= \epsilon' e_{\alpha\sigma,\alpha'\sigma}(\epsilon,\epsilon') + r_{\alpha'}\sqrt{\frac{\Gamma(\epsilon')}{\pi}} b_{\alpha\sigma}(\epsilon)
\end{aligned}$$

that, after some lengthy calculation, determine $b_{\alpha\sigma}(\epsilon)$ and $e_{\alpha\sigma,\alpha'\sigma}(\epsilon,\epsilon')$. The last unknown number must have an absolute value $|a_{\alpha\sigma}(\epsilon)| = 1$ due to normalization constraints. Exploiting the gauge invariance, we can choose $a_{\alpha\sigma}(\epsilon) = 1$. The scattering states for the non-interacting problem now read

$$\begin{aligned}\gamma_{\alpha\sigma}(\epsilon) =& c_{\alpha\sigma}(\epsilon) + r_{\alpha}\sqrt{\frac{\Gamma(\epsilon)}{\pi}} G_d(\epsilon + \mathrm{i}\delta) \\ &\times \Big[d_{\sigma} + \sum_{\alpha'} \int r_{\alpha'} \sqrt{\frac{\Gamma(\epsilon')}{\pi}} \frac{1}{\epsilon + \mathrm{i}\delta - \epsilon'} c_{\alpha'\sigma}(\epsilon')\mathrm{d}\epsilon' \Big],\end{aligned} \tag{4.5.10}$$

where the complex shift $\widetilde{\epsilon} = \epsilon + \mathrm{i}\delta$ is needed as a regularization in the continuous energy representation. Here $G_d(\epsilon + \mathrm{i}\delta)$ is the local Green's function

$$G_d(\epsilon + \mathrm{i}\delta) = \frac{1}{\epsilon + \mathrm{i}\delta - \epsilon_d - \Delta(\epsilon + \mathrm{i}\delta)} \tag{4.5.11}$$

with

$$\Delta(\epsilon + \mathrm{i}\delta) = \int \frac{\Gamma(\epsilon')}{\pi} \frac{1}{\epsilon + \mathrm{i}\delta - \epsilon'} \mathrm{d}\epsilon'. \tag{4.5.12}$$

The above derivation is valid for a continuum of states. We remark that the new dispersion in the continuum representation is retained up to an infinitesimal imaginary part for regulatory purposes. In the discrete notation the new dispersion $\widetilde{\epsilon}_{\alpha\vec{k}}$ reads

$$\widetilde{\epsilon}_{\alpha\vec{k}} a_{\alpha\sigma\vec{k}} = \epsilon_{\alpha\vec{k}} a_{\alpha\sigma\vec{k}} + b_{\alpha\sigma\vec{k}} V^{*}_{\alpha\vec{k}}, \tag{4.5.13}$$

where $a_{\alpha\sigma\vec{k}}$ and $b_{\alpha\sigma\vec{k}}$ are the coefficients that appear in the discrete equivalent of Eq. (4.5.6). Since the hybridization function, $\Gamma(\epsilon)$, must remain invariant when the number of $\vec{k}$-points is increased, we know that $V_{\alpha\vec{k}} \sim 1/\sqrt{N}$. Any energy shift thus vanishes in the thermodynamic limit, $N \to \infty$, up to the aforementioned regularization imaginary part.

The transformation can be inverted by an analogous ansatz for d_σ and $c_{\alpha\sigma}(\epsilon)$. The details are readily worked out and the final results read

$$d_\sigma = \sum_\alpha r_\alpha \int \sqrt{\frac{\Gamma(\epsilon)}{\pi}} G_d(\epsilon - \mathrm{i}\delta)\gamma_{\alpha\sigma}(\epsilon)\mathrm{d}\epsilon \tag{4.5.14}$$

$$c_{\alpha\sigma}(\epsilon) = \gamma_{\alpha\sigma}(\epsilon) + \sum_{\alpha'} r_\alpha r_{\alpha'} \sqrt{\frac{\Gamma(\epsilon)}{\pi}}\sqrt{\frac{\Gamma(\epsilon')}{\pi}} \frac{G_d(\epsilon - \mathrm{i}\delta)}{\epsilon - \epsilon' - \mathrm{i}\delta}\gamma_{\alpha'\sigma}(\epsilon')\mathrm{d}\epsilon'. \tag{4.5.15}$$

The inverse transformation for d_σ is of particular interest. We can define two new fermionic operators $d_{\alpha\sigma}$ such that

$$d_\sigma = r_L d_{L\sigma} + r_R d_{R\sigma}, \qquad d_{\alpha\sigma} = \overline{V} \int \sqrt{\rho(\epsilon)} G_d(\epsilon - \mathrm{i}\delta)\gamma_{\alpha\sigma}(\epsilon)\mathrm{d}\epsilon, \tag{4.5.16}$$

where we used $\Gamma(\epsilon) = \pi\overline{V}^2\rho(\epsilon)$. Furthermore, we can split the Green's function into complex phase and absolute value and absorb the phase in the definition of the LS states

$$\begin{aligned} d_{\alpha\sigma} &= \overline{V} \int \sqrt{\rho(\epsilon)}|G_d(\epsilon - \mathrm{i}\delta)|\mathrm{e}^{\mathrm{i}\Phi_\sigma(\epsilon)}\gamma_{\alpha\sigma}(\epsilon)\mathrm{d}\epsilon \\ &= \overline{V} \int \sqrt{\rho(\epsilon)}|G_d(\epsilon - \mathrm{i}\delta)|\widetilde{\gamma}_{\alpha\sigma}(\epsilon)\mathrm{d}\epsilon. \end{aligned} \tag{4.5.17}$$

This has the benefit that hopping parameter and level positions of the Wilson chain are completely real [13]. In the following, we leave out the tilde and simply write $\gamma_{\alpha\sigma}(\epsilon)$ for the gauged LS states.

As a final remark, in addition to the continuum states $\gamma_{\alpha\sigma}(\epsilon)$, that are the relevant states for electron transport, there are two additional states located below and above the conduction band. The ansatz for these two bound states $D_{i\sigma}, i = 1, 2$ reads

$$D_{i\sigma} = \overline{z}_i d_\sigma + \sum_\alpha \int A_\alpha(\epsilon) c_{\alpha\sigma}(\epsilon)\mathrm{d}\epsilon \tag{4.5.18}$$

with additional coefficients $\overline{z}_i$ and $A_\alpha(\epsilon)$ that can be determined as before. We ignore these bound states here because their spectral weight is inversely proportional to the bandwidth. In the wide band limit $D \to \infty$, the bound states vanish.

4.5.1 Logarithmic Discretization of Scattering States Continuum

In the last section we established a solution to the non-interacting two-leads model in terms of the non-interacting LS states $\gamma_{\alpha\sigma}(\epsilon)$. Most importantly, we established a inverse transformation that allows us to express the local fermionic operators d_σ via $\gamma_{\alpha\sigma}(\epsilon)$. We continue the approach outlined in Ref. [13, 166] and perform an adapted NRG transformation. The Hamiltonian reads

$$H = \sum_{\alpha\sigma} \int \epsilon \gamma^\dagger_{\alpha\sigma}(\epsilon)\gamma_{\alpha\sigma}(\epsilon)\mathrm{d}\epsilon + U d^\dagger_\uparrow d_\uparrow d^\dagger_\downarrow d_\downarrow \tag{4.5.19}$$

after the LS transformation and including a local Coulomb repulsion. The first term describes a continuum not unlike the bands in the standard NRG transformation. Analogous to the conventional approach, we introduce a discretization parameter $\Lambda > 1$ and divide the continuum logarithmically into intervals $I^s_n, n = 0, \ldots, \infty, s = \pm$. We then introduce a new set of fermionic operators $a_{snp\sigma\alpha}$ that are only defined for the respective interval I^s_n, Eq. (2.3.8) and Eq. (2.3.9), before we expand the LS states in this new operators

$$\gamma_{\alpha\sigma}(\epsilon) = \sum_{n=0}^{\infty} \sum_{s=\pm} \sum_{p=-\infty}^{\infty} d_n^{-1/2} \mathrm{e}^{s\mathrm{i}\frac{2\pi p\epsilon}{d_n}} a_{snp\sigma\alpha}. \tag{4.5.20}$$

We recall that the local operator $d_\sigma = \sum_\alpha r_\alpha d_{\alpha\sigma}$ and that the inverse transformation reads

$$d_{\alpha\sigma} = \int \sqrt{\frac{\Gamma(\epsilon)}{\pi}} |G_d(\epsilon - \mathrm{i}\delta)| \gamma_{\alpha\sigma}(\epsilon)\mathrm{d}\epsilon, \tag{4.5.21}$$

where $\Gamma(\epsilon)$ is the hybridization function and $|G_d(\epsilon - \mathrm{i}\delta)|$ the absolute value of the local Green's function whose phase has been gauged away and absorbed into the LS states. We want to express $d_{\alpha\sigma}$ in terms of the new operators $a_{nsp\sigma\alpha}$ such that we can choose $d_{\alpha\sigma}$ as the starting linear combination for the tridiagonalization algorithm. The expansion reads

$$\begin{aligned}
d_{\alpha\sigma} &= \sum_{nsp} \int \underbrace{d_n^{-1/2}}_{=[\psi^s_{n0}(\epsilon)]^*} d_n^{1/2} \sqrt{\frac{\Gamma(\epsilon)}{\pi}} |G_d(\epsilon - \mathrm{i}\delta)| \psi^s_{np}(\epsilon) a_{nsp\sigma\alpha}\mathrm{d}\epsilon \\
&= \sum_{ns} d_n^{1/2} \sqrt{\frac{\Gamma(\epsilon_{ns})}{\pi}} |G_d(\epsilon_{ns} - \mathrm{i}\delta)| \sum_p a_{nsp\sigma\alpha} \underbrace{\int_{I^s_n} [\psi^s_{n0}(\epsilon)]^* \psi^s_{np}(\epsilon)\mathrm{d}\epsilon}_{=\delta_{0,p}} \\
&= \sum_{ns} d_n^{1/2} \sqrt{\frac{\Gamma(\epsilon_{ns})}{\pi}} |G_d(\epsilon_{ns} - \mathrm{i}\delta)| a_{ns\sigma\alpha} \\
&:= \sum_{ns} F_{ns} a_{ns\sigma\alpha}.
\end{aligned} \tag{4.5.22}$$

In the second line we approximate the hybridization and Green's function as a constant in each interval I_n^s shifting all energy dependency into the dispersion [11, 16]. In the third line we simply exploit the orthogonality property of our wave factors $\psi_{np}^s(\epsilon)$

$$\int [\psi_{np}^s(\epsilon)]^* \psi_{n'p'}^{s'}(\epsilon') \mathrm{d}\epsilon = \delta_{n,n'}\delta_{s,s'}\delta_{p,p'}\delta(\epsilon - \epsilon'). \tag{4.5.23}$$

Only the $p = 0$ modes contribute to the physical orbital. At this point the conventional NRG approximation is applied. The $p \neq 0$ modes are neglected and the index p is suppressed. We proceed with the tridiagonalization algorithm and choose $f_{o\alpha\sigma} := d_{\alpha\sigma}$ as the starting orbital. Its level position can be calculated by

$$\omega_{0\alpha\sigma} = \sum_{ns} |F_{ns}|^2 \xi_n^s \tag{4.5.24}$$

where ξ_n^s are the single particle energies that occur during transformation of the term for the kinetic energy

$$\sum_{\alpha\sigma} \int \epsilon \gamma_{\alpha\sigma}^\dagger(\epsilon)\gamma_{\alpha\sigma}(\epsilon)\mathrm{d}\epsilon \approx \sum_{\alpha\sigma}\sum_{ns} \xi_n^s a_{ns\sigma\alpha}^\dagger a_{ns\sigma\alpha}, \tag{4.5.25}$$

where the $p \neq 0$ modes are already dropped. According to Bulla [11, 16] ξ_n^s can be expressed alternatively as

$$\xi_n^s = \frac{\int_{I_n^s} \sqrt{\Gamma(\epsilon)}|G_d(\epsilon - \mathrm{i}\delta)|\epsilon \mathrm{d}\epsilon}{\int_{I_n^s} \sqrt{\Gamma(\epsilon)}|G_d(\epsilon - \mathrm{i}\delta)|\mathrm{d}\epsilon}. \tag{4.5.26}$$

In our case $\sqrt{\Gamma(\epsilon)}|G_d(\epsilon - \mathrm{i}\delta)|$ serves as an effective hybridization function.

In the wide band limes and for $\Lambda \to 1$ the level position for the first chain site coincides with the original level ϵ_d [13, 166]

$$\begin{aligned} \lim_{\Lambda\to 1} \omega_0 &= \int_{-D}^{D} \frac{\Gamma(\epsilon)}{\pi} |G_d(\epsilon - \mathrm{i}\delta)|^2 \epsilon \mathrm{d}\epsilon \\ &= \int_{-D}^{D} \frac{1}{\pi} \frac{\Gamma(\epsilon)}{(\omega - \epsilon_d)^2 + \Gamma(\epsilon)^2} \epsilon \mathrm{d}\epsilon \\ &= \epsilon_d, \end{aligned} \tag{4.5.27}$$

where the Lorentz peak filters out ϵ_d for large D.

We continue with the tridiagonalization and end up with the semi-infinite Wilson chains [166]

$$H(\Lambda) = \sum_{\alpha\sigma}\sum_{n=0}^{\infty} \omega_{n\alpha\sigma} f_{n\alpha\sigma}^\dagger f_{n\alpha\sigma} + \sum_{\alpha\sigma}\sum_{n=0}^{\infty} \left(t_{n\alpha\sigma} f_{n\alpha\sigma}^\dagger f_{n+1\alpha\sigma} + t_{n\alpha\sigma}^* f_{n+1\alpha\sigma}^\dagger f_{n\alpha\sigma} \right) + H_U, \tag{4.5.28}$$

where the hopping elements decay as $t_{n\alpha\sigma} \propto \Lambda^{-n/2}$ for large n. The interaction part is still expressed in terms of the original fermionic operators d_σ

$$H_U = U d_\uparrow^\dagger d_\uparrow d_\downarrow^\dagger d_\downarrow. \tag{4.5.29}$$

By using the relation $d_\sigma = r_L d_{L\sigma} + r_R d_{R\sigma}$ one can rewrite H_U in the new degrees of freedom. Since $d_{\alpha\sigma}$ are chosen as the starting orbitals for the Wilson chain, the interaction term remains completely constrained to the first chain site even though the LS states intermingle local and band degrees of freedom [13, 166].

4.5.2 Hershfield's Exact Reformulation of Non-equilibrium Statistical Quantum Mechanics

Hershfield [15] provides us with a particular useful description of non-equilibrium statistical quantum mechanics. He realized that the expectation value of an operator A in a steady-state non-equilibrium quantum system can be written as

$$\langle A \rangle = \frac{\mathrm{Tr}\{\mathrm{e}^{-\beta(H-Y)}A\}}{\mathrm{Tr}\{\mathrm{e}^{-\beta(H-Y)}\}} \tag{4.5.30}$$

which is strikingly similar in form to the expectation value in equilibrium where $H - Y$ is substituted by $H - \mu N$. The steady-state problem therefore reduces to calculating this new operator Y. In general Y will differ from μN but the Boltzmann form carries over to the steady state [15].

In the following we review Hershfield's derivation of the Y operator in the context of electron transport through a strongly correlated quantum region. In his original paper he explicitly relies on the existence of additional relaxation mechanism for the system to arrive in steady state [15, 167] but other equivalent derivations based on the time-dependent open-system approach [167] have been carried out as well.

Let us assume that the system rests in equilibrium at some distant time $t = -\infty$. It is disturbed by a perturbation H_1 that is switched on adiabatically and drives the system out of equilibrium, e.g. by turning on a tunneling between two large systems with different chemical potential. One can switch to the interaction picture $H_{1,I}(t) = \exp(\mathrm{i}H_0 t) H_1 \exp(-\mathrm{i}H_0 t)$ and expand the expectation value of any operator A in orders of the perturbation H_1

$$\begin{aligned}\langle A \rangle =& \frac{1}{\mathrm{Tr}\,\rho_0} \mathrm{Tr}\Big\{\rho_0\Big(A - \mathrm{i}\int_{-\infty}^{0} [A, H_{1,I}(t_1)]\,\mathrm{d}t_1 \\ &+ (-\mathrm{i})^2 \int_{-\infty}^{0}\int_{-\infty}^{t_1} [[A, H_{1,I}(t_1)], H_{1,I}(t_2)]\,\mathrm{d}t_2\mathrm{d}t_1 + \dots\Big)\Big\},\end{aligned} \tag{4.5.31}$$

where ρ_0 is the initial density matrix. Hershfield continues by evaluating each real time integral for every order n in Eq. (4.5.31) explicitly, assuming the existence

of a relaxation process that destroys correlation for large times. He arrives at a differential equation for ρ_n

$$\frac{\partial \rho_{n+1,I}}{\partial t} = \mathrm{i}\left[\rho_{n,I}(t), H_{1,I}(t)\right], \tag{4.5.32}$$

where $\rho_{n,I}(t) = \exp(\mathrm{i}H_0 t)\rho_n \exp(-\mathrm{i}H_0 t)$ in the limit $\eta \to 0$ [15], and the initial condition for the zeroth order [15]

$$\rho_0 = \mathrm{e}^{-\beta(H_0 - Y_0)}. \tag{4.5.33}$$

In order to solve the recursive differential equations Eq. (4.5.32), Hershfield introduces a new set of operators Y_n that follow the same equation as the set of density operators [15]

$$\frac{\partial Y_{n+1,I}}{\partial t} = \mathrm{i}\left[Y_{n,I}(t), H_{1,I}(t)\right], \tag{4.5.34}$$

which can be written in an equivalent form [15]

$$[H_0, Y_n] = [Y_{n-1}, H_1] + \mathrm{i}\eta Y_n. \tag{4.5.35}$$

The infinitesimal complex shift $\mathrm{i}\eta$ is introduced for regulatory purpose that arise in the continuum limes [15]. The sum of all Y_n and ρ_n is defined as

$$Y = \sum_{n=0}^{\infty} Y_n \qquad \mathrm{e}^{-\beta(H-Y)} = \sum_{n=0}^{\infty} \rho_n, \tag{4.5.36}$$

and the non-equilibrium expectation value takes the form of Eq. (4.5.30) [15].

The zeroth order Y_0 corresponds to the system without perturbation H_1 and commutes with H_0

$$[H_0, Y_0] = 0. \tag{4.5.37}$$

From this commutator and Eq. (4.5.35) it follows that the commutator of the full Y and $H = H_0 + H_1$ yields an infinitesimal complex shift [15]

$$[Y, H] = \mathrm{i}\eta(Y_0 - Y) \to 0. \tag{4.5.38}$$

Let $H|n\rangle = E_n|n\rangle$. Then we can write the above equation in matrix representation

$$\langle n|\left[Y, H\right]|m\rangle = \mathrm{i}\eta\langle n|(Y_0 - Y)|m\rangle \tag{4.5.39}$$

$$\Rightarrow [Y]_{nm}(E_m - E_n) = \mathrm{i}\eta([Y_0]_{nm} - [Y]_{nm}) \tag{4.5.40}$$

$$[Y]_{nm} = \frac{\mathrm{i}\eta}{E_m - E_n + \mathrm{i}\eta}[Y_0]_{nm}, \tag{4.5.41}$$

which emphasizes the regulatory property of $\mathrm{i}\eta$ and enables us to express Y in terms of eigenvalues of H and matrix elements of Y_0. We make use of this relation later in Sec. 4.7 to develop an ansatz for a steady-state NRG that does not rely on the TDNRG algorithm for the non-equilibrium Green's function.

Let us have a closer look at the operators Y and Y_0 for a given problem. For this we go back to our toy-model that comprises two leads $\alpha = L, R$ and a possibly interacting region that may connect both leads, e.g. a single orbital with hopping V_α to each lead and Coulomb interaction U. The situation is depicted in Fig 4.1. If both leads are disconnected, then $Y_0 = \sum_\alpha \mu_\alpha N_\alpha$ where N_α measures the number of particles in lead α which is $N_\alpha = \sum_k c^\dagger_{\alpha,k} c_{\alpha,k}$ for a discrete problem [Fig. 4.1 (a)]. The system decays into two separate sub-systems that are each in equilibrium with $H_1 = 0$.

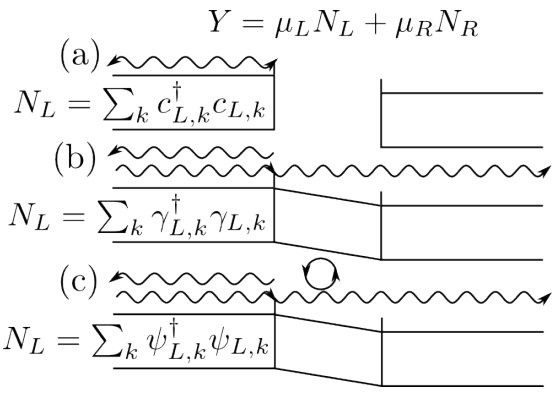

Figure 4.1: Schematic depiction of the Y operator for two infinite leads with different chemical potentials μ_L and μ_R. (a) Both leads are separated and Y (as well as Y_0) measures the number of particles $c_{\alpha k}$ in the left or right lead. (b) Both leads are connected via a non-interacting region. The Y operator measures the left and right-moving non-interacting scattering states $\gamma_{\alpha,k}$ weighted with the corresponding chemical potential. (c) Both leads are connected via an interacting region. The interactions scatters between left and right-moving states and Y measures the many-body scattering states $\psi_{\alpha,k}$ which include many-body excitations. Adapted after Fig. 1 from Ref. [15].

If we switch on the hoppings V_α but forego many-body interactions, i.e. $U = 0$, then the number operators entering in Y_0 represent the non-interacting Lippmann-Schwinger states or scattering states instead of the original particles [Fig. 4.1 (b)]. We can still write $Y_0 = \sum_\alpha \mu_\alpha N_\alpha$ but now reinterpret the meaning of N_α in terms of the scattering states and μ_α as the chemical potential for left and right-moving states. In this case, $Y = Y_0$ still holds. The Hamiltonian can be diagonalized in terms of the non-interacting Lippmann-Schwinger states and thus $[H, Y_0] = 0$. Equivalently, H and Y_0 can both be diagonalized simultaneously which directly yields $Y = Y_0$ according to Eq. (4.5.41). This result can alternatively be understood from a symmetry point of view. Without an interaction α remains a good quantum number even when the hopping is switched on. The system decays again into two sub-systems, one for left- and one for right-moving scattering states, while mixing is prohibited. We are thus back at the situation described in (a) only with an reinterpreted occupation number operator N_α.

In the last case, we switch on a hopping as well as a many-body interaction H_1 that mixes left- and right-moving states. Now, $[Y_0, H_1] \neq 0$ and one can interpret Y as the operator that evolved from Y_0 under the Hamiltonian H_1 [15]. The operator Y can still be written formally as $Y = \sum_\alpha \mu_\alpha N_\alpha$ although N_α now measures the occupation of the fully interacting Lippmann-Schwinger ψ_k states [Fig. 4.1 (c)]. The zeroth order Y_0 is no longer diagonal in the new eigenbasis of H. If we take the limes $\eta \to 0$ in Eq. (4.5.41), we end up with a delta function for the energies $\delta(E_m - E_n)$. In this limes, Y does not change the eigenstates themselves (modulo a possible mixing due to energetic degeneracy), but rather

changes the distribution of the eigenstates [15].

4.6 Magnetic Impurities Coupled to Helical Edge Bands of a Quantum Spin Hall Insulator

A particular interesting system in a steady-state out of equilibrium are the edge states of quantum spin Hall insulators (QSHI) coupled to a local magnetic imperfection. A QSHI is effectively a 2d system with two counter-propagating electronic modes located at its 1d surface. These edge states are topologically protected which, in theory, should yield perfect conductance along the edge. Experimental studies, however, find deviations from perfect conductance [168, 169, 170, 171] and possible explanations encompass among other electron-electron interactions, disorder, or inelastic scattering [172, 173, 174, 175, 176, 177, 178, 179, 180, 181].

We investigate the influence of magnetic impurities at those edges and study the effect of a spin-spin exchange interaction between edge electrons and impurity on the conductance. The general picture in literature [182, 183] is that the edge electrons will participate in Kondo screening of the magnetic impurity when the temperature is low enough. The resulting Kondo singlet essentially severs the conducting surface channels at the location of the impurity. The conducting modes then restore themselves around the screened impurity and electron transport remains uninterrupted due to its topological nature. Tanaka et al. [184] argue that one needs an anisotropic Kondo coupling to affect the perfect edge conductance.
The effect of a Rashba spin-orbit coupling between electrons on the edge in the presence of electron-electron interactions has been investigated before [185]. A Rashba interaction allows for scattering via spin-flips while preserving time-reversal symmetry. The authors found that a spatially disordered Rashba coupling leads to a breakdown of the perfect conductance if the electron-electron interaction between the edge electrons is strong enough. Eriksson et al. [186] built upon these findings, and included a magnetic impurity coupled via a Kondo coupling to the edge electrons. They found a competition between Kondo screening and Rashba induced scattering for an anisotropic Kondo coupling even though time-reversal symmetry is preserved.

We describe the magnetic impurity by an effective model that consists of a localized $s = 1/2$ spin coupled to a non-interacting spin-full orbital (labeled d orbital). The edge electrons constitute of two spin-filtered bands. A finite bias voltage, eV, is applied to the edge resulting in different chemical potential μ_σ for the up and down electrons. Electrons from these bands can hop onto the local non-interacting orbital. Without a spin-spin exchange interaction $J_{\alpha\beta}$ between d orbital and local spin, the edge electrons that hop on the d orbital cannot be scattered between both bands as they cannot change their spin. The number of electrons in each channel is conserved and conductance remains perfect. The conductance depends on the symmetry property of the matrix elements $J_{\alpha\beta}$: as

long as the coupling is isotropic, the total S_z spin component is conserved. In this case, magnetic scattering can only change the spin of incoming electrons from one band when there is an equivalent amount of scattering processes for incoming electrons from the other band. Thus, the effect of all scattering events on the conductance cancels out. Only when the coupling is not isotropic, i.e. when S_z ceases to be a good quantum number, can magnetic scattering induce a current.

We employ the SNRG as described in Sec. 4.5 for the above quantum impurity model and discuss our results, that are published in Ref. [12]. At first, however, we briefly sketch some of the foundations surrounding QSHI and edge states. This overview is by no means intended to be a comprehensive introduction to the field of topological insulators. The reader is referred to reviews such as Ref. [187, 188].

Haldane [73] initially developed a model for the Quantum Hall effect based on edge states in armchair graphene samples. In his model, time-reversal symmetry is broken by a magnetic field yielding a band structure with a single band located inside the gap. The electrons of this band propagate along the edge in one direction.
The question arose whether protected edge states can be realized without breaking time-reversal symmetry. Kane and Mele [76, 77] postulated the existence of such states in graphene as a result of a presumably large spin-orbit coupling. They drew from the mathematical field of topology and introduced the $\mathbb{Z}_2$ topological classification to distinguish between conventional and topological insulators. In a nutshell, Kane and Mele's classification reduces to whether an insulating system with surface states inside its gap exhibits an even or odd number of band crossings at the Fermi level [77, 188]. The edge states at the Fermi level come in so-called Kramer's pairs (one pair equals two states) and are counter-propagating.

Let us assume that the 1d surface edge is parallel to the x axis. The system is translational invariant such that Bloch's theorem holds and we can define the momentum k_x. Subplot 4.2 (a) describes the band structure of a topological insulator. The band structure exhibits two states (one Kramer's pair) for any given Fermi energy E_F inside the gap. Furthermore, the band structure is symmetric with respect to $k_x = 0$, where both bands cross, reflecting time-reversal symmetry [187, 188]. On the other hand, subplot 4.2 (b) shows the band structure for the time-reversal broken case discussed by Haldane.

The edge states for the topological QSHI are called 'chiral' or 'helical' meaning that electron propagation and spin orientation are interlinked. In our case here, the topological nature of the problem does not play a role beyond providing a physical motivation for the counter-propagating and spin-filtered bands. We thus do not delve into topology much further in this work.

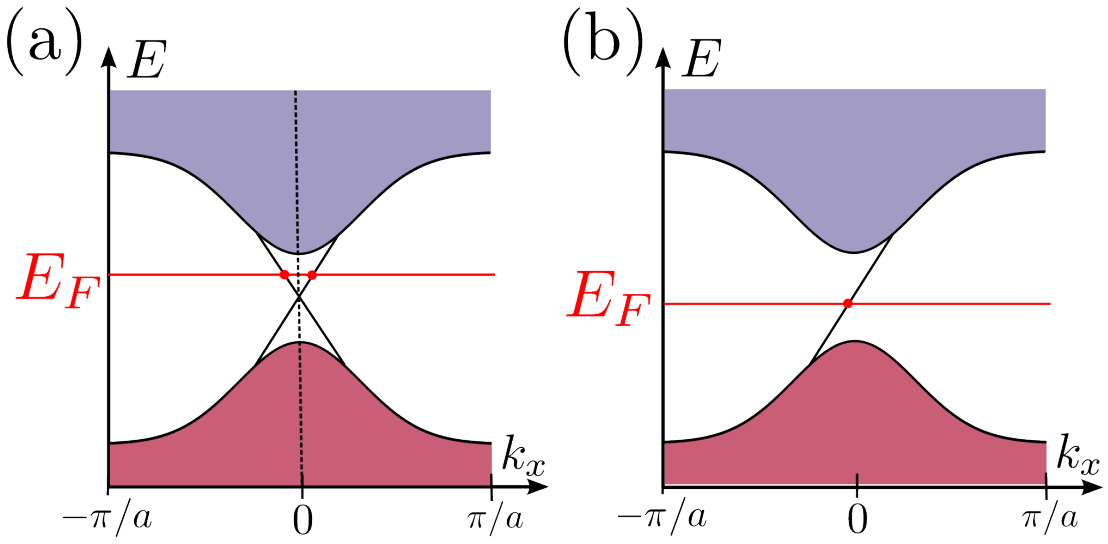

Figure 4.2: Schematic representation of conduction and valence band and edge states for (a) time-reversal symmetric model and (b) broken time-reversal symmetry. The situation in (a) represents a QSHI whereas (b) describes a Quantum Hall State. E_F is the Fermi energy.

4.6.1 Modeling of Helical Edge Modes Coupled to a Magnetic Impurity

We return to the edge of an QSHI for which we can define a spin up and down orientation for the spin of the electrons traversing along the edge. Note that the definition is only valid locally, i.e. one may locally define up and down state but their orientation may change along the edge. In practice, the local nature of this definition is only secondary for our problem and we simply assign counter-propagating electrons different spin orientations. In addition, the edge electrons are taken to be non-interacting.

Let us apply a chemical potential difference between left- and right-moving electrons on the edge by using an external bias voltage eV. An electric current I_0 is driven by the different occupation numbers of left- and right-movers [12]

$$I_0 \approx \frac{G_0}{e}(\mu_\uparrow + \mu_\downarrow) \tag{4.6.1}$$

where $G_0 = e^2/h$ is the conductance quantum and μ_σ the chemical potential for the respective spin channel, $eV = \mu_\uparrow + \mu_\downarrow$.

As mentioned above, we want to investigate the influence of a magnetic impurity located at the helical edge onto the edge current. We consider a model that consists of two spin-filtered bands for a 1d edge [12]

$$H_e = -\mathrm{i}v_F \sum_\nu \sigma \int \psi_\nu^\dagger(x)\partial_x\psi_\nu(x)\mathrm{d}x \tag{4.6.2}$$

where v_F is the Fermi velocity and $\psi_\nu(x)$ are the field operators for the spin projection ν. The index $\nu = \uparrow, \downarrow$ simultaneously represents the left- or right-moving nature. Without loss of generality, we identify spin up with left- and spin down with right-movers. The edge electrons hybridize with a single orbital located at $x = 0$. The hybridization term reads [12]

$$H_t = \sum_\nu (t_\nu \psi_\nu^\dagger(0) d_\nu + h.c.), \tag{4.6.3}$$

where t_ν is the hybridization and d_ν the fermionic operator for the localized orbital. The magnetic impurity encompasses a single $s = 1/2$ localized spin that interacts with the electrons on the d orbital. The Hamiltonian for the local part takes the form [12]

$$\begin{aligned} H_{\text{loc}} &= H_d + H_J \\ &= \sum_\nu \epsilon_d d_\nu^\dagger d_\nu + U n_\uparrow^d n_\downarrow^d + \sum_{\alpha,\beta,\lambda,\mu} J_{\alpha,\beta} S_\alpha d_\lambda^\dagger \sigma_{\lambda,\mu}^\beta d_\mu. \end{aligned} \tag{4.6.4}$$

It is formally split into a contribution H_d that comprises the level position ϵ_d and a possible Coulomb interaction U, and H_J that describes an anisotropic spin-spin exchange interaction $J_{\alpha,\beta}$ with the additional local spin $\vec{S}$. The spin for the local d orbital, $\vec{s}$, is expressed in terms of its fermionic operators with the sums over μ and λ going over $\uparrow$ and $\downarrow$ and α and β being x, y, z. A schematic picture of the model is shown in Fig. 4.3.

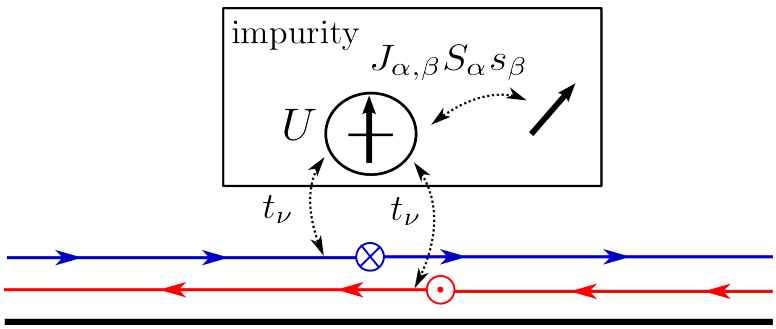

Figure 4.3: Schematic representation of the helical edge and impurity model. Electron propagation in x axis on the edge is interlinked with spin orientation. At $x = 0$ electrons from both helical bands can hop onto a localized orbital. The effective spin $\vec{s}$ of the d electrons is interacting with an additional spin $\vec{S}$ via an exchange interaction $J_{\alpha,\beta}$.

Our impurity can contain two spins: the localized $\vec{S}$ and the spin of the electron in the d orbital. Two different screening processes are therefore possible in our model in equilibrium. The first screening process can be best understood for $t_\uparrow = t_\downarrow$ and $J_{\alpha,\beta} = 0$. Our model then represents a SIAM with an additional dangling $s = 1/2$ spin that contributes to the residual entropy. The electrons of the band, which is formally split into two spin-filtered parts, can screen the spin of the electron in the d orbital as discussed in Sec. 2.2. If $U = 0$, then the system still reaches the same fixed point but on a temperature scale of Γ_0 [35].

A second screening process takes place where the local spin, $\vec{S}$, is screened. For this, we switch on a diagonal anti-ferromagnetic exchange interaction $J_{\alpha,\alpha} \neq 0$. For $U = 0$, the spectral density of the local orbital takes the form of a Lorentzian that plays the role of an effective density of states for this second screening process. We are interested in this second process and choose $U = 0$ in the following except when explicitly noted otherwise.

We also remark, that the helical nature of the edge states results in a simplified Lippmann-Schwinger transformation. Only two of the four LS operators in Eq. (4.5.10) appear which simplifies the inverse transformation Eq. (4.5.16) as well.

Let us take a look at the exchange interaction and possible quantum numbers. If $J_{xx} = J_{yy}$, then the total S_z component, including the d orbital, local spin, and edge electrons, is a good quantum number. We can perform a global gauge transformation $\exp(\mathrm{i}\theta S_z/2)$ by rotation at the joint spin z-axis by a phase θ that leaves the Hamiltonian invariant and preserves time-reversal symmetry. The system is invariant under a $U(1)$ rotation symmetry in the spin space. Furthermore, we can write down Hershfield's Y directly [12]

$$Y = \frac{\mu_\uparrow - \mu_\downarrow}{2} S_z - \frac{\mu_\uparrow + \mu_\downarrow}{2} N_{\mathrm{tot}} \tag{4.6.5}$$

where N_{tot} is the total number of fermions. This formula holds as long as $[H, S_z] = 0$, i.e. as long as the exchange coupling is isotropic. The first term is equivalent to a global magnetic field applied in z direction and the problem can essentially be mapped onto an effective equilibrium problem with magnetic field.

4.6.2 Backscattering Current and Linear Conductance

We are interested in the backscattering current, I_B, or rather the linear conductivity, $G = I_B/V$, that is induced by our magnetic impurity when in steady-state. We present the deviation for a formula in terms of the fully interacting Green's function in steady-state [12]. We start with the definition for the backscattering current operator

$$\begin{aligned} \hat{I}_B &= \frac{\mathrm{e}}{2}\frac{\mathrm{d}}{\mathrm{d}t}\Big(N_L - N_R\Big) \\ &= \frac{\mathrm{ie}}{2}\Big[t_\downarrow \psi_\downarrow^\dagger(0) d_\downarrow - t_\uparrow \psi_\uparrow^\dagger d_\uparrow - h.c.\Big]. \end{aligned} \tag{4.6.6}$$

Here, N_L and N_R are the left- or right-moving number operators for the Lippmann-Schwinger modes. The second line follows from Heisenberg's equation of motion and evaluation of the occurring commutator. We write the expectation values in terms of the lesser Green's function $G^<_{AB}(\tau, \tau') = \langle B(\tau')A(\tau)\rangle$. We then transform the expression into Fourier space since we are interested in the steady-state

limit where only the time difference $t = \tau - \tau'$ plays a role. The current then reads

$$I_B = \langle \hat{I}_B \rangle = \mathrm{e}\Im \int \left[t_\uparrow G^<_{d_\uparrow \psi^\dagger_\uparrow}(\omega) - t_\downarrow G^<_{d_\downarrow \psi^\dagger_\downarrow}(\omega) \right] \frac{\mathrm{d}\omega}{2\pi}. \tag{4.6.7}$$

We now turn to conventional diagrammatic expansion and write the occurring lesser Green's function as a product of the local GF for the full Hamiltonian, $G_{d_\nu d^\dagger_\nu}$, and the free GF for the edge, $g_{\psi_\nu \psi^\dagger_\nu}$,

$$G^<_{d_\nu \psi^\dagger_\nu}(\omega) = t^*_\nu \Big[G_{d_\nu d^\dagger_\nu}(\omega) g_{\psi_\nu \psi^\dagger_\nu}(\omega) \Big]^<. \tag{4.6.8}$$

We can evaluate the lesser part of this product by using Langreth rules introduced in Sec. 4.2

$$\Big[G_{d_\nu d^\dagger_\nu} g_{\psi_\nu \psi^\dagger_\nu} \Big]^< = G^r_{d_\nu d^\dagger_\nu} g^<_{\psi_\nu \psi^\dagger_\nu} + G^<_{d_\nu d^\dagger_\nu} g^a_{\psi_\nu \psi^\dagger_\nu} \tag{4.6.9}$$

$$g_{\psi_\nu \psi^\dagger_\nu}(\omega)^{r/a} = \mp \mathrm{i}\pi\rho_0 \tag{4.6.10}$$

$$g_{\psi_\nu \psi^\dagger_\nu}(\omega)^< = 2\pi\rho_0 f(\omega - \mu_\nu), \tag{4.6.11}$$

where r/a signifies the retarded or advanced part and ρ_0 represents the constant DOS of the edge.
Inserting everything into the expression for the currents yields [12]

$$\begin{aligned} I_B = \frac{G_0}{\mathrm{e}} \Gamma_0 \int \Big[& G^<_{d_\uparrow d^\dagger_\uparrow}(\omega) + 2\Im G^r_{d_\uparrow d^\dagger_\uparrow}(\omega) f(\omega - \mu_\uparrow) \\ & - G^<_{d_\downarrow d^\dagger_\downarrow}(\omega) - 2\Im G^r_{d_\downarrow d^\dagger_\downarrow}(\omega) f(\omega - \mu_\downarrow) \Big] \mathrm{d}\omega. \end{aligned} \tag{4.6.12}$$

One directly sees, that the backscattered current vanishes identically in each spin channel separately in equilibrium where the fluctuations-dissipations theorem

$$G^<_{d_\nu d^\dagger_\nu}(\omega) = -2\Im G^r_{d_\nu d^\dagger_\nu}(\omega) f(\omega - \mu_\nu) \tag{4.6.13}$$

holds.

The backscattered current depends on the anisotropy of the exchange interaction $J_{\alpha,\beta}$. We define 'symmetrical' and 'asymmetrical' exchange coupling with regards to the commutator $[H_J, S_z]$ where S_z describes the z component of the total spin. If the commutator vanishes, the exchange coupling is 'symmetrical', and the $U(1)$ rotational symmetry discussed above is retained. A symmetrical or asymmetrical interaction can be fully realized by changing J_{xx} and J_{yy} [12]. The last diagonal element, J_{zz}, does not affect the symmetry property and can be used to adjust the Kondo temperature [12]. The off-diagonal elements are not needed and set to zero in the following.

4.6.3 Effective Equilibrium with Applied Magnetic Field for Symmetrical Interaction

In case of a symmetrical exchange interaction, $J_{xx} = J_{yy}$, or for $J_{\alpha,\beta} = 0$, we already discussed that the total S_z is a good quantum number, and the system assumes an effective equilibrium state even for finite bias V. The chemical potential difference directly maps onto an effective magnetic field according to Eq. (4.6.5). We can therefore compare our calculations for finite V to an equilibrium SIAM and magnetic field. Fig. 4.4 (a) shows the local spectral function for the d orbital for each spin sector for our helical model with $\epsilon_d = -U/2$, $U/\Gamma_0 = 10$, and $eV/\Gamma_0 = 0.5$ compared to ρ_{d_ν} for a SIAM with magnetic field $B/\Gamma_0 = 0.5$. In case of the SIAM, the Zeeman splitting is $\Delta E = g_{\text{eff}} B$ with $g_{\text{eff}} \approx 2$. The Kondo peak resides at $\pm B$ for spin up and down respectively. In case of the helical model, the Kondo peak rests at $\pm\mu$. A simple shift of the energy axis by $\pm eV/2$ is sufficient for both curves to be identical.

Next, we calculate the equilibrium Kondo temperature, T_K^{eq}, for the second screening process that involves the local spin. We employ the same approach as discussed in Sec. 2.3.2. The susceptibility is in turn calculated by applying a small local magnetic field $B \sim O(10^{-8}\Gamma_0)$ and measuring the difference in spin up and down and dividing the result by B. We emphasize that T_K^{eq} is the equilibrium Kondo temperature for $eV = 0$. Fig. 4.4 (b) shows the results for $J_{xx} = J_{yy} = \Gamma_0$ and various J_{zz}. If scaled accordingly, all χ_{spin} curves completely fall onto each other demonstrating universal behavior.

Now that we have established our calculation scheme for T_K^{eq}, we set $\epsilon_d = U = 0$ and focus on the influence of the ratio J_{xx}/J_{yy} on T_K^{eq}. Fig. 4.4 (c) depicts T_K^{eq} in absolute values as function of J_{yy} for $J_{xx} = J_{zz}$. We emphasize that the Kondo temperature depends non-linear but monotonic on J_{yy}, i.e. the larger J_{yy} the larger T_K^{eq}. The ratio of T_K^{eq} and V is important as the highest of both low-energy scales defines the low-energy behavior of our system.

Until now, our calculations were done for the equilibrium case. We rely on the TDNRG algorithm to generate the correct density-matrix as we now turn to the steady-state problem. From this point onward, quenches refer to a change in $J_{\alpha\beta}$ and are always taken with regard to the initial symmetrical coupling $J_{xx}^{\text{i}} = J_{yy}^{\text{i}} = J_{zz}^{\text{i}} = \Gamma_0$. In the following, the couplings $J_{\alpha\beta}$ shown in figures or listed in text represent the final value after the TDNRG quench.

Before we discuss the different regimes depending on the ratio eV/T_K^{eq}, we look at the behavior of the spectral function. Fig. 4.5 shows the lesser GF and spectral density for retained and broken $U(1)$ symmetry. $G_\nu^<$ equals the spectral density times Fermi function exactly if $U(1)$ symmetry is conserved [subplot 4.5 (a) and (b)]. This equivalence is the embodiment of the fluctuations-dissipations theorem mentioned above, and the backscattering current vanishes in each spin channel separately. On the other hand, $G_\nu^<(\omega)$ and $2\rho_\nu(\omega) f(\omega - \mu_\nu)$ differ if the $U(1)$ symmetry is broken, driving a finite current [subplot 4.5 (c) and (d)]. Finite

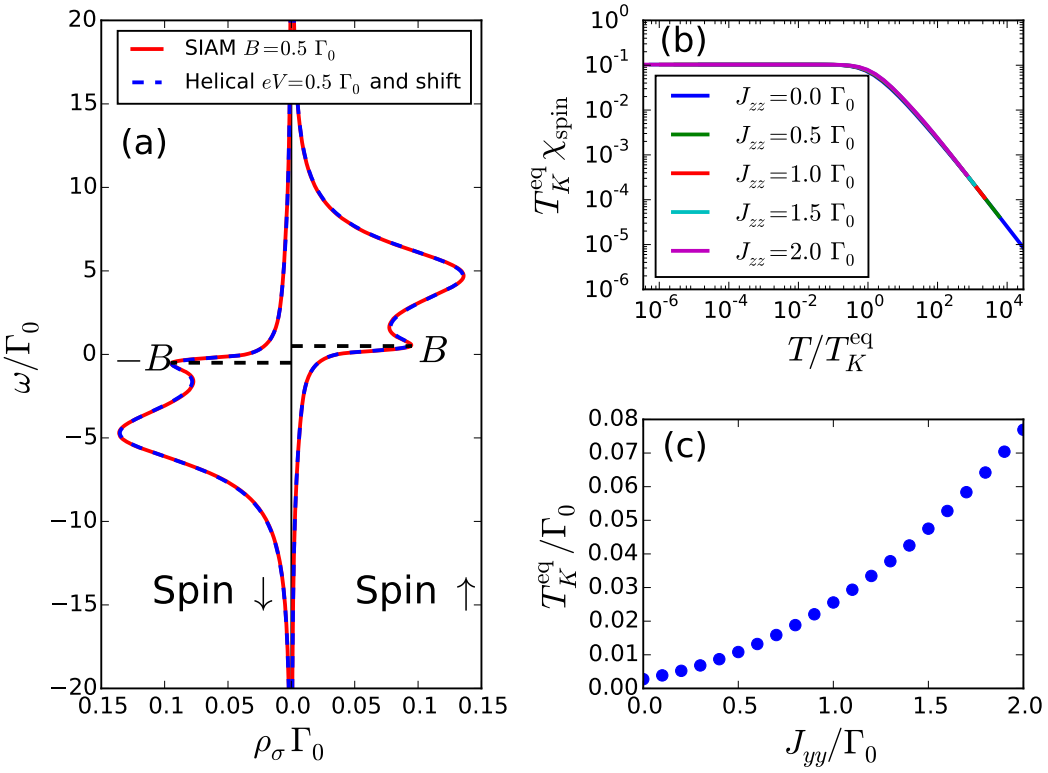

Figure 4.4: (a) $\rho_\nu^{\rm helical}$ for $V/\Gamma_0 = 0.5, J_{\alpha,\beta} = 0$ (blue dashed line) and $\rho_\nu^{\rm SIAM}$ (red solid line) for $B/\Gamma_0 = 0.5$. In both cases, $\epsilon_d = -U/2$ and $U/\Gamma_0 = 10$. $\rho_\nu^{\rm helical}$ is shifted by an additional $\pm V$. (b) $\chi_{\rm spin}$ for the helical model in equilibrium $V = 0$, $J_{xx} = J_{yy} = \Gamma_0$, and $\epsilon_d/\Gamma_0 = -0.5$ and $U = 0$. (c) Kondo temperature calculated from $\chi_{\rm spin}$ via Eq. (2.3.38) for $J_{xx} = J_{zz}$ and $\epsilon_d = U = 0$. The figure is taken from Ref. [12].

eV and broken $U(1)$ symmetry result in a genuine non-equilibrium steady-state problem.

4.6.4 Competition Between V and $T_K^{\rm eq}$ as Relevant Low-Energy Scale

The low-temperature behavior of the backscattered conductance depends on the ratio $eV/T_K^{\rm eq}$. If $T_K^{\rm eq}$ is the largest low-energy scale, then G becomes zero for $T \to 0$ as the system approaches a strong coupling (SC) fixed point. A Kondo singlet forms and magnetic scattering is suppressed as the local spin decouples from the helical modes that constitutes the edge.

Fig. 4.6 (a) shows the conductance for five different coupling strengths J_{yy} for broken $U(1)$ symmetry and fixed bias $eV/\Gamma_0 = 0.01$. We recall that $T_K^{\rm eq}$ depends monotonic on J_{yy} and distinguish two different regimes: $eV < T_K^{\rm eq}$ if $J_{yy}/\Gamma_0 > 0.5$ and $T_K^{\rm eq} < eV$ if $J_{yy}/\Gamma_0 < 0.5$. In the former case, the SC fixed point is reached for $T < T_K^{\rm eq}$ and the above discussion hold. In the latter scenario,

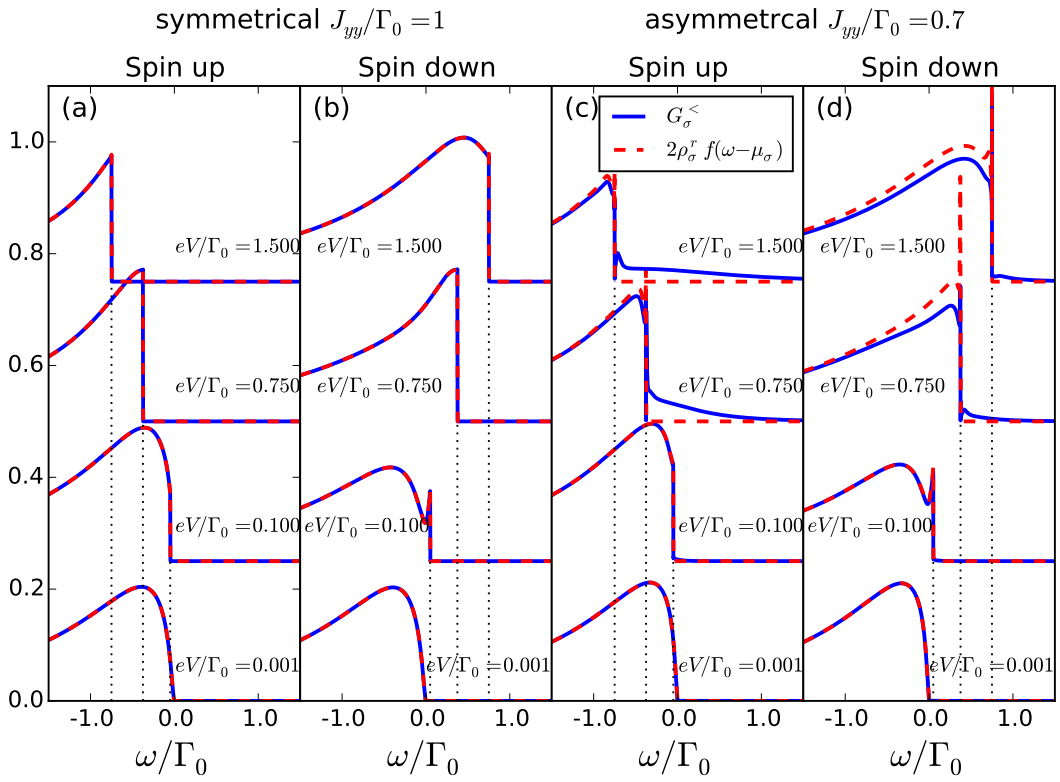

Figure 4.5: $G_\nu^<(\omega)$ (blue solid line) and $2\rho_\nu(\omega)f(\omega-\mu_\nu)$ for: retained $U(1)$ symmetry for spin (a) up and (b) down and broken $U(1)$ symmetry for spin (c) up and (d) down. The lines for different bias voltages are shifted by $a = 0.25$ for visibility. The legend applies to all plots. The figure is taken from Ref. [12].

eV is the largest low-energy scale. From a renormalization group point of view, the flow equations that drive the system towards the SC fixed point are cut-off by eV before T_K^{eq} is reached [12]. The system thus shows a finite backscattered conductance for $T < T_K^{\text{eq}}$ which depends on the ratio eV/T_K^{eq}. The larger eV compared to the Kondo temperature, the larger the residual conductance (cyan and magenta curves). The case $J_{yy}/\Gamma_0 = 0.5$ (red curve) is interesting since here $T_K^{\text{eq}} \approx eV$. The conductance vanishes almost but still shows a small finite residual G.

We make a power-law ansatz for the conductance below T_K^{eq}

$$T_K^{\text{eq}} G(T) = b(T/T_K^{\text{eq}})^\alpha + c \tag{4.6.14}$$

and fit the data presented in Fig. 4.6 (a). The resulting fits are shown in Fig. 4.6 (b). We find that the system behaves differently depending on eV/T_K^{eq}. In the case where the bias voltage is the largest low-energy scale, $\alpha \approx 1-1.5$. However, if the Kondo temperature exceeds eV, then $\alpha = 2$ as is expected for a Fermi liquid [35, 12]. The different exponents are depicted in Fig. 4.6 (c).

Next we focus on the voltage dependence of G in Fig. 4.7. Subplot (a) and (b) show the linear conductance and current for different exchange couplings. The

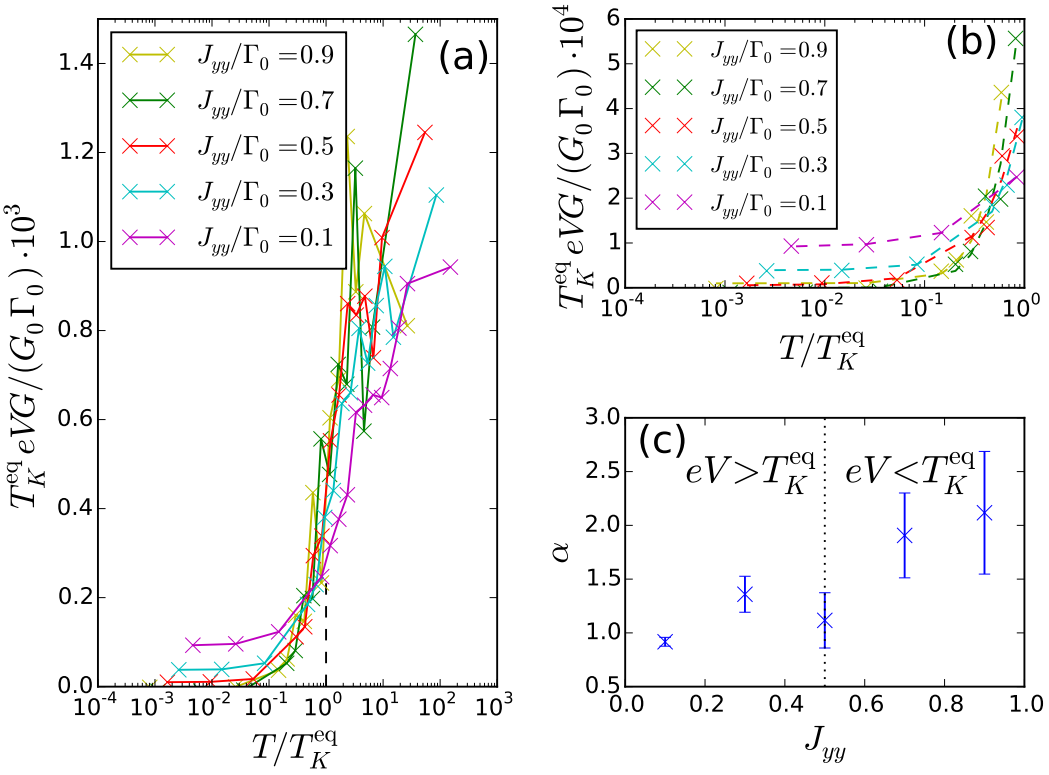

Figure 4.6: (a) Backscattered conductance $G(T)$ for $eV/\Gamma_0 = 0.01$ and different J_{yy}. The low-temperature behavior depends on the ratio $eV/T_K^{\mathrm{eq}}(J_{yy})$. (b) Power-law fits for $T < T_K^{\mathrm{eq}}$ according to Eq. (4.6.14). (c) Exponents α of the power-law fit in (b). $\alpha = 2$ if $T_K^{\mathrm{eq}} > eV$. The error bars are due to the numerical fitting process. The figure is taken from Ref. [12].

temperature is always much smaller than any other energy scale $T \ll T_K^{\mathrm{eq}}, eV$. For $eV < T_K^{\mathrm{eq}}$, the current vanishes as the SC fixed point dynamically restores perfect conductance. For $eV > T_K^{\mathrm{eq}}$, we have to distinguish between retained and broken $U(1)$ symmetry. At the symmetrical point, the conductance is independent of eV and $G = 0$ identical due to the fluctuations-dissipations theorem. Deviation from $U(1)$ symmetry, on the other hand, yields a finite conductance that grows proportional to $\ln(eV/T_K^{\mathrm{eq}})$. We make an ansatz

$$G/J_B = a_{\mathrm{slope}} \ln(eV/T_K^{\mathrm{eq}}) + b \tag{4.6.15}$$

where

$$J_B = \left[\frac{(|J_x|^2 - |J_y|^2)^2 + 4(J_x J_y)^2}{J_x^2 + J_y^2}\right]^{1/2} \tag{4.6.16}$$

is a measure for the anisotropy of the exchange interaction. The determined slopes for the logarithmic increase are shown in Fig. 4.7 (c). They are roughly constant in the $U(1)$ symmetry broken regime albeit the numerical error bars are relatively large.

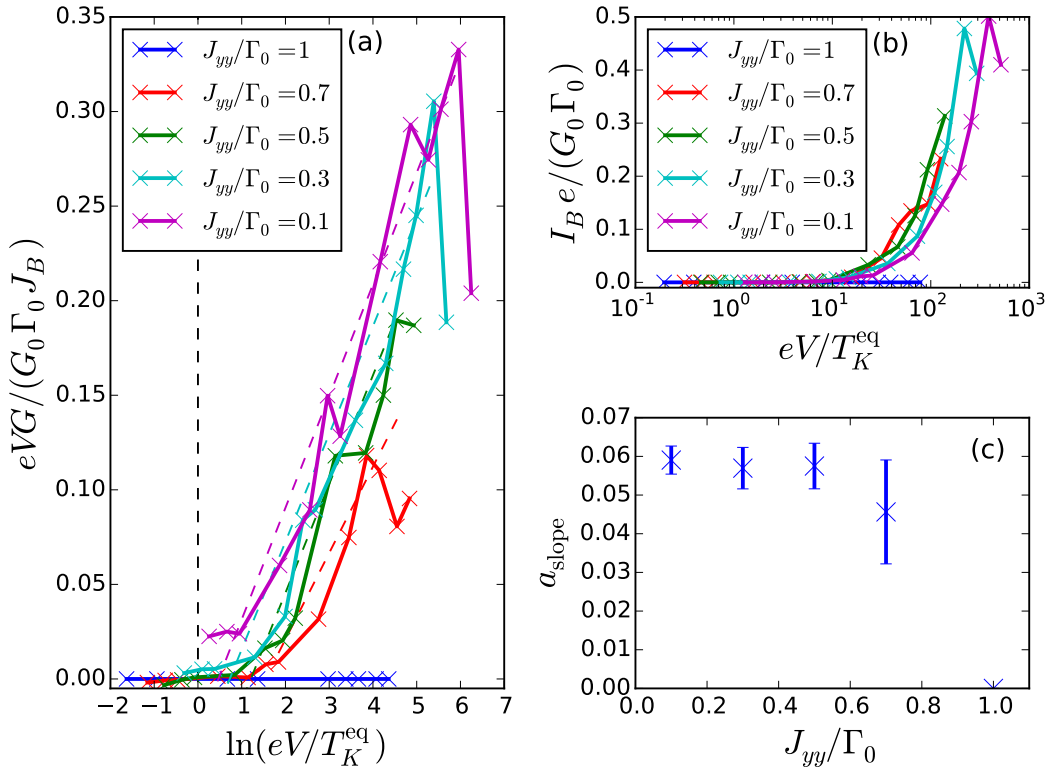

Figure 4.7: (a) G and (b) I_B as function of eV/T_K^{eq} and different J_{yy}. The black dashed line indicates $eV = T_K^{\mathrm{eq}}$. (c) Fitting parameter a_{slope} as determined from Eq. (4.6.15). The error bars stem from the numerical fitting procedure. The figure was taken from Ref. [12].

Lastly, we examine the conductive behavior as function of the anisotropy. We define a deviation from symmetrical coupling by

$$\Delta J_{yy} = J_{yy}^{\mathrm{f}} - J_{yy}^{\mathrm{i}}, \tag{4.6.17}$$

where $J_{yy}^{\mathrm{i}} = \Gamma_0$ stands for the initial value before the TDNRG quench. We recall that we quench from the symmetrical point $J_{xx}^{\mathrm{i}} = J_{yy}^{\mathrm{i}} = \Gamma_0$ to the final value J_{yy}^{f}. We drop the superscripts i and f again in the following. Fig. 4.8 shows the conductance as a function of this anisotropy measure.

The conductance vanishes at the symmetrical point $\Delta J_{yy} = 0$. The smaller the coupling after the quench the smaller the corresponding Kondo temperature. We lower J_{yy} until at some point $eV > T_K^{\mathrm{eq}}$ and a finite conductance sets in. The bias voltage takes over as the highest low-energy scale and the dynamical reconstruction of perfect conductance is interrupted. For large voltage $eV/\Gamma_0 = 0.5$, we do not see this switch between eV and T_K^{eq} and find a finite G for all $\Delta J_{yy} \neq 0$ as the Kondo temperature is the smallest energy scale regardless of J_{yy}. This residual conductance is asymmetric with regards to $\Delta J_{yy} = 0$ since the renormalization process is cut-off earlier for negative ΔJ_{yy}.

Note that we do find a finite conductance for $\Delta J_{yy} > 0$ for all other bias voltages as well. However, we attribute this conductance to numerical issues that occur in the calculation of G. First of all, the Green's functions are not calculated from the self-energy, as discussed in Sec. 2.3.1, due to the need for an equation of motion for the lesser GF. Secondly, we subtract two functions that are almost identical when evaluating Eq. (4.6.12). Thirdly, we must then perform numerical integration, and, lastly, we demand a precision of at least $O(eV)$ relevant digits in the end because we calculate $G = I_B/V$.

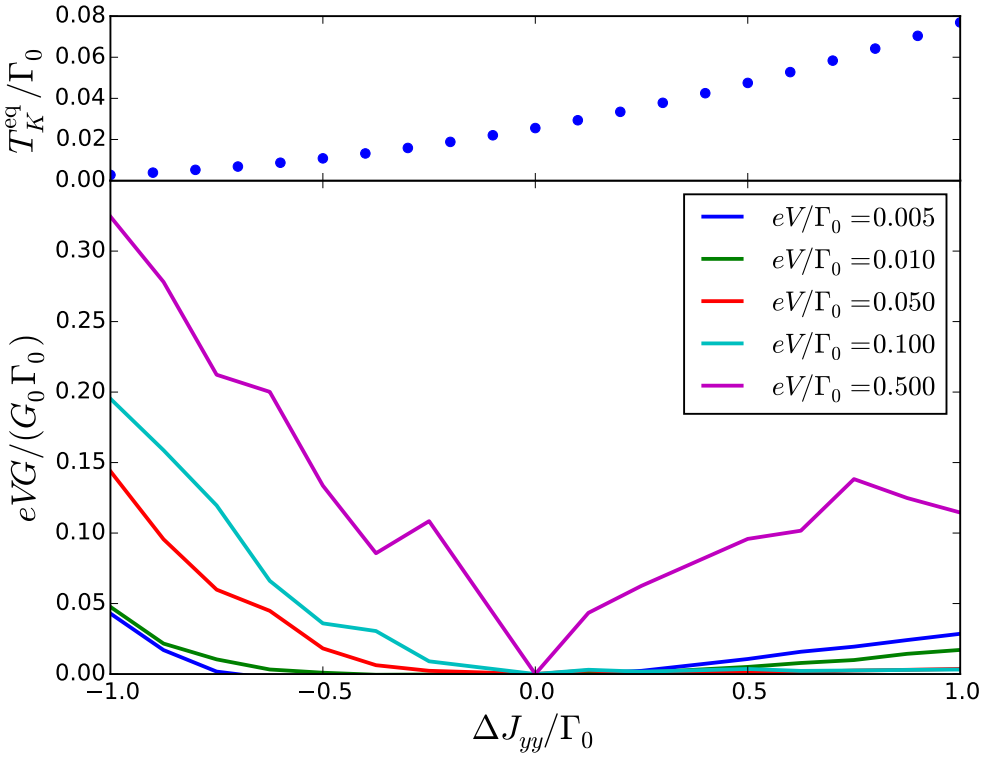

Figure 4.8: Conductance as function of anisotropy and for different bias voltages. The symmetrical point corresponds to $\Delta J_{yy} = 0$. Negative (positive) values mean quenching to smaller (higher) couplings. The upper subplot shows the equilibrium Kondo temperature for ΔJ_{yy}. The x axis applies to both plots. Taken from Ref. [12].

4.7 Novel Scattering-States NRG Based on Hershfield's Y Operator

In this section, we present our novel approach to steady-state transport. We adapt the Scattering-States NRG with the help of Hershfield's Y operator: instead of relying on the TDNRG algorithm to calculate the correct steady-state density matrix, and thus the Y operator indirectly, we can employ the representation of Y

in terms of the many-body eigenstates of H, Eq. (4.5.41), and calculate Y directly. We thus no longer need the TDNRG algorithm, including the two simultaneous calculations, for the density matrix. Before we lay down the algorithm, let us discuss the key idea behind this novel approach.

First, let us recall the functioning of the equilibrium NRG. We again use our single orbital coupled to a left and a right bath of non-interacting spin-full electrons as a tangible example. For now, consider only a single chemical potential μ for both bands with the same constant DOS. The system rests in equilibrium. Both bands are logarithmically discretized around the chemical potential. In the end, the chemical potential effectively results in a shift of the single particle energy, $\epsilon_d - \mu$. We thus calculate the eigenvalues of $H - \mu N$ during the NRG, which are then used for the truncation scheme each iteration.

The process above is not sufficient for a genuine steady-state problem since $H - Y$ governs the density matrix in this case. We cannot calculate the expectation values of any operator nor does the truncation scheme makes sense anymore. These problems have been circumvented by the use of the TDNRG to calculate the steady-state density matrix from the limit of long times, and thus Y only indirectly.

However, we want to remove the TDNRG completely from our new approach, and instead employ a NRG calculation directly for the steady-state. This complicates the algorithm because we then must manage two different matrices: the Hamiltonian H and the matrix $K = H - Y$. We need the eigenvalues of K for the steady-state expectation values of any operator, but the eigenvalues of H for the calculation of Y according to Eq. 4.5.41. Our new algorithm works by explicitly adding and subtracting Y in each NRG iteration. Since we need the eigenvalues of both, H and K, this comes with the cost of an additional matrix diagonalization each iteration.

We now add some detail. Fig. 4.9 shows a schematic flow diagram of the algorithm for a given NRG iteration n, and should be referred to for guidance in the following. The modified NRG iteration comprises the following steps:

(i) Calculate $Y_{0,n}$.

(ii) Calculate H_n.

(iii) Diagonalize H_n.

(iv) Calculate Y_n from the eigenvalues of H_n and knowledge of $Y_{0,n}$.

(v) Calculate K_n.

(vi) Diagonalize K_n. Rotate all local matrices into the eigenbasis of K_n and evaluate expectation values.

(vii) Calculate the Hamiltonian H_n^{rec} in the eigenbasis of K_n.

(viii) Pass on the truncated version of the Hamiltonian H_n^{trunc} as well as $Y_{0,n}$. Both are expressed in the eigenbasis of K_n.

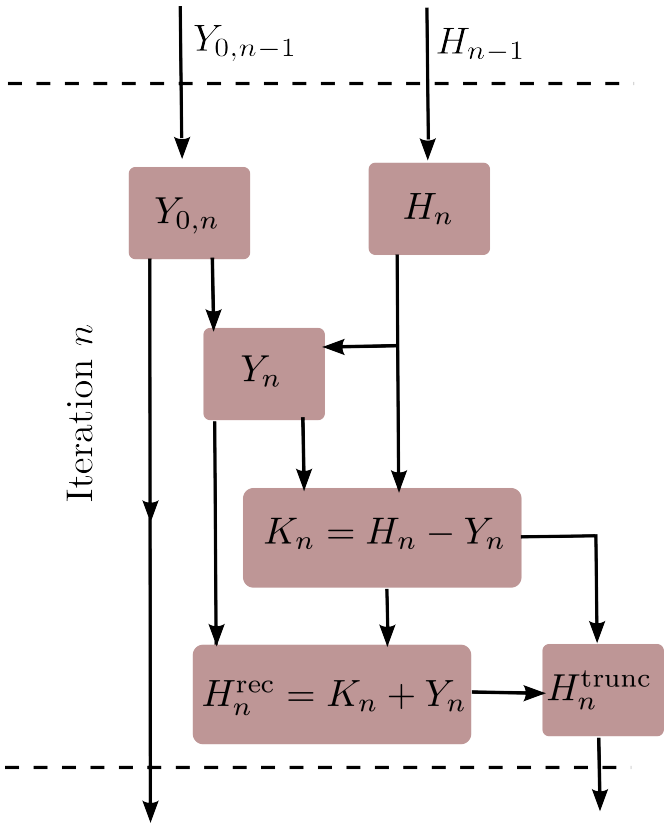

Figure 4.9: Schematic flow diagram for a NRG iteration n. The algorithm takes $Y_{0,n-1}$ and H_{n-1} as input from which one calculates (i) $Y_{0,n}$ and (ii) H_n first. After (iii) diagonalization of H_n one calculates (iv) Y_n which together with H_n yields (v) K_n. K_n is (vi) diagonalized as well. (vii) H_n^{rec} is reconstructed in the eigenbasis of K_n and its (viii) truncated representation is passed on as Hamiltonian together with $Y_{0,n}$ for the next iteration.

At any iteration n we begin by adding a new site to the Wilson chain and enlarging the Fockspace as usual. We now also need $Y_{0,n-1}$ from the prior iteration in addition to H_{n-1}. The new operator $Y_{0,n}$ is constructed analogous to H_n

$$Y_{0,n} = \sqrt{\Lambda} Y_{0,n-1} + \mu_{L,\text{eff}} n_L + \mu_{R,\text{eff}} n_R, \tag{4.7.1}$$

where n_α are the occupation number operators for the newly added chain site. The chemical potential $\mu_{\alpha,\text{eff}}$ has to be scaled appropriately by $\Lambda^{n/2}$ as it is the case for all energy scales. In the conventional NRG algorithm, all matrices are rotated into the eigenbasis of H_{n-1} before adding a new chain site. As a result only the eigenvalues of the old Hamiltonian are usually needed to calculate H_n. As we see shortly, the final basis of H_{n-1} at the end of iteration $n-1$ is in general not the eigenbasis of H_{n-1} and we pass on H_{n-1} in matrix form.

After we calculate H_n and $Y_{0,n}$, we diagonalize the Hamiltonian

$$H_n|h\rangle_n = E_h^n|h\rangle_n. \tag{4.7.2}$$

With the help of the rotation matrix $U_{0\to H}$ that translates from the original basis to the eigenbasis of H_n and the eigenenergies E_h^n, we construct Y_n in the eigenbasis of H_n. In general, Y_n will differ from $Y_{0,n}$ and not commute with H_n, i.e. it will not be diagonal in this basis. Furthermore, Y_n will have a complex part depending on η in Eq. (4.5.41) which we discuss later. From knowledge of Y_n and H_n we calculate $K_n = H_n - Y_n$. Note that K_n is hermitian but not necessary real. We diagonalize K_n:

$$K_n|k\rangle_n = E_k^n|k\rangle_n, \tag{4.7.3}$$

and rotate all matrices from the eigenbasis of H_n to the eigenbasis of K_n with $U_{H\to K}$ (or alternatively calculate the whole rotation matrix $U_{0\to K}$ and rotate just once). Now we have two sets of different eigenenergies: E_h^n and E_k^n. The second set is needed for our truncation scheme since the density operator $\rho \propto \exp\left[-\beta(H-Y)\right]$. We thus truncate according to E_k^n. The difference in truncation is visualized in Fig. 4.10.

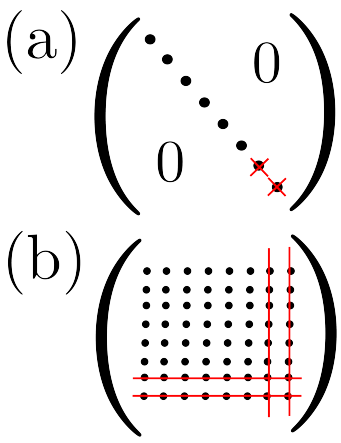

Figure 4.10: Schematic representation of truncation. (a) Conventional truncation algorithm where H_n is diagonal and only the l lowest eigenenergies are passed on to iteration $n+1$. (b) Truncation scheme when H_n is not diagonal. The whole matrix is passed on but only a sub-matrix is used. The rows and columns marked by the red line are neglected.

Since we truncate according to E_k^n, we need to reconstruct H_n in the eigenbasis of K_n by

$$H_n^{\text{rec}} = K_n + Y_n, \tag{4.7.4}$$

where K_n is diagonal and Y_n is rotated into the eigenbasis of K_n. Note that H_n^{rec} is in general complex and hermitian due to the imaginary part of Y_n. It is H_n^{rec} that is passed on to the next iteration $n+1$ to construct the Hamiltonian for the extended Wilson chain.

Before we discuss some of the results, we emphasize that this algorithm reduces to the conventional algorithm for a non-interacting problem, i.e. $H_U = 0$ but μ_α may be finite. Left- and right-moving particles do not couple and the problem is composed of two disjunct sub-problems. In this case, the chemical potential enters directly as a shift of the single particle energies. Y_n and $Y_{0,n}$ are the same regardless of η, and H_n and K_n are both diagonal simultaneously. The algorithm presented above is then a more complex, but exact, reformulation of two separate Wilson chains with their respective chemical potential.

4.8 Preliminary Results for the Y Operator Based Scattering NRG

We discuss some results for the NRG algorithm based on Hershfield's Y operator outlined above. We first look at the non-interacting problem and confirm the validity of our new approach in this limit. Then we focus on the first chain site in more detail. After this, we turn to the numerical calculation of Y and analyze the influence of the regulatory factor η. We show the level flow for different choices of η. Finally, we look at the limit $V \to 0$ where we study the current in the interacting case.

For the calculation of the current through the quantum level, we resort to a formula by Anders [189]. We sketch the idea here and only state the final result. The derivation uses the anti-symmetric form of the current operator [165, 190, 155]. It further relies on the gauge transformation for the scattering states mentioned in Sec. 4.5. The phase enters explicitly in the calculation and is used to express the current in terms of the local fermionic operators $d_{\sigma\alpha}$ [189]

$$\begin{aligned} I =& \frac{e}{h}\frac{V_L V_R \Gamma_0}{\overline{V}^2}\sum_\sigma \Big[2d^\dagger_{\sigma R}d_{\sigma R} - 2d^\dagger_{\sigma L}d_{\sigma L} \\ &+ \left(\frac{r_L}{r_R} - \frac{r_R}{r_L}\right) d^\dagger_{\sigma L}d_{\sigma R} + \left(\frac{r_L}{r_R} - \frac{r_R}{r_L}\right) d^\dagger_{\sigma R}d_{\sigma L}\Big], \end{aligned} \tag{4.8.1}$$

where $r_\alpha^2 = V_\alpha^2/(V_L^2 + V_R^2) = V_\alpha^2/\overline{V}^2$ is a dimensionless measure for the hybridization. For a symmetric coupling, the last two terms vanish and the current reduces to the difference between left- and right-moving electrons in the effective $d_{\sigma\alpha}$ orbitals. In the non-interacting case, this formula can be further simplified [189], and reduces to the known Landauer-Büttiker formula

$$\langle I\rangle = \frac{e}{h}\sum_\sigma \int_{-\infty}^{\infty} \left[f(\omega-\mu_R) - f(\omega-\mu_L)\right]\rho_d(\omega)\mathrm{d}\omega, \tag{4.8.2}$$

where

$$\rho_d(\omega) = \frac{1}{\pi}\frac{\Gamma_0}{(\omega-\epsilon_d)^2 + \Gamma_0^2}. \tag{4.8.3}$$

The spectral density is described by a Lorentz peak for the non-interacting d level.

We choose symmetric coupling $r_\alpha^2 = 1/2$, a non-interacting central orbital $U = 0$, and employ our NRG algorithm based on the Y operator. Without finite U, the problem reduces to two separate sub-problems for the left- and right-moving electrons for which we may define an additional quantum number α. The choice of η does not matter as Y contains just an energy shift by the chemical potential. We calculate the current Eq. (4.8.1) from the occupation numbers $n_{\sigma\alpha}$. The latter terms vanish due to the symmetric coupling. Fig. 4.11 shows the current compared to the analytic solution Eq. (4.8.2) for two different level positions ϵ_d. The NRG results and the analytic formula coincide perfectly for all voltages.

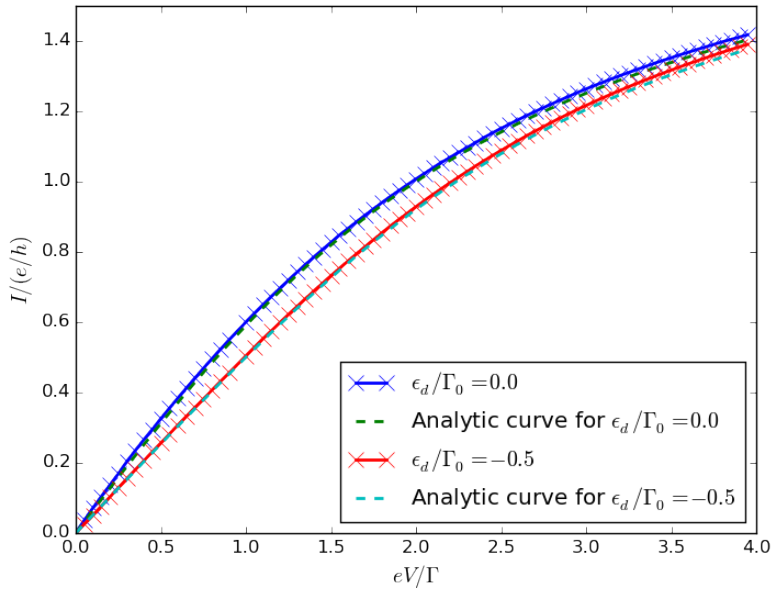

Figure 4.11: Current through single spin-full but non-interacting orbital as function of voltage for different level positions ϵ_d. The current is calculated via Eq. (4.8.1) from the Y operator based NRG algorithm. The dashed line represents a numerical evaluation of the exact formula (4.8.2). We used $\Lambda = 4$ and kept $N_s = 1500$ states for the NRG calculations.

4.8.1 Local Degrees of Freedom and Hartree Transformation

We now turn to the interacting problem. Before we study the whole chain Hamiltonian, let us focus on the local degrees of freedom alone. The initial physical Hamiltonian consists of a single spin-full orbital coupled to two bands. We performed a LS transformation and exploited the inverse transformation to express all local interaction terms via two orbitals, described by the fermionic operators $d_{\alpha\sigma}$. However, there is another orbital that is essentially decoupled from the impurity [165]. The anti-symmetric linear combination reads

$$\overline{d}_\sigma = r_R d_{L\sigma} - r_L d_{R\sigma} \tag{4.8.4}$$

compared to the inverse transformation for the d_σ operators, Eq. (4.5.16),

$$d_\sigma = r_R d_{R\sigma} + r_L d_{L\sigma}. \tag{4.8.5}$$

The anti-symmetric linear combination belongs to the bands and its single particle energy should remain at zero. In this section, we explicitly include both orbitals, d_σ and $\overline{d}_\sigma$, and compare the eigenspectrum of the different Hamiltonians for the initial Wilson site labeled by the subscript 0. The Hamiltonian for the physical d and itinerant $\overline{d}$ reads

$$H_{d\bar{d},0} = \sum_\sigma \epsilon_d d_\sigma^\dagger d_\sigma + \sum_\sigma \epsilon_{\overline{d}} \overline{d}_\sigma^\dagger \overline{d}_\sigma + U n_\uparrow^d n_\downarrow^d. \tag{4.8.6}$$

We compare this Hamiltonian to $H_{\mathrm{LS},0}$ for the first chain site after performing the LS transformation, i.e. the starting orbital for the SNRG algorithm

$$H_{\mathrm{LS},0} = \sum_{\sigma\alpha} \omega_0 d^\dagger_{\sigma\alpha} d_{\sigma\alpha} + U n^d_\uparrow n^d_\downarrow, \tag{4.8.7}$$

We recall that $\omega_0 \to \epsilon_d$ and that the occupation number needed for the Coulomb interaction must be expressed in the new degrees of freedom

$$n^d_\sigma = \sum_{\alpha\alpha'} r_\alpha r_{\alpha'} d^\dagger_{\sigma\alpha} d_{\sigma\alpha'}. \tag{4.8.8}$$

We assume particle-hole symmetric parameters for the d orbital and the same single particle energy $\epsilon_d = \epsilon_{\overline{d}} = \omega_0$. Table 4.1 lists the 16 eigenstates ordered by their energy. Note that the states are written in different bases and one has to translate from one to the other by inserting the above transformations Eq. (4.8.4) and (4.8.5). Both Hamiltonians are completely equivalent and the eigenstates can be readily obtained by a simple basis transformation. We stress, however, that this statement only holds if $\epsilon_d = \epsilon_{\overline{d}}$. The $\overline{d}$ orbital cannot be pinned to $\epsilon_{\overline{d}} = 0$ for any finite ϵ_d without breaking this equivalency.

			$H_{\mathrm{LS},0}$ Eq. (4.8.7)	$H_{d\overline{d},0}$ Eq. (4.8.6)
#	Q	S_z	$\lvert n_L, n_R\rangle$	$\lvert n_d, n_{\overline{d}}\rangle$
0	1	1/2	$2^{-1/2}(\lvert\uparrow,\uparrow\downarrow\rangle + \lvert\uparrow\downarrow,\uparrow\rangle)$	$\lvert\uparrow,\uparrow\downarrow\rangle$
1	1	-1/2	$2^{-1/2}(\lvert\downarrow,\uparrow\downarrow\rangle + \lvert\uparrow\downarrow,\downarrow\rangle)$	$\lvert\downarrow,\uparrow\downarrow\rangle$
2	2	0	$\lvert\uparrow\downarrow,\uparrow\downarrow\rangle$	$\lvert\uparrow\downarrow,\uparrow\downarrow\rangle$
3	0	0	...	$\lvert\downarrow,\uparrow\rangle$
4	0	0	...	$\lvert\uparrow,\downarrow\rangle$
5	0	0	...	$\lvert 0,\uparrow\downarrow\rangle$
6	0	1	$\lvert\uparrow,\uparrow\rangle$	$\lvert\uparrow,\uparrow\rangle$
7	0	-1	$\lvert\downarrow,\downarrow\rangle$	$\lvert\downarrow,\downarrow\rangle$
8	1	1/2	$2^{-1/2}(\lvert\uparrow,\uparrow\downarrow\rangle - \lvert\uparrow\downarrow,\uparrow\rangle)$	$\lvert\uparrow\downarrow,\uparrow\rangle$
9	1	-1/2	$2^{-1/2}(\lvert\downarrow,\uparrow\downarrow\rangle - \lvert\uparrow\downarrow,\downarrow\rangle)$	$\lvert\uparrow\downarrow,\downarrow\rangle$
10	-1	1/2	...	$\lvert\uparrow,0\rangle$
11	-1	1/2	...	$\lvert 0,\uparrow\rangle$
12	-1	-1/2	...	$\lvert\downarrow,0\rangle$
13	-1	-1/2	...	$\lvert 0,\downarrow\rangle$
14	0	0	...	$\lvert\uparrow\downarrow,0\rangle$
15	-2	0	$\lvert 0,0\rangle$	$\lvert 0,0\rangle$

Table 4.1: Eigenspectrum of the Hamiltonians in Eq. (4.8.6) and Eq. (4.8.7). The first column labels the states from lowest to highest eigenenergy, the second and third column lists their quantum numbers. Q is taken from half-filling. Column three and four list the eigenstates as linear combinations of the original occupation basis. Ellipsis indicate a lengthy linear combination that is omitted for visual clarity. The horizontal lines group energy degenerate states.

We now absorb the density term of the Coulomb interaction into the level position by performing a Hartree transformation (HT) [165, 13]

$$\begin{aligned}\widetilde{H}_{\mathrm{LS},0} &= \sum_{\sigma\alpha}\left(\omega_0+\frac{U}{2}\right)n_{\sigma\alpha}+\frac{U}{2}\left(\sum_{\sigma}n_\sigma-1\right)^2 \\ &= \sum_{\sigma\alpha}\left(\omega_0+\frac{U}{2}\right)d^\dagger_{\sigma\alpha}d_{\sigma\alpha}+Un^d_\uparrow n^d_\downarrow-\frac{U}{2}(n^d_\uparrow+n^d_\downarrow)+\frac{U}{2}.\end{aligned} \tag{4.8.9}$$

Note that the number operator in the last term must also be written in terms of the $d_{\alpha\sigma}$ operators with the help of Eq. (4.8.8).

Alternatively, one can apply the Hartree transformation to the Hamiltonian in Eq. (4.8.6). Only the d orbital is subject to the Coulomb interaction and therefore only the single particle position for the d electrons are shifted:

$$\widetilde{H}_{d\overline{d},0} = \sum_\sigma\Big(\epsilon_d+\frac{U}{2}\Big)d^\dagger_\sigma d_\sigma+\sum_\sigma\epsilon_{\overline{d}}\overline{d}^\dagger_\sigma\overline{d}_\sigma+\frac{U}{2}\Big(\sum_\sigma n^d_\sigma-1\Big)^2. \tag{4.8.10}$$

Diagonalization of the Hamiltonians (4.8.9) and (4.8.10) reveals two different eigenspectra. We can bring both spectra into line by shifting the $\overline{d}$ position in Eq. (4.8.10) as well, such that it also lies at zero energy in the particle-hole symmetric case. The modified Hamiltonian reads

$$\begin{aligned}\widetilde{H}'_{d\overline{d},0} &= \sum_\sigma\left(\epsilon_d+\frac{U}{2}\right)d^\dagger_\sigma d_\sigma+\sum_\sigma\left(\epsilon_{\overline{d}}+\frac{U}{2}\right)\overline{d}^\dagger_\sigma\overline{d}_\sigma+\frac{U}{2}\left(\sum_\sigma n^d_\sigma-1\right)^2 \\ &= \sum_\sigma\left(\epsilon_d+\frac{U}{2}\right)d^\dagger_\sigma d_\sigma+\sum_\sigma\left(\epsilon_{\overline{d}}+\frac{U}{2}\right)\overline{d}^\dagger_\sigma\overline{d}_\sigma+Un^d_\uparrow n^d_\downarrow-\frac{U}{2}\left(n^d_\uparrow+n^d_\downarrow\right)+\frac{U}{2}.\end{aligned} \tag{4.8.11}$$

The spectra of the modified Hamiltonian (4.8.11) and of the Hamiltonian (4.8.9) are shown in Tab. 4.2.

Without HTT, the Hamiltonian for the first chain site after LST is equivalent to the Hamiltonian for the physical orbital as long as we include the $\overline{d}$ orbital with $\epsilon_d = \epsilon_{\overline{d}}$. This means that the $\overline{d}$ orbital is not pinned to zero energy after LST.
When we perform HTT, then the $\overline{d}$ orbital rests at $\epsilon_{\overline{d}} + U/2$ which is zero for particle-hole parameters.
We remark that the HTT is irrelevant for $U = 0$. But even in this case, $\epsilon_d = \epsilon_{\overline{d}}$ in order for the spectra of the physical impurity including $\overline{d}$ orbital and first chain site Hamiltonian to be equal.

			$\widetilde{H}_{\mathrm{LS},0}$ Eq. (4.8.9)	$\widetilde{H}'_{d\bar{d},0}$ Eq. (4.8.11)
#	Q	S_z	$\lvert n_L, n_R\rangle$	$\lvert n_d, n_{\bar{d}}\rangle$
0	-1	-1	$2^{-1/2}(\lvert\downarrow,0\rangle + \lvert 0,\downarrow\rangle)$	$\lvert\downarrow,0\rangle$
1	-1	1	$2^{-1/2}(\lvert\uparrow,0\rangle + \lvert 0,\uparrow\rangle)$	$\lvert\uparrow,0\rangle$
2	1	-1	$2^{-1/2}(\lvert\uparrow\downarrow,\downarrow\rangle + \lvert\uparrow\downarrow,\downarrow\rangle)$	$\lvert\downarrow,\uparrow\downarrow\rangle$
3	1	1	$2^{-1/2}(\lvert\uparrow\downarrow,\uparrow\rangle + \lvert\uparrow\downarrow,\uparrow\rangle)$	$\lvert\uparrow,\uparrow\downarrow\rangle$
4	0	0	...	$\lvert\uparrow,\downarrow\rangle$
5	0	0	...	$\lvert\downarrow,\uparrow\rangle$
6	0	2	$\lvert\uparrow,\uparrow\rangle$	$\lvert\uparrow,\uparrow\rangle$
7	0	-2	$\lvert\downarrow,\downarrow\rangle$	$\lvert\downarrow,\downarrow\rangle$
8	1	1	$2^{-1/2}(\lvert\uparrow\downarrow,\uparrow\rangle - \lvert\uparrow\downarrow,\uparrow\rangle)$	$\lvert\uparrow\downarrow,\uparrow\rangle$
9	1	-1	$2^{-1/2}(\lvert\uparrow\downarrow,\downarrow\rangle - \lvert\uparrow\downarrow,\downarrow\rangle)$	$\lvert\uparrow\downarrow,\downarrow\rangle$
10	-1	1	$2^{-1/2}(\lvert\uparrow,0\rangle - \lvert 0,\uparrow\rangle)$	$\lvert 0,\uparrow\rangle$
11	-1	-1	$2^{-1/2}(\lvert\downarrow,0\rangle - \lvert 0,\downarrow\rangle)$	$\lvert 0,\downarrow\rangle$
12	2	0	$\lvert\uparrow\downarrow,\uparrow\downarrow\rangle$	$\lvert\uparrow\downarrow,\uparrow\downarrow\rangle$
13	0	0	...	$\lvert 0,\uparrow\downarrow\rangle$
14	0	0	...	$\lvert\uparrow\downarrow,0\rangle$
15	-2	0	$\lvert 0,0\rangle$	$\lvert 0,0\rangle$

Table 4.2: Eigenspectrum of the Hamiltonians in Eq. (4.8.11) and Eq. (4.8.9). The first column labels the states from lowest to highest eigenenergy, the second and third column lists their quantum numbers. Q is taken from half-filling. Column three and four list the eigenstates as linear combinations of the original occupation basis. Ellipsis indicate a lengthy linear combination that is omitted for visual clarity. The horizontal line group energy degenerate states.

4.8.2 Regulatory shift η and Numerical Calculation of Y

We recall that the numerical calculation of Y in Eq. (4.5.41) requires a complex regularization η. We repeat Eq. (4.5.41) for ease of reading

$$[Y]_{nm} = \frac{\mathrm{i}\eta}{E_m - E_n + \mathrm{i}\eta}[Y_0]_{nm}, \tag{4.8.12}$$

where n and m label all states in the respective sub-space and E_n are the corresponding eigenenergies. In the continuum limit, this shift $\eta \to 0$ and thus

$$\lim_{\eta\to 0} \frac{\mathrm{i}\eta}{E_m - E_n + \mathrm{i}\eta} = \delta_{E_m,E_n}. \tag{4.8.13}$$

However, it is not clear a priori how to choose η in a finite discrete system. Before we discuss different ways to adjust η, we analyze its effect on the calculation of Y and the level spectrum by examination of the first Wilson chain site.

We look at the Y-NRG algorithm outlined in Sec. 4.7 and focus on a single sub-space for the first chain site with quantum numbers $Q = 1$ and $S_z = -1/2$ where Q labels the total number of electrons with respect to half-filling and S_z the total spin component in z axis. This sub-space contains two states $\lvert\uparrow\downarrow,\downarrow\rangle$

and $|\downarrow,\uparrow\downarrow\rangle$ which are themselves product states $|n_L, n_R\rangle = |n_L\rangle \otimes |n_R\rangle$ describing the occupation of the $d_{\alpha\sigma}$ orbitals. We do not perform the Hartree transformation mentioned in Sec. 4.8.1 because the discussion here is indifferent to whether or not it is employed.

Let us first assume that $U = 0$ and ϵ_d and V are finite. The Hamiltonian is diagonal with two eigenenergies $E_{1,2} = \epsilon_d$. The matrix Y_0 is also diagonal in the same basis as H, which is simultaneously the eigenbasis of both matrices because $[H, Y_0] = 0$. Equivalently, one can define a preserved quantum number for left- and right-moving electrons. We then use Y_0 to calculate Y. In the case here, the value of η is irrelevant since either the fraction in Eq. (4.8.12) cancels out exactly or $[Y_0]_{nm} = 0$ for $n \neq m$ and, thus, $Y = Y_0$. Following the algorithm, we calculate $K = H - Y$, which is already diagonal and contains the eigenenergies of H shifted by μ.

This exemplifies how the non-interacting limit is recovered in our algorithm. We emphasize that the numerical value of η is irrelevant if $U = 0$. This trivially holds true if $eV = 0$ as well since then $Y = Y_0 = 0$ and $H = K$.

Next, we choose particle-hole symmetric parameters $U = -2\epsilon_d$ and finite eV. The Hamiltonian H is not-diagonal in the occupation basis $|n_L, n_R\rangle$ as U mixes left- and right-movers. Furthermore, Y_0 and Y are both not diagonal in the eigenbasis of H. In our particular sub-space, Y_0 is zero on the diagonal and has two symmetrical and real non-diagonal entries. Consequently, Y is also non-diagonal but with two complex non-diagonal elements such that Y is hermitian. The real and imaginary part both depend monotonous on the value of η. The difference $K = H - Y$ becomes complex as well with new eigenenergies that are different to those of H. However, this difference depends strongly on the ratio η/eV. If η is much smaller than eV, the effect is negligible and the eigenvalues are identical. If $\eta \gg eV$, the eigenvalues of K quickly stop changing. The influence of η on the eigenvalues is rather small even for large η and in the order of a few percent for the first iteration.

This makes up the second important point: the ratio η/eV is relevant when $U \neq 0$. If we, guided by the analytic relation for η, choose $\eta \ll eV$, we would end up with the same eigenenergies for the truncation as if $eV = 0$. We stress that it is unclear whether this effect has physical meaning or is an artifact of the algorithm. However, the influence on the eigenvalues in the first iteration is quite small and in the order of a few percent at most unless eV is unrealistic large.

4.8.3 Different Choices for η, Level Flow, and $V \to 0$

From the point of view of the numerical algorithm, the effect of η is to mix eigenstates of H that are (nearly) energetically degenerate. Following the regulatory argument, the factor in Eq. (4.8.12) reduces to a Kronecker δ_{E_m,E_n} in the limit $\eta \to 0$. A finite η broadens this δ peak slightly yielding finite non-diagonal matrix elements in Y. We discuss two different choices for η and look at the level flow.

We present results for finite voltage V and small voltages where the system is expected to show Fermi Liquid behavior.

First, we assume a constant η in each iteration, i.e. the same η in Eq. (4.8.12). Let ω_N be the energy scale of iteration N and $\eta_{\text{eff}} \propto \omega_N$. The label 'eff' implies that η is scaled by an appropriate factor $\sqrt{\Lambda}$ between successive iterations such that the value entering in Eq. (4.8.12) is the same each iteration. The proportionality factor can be adjusted freely. The line of reasoning is that η introduces a mixing of nearly degenerate states in the Y operator. If this mixing is large in each iteration, the difference between the eigenbasis of H and the eigenbasis of K is larger as well. Since we want to reach the steady-state governed by K, a larger rotation might facilitate this process.

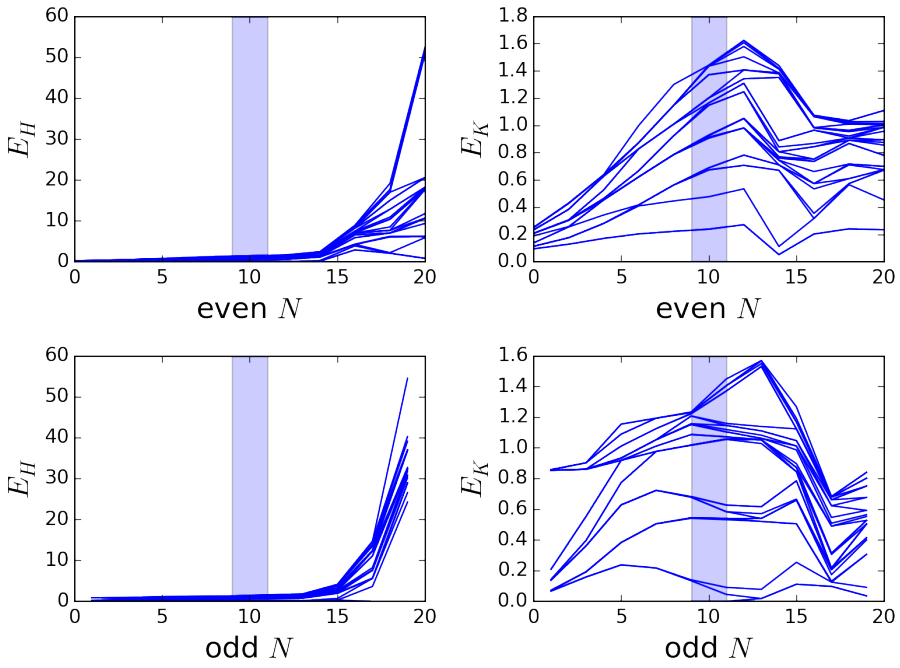

Figure 4.12: Level flow of the lowest 40 eigenenergies for H_N (left column) and $K_N = H_N - Y_N$ (right column). $\epsilon_d/\Gamma_0 = -2$, $U/\Gamma_0 = 4$, and $eV/\Gamma_0 = 0.1$. The complex shift $\eta_{\text{eff}} = \omega_N$. The shaded area indicates the iterations where $\mu_{\text{eff}} \sim T$. The number of retained states is $N_s = 1500$, NRG discretization parameter $\Lambda = 3$, and $D/\Gamma_0 = 40$.

Fig. 4.12 shows the lowest energy levels of H_N and $K_N = H_N - Y_N$ for $\epsilon_d/\Gamma_0 = -2, U/\Gamma_0 = 4, V/\Gamma_0 = 0.1$ and $\eta_{\text{eff}} = \omega_N$. We distinguish between the level flow for H_N and $K_N = H_N - Y_N$ (left and right column) as well as even and odd iterations N (top and bottom). The energies of H_N grow rapidly for later iterations since we add the scaled chemical potential $\mu_{\alpha,\text{eff}} = \mu_\alpha \Lambda^{N/2}$ to the Y operator. The spectrum of $K_N = H_N - Y_N$, on the other hand, shows a more conventional picture. However, we do not see that the system arrives close to any fixed point. Instead, the behavior for low temperature (high iterations) shows a rather erratic behavior.

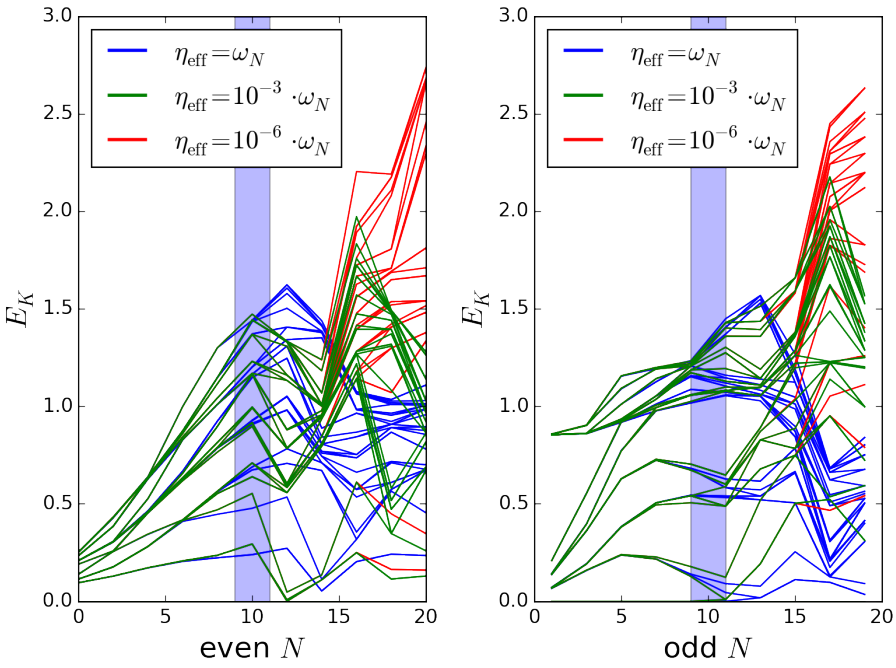

Figure 4.13: Level flow of the lowest 40 eigenenergies for $K_N = H_N - Y_N$ for even (left) and odd (right) iterations N for different η_{eff}. $e_d/\Gamma_0 = -2$, $U/\Gamma_0 = 4$, and $eV/\Gamma_0 = 0.1$. The shaded area indicates the iterations where $V_{\text{eff}} \sim T$. The number of retained states is $N_s = 1500$, NRG discretization parameter $\Lambda = 3$, and $D/\Gamma_0 = 40$.

This behavior is not limited to our choice of η_{eff}. Fig. 4.13 shows the level flow for K_N for different η_{eff}. Up until $\mu_{\text{eff}} \sim T_N$ (blue shaded area), all levels for different η_{eff} are converged and η_{eff} has no noticeable effect on the energies. This is in accordance to our discussion in Sec. 4.8.2. The effect on the eigenenergies is small for the first iterations regardless of η_{eff}. When we continue the algorithm and reach a temperature scale where $\mu_{\text{eff}} > T_N$, the choice of η_{eff} influences the eigenenergies drastically and the low temperature level flow differs significantly.

One can alternatively argue that $\eta \to 0$ on an absolute scale from the analytic considerations. The lowest energy scale in the NRG is given by the energy scale $\omega_{N_{\text{max}}}$ of the last iteration N_{max}. We choose $\eta = \omega_{N_{\text{max}}}$ and do not scale it for iterations $N < N_{\text{max}}$. This has the effect that η is small for the first iterations, but on the same scale as the eigenenergies of K_N in the last iteration. Note that we use the eigenvalues of H_N in Eq. (4.8.12) and that the difference ΔE_{nm} might still be orders of magnitude larger than η due to the growing eigenvalues of H_N.

Fig. 4.14 shows a comparison between the level flows for scaled $\eta_{\text{eff}} = \omega_N$ plotted in Fig. 4.12 and absolute $\eta = \omega_{N_{\text{max}}}$. We find that the level flow is almost converged until $\mu_{\text{eff}} \sim T_N$. The value of η does not matter from the perspective of the eigenenergies if $\mu_{\text{eff}} < T_N$. The low temperature behavior shows a comparable erratic behavior without any clear fixed point.

We now focus on the limit where $\mu_{\text{eff}} < T_N$. The discussion above indicates

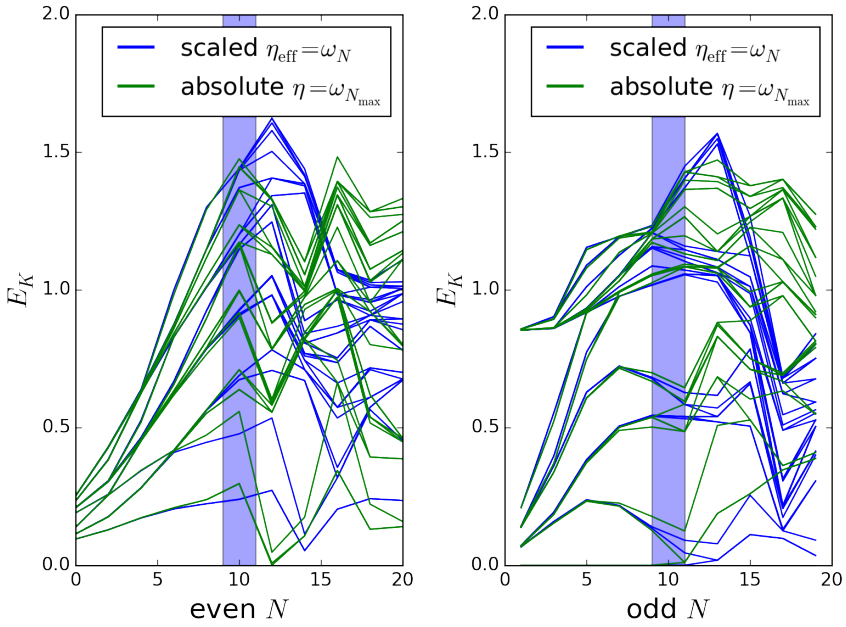

Figure 4.14: Level flow of the lowest 40 eigenenergies for $K_N = H_N - Y_N$ for even (left) and odd (right) iterations N for $\eta_{\text{eff}} = \omega_N$ (blue curves) and $\eta = \omega_{N_{\max}}$ (green curves). $e_d/\Gamma_0 = -2$, $U/\Gamma_0 = 4$, and $eV/\Gamma_0 = 0.1$. The shaded area indicates the iterations where $\mu_{\text{eff}} \sim T_N$. The number of retained states is $N_s = 1500$, NRG discretization parameter $\Lambda = 3$, and $D/\Gamma_0 = 40$.

that the choice of η is unimportant as long as $T_N \ll \mu_{\text{eff}}$. We keep the absolute $\eta = \omega_{N_{\max}}$ and compare the eigenenergies of K_N for $eV = 0$ and $eV/\Gamma_0 = 5 \cdot 10^{-5}$ in Fig. 4.15. There are only minor differences in both level flows. All levels are flat which indicates that the system reached its low-temperature fixed point.

We calculate the occupation numbers for the left- and right-moving many-body particles and evaluate Eq. (4.8.1) to determine the current through the quantum level. It is shown in Fig. 4.16. The current is linear with different slopes, and the larger U the flatter the slope. This kind of behavior would be expected in the Coulomb blockade regime where the repulsion between electrons in the intermediate nanoscale region hampers transport, and thus suppresses the current. In the extreme case, only a single electron can occupy the local orbital, and the question arises whether a description via scattering states is still valid in this limit. It is a promising sign that our approach seems to reproduce the Coulomb blockade behavior, at least qualitatively. Unfortunately, the current should exhibit a universal behavior in the limit $eV \to 0$, regardless of U. The system should reach the strong coupling fixed point, for which we expect a linear $I(eV)$ behavior with the same slope. As it stands now, our approach is not able to reproduce this behavior.

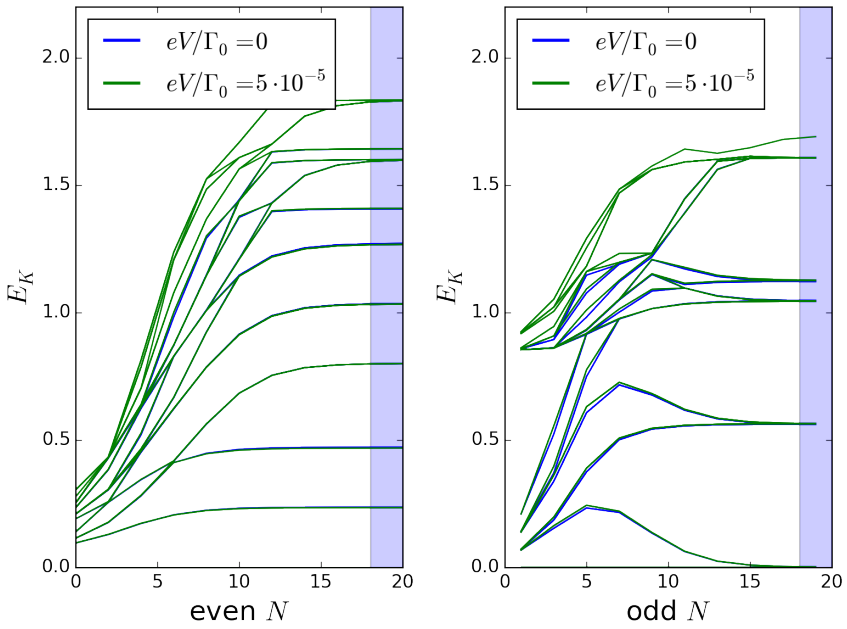

Figure 4.15: Level flow of the lowest 40 eigenenergies for $K_N = H_N - Y_N$ for even (left) and odd (right) iterations N for $eV = 0$ and $eV/\Gamma_0 = 5 \cdot 10^{-5}$. The levels are almost identical. The shaded area indicates where $\mu_{\text{eff}} \sim T_N$ for the finite $eV/\Gamma_0 = 5 \cdot 10^{-5}$. The number of retained states is $N_s = 1500$, NRG discretization parameter $\Lambda = 3$, and $D/\Gamma_0 = 40$.

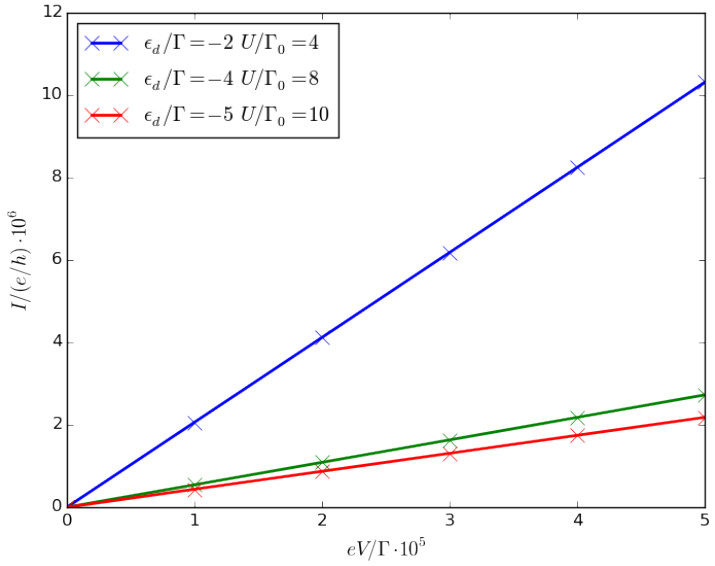

Figure 4.16: Current through the nano-junction after Eq. (4.8.1) as function of eV in the limit $eV \to 0$ for different particle hole symmetric parameters.

4.9 Conclusion of the Steady-State Transport Chapter

In the last chapter, we discussed steady-state transport through strongly correlated regions. We introduced the prime model for these systems that consists of two infinite large bands that are coupled to a single correlated quantum level. A finite external voltage drop induces a chemical potential difference and an unbalance between left- and right-moving quasi-particles. The Meir-Wingreen formula describes the electronic current through such a quantum level under the influence of a many-body interaction in terms of the non-equilibrium Green's functions. We introduced our numerical method of choice, the TDNRG, and the extension to steady-state transport problems, the Scattering States NRG, which relies on the TDNRG algorithm for calculating the correct steady-state density operator.

We successfully applied the SNRG in the context of electron transport along the edge of a QSHI under the influence of a quantum impurity. The 1d surface of a QSHI shows two counter-propagating electronic modes, called helical edge states, that couple propagation direction and spin orientation. Left- and right-moving particles are protected by a spin symmetry. If this symmetry is retained, the system can be mapped onto an effective equilibrium problem and backscattering at the quantum impurity vanishes. On the other hand, backscattering diminishes the perfect conductance if the spin symmetry is broken. The total S_z spin component is not conserved and incoming spin up electrons may scatter into outgoing spin down electrons at the impurity without limitation. However, one can dynamically restore perfect conductance if the equilibrium Kondo temperature is the highest low-energy scale. A Kondo singlet forms, magnetic scattering is suppressed, and perfect conductance is retained.

We then introduced a new approach to steady-state quantum impurity systems. We adopted the SNRG algorithm by directly calculating Hershfield's Y operator that enters in the steady-state density operator $\rho \sim \exp(-\beta[H - Y])$. We first tested our framework in the non-interacting and analytically solvable limit $U = 0$ for our toy-model where our results matched the expectations perfectly. We then focused on the regulatory factor η and its influence in our numerical algorithm. We discussed two different approaches: η was either taken to be constant on each energy shell separately or on an absolute scale. We found that the choice of η does not matter much if $T_N > \mu_{\text{eff}}$ where μ_{eff} is the appropriately scaled chemical potential. However, the level flow differs widely below $T_N \sim \mu_{\text{eff}}$. One cannot discern a fixed point from the energy spectrum of K_N. It is still unclear whether the level flow of K_N can even be meaningfully interpreted in terms of different fixed points. We finished with the limit $eV \to 0$ where the system is expected to show Fermi Liquid behavior for $T < T_K$. Here, the level flow is almost identical to $eV = 0$. The current is linear with eV but with different slopes for different particle-hole symmetric combinations of ϵ_d and U in contrast to expectations.

The TDNRG and its extension, the SNRG, are two powerful numerical meth-

ods for non-equilibrium quantum impurity systems as we have demonstrated in the case of helical spin transport. The adaptation to directly calculate the steady-state density operator from Hershfield's Y operator, that we proposed in this thesis, is still in the developmental stages. The non-interacting limit is already perfectly reproduced but multiple questions remain for $U \neq 0$ where calculations do not yield expected results. First of all, there is the nature of the $\overline{d}$ orbital, that has band character, and its level position. As it stands now, the orbital rests at the same energy as the physical d orbital. Next, we have the issue of the discretization of the Lippmann-Schwinger bands. The LS transformation is only well-defined for quasi-continuous bands. It is unclear whether there are additional pitfalls that were overlooked when attempting to discretize the LS continuum. Finally, a major problem is that the current does not show the expected universal behavior for small bias voltages. One reason may that the formula for the current might be missing additional contributions. Brief attempts to incorporate terms that stem from the imaginary part were not fruitful, yielded no change, and were abandoned.

In the end, non-equilibrium steady-state transport through quantum impurity systems for arbitrary parameter regimes remains an elusive problem. Our attempt for a Numerical Renormalization Group technique directly for the steady-state based on Hershfield's Y operator is not yet fully-fledged and needs further development beyond the scope of this work.

Chapter 5

Conclusion

We first looked at carbon impurities in graphene and their magnetic properties in Chapter 3, motivated by a recent STM study [9] that found two types of carbon vacancies distinguished by their characteristic experimental $\mathrm{d}I/\mathrm{d}V$ spectra. We developed a comprehensive picture for these different types of vacancies based on the effective two-orbital model by Cazalilla et al [116]. The method of choice for our numerical study was Wilson's Numerical Renormalization Group [10, 11]. The experimental results are perfectly described by assuming a variable hybridization strength that couples the carbon impurity and the π bands of graphene. We postulated that this variation in hybridization stems from the different curvature at the different vacancy sites [9, 19]. In the end, we were left with two free parameters: the chemical potential and this hybridization strength. We mapped the parameter space and analyzed the different regimes in detail. We compared our calculated Kondo temperatures to the experimental data and found very good qualitative agreement with just minor quantitative deviations.

We then turned to non-equilibrium systems with focus on steady-state transport under the influence of magnetic impurities. We employed the Scattering States Numerical Renormalization Group [13], an extension of the equilibrium NRG to steady-state problems, to study the conductive behavior of helical edge modes coupled via an anisotropic spin exchange to a localized impurity spin [12]. This setup was motivated by the helical edge modes that are present on the 1d surface of Quantum Spin Hall Insulators. We found that an anisotropic exchange interaction can lead to a finite backscattering current even though the spin interaction respects time-reversal symmetry. If the Kondo temperature is the dominant low energy scale, however, the perfect conductance is dynamically restored [12].
Finally, we presented our novel approach to steady-state transport based on the SNRG [13] and Hershfield's Y operator [15]. The goal is a NRG variant tailor-made for the steady-state in order to circumvent the need for time-evolution of the density-matrix in the conventional SNRG algorithm. Preliminary results are promising and the analytically solvable limit can be reproduced perfectly, but further work and development is needed for the interacting problem.

Bibliography

[1] Anderson, P. W. Localized Magnetic States in Metals. *Phys. Rev.* **124**, iss. 1, 1961: 41–53. DOI: 10.1103/PhysRev.124.41.

[2] Kondo, Jun. Resistance Minimum in Dilute Magnetic Alloys. *Progress of Theoretical Physics* **32**, no. 1, July 1964: 37–49. DOI: 10.1143/PTP.32.37. eprint: http://oup.prod.sis.lan/ptp/article-pdf/32/1/37/5193092/32-1-37.pdf.

[3] Žutić, Igor, Fabian, Jaroslav, and Das Sarma, S. Spintronics: Fundamentals and applications. *Rev. Mod. Phys.* **76**, iss. 2, 2004: 323–410. DOI: 10.1103/RevModPhys.76.323.

[4] Nair, R. R. et al. Dual origin of defect magnetism in graphene and its reversible switching by molecular doping. *Nature Communications* **4**, 2013: 2010 EP.

[5] Nair, R. R. et al. Spin-half paramagnetism in graphene induced by point defects. *Nat Phys* **8**, no. 3, 2012: 199–202. DOI: 10.1038/nphys2183.

[6] Chen, Jian-Hao et al. Tunable Kondo effect in graphene with defects. *Nat Phys* **7**, no. 7, 2011: 535–538. DOI: 10.1038/nphys1962.

[7] Wang, Yan et al. Room-Temperature Ferromagnetism of Graphene. *Nano Letters* **9**, no. 1, 2009: 220–224. DOI: 10.1021/nl802810g.

[8] Ugeda, M. M. et al. Missing Atom as a Source of Carbon Magnetism. *Phys. Rev. Lett.* **104**, iss. 9, 2010: 096804. DOI: 10.1103/PhysRevLett.104.096804.

[9] Jiang, Yuhang et al. Inducing Kondo screening of vacancy magnetic moments in graphene with gating and local curvature. *Nature Communications* **9**, no. 1, 2018: 2349. DOI: 10.1038/s41467-018-04812-6.

[10] Wilson, Kenneth G. The renormalization group: Critical phenomena and the Kondo problem. *Rev. Mod. Phys.* **47**, iss. 4, 1975: 773–840. DOI: 10.1103/RevModPhys.47.773.

[11] Bulla, Ralf, Costi, Theo A., and Pruschke, Thomas. Numerical renormalization group method for quantum impurity systems. *Rev. Mod. Phys.* **80**, iss. 2, 2008: 395–450. DOI: 10.1103/RevModPhys.80.395.

[12] Vinkler-Aviv, Yuval, May, Daniel, and Anders, Frithjof B. Analytical and Numerical study of the out-of-equilibrium current through a helical edge coupled to a magnetic impurity. 2019. arXiv: 1912.02838 [cond-mat.str-el].

[13] Anders, Frithjof B. Steady-State Currents through Nanodevices: A Scattering-States Numerical Renormalization-Group Approach to Open Quantum Systems. *Phys. Rev. Lett.* **101**, iss. 6, 2008: 066804. DOI: 10.1103/PhysRevLett.101.066804.

[14] Anders, Frithjof B. and Schiller, Avraham. Spin precession and real-time dynamics in the Kondo model: Time-dependent numerical renormalization-group study. *Phys. Rev. B* **74**, iss. 24, 2006: 245113. DOI: 10.1103/PhysRevB.74.245113.

[15] Hershfield, Selman. Reformulation of steady state nonequilibrium quantum statistical mechanics. *Phys. Rev. Lett.* **70**, iss. 14, 1993: 2134–2137. DOI: 10.1103/PhysRevLett.70.2134.

[16] Bulla, R, Pruschke, Th, and Hewson, A C. Anderson impurity in pseudo-gap Fermi systems. *Journal of Physics: Condensed Matter* **9**, no. 47, 1997: 10463–10474. DOI: 10.1088/0953-8984/9/47/014.

[17] Vojta, M., Fritz, L., and Bulla, R. Gate-controlled Kondo screening in graphene: Quantum criticality and electron-hole asymmetry. *EPL (Europhysics Letters)* **90**, no. 2, 2010: 27006.

[18] Ingersent, Kevin. Behavior of magnetic impurities in gapless Fermi systems. *Phys. Rev. B* **54**, iss. 17, 1996: 11936–11939. DOI: 10.1103/PhysRevB.54.11936.

[19] May, Daniel et al. Modeling of the gate-controlled Kondo effect at carbon point defects in graphene. *Phys. Rev. B* **97**, iss. 15, 2018: 155419. DOI: 10.1103/PhysRevB.97.155419.

[20] Bulla, Ralf, Tong, Ning-Hua, and Vojta, Matthias. Numerical Renormalization Group for Bosonic Systems and Application to the Sub-Ohmic Spin-Boson Model. *Phys. Rev. Lett.* **91**, iss. 17, 2003: 170601. DOI: 10.1103/PhysRevLett.91.170601.

[21] Bulla, Ralf et al. Numerical renormalization group for quantum impurities in a bosonic bath. *Phys. Rev. B* **71**, iss. 4, 2005: 045122. DOI: 10.1103/PhysRevB.71.045122.

[22] Hewson, A C and Meyer, D. Numerical renormalization group study of the Anderson-Holstein impurity model. *Journal of Physics: Condensed Matter* **14**, no. 3, 2001: 427–445. DOI: 10.1088/0953-8984/14/3/312.

[23] Meyer, D., Hewson, A. C., and Bulla, R. Gap Formation and Soft Phonon Mode in the Holstein Model. *Phys. Rev. Lett.* **89**, iss. 19, 2002: 196401. DOI: 10.1103/PhysRevLett.89.196401.

[24] Lechtenberg, Benedikt, Peters, Robert, and Kawakami, Norio. Interplay between charge, magnetic, and superconducting order in a Kondo lattice with attractive Hubbard interaction. *Phys. Rev. B* **98**, iss. 19, 2018: 195111. DOI: 10.1103/PhysRevB.98.195111.

[25] Nozières, Ph. and Blandin, A. Kondo effect in real metals. *J. Phys. France* **41**, no. 3, 1980: 193–211. DOI: 10.1051/jphys:01980004103019300.

[26] Jones, B. A. and Varma, C. M. Study of two magnetic impurities in a Fermi gas. *Phys. Rev. Lett.* **58**, iss. 9, 1987: 843–846. DOI: 10.1103/PhysRevLett.58.843.

[27] Ingersent, Kevin, Jones, Barbara A., and Wilkins, John W. Study of the two-impurity, two-channel Kondo Hamiltonian. *Phys. Rev. Lett.* **69**, iss. 17, 1992: 2594–2597. DOI: 10.1103/PhysRevLett.69.2594.

[28] Lechtenberg, Benedikt, Eickhoff, Fabian, and Anders, Frithjof B. Realistic quantum critical point in one-dimensional two-impurity models. *Phys. Rev. B* **96**, iss. 4, 2017: 041109. DOI: 10.1103/PhysRevB.96.041109.

[29] Lechtenberg, Benedikt and Anders, Frithjof B. Equilibrium and real-time properties of the spin correlation function in the two-impurity Kondo model. *Phys. Rev. B* **98**, iss. 3, 2018: 035109. DOI: 10.1103/PhysRevB.98.035109.

[30] Eickhoff, Fabian, Lechtenberg, Benedikt, and Anders, Frithjof B. Effective low-energy description of the two-impurity Anderson model: RKKY interaction and quantum criticality. *Phys. Rev. B* **98**, iss. 11, 2018: 115103. DOI: 10.1103/PhysRevB.98.115103.

[31] Anderson, P W. A poor man's derivation of scaling laws for the Kondo problem. *Journal of Physics C: Solid State Physics* **3**, no. 12, 1970: 2436–2441. DOI: 10.1088/0022-3719/3/12/008.

[32] Haas, W.J. de, Boer, J. de, and Berg, G.J. Van Den. The electrical resistance of gold, copper and lead at low temperatures. *Physica* **1**, no. 7, 1934: 1115 –1124. DOI: https://doi.org/10.1016/S0031-8914(34)80310-2.

[33] Haas, W.J. De and Berg, G.J. Van Den. The electrical resistance of gold and silver at low temperatures. *Physica* **3**, no. 6, 1936: 440 –449. DOI: https://doi.org/10.1016/S0031-8914(36)80009-3.

[34] Kasuya, Tadao. A Theory of Metallic Ferro- and Antiferromagnetism on Zener's Model. *Progress of Theoretical Physics* **16**, no. 1, July 1956: 45–57. DOI: 10.1143/PTP.16.45. eprint: http://oup.prod.sis.lan/ptp/article-pdf/16/1/45/5266722/16-1-45.pdf.

[35] Hewson, Alexander Cyril. The Kondo Problem to Heavy Fermions. Cambridge Studies in Magnetism. Cambridge University Press, 1993. DOI: 10.1017/CBO9780511470752.

[36] Barzykin, Victor and Affleck, Ian. Screening cloud in the k-channel Kondo model: Perturbative and large-k results. *Phys. Rev. B* **57**, iss. 1, 1998: 432–448. DOI: 10.1103/PhysRevB.57.432.

[37] Affleck, Ian and Simon, Pascal. Detecting the Kondo Screening Cloud Around a Quantum Dot. *Phys. Rev. Lett.* **86**, iss. 13, 2001: 2854–2857. DOI: 10.1103/PhysRevLett.86.2854.

[38] Sørensen, Erik S. and Affleck, Ian. Kondo Screening Cloud Around a Quantum Dot: Large-Scale Numerical Results. *Phys. Rev. Lett.* **94**, iss. 8, 2005: 086601. DOI: 10.1103/PhysRevLett.94.086601.

[39] Pavarini, Eva et al., eds. The LDA+DMFT approach to strongly correlated materials. Verlag des Forschungszentrum Jülich, 2011.

[40] Pavarini, Eva, Koch, Erik, and Zhang, Shiwei, eds. Many-Body Methods for Real Materials. Verlag des Forschungszentrum Jülich, 2019.

[41] Schrieffer, J. R. and Wolff, P. A. Relation between the Anderson and Kondo Hamiltonians. *Phys. Rev.* **149**, iss. 2, 1966: 491–492. DOI: 10.1103/PhysRev.149.491.

[42] Krishna-murthy, H. R., Wilkins, J. W., and Wilson, K. G. Renormalization-group approach to the Anderson model of dilute magnetic alloys. I. Static properties for the symmetric case. *Phys. Rev. B* **21**, iss. 3, 1980: 1003–1043. DOI: 10.1103/PhysRevB.21.1003.

[43] Krishna-murthy, H. R., Wilkins, J. W., and Wilson, K. G. Renormalization-group approach to the Anderson model of dilute magnetic alloys. II. Static properties for the asymmetric case. *Phys. Rev. B* **21**, iss. 3, 1980: 1044–1083. DOI: 10.1103/PhysRevB.21.1044.

[44] Anders, Frithjof B. and Schiller, Avraham. Real-Time Dynamics in Quantum-Impurity Systems: A Time-Dependent Numerical Renormalization-Group Approach. *Phys. Rev. Lett.* **95**, iss. 19, 2005: 196801. DOI: 10.1103/PhysRevLett.95.196801.

[45] Peters, Robert, Pruschke, Thomas, and Anders, Frithjof B. Numerical renormalization group approach to Green's functions for quantum impurity models. *Phys. Rev. B* **74**, iss. 24, 2006: 245114. DOI: 10.1103/PhysRevB.74.245114.

[46] Weichselbaum, Andreas and Delft, Jan von. Sum-Rule Conserving Spectral Functions from the Numerical Renormalization Group. *Phys. Rev. Lett.* **99**, iss. 7, 2007: 076402. DOI: 10.1103/PhysRevLett.99.076402.

[47] Anders, Frithjof B. A numerical renormalization group approach to non-equilibrium Green functions for quantum impurity models. *Journal of Physics: Condensed Matter* **20**, no. 19, 2008: 195216. DOI: 10.1088/0953-8984/20/19/195216.

[48] Bulla, R, Hewson, A C, and Pruschke, Th. Numerical renormalization group calculations for the self-energy of the impurity Anderson model. *Journal of Physics: Condensed Matter* **10**, no. 37, 1998: 8365.

[49] Bulla, R., Costi, T. A., and Vollhardt, D. Finite-temperature numerical renormalization group study of the Mott transition. *Phys. Rev. B* **64**, iss. 4, 2001: 045103. DOI: 10.1103/PhysRevB.64.045103.

[50] Hofstetter, Walter. Generalized Numerical Renormalization Group for Dynamical Quantities. *Phys. Rev. Lett.* **85**, iss. 7, 2000: 1508–1511. DOI: 10.1103/PhysRevLett.85.1508.

[51] Costi, T. A. Renormalization-group approach to nonequilibrium Green functions in correlated impurity systems. *Phys. Rev. B* **55**, iss. 5, 1997: 3003–3009. DOI: 10.1103/PhysRevB.55.3003.

[52] Costi, T A, Hewson, A C, and Zlatic, V. Transport coefficients of the Anderson model via the numerical renormalization group. *Journal of Physics: Condensed Matter* **6**, no. 13, 1994: 2519–2558. DOI: 10.1088/0953-8984/6/13/013.

[53] Sakai, Osamu, Shimizu, Yukihiro, and Kasuya, Tadao. Single-Particle and Magnetic Excitation Spectra of Degenerate Anderson Model with Finite f–f Coulomb Interaction. *Journal of the Physical Society of Japan* **58**, no. 10, 1989: 3666–3678. DOI: 10.1143/JPSJ.58.3666. eprint: https://doi.org/10.1143/JPSJ.58.3666.

[54] Fano, U. Effects of Configuration Interaction on Intensities and Phase Shifts. *Phys. Rev.* **124**, iss. 6, 1961: 1866–1878. DOI: 10.1103/PhysRev.124.1866.

[55] Goldhaber-Gordon, D. et al. From the Kondo Regime to the Mixed-Valence Regime in a Single-Electron Transistor. *Phys. Rev. Lett.* **81**, iss. 23, 1998: 5225–5228. DOI: 10.1103/PhysRevLett.81.5225.

[56] Güttge, Fabian et al. Hybrid NRG-DMRG approach to real-time dynamics of quantum impurity systems. *Phys. Rev. B* **87**, iss. 11, 2013: 115115. DOI: 10.1103/PhysRevB.87.115115.

[57] Schwarz, F. et al. Nonequilibrium Steady-State Transport in Quantum Impurity Models: A Thermofield and Quantum Quench Approach Using Matrix Product States. *Phys. Rev. Lett.* **121**, iss. 13, 2018: 137702. DOI: 10.1103/PhysRevLett.121.137702.

[58] White, Steven R. Density matrix formulation for quantum renormalization groups. *Phys. Rev. Lett.* **69**, iss. 19, 1992: 2863–2866. DOI: 10.1103/PhysRevLett.69.2863.

[59] Stadler, K. M. et al. Interleaved numerical renormalization group as an efficient multiband impurity solver. *Phys. Rev. B* **93**, iss. 23, 2016: 235101. DOI: 10.1103/PhysRevB.93.235101.

[60] Bunch, J. Scott et al. Electromechanical Resonators from Graphene Sheets. *Science* **315**, no. 5811, 2007: 490–493. DOI: 10.1126/science.1136836. eprint: https://science.sciencemag.org/content/315/5811/490.full.pdf.

[61] Lee, Changgu et al. Measurement of the Elastic Properties and Intrinsic Strength of Monolayer Graphene. *Science* **321**, no. 5887, 2008: 385–388. DOI: 10.1126/science.1157996. eprint: https://science.sciencemag.org/content/321/5887/385.full.pdf.

[62] Bunch, J. Scott et al. Impermeable Atomic Membranes from Graphene Sheets. *Nano Letters* **8**, no. 8, 2008. PMID: 18630972: 2458–2462. DOI: 10.1021/nl801457b. eprint: https://doi.org/10.1021/nl801457b.

[63] Balandin, Alexander A. et al. Superior Thermal Conductivity of Single-Layer Graphene. *Nano Letters* **8**, no. 3, 2008. PMID: 18284217: 902–907. DOI: 10.1021/nl0731872. eprint: https://doi.org/10.1021/nl0731872.

[64] Sun, Zhengzong et al. Growth of graphene from solid carbon sources. *Nature* **468**, 2010: 549 EP.

[65] Ando, Tsuneya, Zheng, Yisong, and Suzuura, Hidekatsu. Dynamical Conductivity and Zero-Mode Anomaly in Honeycomb Lattices. *Journal of the Physical Society of Japan* **71**, no. 5, 2002: 1318–1324. DOI: 10.1143/JPSJ.71.1318. eprint: https://doi.org/10.1143/JPSJ.71.1318.

[66] Gusynin, V. P., Sharapov, S. G., and Carbotte, J. P. Unusual Microwave Response of Dirac Quasiparticles in Graphene. *Phys. Rev. Lett.* **96**, iss. 25, 2006: 256802. DOI: 10.1103/PhysRevLett.96.256802.

[67] Andrei, Eva Y, Li, Guohong, and Du, Xu. Electronic properties of graphene: a perspective from scanning tunneling microscopy and magnetotransport. *Reports on Progress in Physics* **75**, no. 5, 2012: 056501. DOI: 10.1088/0034-4885/75/5/056501.

[68] Wallace, P. R. The Band Theory of Graphite. *Phys. Rev.* **71**, iss. 9, 1947: 622–634. DOI: 10.1103/PhysRev.71.622.

[69] McClure, J. W. Band Structure of Graphite and de Haas-van Alphen Effect. *Phys. Rev.* **108**, iss. 3, 1957: 612–618. DOI: 10.1103/PhysRev.108.612.

[70] Slonczewski, J. C. and Weiss, P. R. Band Structure of Graphite. *Phys. Rev.* **109**, iss. 2, 1958: 272–279. DOI: 10.1103/PhysRev.109.272.

[71] Semenoff, Gordon W. Condensed-Matter Simulation of a Three-Dimensional Anomaly. *Phys. Rev. Lett.* **53**, iss. 26, 1984: 2449–2452. DOI: 10.1103/PhysRevLett.53.2449.

[72] Ajiki, Hiroshi and Ando, Tsuneya. Electronic States of Carbon Nanotubes. *Journal of the Physical Society of Japan* **62**, no. 4, 1993: 1255–1266. DOI: 10.1143/JPSJ.62.1255. eprint: https://doi.org/10.1143/JPSJ.62.1255.

[73] Haldane, F. D. M. Model for a Quantum Hall Effect without Landau Levels: Condensed-Matter Realization of the "Parity Anomaly". *Phys. Rev. Lett.* **61**, iss. 18, 1988: 2015–2018. DOI: 10.1103/PhysRevLett.61.2015.

[74] Novoselov, K. S. et al. Two-dimensional gas of massless Dirac fermions in graphene. *Nature* **438**, no. 7065, 2005: 197–200. DOI: 10.1038/nature04233.

[75] Zhang, Yuanbo et al. Experimental observation of the quantum Hall effect and Berry's phase in graphene. *Nature* **438**, no. 7065, 2005: 201–204. DOI: 10.1038/nature04235.

[76] Kane, C. L. and Mele, E. J. Quantum Spin Hall Effect in Graphene. *Phys. Rev. Lett.* **95**, iss. 22, 2005: 226801. DOI: 10.1103/PhysRevLett.95.226801.

[77] Kane, C. L. and Mele, E. J. Z_2 Topological Order and the Quantum Spin Hall Effect. *Phys. Rev. Lett.* **95**, iss. 14, 2005: 146802. DOI: 10.1103/PhysRevLett.95.146802.

[78] Neto, Antonio Castro, Guinea, Francisco, and Peres, Nuno Miguel. Drawing conclusions from graphene. *Physics World* **19**, no. 11, 2006: 33–37. DOI: 10.1088/2058-7058/19/11/34.

[79] Katsnelson, M. I., Novoselov, K. S., and Geim, A. K. Chiral tunnelling and the Klein paradox in?graphene. *Nature Physics* **2**, no. 9, 2006: 620–625. DOI: 10.1038/nphys384.

[80] Katsnelson, M.I. and Novoselov, K.S. Graphene: New bridge between condensed matter physics and quantum electrodynamics. *Solid State Communications* **143**, no. 1, 2007. Exploring graphene: 3 –13. DOI: https://doi.org/10.1016/j.ssc.2007.02.043.

[81] Castro Neto, A. H. et al. The electronic properties of graphene. *Rev. Mod. Phys.* **81**, iss. 1, 2009: 109–162. DOI: 10.1103/RevModPhys.81.109.

[82] Meyer, Jannik C. et al. The structure of suspended graphene sheets. *Nature* **446**, 2007: 60 EP –.

[83] Fujita, Mitsutaka et al. Peculiar Localized State at Zigzag Graphite Edge. *Journal of the Physical Society of Japan* **65**, no. 7, 1996: 1920–1923. DOI: 10.1143/JPSJ.65.1920. eprint: https://doi.org/10.1143/JPSJ.65.1920.

[84] Nakada, Kyoko et al. Edge state in graphene ribbons: Nanometer size effect and edge shape dependence. *Phys. Rev. B* **54**, iss. 24, 1996: 17954–17961. DOI: 10.1103/PhysRevB.54.17954.

[85] Wakabayashi, Katsunori et al. Electronic and magnetic properties of nanographite ribbons. *Phys. Rev. B* **59**, iss. 12, 1999: 8271–8282. DOI: 10.1103/PhysRevB.59.8271.

[86] Peres, N. M. R., Castro Neto, A. H., and Guinea, F. Conductance quantization in mesoscopic graphene. *Phys. Rev. B* **73**, iss. 19, 2006: 195411. DOI: 10.1103/PhysRevB.73.195411.

[87] Akhmerov, A. R. and Beenakker, C. W. J. Boundary conditions for Dirac fermions on a terminated honeycomb lattice. *Phys. Rev. B* **77**, iss. 8, 2008: 085423. DOI: 10.1103/PhysRevB.77.085423.

[88] Mermin, N. D. and Wagner, H. Absence of Ferromagnetism or Antiferromagnetism in One- or Two-Dimensional Isotropic Heisenberg Models. *Phys. Rev. Lett.* **17**, iss. 22, 1966: 1133–1136. DOI: 10.1103/PhysRevLett.17.1133.

[89] Novoselov, K. S. et al. Electric Field Effect in Atomically Thin Carbon Films. *Science* **306**, no. 5696, 2004: 666–669. DOI: 10.1126/science.1102896. eprint: https://science.sciencemag.org/content/306/5696/666.full.pdf.

[90] Novoselov, K. S. et al. Two-dimensional atomic crystals. *Proceedings of the National Academy of Sciences* **102**, no. 30, 2005: 10451–10453. DOI: 10.1073/pnas.0502848102. eprint: https://www.pnas.org/content/102/30/10451.full.pdf.

[91] Mattevi, Cecilia, Kim, Hokwon, and Chhowalla, Manish. A review of chemical vapour deposition of graphene on copper. *J. Mater. Chem.* **21**, iss. 10, 2011: 3324–3334. DOI: 10.1039/C0JM02126A.

[92] Bommel, A.J. Van, Crombeen, J.E., and Tooren, A. Van. LEED and Auger electron observations of the SiC(0001) surface. *Surface Science* **48**, no. 2, 1975: 463 –472. DOI: https://doi.org/10.1016/0039-6028(75)90419-7.

[93] Forbeaux, I., Themlin, J.-M., and Debever, J.-M. Heteroepitaxial graphite on $6H-$SiC(0001) : Interface formation through conduction-band electronic structure. *Phys. Rev. B* **58**, iss. 24, 1998: 16396–16406. DOI: 10.1103/PhysRevB.58.16396.

[94] Charrier, A. et al. Solid-state decomposition of silicon carbide for growing ultra-thin heteroepitaxial graphite films. *Journal of Applied Physics* **92**, no. 5, 2002: 2479–2484. DOI: 10.1063/1.1498962. eprint: https://doi.org/10.1063/1.1498962.

[95] Memon, Nasir K. et al. Flame synthesis of graphene films in open environments. *Carbon* **49**, no. 15, 2011: 5064 –5070. DOI: https://doi.org/10.1016/j.carbon.2011.07.024.

[96] Hernandez, Yenny et al. High-yield production of graphene by liquid-phase exfoliation of graphite. *Nature Nanotechnology* **3**, 2008. Article: 563 EP –.

[97] Park, Sungjin and Ruoff, Rodney S. Chemical methods for the production of graphenes. *Nature Nanotechnology* **4**, 2009. Review Article: 217 EP –.

[98] Andreoni, Wanda. The Physics of Fullerene-Based and Fullerene-Related Materials. Springer, 2000. DOI: 10.1007/978-94-011-4038-6.

[99] Saito, R., Dresselhaus, G., and S., Dresselhaus M. Physical Properties of Carbon Nanotubes. Imperial College Press, 1998.

[100] Charlier, Jean-Christophe, Blase, Xavier, and Roche, Stephan. Electronic and transport properties of nanotubes. *Rev. Mod. Phys.* **79**, iss. 2, 2007: 677–732. DOI: 10.1103/RevModPhys.79.677.

[101] Hobson, J. P. and Nierenberg, W. A. The Statistics of a Two-Dimensional, Hexagonal Net. *Phys. Rev.* **89**, iss. 3, 1953: 662–662. DOI: 10.1103/PhysRev.89.662.

[102] Reich, S. and Maultzsch, J. and Thomsen, C. and Ordejón, P. Tight-binding description of graphene. *Phys. Rev. B* **66**, iss. 3, 2002: 035412. DOI: 10.1103/PhysRevB.66.035412.

[103] Nanda, B. R. K. and Satpathy, S. Strain and electric field modulation of the electronic structure of bilayer graphene. *Phys. Rev. B* **80**, iss. 16, 2009: 165430. DOI: 10.1103/PhysRevB.80.165430.

[104] Sepioni, M. et al. Limits on Intrinsic Magnetism in Graphene. *Phys. Rev. Lett.* **105**, iss. 20, 2010: 207205. DOI: 10.1103/PhysRevLett.105.207205.

[105] Cervenka, J., Katsnelson, M. I., and Flipse, C. F. J. Room-temperature ferromagnetism in graphite driven by two-dimensional networks of point?defects. *Nature Physics* **5**, 2009. Article: 840 EP –.

[106] Esquinazi, P. et al. Ferromagnetism in oriented graphite samples. *Phys. Rev. B* **66**, iss. 2, 2002: 024429. DOI: 10.1103/PhysRevB.66.024429.

[107] Lehtinen, P. O. et al. Irradiation-Induced Magnetism in Graphite: A Density Functional Study. *Phys. Rev. Lett.* **93**, iss. 18, 2004: 187202. DOI: 10.1103/PhysRevLett.93.187202.

[108] Son, Young-Woo, Cohen, Marvin L., and Louie, Steven G. Half-metallic graphene nanoribbons. *Nature* **444**, no. 7117, 2006: 347–349. DOI: 10.1038/nature05180.

[109] Brar, Victor W. et al. Gate-controlled ionization and screening of cobalt adatoms on a graphene surface. *Nature Physics* **7**, no. 1, 2011: 43–47. DOI: 10.1038/nphys1807.

[110] Fritz, Lars and Vojta, Matthias. The physics of Kondo impurities in graphene. *Reports on Progress in Physics* **76**, no. 3, 2013: 032501.

[111] Rudenko, A. N. et al. Adsorption of cobalt on graphene: Electron correlation effects from a quantum chemical perspective. *Phys. Rev. B* **86**, iss. 7, 2012: 075422. DOI: 10.1103/PhysRevB.86.075422.

[112] Chen, Jian-Hao et al. Defect Scattering in Graphene. *Phys. Rev. Lett.* **102**, iss. 23, 2009: 236805. DOI: 10.1103/PhysRevLett.102.236805.

[113] Nordlund, K., Keinonen, J., and Mattila, T. Formation of Ion Irradiation Induced Small-Scale Defects on Graphite Surfaces. *Phys. Rev. Lett.* **77**, iss. 4, 1996: 699–702. DOI: 10.1103/PhysRevLett.77.699.

[114] Esquinazi, P. et al. Induced Magnetic Ordering by Proton Irradiation in Graphite. *Phys. Rev. Lett.* **91**, iss. 22, 2003: 227201. DOI: 10.1103/PhysRevLett.91.227201.

[115] Mao, Jinhai et al. Realization of a tunable artificial atom at a supercritically charged vacancy in graphene. *Nature Physics* **12**, 2016: 545 EP –.

[116] Cazalilla, M. A. et al. Local Moment Formation and Kondo Effect in Defective Graphene. *ArXiv e-prints*, July 2012. arXiv: 1207.3135 [cond-mat.str-el].

[117] Nanda, B R K et al. Electronic structure of the substitutional vacancy in graphene: density-functional and Green's function studies. *New Journal of Physics* **14**, no. 8, 2012: 083004.

[118] Kanao, Taro, Matsuura, Hiroyasu, and Ogata, Masao. Theory of Defect-Induced Kondo Effect in Graphene: Numerical Renormalization Group Study. *Journal of the Physical Society of Japan* **81**, no. 6, 2012: 063709. DOI: 10.1143/JPSJ.81.063709.

[119] El-Barbary, A. A. et al. Structure and energetics of the vacancy in graphite. *Phys. Rev. B* **68**, iss. 14, 2003: 144107. DOI: 10.1103/PhysRevB.68.144107.

[120] Pereira, Vitor M. et al. Disorder Induced Localized States in Graphene. *Phys. Rev. Lett.* **96**, iss. 3, 2006: 036801. DOI: 10.1103/PhysRevLett.96.036801.

[121] Pereira, Vitor M., Santos, J. M. B. Lopes dos, and Castro Neto, A. H. Modeling disorder in graphene. *Phys. Rev. B* **77**, iss. 11, 2008: 115109. DOI: 10.1103/PhysRevB.77.115109.

[122] Chen, C. J. Introduction to Scanning Tunneling Microscopy. Oxford University Press, 2007.

[123] Fischer, Øystein et al. Scanning tunneling spectroscopy of high-temperature superconductors. *Rev. Mod. Phys.* **79**, iss. 1, 2007: 353–419. DOI: 10.1103/RevModPhys.79.353.

[124] Giaever, Ivar. Energy Gap in Superconductors Measured by Electron Tunneling. *Phys. Rev. Lett.* **5**, iss. 4, 1960: 147–148. DOI: 10.1103/PhysRevLett.5.147.

[125] Luican, Adina, Li, Guohong, and Andrei, Eva Y. Scanning tunneling microscopy and spectroscopy of graphene layers on graphite. *Solid State Communications* **149**, no. 27, 2009. Recent Progress in Graphene Studies: 1151 –1156. DOI: https://doi.org/10.1016/j.ssc.2009.02.059.

[126] Peres, N. M. R. et al. Scanning tunneling microscopy currents on locally disordered graphene. *Phys. Rev. B* **79**, iss. 15, 2009: 155442. DOI: 10.1103/PhysRevB.79.155442.

[127] Li, Guohong, Luican, Adina, and Andrei, Eva Y. Self-navigation of a scanning tunneling microscope tip toward a micron-sized graphene sample. *Review of Scientific Instruments* **82**, no. 7, 2011: 073701. DOI: 10.1063/1.3605664. eprint: https://doi.org/10.1063/1.3605664.

[128] Bardeen, J. Tunnelling from a Many-Particle Point of View. *Phys. Rev. Lett.* **6**, iss. 2, 1961: 57–59. DOI: 10.1103/PhysRevLett.6.57.

[129] Binnig, G. et al. Surface Studies by Scanning Tunneling Microscopy. *Phys. Rev. Lett.* **49**, iss. 1, 1982: 57–61. DOI: 10.1103/PhysRevLett.49.57.

[130] Tersoff, J. and Hamann, D. R. Theory and Application for the Scanning Tunneling Microscope. *Phys. Rev. Lett.* **50**, iss. 25, 1983: 1998–2001. DOI: 10.1103/PhysRevLett.50.1998.

[131] Nagaoka, K. et al. Temperature Dependence of a Single Kondo Impurity. *Phys. Rev. Lett.* **88**, iss. 7, 2002: 077205. DOI: 10.1103/PhysRevLett.88.077205.

[132] Yazyev, Oleg V. and Helm, Lothar. Defect-induced magnetism in graphene. *Phys. Rev. B* **75**, iss. 12, 2007: 125408. DOI: 10.1103/PhysRevB.75.125408.

[133] Vergés, J. A. et al. Fit of Pariser-Parr-Pople and Hubbard model Hamiltonians to charge and spin states of polycyclic aromatic hydrocarbons. *Phys. Rev. B* **81**, iss. 8, 2010: 085120. DOI: 10.1103/PhysRevB.81.085120.

[134] Wehling, T. O. et al. Strength of Effective Coulomb Interactions in Graphene and Graphite. *Phys. Rev. Lett.* **106**, iss. 23, 2011: 236805. DOI: 10.1103/PhysRevLett.106.236805.

[135] Padmanabhan, Haricharan and Nanda, B. R. K. Intertwined lattice deformation and magnetism in monovacancy graphene. *Phys. Rev. B* **93**, iss. 16, 2016: 165403. DOI: 10.1103/PhysRevB.93.165403.

[136] Oleś, A. M. Antiferromagnetism and correlation of electrons in transition metals. *Phys. Rev. B* **28**, iss. 1, 1983: 327–339. DOI: 10.1103/PhysRevB.28.327.

[137] Cox, D. L. and Zawadowski, A. Exotic Kondo effects in metals: Magnetic ions in a crystalline electric field and tunnelling centres. *Advances in Physics* **47**, no. 5, 1998: 599–942. DOI: 10.1080/000187398243500. eprint: https://doi.org/10.1080/000187398243500.

[138] Roch, Nicolas et al. Observation of the Underscreened Kondo Effect in a Molecular Transistor. *Phys. Rev. Lett.* **103**, iss. 19, 2009: 197202. DOI: 10.1103/PhysRevLett.103.197202.

[139] Haug, Hartmut J.W. and Jauho, Antti-Pekka. Quantum Kinetics in transport and Optics of Semiconductors. Springer, 2008.

[140] Schiller, Avraham and Hershfield, Selman. Theory of scanning tunneling spectroscopy of a magnetic adatom on a metallic surface. *Phys. Rev. B* **61**, 2000: 9036.

[141] Affleck, Ian, Ludwig, Andreas W. W., and Jones, Barbara A. Conformal-field-theory approach to the two-impurity Kondo problem: Comparison with numerical renormalization-group results. *Phys. Rev. B* **52**, iss. 13, 1995: 9528–9546. DOI: 10.1103/PhysRevB.52.9528.

[142] Esat, Taner et al. Transfering spin into an extended π orbital of a large molecule. *Phys. Rev. B* **91**, iss. 14, 2015: 144415. DOI: 10.1103/PhysRevB.91.144415.

[143] Economou, L. V. Diagram Technique for Nonequilibrium Processes. *Soviet Physics JETP* **20**, no. 4, 1965: 1018.

[144] Kadanoff, L. P. and Baym, G. Quantum Statistical Mechanics. 1962.

[145] Kehrein, Stefan. Scaling and Decoherence in the Nonequilibrium Kondo Model. *Phys. Rev. Lett.* **95**, iss. 5, 2005: 056602. DOI: 10.1103/PhysRevLett.95.056602.

[146] Schoeller, Herbert and König, Jürgen. Real-Time Renormalization Group and Charge Fluctuations in Quantum Dots. *Phys. Rev. Lett.* **84**, iss. 16, 2000: 3686–3689. DOI: 10.1103/PhysRevLett.84.3686.

[147] Mühlbacher, Lothar and Rabani, Eran. Real-Time Path Integral Approach to Nonequilibrium Many-Body Quantum Systems. *Phys. Rev. Lett.* **100**, iss. 17, 2008: 176403. DOI: 10.1103/PhysRevLett.100.176403.

[148] Werner, Philipp et al. Weak-coupling quantum Monte Carlo calculations on the Keldysh contour: Theory and application to the current-voltage characteristics of the Anderson model. *Phys. Rev. B* **81**, iss. 3, 2010: 035108. DOI: 10.1103/PhysRevB.81.035108.

[149] Weiss, S. et al. Iterative real-time path integral approach to nonequilibrium quantum transport. *Phys. Rev. B* **77**, iss. 19, 2008: 195316. DOI: 10.1103/PhysRevB.77.195316.

[150] Schollwöck, U. The density-matrix renormalization group. *Rev. Mod. Phys.* **77**, iss. 1, 2005: 259–315. DOI: 10.1103/RevModPhys.77.259.

[151] Schollwöck, Ulrich. The density-matrix renormalization group in the age of matrix product states. *Annals of Physics* **326**, no. 1, 2011. January 2011 Special Issue: 96 –192. DOI: https://doi.org/10.1016/j.aop.2010.09.012.

[152] Arrigoni, Enrico, Knap, Michael, and Linden, Wolfgang von der. Nonequilibrium Dynamical Mean-Field Theory: An Auxiliary Quantum Master Equation Approach. *Phys. Rev. Lett.* **110**, iss. 8, 2013: 086403. DOI: 10.1103/PhysRevLett.110.086403.

[153] Landauer, Rolf. Electrical resistance of disordered one-dimensional lattices. *The Philosophical Magazine: A Journal of Theoretical Experimental and Applied Physics* **21**, no. 172, 1970: 863–867. DOI: 10.1080/14786437008238472.

[154] Büttiker, M. Four-Terminal Phase-Coherent Conductance. *Phys. Rev. Lett.* **57**, iss. 14, 1986: 1761–1764. DOI: 10.1103/PhysRevLett.57.1761.

[155] Meir, Yigal and Wingreen, Ned S. Landauer formula for the current through an interacting electron region. *Phys. Rev. Lett.* **68**, iss. 16, 1992: 2512–2515. DOI: 10.1103/PhysRevLett.68.2512.

[156] Ryndyk, Dmitry A. Theory of Quantum Transport at Nanoscale. An Introduction. Springer, 2016.

[157] Landauer, R. Spatial Variation of Currents and Fields Due to Localized Scatterers in Metallic Conduction. *IBM Journal of Research and Development* **1**, no. 3, 1957: 223–231. DOI: 10.1147/rd.13.0223.

[158] Fisher, Daniel S. and Lee, Patrick A. Relation between conductivity and transmission matrix. *Phys. Rev. B* **23**, iss. 12, 1981: 6851–6854. DOI: 10.1103/PhysRevB.23.6851.

[159] Economou, E. N. and Soukoulis, C. M. Static Conductance and Scaling Theory of Localization in One Dimension. *Phys. Rev. Lett.* **46**, iss. 9, 1981: 618–621. DOI: 10.1103/PhysRevLett.46.618.

[160] Jauho, Antti-Pekka. *Introduction to the Keldysh nonequilibrium Green function technique*. URL: materias.df.uba.ar/solidosa2012c2/files/2012/07/jauho.pdf. Notes. Last visited on 2019/10/23. 2012.

[161] Economou, E. N. Green's Functions in Quantum Physics. Ed. by Fulde, Peter. Springer, 1990.

[162] Kamenev, A. Field Theory of Non-Equilibrium Systems. Cambridge University Press, 2011.

[163] Langreth, D. C. Linear and Nonlinear Response Theory with Applications. In: *Linear and Nonlienar Electron Transport in Solids*. Ed. by Devreese, J. T. and Doren, E. Van. Springer, 1976.

[164] Nghiem, H. T. M. and Costi, T. A. Generalization of the time-dependent numerical renormalization group method to finite temperatures and general pulses. *Phys. Rev. B* **89**, iss. 7, 2014: 075118. DOI: 10.1103/PhysRevB.89.075118.

[165] Oguri, Akira. Mixed-state aspects of an out-of-equilibrium Kondo problem in a quantum dot. *Phys. Rev. B* **75**, iss. 3, 2007: 035302. DOI: 10.1103/PhysRevB.75.035302.

[166] Schmitt, Sebastian and Anders, Frithjof B. Comparison between scattering-states numerical renormalization group and the Kadanoff-Baym-Keldysh approach to quantum transport: Crossover from weak to strong correlations. *Phys. Rev. B* **81**, iss. 16, 2010: 165106. DOI: 10.1103/PhysRevB.81.165106.

[167] Dutt, Prasenjit et al. Effective equilibrium theory of nonequilibrium quantum transport. *Annals of Physics* **326**, no. 12, 2011: 2963 –2999. DOI: https://doi.org/10.1016/j.aop.2011.07.001.

[168] Fei, Zaiyao et al. Edge conduction in monolayer WTe2. *Nature Physics* **13**, 2017: 677. DOI: 10.1038/nphys4091.

[169] Sabater, C. et al. Topologically Protected Quantum Transport in Locally Exfoliated Bismuth at Room Temperature. *Phys. Rev. Lett.* **110**, iss. 17, 2013: 176802. DOI: 10.1103/PhysRevLett.110.176802.

[170] Mueller, Susanne et al. Nonlocal transport via edge states in InAs/GaSb coupled quantum wells. *Phys. Rev. B* **92**, iss. 8, 2015: 081303. DOI: 10.1103/PhysRevB.92.081303.

[171] Jia, Zhen-Yu et al. Direct visualization of a two-dimensional topological insulator in the single-layer $1T' - WTe_2$. *Phys. Rev. B* **96**, iss. 4, 2017: 041108. DOI: 10.1103/PhysRevB.96.041108.

[172] Xu, Cenke and Moore, J. E. Stability of the quantum spin Hall effect: Effects of interactions, disorder, and $\mathbb{Z}_2$ topology. *Phys. Rev. B* **73**, iss. 4, 2006: 045322. DOI: 10.1103/PhysRevB.73.045322.

[173] Schmidt, Thomas L. et al. Inelastic Electron Backscattering in a Generic Helical Edge Channel. *Phys. Rev. Lett.* **108**, iss. 15, 2012: 156402. DOI: 10.1103/PhysRevLett.108.156402.

[174] Kainaris, Nikolaos et al. Conductivity of a generic helical liquid. *Phys. Rev. B* **90**, iss. 7, 2014: 075118. DOI: 10.1103/PhysRevB.90.075118.

[175] Väyrynen, Jukka I., Pikulin, Dmitry I., and Alicea, Jason. Noise-Induced Backscattering in a Quantum Spin Hall Edge. *Phys. Rev. Lett.* **121**, iss. 10, 2018: 106601. DOI: 10.1103/PhysRevLett.121.106601.

[176] Väyrynen, Jukka I., Goldstein, Moshe, and Glazman, Leonid I. Helical Edge Resistance Introduced by Charge Puddles. *Phys. Rev. Lett.* **110**, iss. 21, 2013: 216402. DOI: 10.1103/PhysRevLett.110.216402.

[177] Rod, Alexia, Schmidt, Thomas L., and Rachel, Stephan. Spin texture of generic helical edge states. *Phys. Rev. B* **91**, iss. 24, 2015: 245112. DOI: 10.1103/PhysRevB.91.245112.

[178] Aseev, P. P. and Nagaev, K. E. Shot noise in the edge states of two-dimensional topological insulators. *Phys. Rev. B* **94**, iss. 4, 2016: 045425. DOI: 10.1103/PhysRevB.94.045425.

[179] Wang, Jianhui, Meir, Yigal, and Gefen, Yuval. Spontaneous Breakdown of Topological Protection in Two Dimensions. *Phys. Rev. Lett.* **118**, iss. 4, 2017: 046801. DOI: 10.1103/PhysRevLett.118.046801.

[180] Hsu, Chen-Hsuan et al. Nuclear-spin-induced localization of edge states in two-dimensional topological insulators. *Phys. Rev. B* **96**, iss. 8, 2017: 081405. DOI: 10.1103/PhysRevB.96.081405.

[181] Hsu, Chen-Hsuan et al. Effects of nuclear spins on the transport properties of the edge of two-dimensional topological insulators. *Phys. Rev. B* **97**, iss. 12, 2018: 125432. DOI: 10.1103/PhysRevB.97.125432.

[182] Wu, Congjun, Bernevig, B. Andrei, and Zhang, Shou-Cheng. Helical Liquid and the Edge of Quantum Spin Hall Systems. *Phys. Rev. Lett.* **96**, iss. 10, 2006: 106401. DOI: 10.1103/PhysRevLett.96.106401.

[183] Maciejko, Joseph et al. Kondo Effect in the Helical Edge Liquid of the Quantum Spin Hall State. *Phys. Rev. Lett.* **102**, iss. 25, 2009: 256803. DOI: 10.1103/PhysRevLett.102.256803.

[184] Tanaka, Yoichi, Furusaki, A., and Matveev, K. A. Conductance of a Helical Edge Liquid Coupled to a Magnetic Impurity. *Phys. Rev. Lett.* **106**, iss. 23, 2011: 236402. DOI: 10.1103/PhysRevLett.106.236402.

[185] Ström, Anders, Johannesson, Henrik, and Japaridze, G. I. Edge Dynamics in a Quantum Spin Hall State: Effects from Rashba Spin-Orbit Interaction. *Phys. Rev. Lett.* **104**, iss. 25, 2010: 256804. DOI: 10.1103/PhysRevLett.104.256804.

[186] Eriksson, Erik et al. Electrical control of the Kondo effect in a helical edge liquid. *Phys. Rev. B* **86**, iss. 16, 2012: 161103. DOI: 10.1103/PhysRevB.86.161103.

[187] Asbóth, János K., Oroszlány, László, and Pályi, András. A Short Couse on Topological Insulators. Springer, 2016. DOI: 10.1007/978-3-319-25607-8.

[188] Hasan, M. Z. and Kane, C. L. Colloquium: Topological insulators. *Rev. Mod. Phys.* **82**, iss. 4, 2010: 3045–3067. DOI: 10.1103/RevModPhys.82.3045.

[189] Anders, Frithjof B. Private communications. Unpublished as of publication date of this thesis.

[190] Hershfield, Selman, Davies, John H., and Wilkins, John W. Probing the Kondo resonance by resonant tunneling through an Anderson impurity. *Phys. Rev. Lett.* **67**, iss. 26, 1991: 3720–3723. DOI: 10.1103/PhysRevLett.67.3720.